

KIT SCIENTIFIC REPORTS 7686

Proceedings of the 11th IEA International Workshop on Beryllium Technology (BeWS-11)

Barcelona, Spain, 12-13 September 2013

Pavel Vladimirov, Jörg Reimann (eds)

Pavel Vladimirov, Jörg Reimann (eds)

**Proceedings of the 11th IEA International
Workshop on Beryllium Technology (BeWS-11)**

Barcelona, Spain, 12-13 September 2013

Karlsruhe Institute of Technology
KIT SCIENTIFIC REPORTS 7686

Proceedings of the 11th IEA International Workshop on Beryllium Technology (BeWS-11)

Barcelona, Spain, 12-13 September 2013

by
Pavel Vladimirov, Jörg Reimann (eds)

Impressum



Karlsruher Institut für Technologie (KIT)
KIT Scientific Publishing
Straße am Forum 2
D-76131 Karlsruhe

KIT Scientific Publishing is a registered trademark of Karlsruhe
Institute of Technology. Reprint using the book cover is not allowed.

www.ksp.kit.edu



*This document – excluding the cover – is licensed under the
Creative Commons Attribution-Share Alike 3.0 DE License
(CC BY-SA 3.0 DE): <http://creativecommons.org/licenses/by-sa/3.0/de/>*



*The cover page is licensed under the Creative Commons
Attribution-No Derivatives 3.0 DE License (CC BY-ND 3.0 DE):
<http://creativecommons.org/licenses/by-nd/3.0/de/>*

Print on Demand 2014

ISSN 1869-9669

ISBN 978-3-7315-0309-5

DOI: 10.5445/KSP/1000044741

CONTENTS

Summary	i
Beryllium Materials for the ITER First Wall Panels in Russian Federation <i>R. Giniyatulin, I. Mazul, A. Gervash, I. Kupriyanov, V. Sizenev, L. Gitarsky</i>	1
Recent progress on R&D of beryllides as advanced neutron multipliers for DEMO reactors in Japan <i>M. Nakamichi, J.-H. Kim</i>	7
Tritium release from HIDOBE-01 (798 K) beryllium pebbles on annealing with simultaneous electron radiation and magnetic field <i>A. Vitiņš, G. Kizāne, A. Matīss, G. Ivanov, V. Kinerte, J. Jansons, M. Zmitko</i>	15
Tritium and helium release from constrained and unconstrained beryllium pebbles irradiated up to high neutron dose in the HIDOBE-01 experiment <i>V. Chakin, R. Rolli, P. Vladimirov, and A. Moeslang</i>	39
Preliminary Synthesis of plasma-sintered binary beryllides <i>J.-H. Kim, M. Nakamichi</i>	53
Characterisation of Be-Ti rod fabricated by extrusion at 900 °C <i>P. Kurinskiy, A. Moeslang, H. Leiste, A.A. Goraieb, R. Rolli, S. Mueller</i>	57
Optimization of beryllide electrode fabrication as raw material for granulation by the rotating electrode method <i>M. Nakamichi, J.-H. Kim, D. Wakai</i>	65
Prototypic pebbles Fabrication of Titanium beryllidewith different chemical composition <i>J.-H. Kim, K. Yonehara, M. Nakamichi</i>	73
Environmental Control of Beryllium in NGK <i>K. Nojiri</i>	77
Preliminary results of a X-ray photoemission study on the interaction of energetic nitrogen ions with clean beryllium <i>M. Köppen, T. Phan & Ch. Linsmeier</i>	81
Packing Experiments of Beryllium Pebble Beds for the Fusion Reactor HCPB Blanket <i>J. Reimann, A. Abou-Sena, E. Brun, B. Fretz</i>	89
Some Thoughts about Beryllium Resources, Impurities in It and Necessity of Its Detritiation after Irradiation <i>B.N. Kolbasov*, V.I. Khripunov, A.Yu. Biryukov</i>	103

X-ray tomography study of porosity in neutron irradiated beryllium after post irradiation annealing <i>P. Vladimirov¹, C. Ferrero, V. Chakin, P. Kurinskiy, A. Moeslang, R. Pieritz, T. Weitkamp, E. Brun</i>	117
Development of thermo-mechanical computational model for circular beryllium reflector <i>S. V. Evropin, G. M. Kalinin, Y. I. Trifonov, L. S. Gitarsky, I. A. Gvozdkov, V. S. Sizenev</i>	135
Development of beryllium pebbles with fine grain structure for Fusion Application <i>I.B. Kupriyanova, G.N. Nikolaeva, S.K. Zavjalova, L.A. Kurbatovaa, N.E. Zabirovaa, M. Zmitko</i>	145
Fabrication Considerations for Large Beryllium Structures <i>M. A. Gallilee, G. Simmons</i>	153
Ab-initio study of hydrogen on beryllium surfaces <i>D. V. Bachurin, P. V. Vladimirov</i>	159
Hydrogen Interaction on Beryllium (0001) Surface <i>C. Stihl, P. Vladimirov</i>	169
Numerical research of the beryllia ceramics formation process <i>U. K. Zhapbasbayev, G. I. Ramazanova, Z. K. Sattinova</i>	183
Molecular Dynamics Simulation of Atomic Displacement Cascades in Beryllium <i>V. A. Borodin, P. V. Vladimirov</i>	193
Appendix 1: Organisation	199
Appendix 2: Final Programme	201
Appendix 3: Abstracts of presentations without submitted papers	205
Appendix 4: Participants	221

11th IEA International Workshop on Beryllium Technology (BeWS-11)

12-13 September 2013

Barcelona, Spain

The 11th IEA Beryllium Workshop (BeWS-11) was jointly organized by the KIT, Germany and Ciemat, Spain and was held at the Technical University of Catalonia, Barcelona Tech (UCP). The International Organizing Committee (IOC) and all participants expressed their appreciation to the Local Organizing Committee for the truly excellent organization of the workshop at Ciemat. About forty scientists participated, coming mainly from Europe, U.S.A., Russia, Japan, and Kazakhstan.

The workshop was supplemented by the BeYOND industrial forum, presenting a communication platform for researchers and industry with the aim to bring ITER to life and to prepare a “fast track” for DEMO.

The BeWS-11 was divided into one plenary and 6 technical sessions. The plenary session delivered a comprehensive overview of the beryllium related activities in Europe, USRF, RF, and Japan.

The technical sessions were on

- HIDOBE-01 PIE
- Beryllides
- Beryllium Safety
- Beryllium for Fusion
- Advanced Beryllium Production Technologies
- Modeling of Beryllium Materials.

During the workshop 35 presentations were given; the proceedings contain 20 of them as publications. For the remaining ones, the abstracts are listed in an appendix.

Beryllium Materials for the ITER First Wall Panels in Russian Federation

R.Giniyatulin^{*1}, Igor Mazul¹, Alexander Gervash¹, Igor Kupriyanov², Victor Sizenev³,
Leonid Gitarsky³

¹*Efremov Institute, Saint-Petersburg, Russia*

²*Bochvar Institute, Moscow, Russia*

³*JSC "Kompozit", Korolev, Moscow Region, Russia*

ABSTRACT

The ITER first wall (FW) panels will be coated by the beryllium flat tiles. For the present time three beryllium grades (S-65, TGP-56FW and CN-G01) are accepted for the FW application. Basing on the present FW design about four tons of 8-mm thick tiles are required to cover Russian Federation (RF) responsibility in FW production (40% of the FW panels). The beryllium grades TGP-56FW and S-65 will be used for this purpose. The R&D works are performed in the frames of the preparation for serial tiles production.

The results of experimental machining of Be-tiles are presented. Electric discharge machining (EDM) was used to produce developed patches of the small Be-tiles from large cylindrical billet (D~520 mm, H~230 mm). Different cutting regimes were investigated where cutting ratio, thickness of the cutting material and EDM parameters were varied. Performed metallographic analysis showed that surface quality depends from cutting ratio. This helped to optimize cutting ratio to get acceptable surface quality. It was detected that different EDM cutting ratio gives different thickness of the damaged layer with it maximum thickness about 30 micrometers. This layer has cracks which are evidence of the stresses. The chemical milling was used to remove damaged layer.

INTRODUCTION

The beryllium was selected as plasma facing material for the ITER First Wall (FW) from the beginning of the project. This material could be used by the physical boundary between plasma and blanket system (BS) due to the low atomic number, high capability of oxygen gettering, high thermal conductivity and good plasma compatibility. The present design of the FW [1] gives about 10 tons of the beryllium for the FW panels armouring in the case of 8 mm Be-plate thickness. Two types of FW panels will be armoured by beryllium. The normal heat flux (NHF) and enhanced heat flux (EHF) panels will be loading by stationary heat flux of $\sim(1\div 2)$ MW/m² and ≤ 5 MW/m² respectively.

The results of undertaken in Russian Federation (RF) preparation for beryllium armour tiles manufacturing are presented in the paper.

**Presenting Author*

1. DESCRIPTION OF THE REQUIREMENTS

In according with the ITER project agreement about 40% of the FW panels manufacturing and delivering is an obligation of RF. During few last years the design of the FW panels was significantly changed. The main result of the changes is in the increased heat flux up to 5 MW/m^2 . Fig.1 shows the last view of the FW panel with the rectangular-shaped hypervapour-type cooling channels and decreased in planar dimensions beryllium armour tiles.

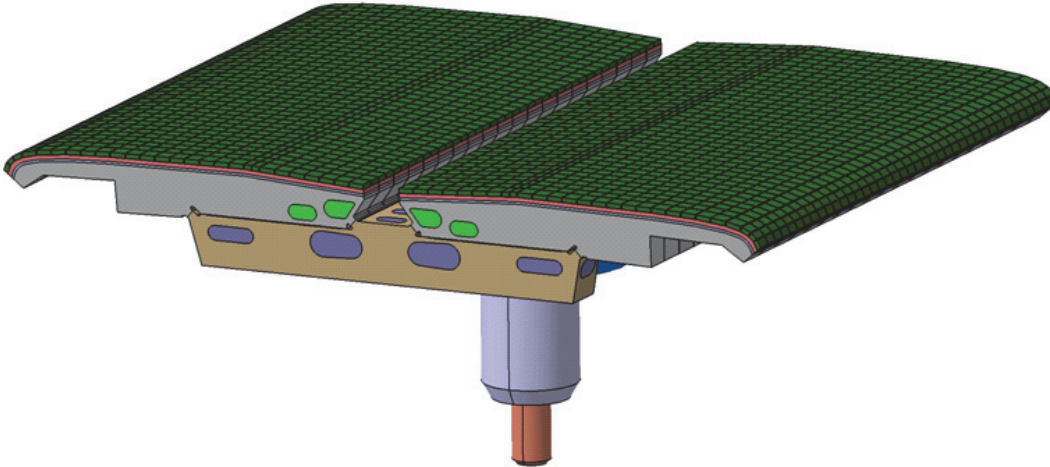


Fig.1. The view of the FW panel

The last experiments [2] have demonstrated that the planer dimensions of the tiles should be less than $(20 \times 20) \text{ mm}^2$ in order withstand to the cyclic heat loading at 5 MW/m^2 . The tiles (Fig.2) with the dimensions of $(16 \times 50 \times 8) \text{ mm}^3$ and with two transversal cut (7 mm deep) were proposed as the main variant for the EHF panels.

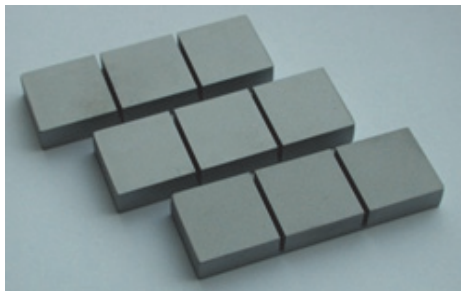


Fig.2. Beryllium tiles $(16 \times 50 \times 8) \text{ mm}^3$ for EHF FW panels

In the frames of RF obligation 179 FW panels (40%) with the area of $\sim 1,5 \text{ m}^2$ each should be covered by such beryllium tiles. The total weight of the tiles is about 4 tons. The total number of the tiles is about 325 000.

2. SELECTION OF THE BERYLLIUM GRADE

During many years work different beryllium grades were investigated [3,4]. The requirements for the beryllium (chemical, physical and mechanical properties) are presented in technical specification (TS) issued by ITER organization (IO) [5]. The selections of the beryllium grades which are accepting to the TS were done by IO and they are S-65 (USA), TGP-56FW (RF) and CN-G01 (China).

Two beryllium grades such as TGP-56FW and S-65 will be used in RF for the armour tiles manufacturing. About 2,4 tons of tiles will be manufactured from TGP-56FW grade and about 1,6 tons from S-65.

3. BERYLLIUM TILES MANUFACTURING AND INDUSTRY PREPARATION

Two technological lines are preparing for the beryllium tiles manufacturing.

The first line starts from the receiving of vacuum-cast beryllium ingots and includes their powdering, powder separating, pressing of the semi-blocks, wire electrical discharge machining (EDM) of the blocks to the tiles and chemical etching of the final tiles. This line is for the tiles from beryllium TGP-56FW.

The second line starts from the receiving of ready-made pressed blocks and includes only wire EDM of the blocks and chemical etching of the final tiles. This line is preparing for the tiles from beryllium S-65.

The significant part (about 60 %) of the tiles cost is in machining. That is why the optimization of this manufacturing step was required.

Wire EDM machining optimization for the beryllium tiles was started several years ago and was performed for the several dimensions of the tiles. At the beginning of the works the tile dimensions were (80x80x10) mm³ and now reduced up to (16x50x8) mm³. The different cutting rates (F) in combination with passing number give different roughness. Second and third “finishing” passes was exanimated (Table 1):

- First pass - F=2 mm/min
- Second pass - F=4 mm/min
- Third pass F=4 mm/min

Table 1. Dependence of the surface roughness from cutting rate and passes number

Mode/ Roughness	1 st pass	1 st +2 nd passes	1 st +2 nd +3 rd passes	1 st +3 rd passes
Ra, μm	1,8-2,5	1,15-1,25	0,5-0,8	0,5-1, 25

For the required roughness of $Ra \leq 6.3$ the first mode with the cutting rate of 2 mm/min and single pass is suitable. This mode was selected as the base technological mode.

The wire EDM machining gives the micro cracks of the surface. The deep of the cracks depends from the cutting rate. It was found that at F=2 mm/min the cracks are about 15 microns and two times deeper at F=4 mm/min. The chemical etching process is using in order to remove damaged layer. The thickness of 50 microns is removing by this way in order to be sure in cracks absence.

At the present time the wire EDM machining area (JSC "Kompozit") was prepared for the manufacturing of the tiles from beryllium S-65 (Fig. 3). Five EDM machines will be placed at this area.



Fig. 3. Wire EDM machining area for beryllium tiles manufacturing

Several pilot batches were produced during the manufacturing technology development (Fig. 4). These samples are using for the different experimental works with beryllium mockups.

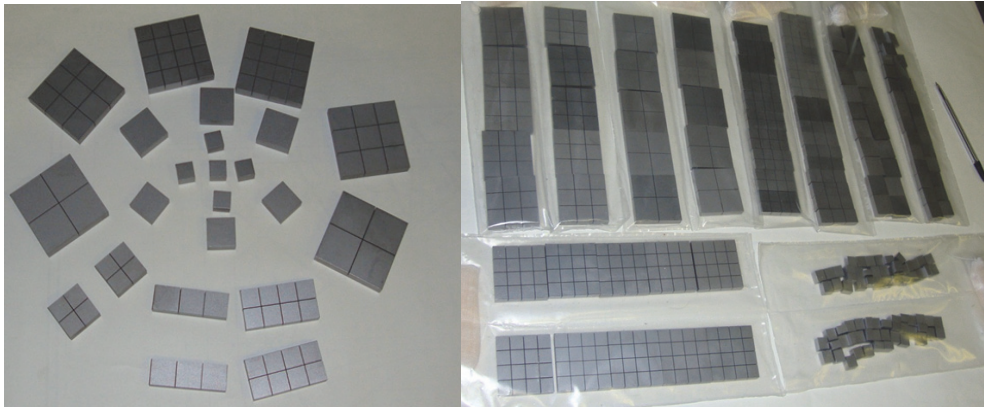


Fig. 4. Beryllium tiles with the dimensions from 12x12 mm² up to 50x50 12x12 mm²

4. CONCLUSIONS

For the present time the beryllium grade TGP-56FW was accepted by for the ITER first wall application. The main technological approaches for the beryllium TGP-56FW manufacturing and for the wire EDM machining were developed and tested. The Russian industry is ready to start serial production of the beryllium tiles.

REFERENCES

- [1] I. Mazul, A. Alekseev, V. Belyakov, D. Bondarchuk, R. Eaton, F. Escourbiac, A. Gervash, D. Glazunov, V. Kuznetsov, M. Merola, A. Labusov, I. Ovchinnikov, R. Raffray, R. Rulev, Russian development of enhanced heat flux technologies for ITER first wall, Fusion Engineering and Design, Volume 87, Issues 5–6, August 2012, Pages 437-442.

- [2] A. Gervash, R. Eaton, D. Glazunov, V. Kuznetsov, I. Mazul, V. Mirgorodsky, R. Mitteau, R. Raffray, R. Rulev, D. Semichev, Qualification of ITER EHF First Wall in Russia, To be presented in the International Symposium on Fusion Nuclear Technology (ISFNT-11), Barcelona, Spain, 16-20 September 2013.
- [3] R. Watson, D. Youchison, D. Dombrovski, R. Giniyatulin, I. Kupriyanov, Low cycle thermal fatigue testing of berylliums, *J. Fusion Engineering and Design* 37 (1997) 553-579.
- [4] A Gervash, R Giniyatulin, I Mazul, Comparative thermal cyclic test of different beryllium grades previously subjected to simulated disruption loads, *Fusion Engineering and Design*, Volume 46, Issues 2-4, November 1999, Pages 229-235.
- [5] V. Barabash, P. Chappuis, R. Eaton, M. Merola, R. Mitteau, R. Raffray, Materials for the ITER blanket first wall, Presented at 10th IEA International Workshop on Beryllium Technology, Karlsruhe, Germany, Sept 19-21 2012.

Recent progress on R&D of beryllides as advanced neutron multipliers for DEMO reactors in Japan

Masaru Nakamichi, Jae-Hwan Kim

*Fusion Research and Development Directorate, Japan Atomic Energy Agency,
2-166 Omotedate, Obuchi, Rokkasho, Aomori 039-3212, Japan*

ABSTRACT

A plasma sintering method has been proposed as new technique for beryllide synthesis and joining. This method results in powder surface activation that enhances powder particle sinterability and reduces high temperature exposure. From the results of beryllide synthesis experiments, it was clarified that the beryllide could be simultaneously synthesized and joined by the plasma sintering method. Beryllide rod of Be_{12}Ti has been successfully fabricated by the plasma sintering method. Using this plasma-sintered beryllide rod, prototype pebble of beryllide was performed by the rotating electrode method. From the results of beryllide granulation experiments, the prototype pebbles of Be_{12}Ti with 1 mm in average diameter were successfully fabricated.

KEYWORDS

Fusion blanket, Neutron multiplier, Beryllium intermetallic compound, Beryllide.

1. INTRODUCTION

Tritium needed as a fuel for fusion reactors is produced in the fusion blanket region by neutron capture reaction of lithium-6 (${}^6\text{Li}$). Neutron multiplier is required for adequate tritium breeding in the blanket of fusion reactors. Pure beryllium metal (Be) is one of the candidate materials for neutron multipliers in the fusion blanket [1,2]. However, in fusion reactors under high neutron flux and high temperature, some problems have been anticipated such as volumetric swelling and hydrogen generation reaction of Be [3]. Accordingly, advanced neutron multipliers with lower swelling and higher stability at high temperature are desired in pebble-bed blankets where both neutron multipliers and tritium breeders are supposed to be loaded as type of pebble, which would greatly affect fusion reactor design, especially the blanket operating temperature.

In parallel to the international thermonuclear experimental reactor (ITER) program, Broader Approach (BA) activities are being implemented by the EU and Japan, aiming at early realization of the fusion energy. Beryllium intermetallic compound (beryllide) such as Be_{12}Ti is a candidate of the advanced neutron multipliers because beryllide has more excellent potential under higher temperature than Be [4]. Based on the common interests of the EU and Japan in the demonstration fusion power (DEMO) reactors, the research and development (R&D) on beryllide are carried out through the DEMO R&D of the International Fusion Energy Research Centre (IFERC) project as a part of the BA activities from 2007 to 2016. This activity has the objective of development of granulation technique of beryllide and its characterization.

2. EXPERIMENTAL FACILITY

Beryllium and its alloys (> 3 wt.% Be) are defined as controlled chemical substances in Japan. The equipment for safely handling beryllium is required; furthermore, regulatory authorities need to be notified of its use. Therefore, the beryllium handling room was prepared for safety handling of beryllium [5]. This room consists of a beryllium handling area, an exhaust system room and an entrance area. Apparatuses for beryllium handling in the beryllium handling area were connected to an exhaust blower of a local ventilation system through a pre-filter and a high efficiency particulate air (HEPA) filter.

The maximum concentration of beryllium was limited to $< 0.001 \text{ mg/m}^3$, the beryllium content in the beryllium handling area was monitored twice a year, and the controlled air velocity of the hoods where beryllium is handled was maintained at 1 m/s according to the regulations. The protective wears included a Tyvek suit, impervious gloves, protective dust mask and protective shoes to prevent exposure to beryllium.

3. GRANULATION FLOW OF BERYLLIDE

Figure 1 shows a granulation flow scheme for the beryllide. To fabricate the beryllide pebbles, the rotating electrode method (REM) was selected because the experience base for its use is broad, not only for Be pebbles but also metallic pebbles in industry in general. For granulation by this method, beryllide with a rod shape is necessary for use as a raw electrode material. Major material synthesis methods are composed of sintering and melting methods for block fabrication. The sintering method is conducted with the compaction of raw material powder and the consolidation below the melting point such a powder metallurgy and a hot isostatic pressing methods. On the other hand, the melting method is carried out by the melting of raw material above the melting point and the mixing of molten materials such as a casting and an arc melting methods.

Conventional beryllide synthesis involves a powder metallurgy process involving a hot isostatic pressing method, a casting method, and an arc-melting method. However, beryllide synthesized conventionally is so brittle that it was not easy to fabricate the rod type by these methods. And, it was clarified that these methods had have problematic in terms of its complicated process, time-consuming characteristics and difficulty in composition control. On the other hand, the plasma sintering process is simple and easy to control. Therefore, the plasma sintering method has been proposed as new beryllide synthesis method [6, 7].

From the plasma-sintered beryllide electrode, prototypic beryllide pebbles of 1 mm average diameter were successfully fabricated, although the pebbles were composed of Be, $\text{Be}_{17}\text{Ti}_2$, and Be_{12}Ti phases due to a peritectic reaction caused by remelting [8]. Subsequently, a procedure using annealing treatments to homogenize to the Be_{12}Ti phase was evaluated. From the results of the annealing treatments on the prototypic pebbles, the pebble phase was homogenized to a single phase of Be_{12}Ti by annealing either at 1473 K for more than 8 h or at 1673 K for 1 h [9].

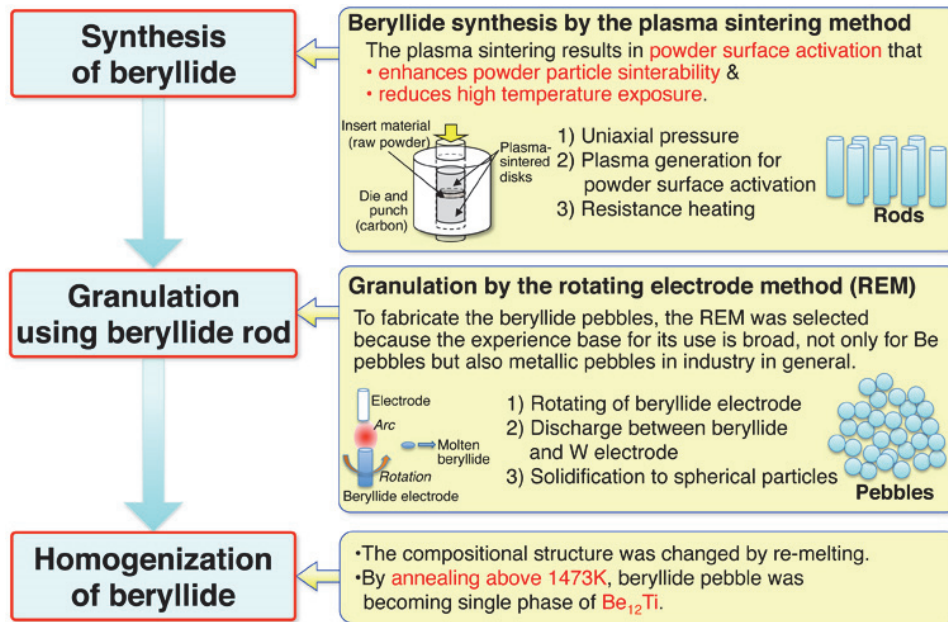


Figure 1. Granulation flow scheme of prototypic beryllide pebbles.

4. TRIAL FABRICATION OF BERYLLIDE PEBBLES BERYLLIDE ELECTRODE FABRICATION THE PLASMA SINTERING METHOD

The plasma sintering is an unconventional consolidation process that consists of plasma generation, resistance heating, and pressure application. The plasma discharge results in particle surface activation that enhances sinterability and reduces high temperature exposure. In addition, pressure application assists the densification process. Synthesis of intermetallic compounds starts with mixed elemental powder particles. In this process, the starting powder is loaded into the punches and die unit, and uniaxial pressure is applied for cold compaction. An electric current is applied to create the plasma environment and thus activate the particle surfaces. The powder compact is resistance-heated while uniaxial pressure is still applied to the material in the sintering mold. The plasma sintering apparatus (KE-Pas III) made by KAKEN Co. Ltd. was used. The joining schematic drawing by the plasma sintering method is shown in Fig. 2. To fabricate the beryllide electrode for the REM, joining to create a beryllide block was performed by use of two plasma-sintered beryllide disks.

To synthesize the beryllide disks, beryllium powder (purity: 99.4 wt.%) from RARE METALLIC Co. Ltd. and titanium powder (purity: 99.9 wt.%) from KOJUNDO CHEMICAL LABORATORY Co. Ltd. were mixed for 30 min using pestle and mortar made of Al₂O₃. The size of the Be and Ti powders was less than 45 μm. The mixed powder composition was 92.3 at.% Be and 7.7 at.% Ti for as much as a stoichiometric value of Be₁₂Ti beryllide. The plasma sintering was conducted at 1273 K for 20 min under a pressure of 50 MPa. Heating and cooling rates were approximately 100 and 30 K/min, respectively. The plasma-sintered beryllide disks were 20 mm in diameter and 4 mm in thickness.

Raw material powder (i.e., the same raw material used to fabricate the beryllide disks) was inserted between the plasma-sintered disks. The plasma sintering conditions for joining were the same as those for fabrication of the beryllide disk. The size of the joined beryllide block was

20 mm in diameter and 9 mm in length. Consolidation and joining of the beryllide were evaluated by hardness measurement and microstructure analysis using an electron probe micro-analyzer (EPMA; JXA-8530F by JEOL Co. Ltd.).

Neither cracks nor boundary lines were observed on the surface of the plasma-sintered joined block (see Fig.2). There is no defect in appearance. The plasma-sintered joined block showed metallic luster and was a dense material. Formations of Be_{12}Ti , $\text{Be}_{17}\text{Ti}_2$, and Be_2Ti intermetallic compounds and Be phase were identified. Microstructural observation showed no difference in microstructures between the inserted material and the bulk region of the plasma-sintered disk. The hardness on the insert material region and bulk material region were also identical. Thus, it was clarified that the beryllide can be directly synthesized and jointed by the plasma sintering method.

Based upon those joining examination results, a beryllide block 20 mm in diameter and 60 mm in length was successfully fabricated by the plasma sintering method. Because an electrode with 10 mm in diameter was necessary in the REM apparatus, the beryllide rod with 10 mm in diameter and 60 mm in length could be machined by a wire electric discharge (WED: Alpha-0iD made by FANUC Co. Ltd.) method from the plasma-sintered beryllide block with 20 mm in diameter and 60 mm in length. It has become clear that difficult-to-machine beryllide could be machined by the WED method accurately and efficiently.

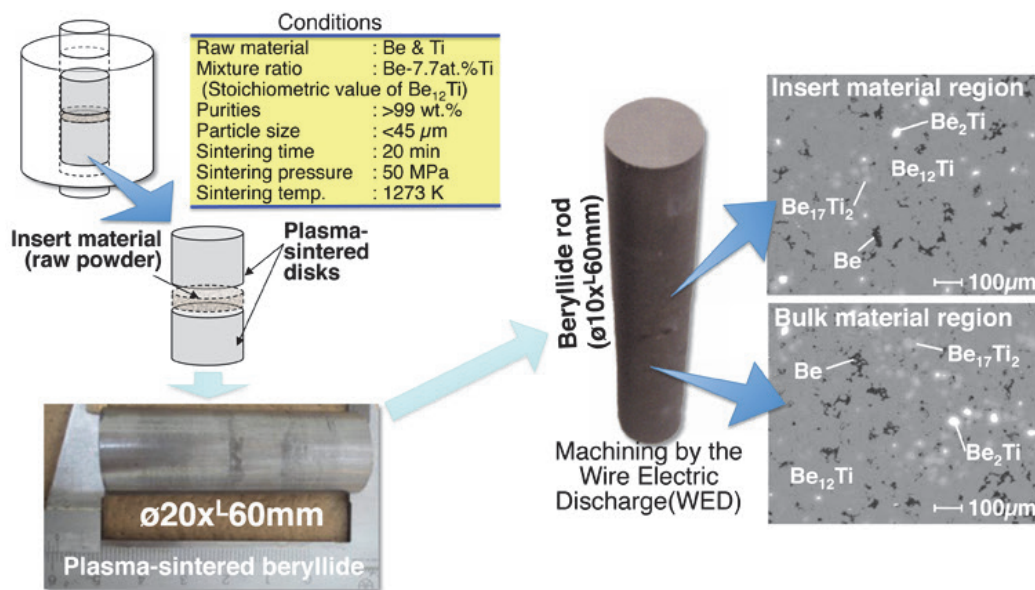


Fig. 2 Joining schematic drawing by the plasma sintering method for fabrication of beryllide electrode.

Trial fabrication of beryllide pebbles by the rotating electrode method

With this plasma-sintered beryllide electrode machined by the WED method, trial fabrication of prototypic beryllide pebbles was performed using a commercially available apparatus of the REM. Figure 3 shows real-time photograph of process, granulation conditions and photographs of the prototypic beryllide pebbles. In the REM a metal particle is produced as the end of a metal rod is melted while being rotated along its longitudinal axis. The melted metal is centrifugally ejected and forms droplets that solidify to spherical particles. In the present study, a granulation apparatus of the REM made by MINERVA KIKI Co. Ltd. that has a granulation chamber of 1000 mm in diameter was used. Specifications of this apparatus are 200 A in the maximum heating current and 20000 rpm in the maximum rotating speed.

The prototypic beryllide pebbles with 1 mm in diameter were successfully fabricated by the REM apparatus using a current of 80 A, a rotating speed of 6000 rpm, and the plasma-sintered beryllide rod as an electrode. The pressure of the granulation vacuum chamber with replacement of pure He gas was approximately 0.1 MPa. However, some molten particles were crushed against the inner surface of the granulation chamber before solidification. Therefore, the optimization of the granulation condition will be carried out using a custom-built rotating electrode granulation apparatus that has a larger granulation chamber.

As results of the granulation by the REM, it was clear that the beryllide pebbles were successfully fabricated from the plasma-sintered beryllide electrode, however, it was revealed that the compositional structure of the pebble was changed from re-melting that occurred during the granulation process. The pebble was composed of majority composition of $\text{Be}_{17}\text{Ti}_2$ with 55 % whereas the majority of the electrode was Be_{12}Ti with 91 %. This variation is due to heating of the arc discharge in this process and then re-melting of the beryllide, leading to the nucleation and crystal growth of a $\text{Be}_{17}\text{Ti}_2$ phase with the cooling process, followed by formation of a Be_{12}Ti phase outside of the $\text{Be}_{17}\text{Ti}_2$ phase according to a peritectic reaction. Therefore, an additional process would be necessary to homogenize the beryllide pebble to the Be_{12}Ti phase as the compositional target. The annealing treatment was examined to induce homogenization to the Be_{12}Ti phase.

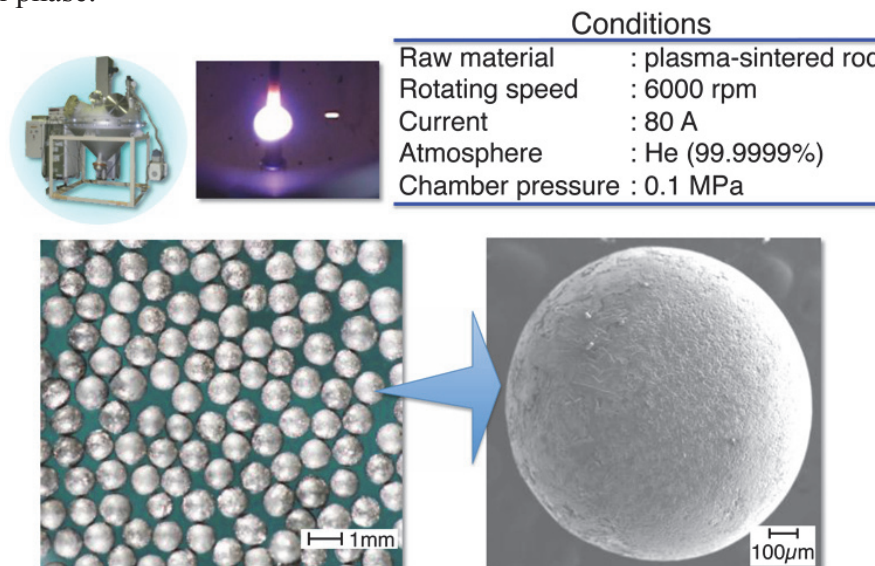


Fig.3 Real-time photograph of process, granulation conditions and photographs of the prototypic beryllide pebbles by the rotating electrode method

Homogenization of compositional structure of prototypic beryllide pebbles by the annealing treatment

The effect of the annealing time on compositional structure was evaluated at 1273 K for 1, 4 and 8 h under Ar atmosphere. Compositional images and the area fractions change of compositional structure in prototypic beryllide pebble by annealing treatments for each sintering time are shown in Fig. 4. It was confirmed from the result of the annealing treatment at 1473 K that the Be_{12}Ti phase increased with annealing time. Only the Be_{12}Ti phase was identified as a dark gray area; the black areas were confirmed as pores generated during the annealing treatment at 1473 K for 8 h. From the results of the annealing treatments on the prototypic pebbles, the pebble phase was homogenized to a single phase of Be_{12}Ti by consolidation enhancement.

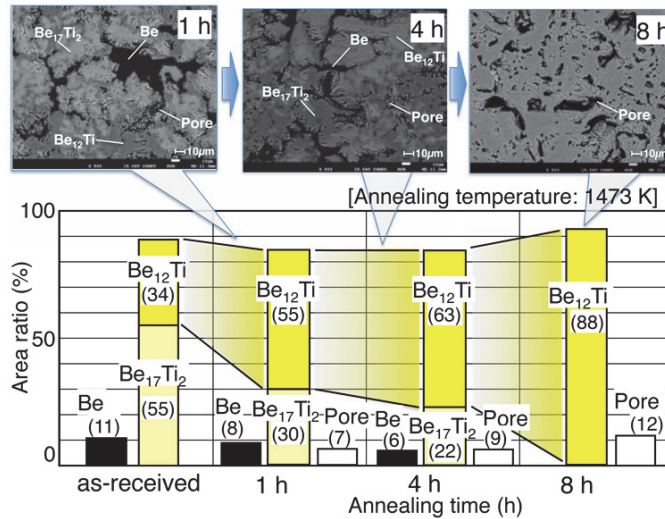


Fig.4 Compositional images and the area fractions change of compositional structure in prototypic beryllide pebble by annealing treatments for each sintering time

5. NEW CUSTOM BUILD GRANULATION APPARATUS

The prototypic beryllide pebbles with 1 mm in diameter were successfully fabricated using commercially available apparatus of the REM. However, some molten particles were crushed against the inner surface of the granulation chamber before solidification. Yield and volume of prototypic beryllide pebbles made by the commercially available apparatus was low. Therefore, new custom build apparatus of the REM was produced for the optimization of the beryllide granulation for mass production.

First of all, major granulation factors such as chamber size, electrode size, arc current, rotation control and insertion rate were extracted and organized. And then, combinatorial optimization of these factors was evaluated for higher yield with larger volume. From these results, new custom build apparatus by the REM was developed and installed in the DEMO R&D building in Rokkasho, BA site. From the result of granulation examination using this new apparatus, beryllide pebbles were successfully fabricated with high yield of more than 80% and quadruple volume.

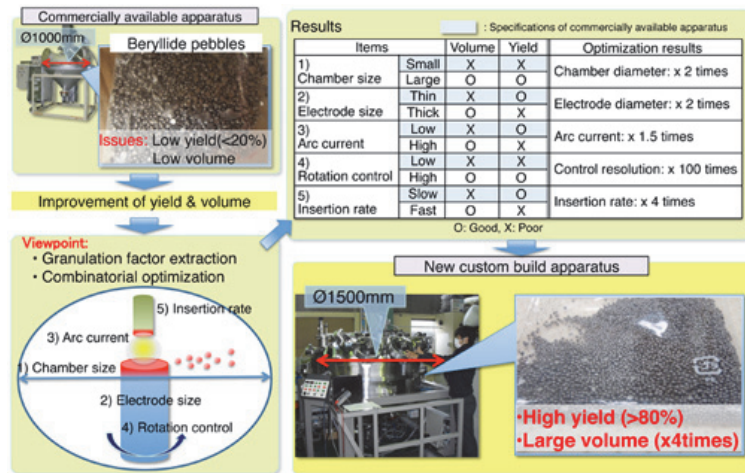


Fig.5 Optimization study for beryllides granulation using new custom build apparatus by the REM.

6. CONCLUSION

The plasma sintering method has been selected as a new synthesis method for beryllides because this method is very simple and easy to control. It was demonstrated that a beryllide could be simultaneously synthesized and joined by the plasma sintering method. Next, a beryllide electrode as raw material for granulation was successfully fabricated. Prototypic beryllide pebbles of 1 mm average diameter were successfully fabricated using the plasma-sintered beryllide electrode by the rotating electrode method.

It was revealed that the compositional structure of beryllide pebble was changed due to re-melting during the granulation process of the rotating electrode method. A procedure using annealing treatments to homogenize to the Be_{12}Ti phase was evaluated. From the results of the annealing treatments on the prototypic pebbles, the pebble phase was homogenized to a single phase of Be_{12}Ti by annealing at 1473 K for 8 h.

New custom build apparatus of the REM was produced for the optimization of the beryllide granulation for mass production. From the results of optimization study of new custom build apparatus by the REM, beryllide pebbles were successfully fabricated with high yield of more than 80% and quadruple volume.

REFERENCES

- [1] D. Tsuru, H. Tanigawa, T. Hirose, K. Mohri, Y. Seki, M. Enoeda, K. Ezato, S. Suzuki, H. Nishi M. Akiba, Achievements in the development of the water cooled solid breeder test blanket module of Japan to the milestones for installation in ITER, Nuclear Fusion, 9 (2009) 06524 (8pp).
- [2] F. Cismondi, S. Kecskés, M. Ilic, G. Légrádi, B. Kiss, O. Bitz, B. Dolensky, H. Neuberger, L.V. Boccaccini, T. Ihli, Design update, thermal and fluid dynamic analyses of the EU-HCPB TBM in vertical arrangement, Fusion Engineering and Design, 84 (2009) 607-612.
- [3] R.A. Anderl, K.A. McCarthy, M.A. Oates, D.A. Petti, R.J. Pawelko, G.R. Smolik, Steam-chemical reactivity for irradiated beryllium, Journal of Nuclear Materials, 258-263 (1998) 750-756.

- [4] M. Nakamichi, J.H. Kim, K. Munakata, T. Shibayama, K. Miyamoto, Preliminary characterization of plasma-sintered beryllides as advanced neutron multipliers, *Journal of Nuclear Materials*, In press, Corrected Proof, Available online 18 October 2012.
- [5] T. Hoshino, M. Nakamichi, Development of fabrication technologies for advanced breeding functional materials for DEMO reactors, *Fusion Engineering and Design*, 87 (2012) 486-492.
- [6] M. Nakamichi, K. Yonehara, Sintering properties of beryllides for advanced neutron multipliers, *Journal of Nuclear Materials*, 417 (2011) 765-768.
- [7] M. Nakamichi, J.H. Kim, D. Wakai, K. Yonehara, Development of a synthesis method of beryllides as advanced neutron multiplier for DEMO reactors, *Fusion Engineering and Design*, 84 (2012) 896-899.
- [8] M. Nakamichi, J. H. Kim, K. Yonehara, Novel granulation process of beryllides as advanced neutron multipliers, *Fusion Eng. Des.*, In Press Corrected Proof, Available online 26 March 2013.
- [9] M. Nakamichi, J. H. Kim, Homogenization treatment to stabilize the compositional structure of beryllide pebbles, *Journal of Nuclear Materials*, In Press, Corrected Proof, Available online 13 March 2013.

Tritium release from HIDOBE-01 (798 K) beryllium pebbles on annealing with simultaneous electron radiation and magnetic field

Aigars Vītiņš (a), Gunta Kizāne (a), Andris Matīss (a), Gennady Ivanov (a),
Valentīna Kinerte (a), Juris Jansons (a), Milan Zmitko (b)

(a) *Institute of Chemical Physics, University of Latvia, 4 Kronvalda Blvd.,
Riga, LV-1010, Latvia*

(b) *Fusion for Energy (F4E), c/ Josep Pla, n° 2, Torres Diagonal Litoral, Edificio B3,
08019 Barcelona, Spain*

ABSTRACT

This study presents results on tritium release from the beryllium pebbles irradiated for 646 full power days to the neutron fluence of $6.94 \times 10^{25} \text{ m}^{-2}$ ($E > 1.0 \text{ MeV}$) in the temperature zone 798 K in the first HIGH DOSE irradiation of BERYLLIUM (HIDOBE-01) experiment in the High Flux Reactor at Petten, The Netherlands. Post neutron-irradiation tritium release (PITR) was measured on annealing the pebbles at 773-1079 K for 3 h in a flow of 14-15 L/h of He + 0.1% H₂ purge gas with simultaneous 5 MeV fast electron irradiation of 10-13 MGy/h both without ($B=0$) and in a magnetic field of 1.5-1.7 T ($B=1.7 \text{ T}$). Seven successive electron irradiations at 780, 830, 880, 930, 978, 1045 and 1078 K released 16.6 GBq/g ($B=1.7 \text{ T}$) and 9.9 GBq/g ($B=0$) of tritium from the pebbles with $\varnothing \approx 1 \text{ mm}$. In these PITR experiment series for both $B=0$ and $B=1.7 \text{ T}$, a considerable tritium release ($>0.5 \text{ GBq/g}$) was observed only at temperatures above 920 K, but a considerable facilitating effect ($>50\%$) of a magnetic field of 1.5-1.7 T was observed at temperatures above 1040 K. An electron irradiation at 1070-1079 K released 22.2 GBq/g ($B=1.7 \text{ T}$) and 14.3 GBq/g ($B=0$) of tritium from the pebbles with $\varnothing \approx 0.5 \text{ mm}$. The tritium release rate, particularly in the case of the pebbles with $\varnothing \approx 1 \text{ mm}$, had strong irregular oscillations; the sharp peaks are indicative of burst release. The distinctive ascending trend of the tritium release rate on annealing at a constant temperature 830-1081 K with simultaneous 5 MeV fast electron radiation and a considerable following released fraction from a cooling pebble after the end of the annealing are indicative of activation of the tritium release by the electron radiation – possibly by production of structural changes, e.g. microcrevices, in the neutron-irradiated Be pebbles that facilitate the tritium release. The ascending curves of the tritium release rate at a constant temperature correspond to a release process that is different from the release determined by atomic diffusion, which is characterized by a descending tritium release rate at a constant temperature. A considerable facilitating effect (56-67%) of a magnetic field of 1.5-1.7 T with the simultaneous 5 MeV fast electron radiation on the tritium release from the HIDOBE-01 798 K 1.0 and 0.5 mm Be pebbles on annealing at temperatures above 1040 K was observed, but because of the fact that only one pair of pebbles was investigated on the magnetic field effect from each batch, the ability to draw general quantitative conclusions about the magnetic field effect is very limited by possible dissimilarity of the pebbles within the batch with respect to their initial total tritium amount and their tritium release properties.

1. INTRODUCTION

Beryllium pebbles are foreseen as a neutron multiplier to ensure sufficient tritium breeding in a ceramic breeder in the European Helium-Cooled Pebble-Bed (HCPB) breeding blanket for a future demonstration fusion power reactor (DEMO) [1, 2]. The 1 mm Be pebbles produced by Rotating Electrode Process (REP) are at present the reference multiplier material for the HCPB breeding blanket and will be used in the first HCPB Test Blanket Modules (TBMs) [2]. In the HCPB, the beryllium pebbles will be operated at 573-923 K under intense fast neutron radiation of about 10^{18} n m⁻² s⁻¹ and a high magnetic field of 7-10 T. Helium and tritium are produced in beryllium as a result of neutron-induced transmutations, causing swelling and tritium inventory. According to estimations of the present European HCPB concept, in a 40000 h operating time, the beryllium pebbles will receive the neutron fluence up to 3×10^{26} n m⁻² ($E_n > 1$ MeV), which will produce the displacement damage of about 80 dpa, 25700 appm helium and 640 appm tritium in beryllium [3-6]. The helium to tritium total yield ratio depends on the local neutron spectrum and can be from 10 to 100 [6]. One of tasks of blanket designing is to reduce tritium inventory in the beryllium pebble beds while maintaining their structural integrity and functional ability for their whole operating period. In the frame of the European programme for the development of the HCPB, a high dose irradiation of beryllium (HIDOBE) was performed in the High Flux Reactor at Petten, The Netherlands, to study neutron irradiation behaviour of beryllium pebble beds with respect to their dimensional stability and tritium inventory under DEMO relevant dpa/He ratios and temperatures [2, 7-15].

Therefore from the viewpoint of the future application in the HCPB, it is relevant to know how the operating factors of the HCPB, namely temperature, radiation and magnetic field, can affect the tritium inventory of the neutron-irradiated beryllium pebbles. In the present study, post-neutron-irradiation experiments were carried out to assess effects of temperature 470-1080 K, 5 MeV fast electron radiation of the dose rate of 10-13 MGy/h and a magnetic field of 1.5-1.7 T on tritium release from the beryllium pebbles irradiated in the HIDOBE-01 798 K temperature zone. A facilitating synergetic effect of the fast electron radiation and magnetic field on the tritium release on annealing of the BERYLLIUM and EXOTIC 8-3/13 neutron-irradiated beryllium pebbles was reported previously [16-19].

2. SAMPLES INVESTIGATED

The beryllium pebbles of a diameter 0.5 and 1.0 mm were manufactured by the rotating electrode method (REM) [20-23] at NGK Insulators Ltd., Handa City, Japan [7, 8, 11-15]. The BeO content in the pebbles is reported to be 0.36 wt.% BeO [8, 11, 15]; Fe, Al, Si, Mg are <0.1 wt.% each [11, 15]; U and Sc <0.01 wt.% each [11, 15]; Co <0.001 wt.% [11, 15]. The pebbles of a diameter 0.5 mm (pebble code 38sPC/3 [11]) and the pebbles of a diameter 1.0 mm, labelled with the year of production 2001 (pebble code 46sPC/3 [11]) were investigated in this study. The pebbles investigated in this study had been irradiated with neutrons in the temperature zone of 798 K of the HIDOBE-01 experiment (Table 1). The initial total tritium amount in these pebbles can be approximately estimated from the calculated amount of tritium produced 213 appm [11, 13] (i.e. 25.4 GBq/g in October 2007 and 19.2 GBq/g after 5 years in October 2012 as a result of tritium decay) as no considerable tritium release occurred at the HIDOBE neutron irradiation at 798 K [11, 13].

Table 1. Irradiation parameters of the beryllium pebbles in the temperature zone of 798 K of the HIDOBE-01 experiment [9-13]

Starting date of the HIDOBE-01 irradiation	08.06.2005
Termination date of the HIDOBE-01 irradiation	21.10.2007
Number of irradiation cycles	25
Number of full power (> 40 MW) days	646
Thermal neutron fluence (m^{-2})	5.21×10^{25}
Fast ($E > 1.0$ MeV) neutron fluence (m^{-2})	6.94×10^{25}
Displacements per atom (dpa) produced in beryllium	13.9
Amount of helium produced (appm)	2300
Amount of tritium produced (appm)	213
Activity of tritium produced in 1 g of the Be pebbles (GBq/g)	25.4

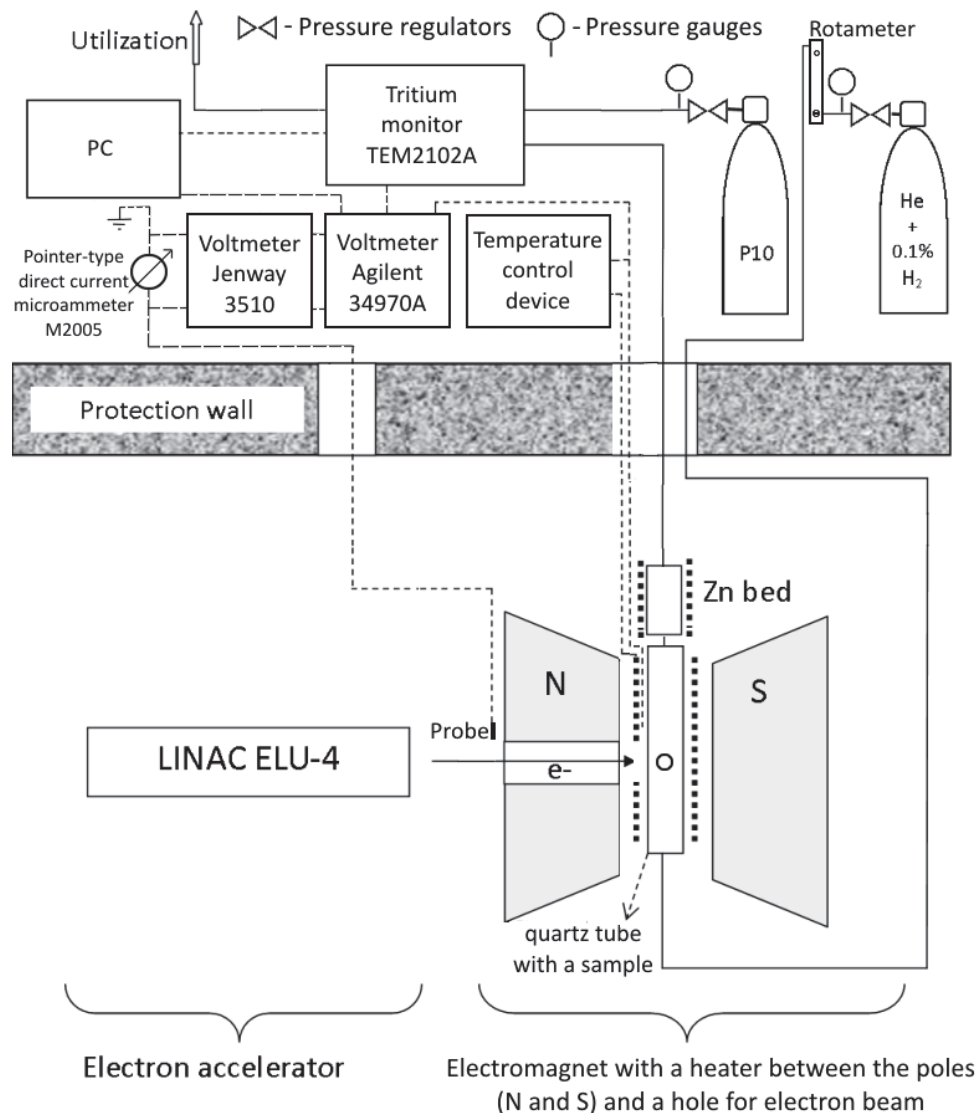


Fig. 1. Schematic view of the setup for investigation of effects of electron radiation and magnetic field on tritium release from pre-irradiated samples.

3. SETUP FOR ANNEALING WITH SIMULTANEOUS ELECTRON RADIATION AND MAGNETIC FIELD

3.1. General description of the experimental setup

Neutron-irradiated beryllium pebbles were annealed at temperatures up to 1083 K in a continuous flow of He + 0.1% H₂ purge gas at 14-15 L/h in a setup enabling exposure to 5 MeV fast electrons of 10-18 MGy/h and a magnetic field of 1.5-1.7 T. A schematic view of the setup is shown in Fig. 1. The source of electron radiation was a linear electron accelerator ELU-4, which emits 4 μ s long pulses of a 5 MeV electron beam with the frequency of 200 Hz. The magnetic field of 1.5-1.7 T was applied by means of a water-cooled electromagnet with a direct current of 55-60 A. The electromagnet has the interpolar gap of 20 mm in width and the channel of 20 mm in diameter in one of the poles for the electron beam. As it is shown in Fig. 1, interaction of electrons with magnetic field is minimized by directing the electron beam along the magnetic field lines in the setup. A temperature program up to 1083 K was imposed on the sample under study with an external electric heater near a quartz tube in the interpolar space of the electromagnet. One Be pebble was annealed in each tritium release experiment. Estimation of the dose rate of the electron radiation in the interpolar space is given below in section 3.2. A more detailed explanation of the components of the rig is given below in section 3.3.

3.2. Estimation of the dose rate of the electron radiation in the interpolar space

A setup for the dose rate estimation in the interpolar space is shown in Fig. 2. The dose rate of the 5 MeV electron radiation in the interpolar space was estimated with an aluminium plate of thickness more than 15 mm connected with the white wire through a light-spot direct-current microammeter M95 of the range 0-10 μ A to the earth. In order to estimate the dose of the 5 MeV electron radiation received by the sample, the current collected with the aluminium plate (Fig. 2) was related to the current collected with the copper plate used as a beam current detection probe (Fig. 3).



Fig. 3 (above). A copper plate as a beam current detection probe in front of the electromagnet core. The channel for the electron beam through an electromagnet pole is visible in the centre.

Fig. 2 (on the left-hand side). An aluminium plate of thickness more than 15 mm for the dose rate estimation in the interpolar space.

The results of the dose rate estimation are shown in Fig. 4, where the current collected with the aluminium plate, i.e. the manually-recorded readings of microammeter M95, have been calculated to the dose rate [Gy/h] according to: $P = I \times U \times 3600 / (m \times S)$, where I – the current [A] measured with microammeter M95; $U = 5 \times 10^6$ V – the voltage corresponding to the accelerated electrons; 3600 – the number of seconds in 1 h; $m = 0.00255$ kg/cm² – the mass of the layer, where a uniform absorption of the 5 MeV electron radiation is assumed [24]; $S = 3.14$ cm² – the cross-section area of the channel ($\varnothing = 20$ mm) for the electron beam through an electromagnet pole. It is worth noting that thickness 15 mm of the aluminium plate in the interpolar space was sufficient for a complete absorption of the 5 MeV electron beam as the density of aluminium is 2.7 g/cm³. From the comparison shown in Fig. 4, we may conclude that the current [μ A] collected with the copper probe may be multiplied by an empirical factor of 0.175 to get the estimation of the dose rate [MGy/h] of the 5 MeV electron radiation in the interpolar space of the electromagnet.

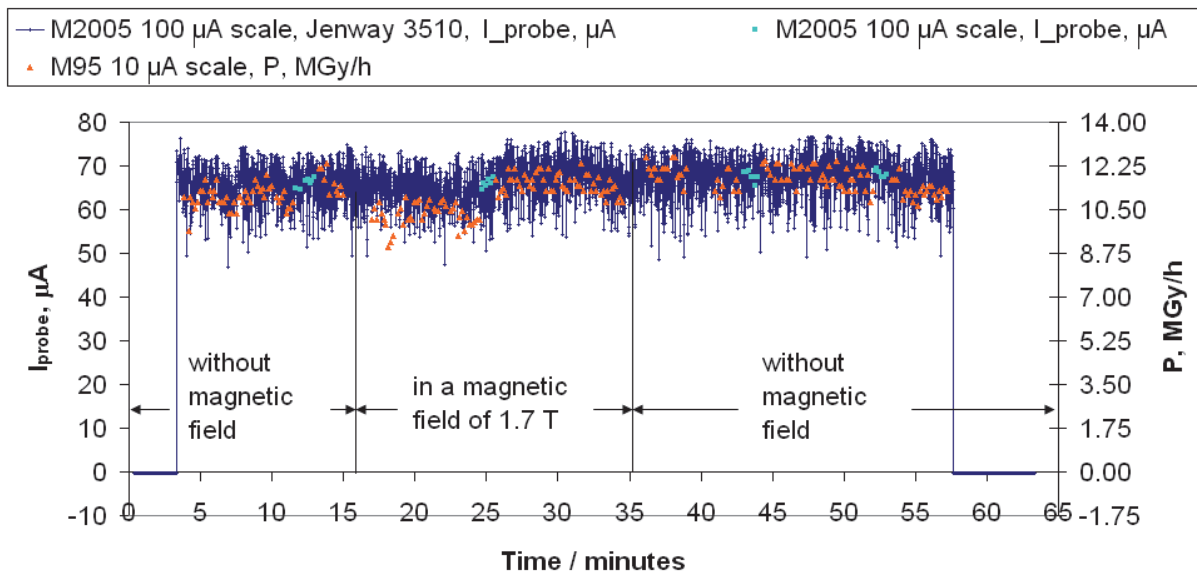


Fig. 4. Dose rate estimation of the 5 MeV electron radiation in the interpolar space of the electromagnet.

3.3. Description of the components of the experimental setup for annealing of samples

An assembled set of the quartz tube for the Be pebble under study is shown in Fig. 5. The Be pebble under study was placed in removable inner tube 3, which was put into outer tube 2 through the ground glass joint. The flow of the purge gas He + 0.1% H₂ entered tube 2 through inlet tube 1 and exited through the silicon rubber tube on the outlet of tube 2. Inner tube 3 had a slit enabling gas flow in the vicinity of the sample under study. Type S thermocouple 6 was used both to measure the sample temperature and to drive the temperature control device for the given temperature program.

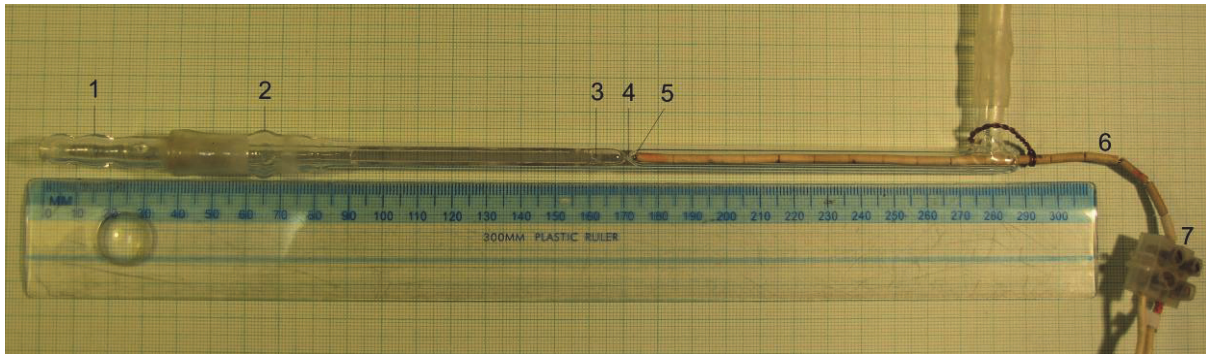


Fig. 5. Quartz tubes for the Be pebble under study: 1 – an inlet quartz tube with an inner conical ground glass joint; 2 – an outer quartz tube with an outer conical ground glass joint; 3 – a removable inner quartz tube for the Be pebble under study; 4 – a sealed-in inner quartz tube for a type S thermocouple; 5 – the hot junction of the type S thermocouple; 6 – the type S thermocouple; 7 – the cold junction of the type S thermocouple.

A setup for the Be pebble under study in the interpolar space of the electromagnet is shown in Fig. 6. Outer quartz tube 2 had been fixed so that the inner removable quartz tube was in the electron beam, i.e. it was visible just above the edge through the channel in the pole from the front of the electromagnet (Fig. 3), but the hot junction of the type S thermocouple was not in the electron beam, i.e. it was below the edge of the channel. Outer quartz tube was fixed with a metal clamp resting on thermal insulation blocks 8 (Fig. 6), which were fixed with a wedge-shaped aluminium plate and with additional aluminium plates. As the type S thermocouple was only 18 cm in length, the temperature of its cold junction was measured with type K thermocouple 5 (Fig. 6) with respect to ice bath 9 (Fig. 7). The 5 MeV electron radiation itself heated the Be pebble under study up to about 473 K. In order to apply higher programmed temperatures to the pebble, an electrical heater embedded in thermal insulation blocks 8 was operated by means of a temperature control device based on a derivatograph “MOM” (Budapest, Hungary).

An electrical heater surrounded the quartz tube in the thermal insulation blocks. The thermal insulation block on the side of the electron beam (the left block in Fig. 6) had a hole where the sample under study was supposed to be so that the thermal insulation did not cover the sample from the side of the electron beam. Regarding the estimation of the dose absorbed by the sample under study, we must note that the dose rate estimation described in section 3.2 is based on the assumption that the 5 MeV electron radiation is uniformly absorbed by material proportionally to its density in the layer of mass 2.55 g/cm^2 [24]. The sample was separated from the electron beam only by two quartz tube walls of thickness less than 2 mm each. The density of quartz is less than 2.7 g/cm^3 ; and total thickness of the separating quartz walls was less than 4 mm. Therefore, the mass of the separating quartz layer was less than 1.08 g/cm^2 . A beryllium pebble with diameter 1 mm and the density of 1.85 g/cm^3 has the maximum layer mass of 0.185 g/cm^2 . Therefore, the total layer mass was 1.265 g/cm^2 , which was less than 2.55 g/cm^2 . That means that the pebble under study in the experimental setup was under the 5 MeV electron radiation within the range of its uniform absorption.

An assembled view of the thermo-magnetic rig ready for tritium release experiments is shown in Fig. 7. Beam current detection copper plate 3 is visible between flange 1 and the electromagnet. Plate 3 was connected via the red wire through a pointer-type direct current microammeter M2005 of the range 0-100 μA to the earth. The temperature of the zinc bed was measured with a type K thermocouple with respect to ice bath 9 and maintained at 673-683 K during the tritium release experiments with tube furnace 8 and a temperature controller

based on a controlling millivoltmeter III4541. A pair of steel tubes (outside \varnothing 6 mm, inside \varnothing 4 mm, each about 15 m in length) was used for the purge gas He + 0.1% H₂ flow from a laboratory room to an accelerator room and back to the laboratory room. Transparent bendable PVC tubes 4 and 5 (Fig. 7, outside \varnothing 9 mm, inside \varnothing 6 mm, each about 1-1.5 m in length) were used to connect the thermo-magnetic rig to the purge gas He + 0.1% H₂ flow.

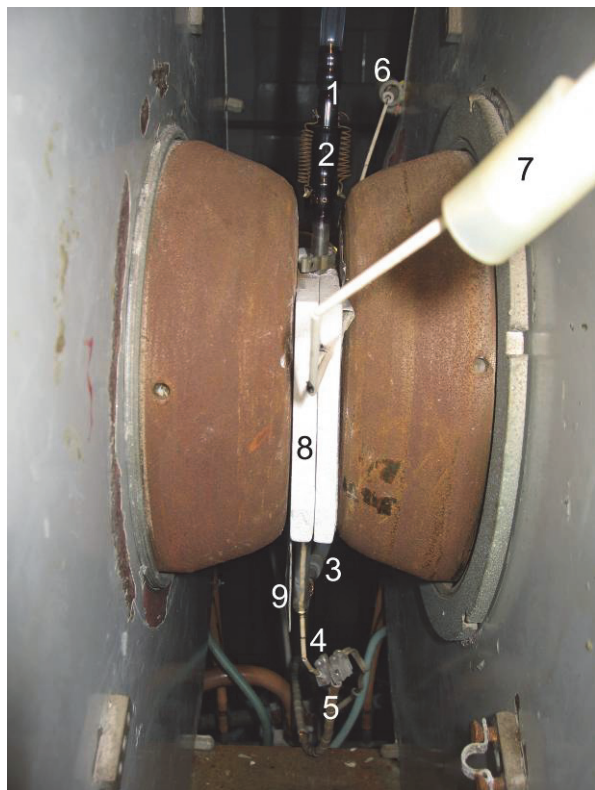


Fig. 6. Setup for the Be pebble under study in the inter-polar space: 1 – the inlet quartz tube; 2 – the outer quartz tube; 3 – the outlet silicon rubber tube to the zinc bed; 4 – the cold junction of the type S thermocouple; 5 – a type K thermocouple to measure the temperature of cold junction 4; 6 and 7 – connecting wires to the electrical heater of the sample under study; 8 – thermal insulation blocks for the electrical heater; 9 – wedge-shaped aluminium plate to fix blocks 8 in the inter-polar space.



Fig. 7. Assembled view of the thermo-magnetic rig: 1 – a flange of the electron beam window of electron accelerator ELU-4; 2 – an aluminium tube for a cooling stream of pressurized air; 3 – a copper plate as an electron beam detecting probe; 4 and 5 – inlet and outlet tubes of the purge gas He + 0.1% H₂ respectively; 6 – the outer quartz tube; 7 – thermal insulation blocks for the electrical heater; 8 – a tube furnace for heating the zinc bed; 9 – a Dewar flask with an ice bath for the cold junctions of type K thermocouples.

4. MEASUREMENT OF TRITIUM RELEASE AND DATA ACQUISITION WITH PC

The tritium release was performed in a continuous flow of He + 0.1% H₂ purge gas at 14-15 L/h. The He + 0.1% H₂ gas and the Ar + 10% CH₄ (P-10) counting gas were supplied by “AGA Gas AB” (Enköping, Sweden) and used as-received without further purification. Both the gas cylinders were equipped with “Linde” BASELINE™ two-stage pressure regulators C106/2A for the output pressure 0-50 psi (0-3.45 bar). Pressure regulators C106/2A enabled steady gas flows during long-duration tritium release experiments. In our experiments, the output pressure of the regulators was in the range 0.4-0.8 bar. The rate of He + 0.1% H₂ flow was set to 14-15 L/h with a high-resolution valve of a 150-mm “Cole-

Parmer” flowmeter RZ-03295-10 of the range 0-283 mL/min (0-17 L/h). The tritium activity in the purge gas He + 0.1% H₂ was continuously measured with a proportional counter DDH 32 with an operating volume of 300 cm³ built in a tritium monitor TEM 2102A operated as a frequency counter in the repeat mode at the counting time of 120 s and registered in a file with a PC using an RS-232 serial printer interface of TEM 2102A and the Eltima RS232 Data Logger software. The Ar + 10% CH₄ (P-10) counting gas in the proportional counter had the flow rate 42-45 L/h so that the ratio of the counting gas to the purge gas was 3:1. The count rate was corrected for the system background as determined at the start and the end of each experiment. The tritium release rate of the sample was calculated from the corrected count rate and the measured flow rate of the purge gas. The total released tritium activity was calculated by integrating the release rate over the time where a release was measurable. The radioactivity of tritium released was calculated as GBq/g to 1 g of the sample of Be pebbles.

The temperatures of the sample (thermo-emfs of the type S and K thermocouples) and the Zn bed, indicating voltages of the high voltages reduced by 1:1000 and gas-flow sensors of TEM 2102A and output voltage of millivoltmeter Jenway 3510 (Fig. 1) were continuously measured with an Agilent 34970A multichannel digital voltmeter with an Agilent 34902A multiplexer and recorded with a PC using the Agilent BenchLink Data Logger 3 software.

In order to estimate the dose rate of the 5 MeV electron radiation received by the sample, the current collected with the copper plate used as a beam current detection probe (Fig. 3) was continuously measured with a pointer-type direct-current microammeter M2005 in the range of 0-100 μ A. As the linear electron accelerator ELU-4 emits 5 MeV electron beam as pulses of duration of 4 μ s with frequency 200 Hz, for meaningful data acquisition with voltmeter Agilent 34970A connected to PC, millivoltmeter Jenway 3510 was connected in parallel to microammeter M2005, and the output voltage of Jenway 3510 was measured with Agilent 34970A and collected with PC.

5. RATIONALE OF THE POST NEUTRON-IRRADIATION TRITIUM RELEASE EXPERIMENTS

The maximum temperature of the beryllium pebble bed and the maximum temperature of the structural EUROFER steel contact surface with the Be pebbles are supposed to be 923 and 823 K respectively in the HCPB design [1, 2]. Therefore, tritium release experiments in the range of the operating temperatures of 573-923 K [1, 2, 4] is of the maximum interest from the viewpoint of the HCPB design. The temperature range of the experiments extended to higher temperatures up to 1073 K is significant to study tritium release properties of neutron-irradiated Be pebbles for possible future development of the pebble bed blanket [2, 25]. Effect of radiation on the tritium release was investigated using 5 MeV fast electron radiation. The time of irradiation with electrons in one experiment was 3 h, which was the optimum to get sufficient results of the tritium release and for normal operation of the electron accelerator. Therefore, experiment series of successive irradiations with 5 MeV fast electrons were planned for this study with successively increasing temperatures of the Be pebble under study: 480 (without additional heating), 780, 830, 880, 930, 978, 1045 and 1078 K. Pairs of experiments of each type were performed – one without magnetic field and another one with a magnetic field of 1.5-1.7 T.

6. RESULTS

6.1. Results of tritium release experiments with a pair of 1.0 mm pebbles

Tritium release curves of the series of post neutron-irradiation experiments with a pair of the 1.0 mm pebbles labelled with the year of production 2001 (pebbles code 46sPC/3/08 and 46sPC/3/09) are shown in Figs. 8-23. The mass of pebbles 46sPC/3/08 and 46sPC/3/09 was 1.24 and 1.23 mg respectively; their diameters were measured with digital callipers as 0.91-1.21 mm (pebble 46sPC/3/08 was an oblong pebble) and 1.09 mm respectively. The PC-recorded curves of the probe current (the light blue curves in Figs. 8-23) indicate the presence of the 5 MeV electron radiation for 3 h during the experiments. The acting factors in figures are denoted as T – temperature as a result of external heating under the given temperature program, R – 5 MeV fast electron radiation of the dose rate 10-13 MGy/h, M – a magnetic field of 1.5-1.7 T.

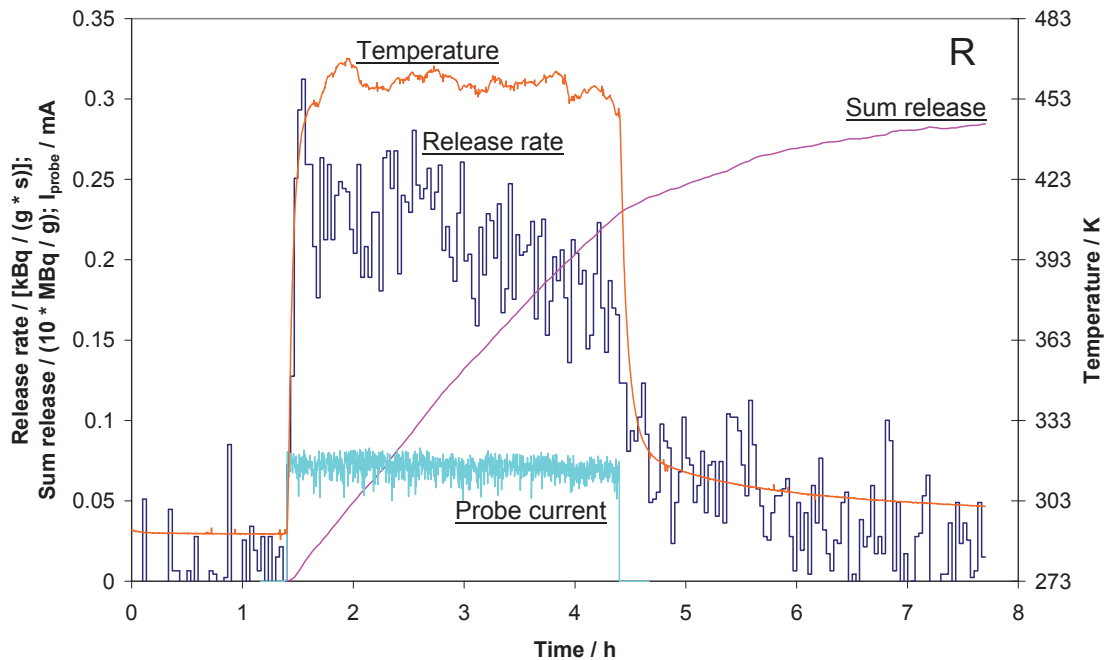


Fig. 8. Tritium release from pebble 46sPC/3/08. The maximum temperature: 468 K. The estimated dose of the electron irradiation: 37.3 MGy (the average electron flux 1.097×10^{13} electrons $\text{cm}^{-2} \text{s}^{-1}$). The final tritium sum release: 2.85 MBq/g (0.015% of the estimated initial total tritium 19.2 GBq/g).

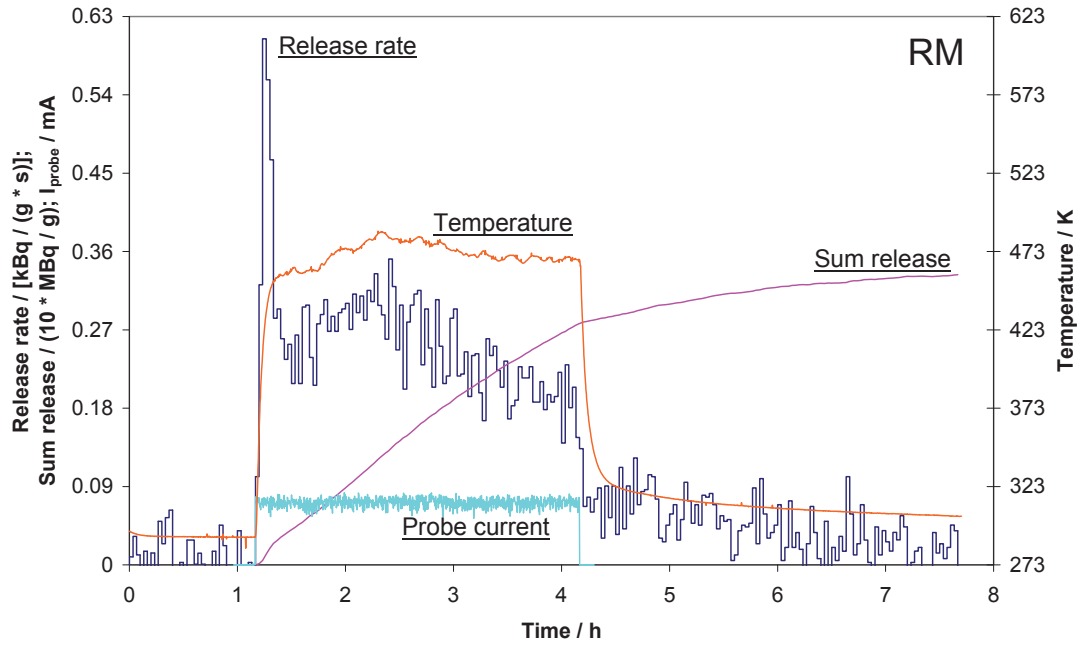


Fig. 9. Tritium release from pebble 46sPC/3/09. The maximum temperature: 486 K. The estimated dose of the electron irradiation: 37.5 MGy (the average electron flux 1.104×10^{13} electrons $\text{cm}^{-2} \text{s}^{-1}$). The final tritium sum release: 3.33 MBq/g (0.017% of the estimated initial total tritium 19.2 GBq/g).

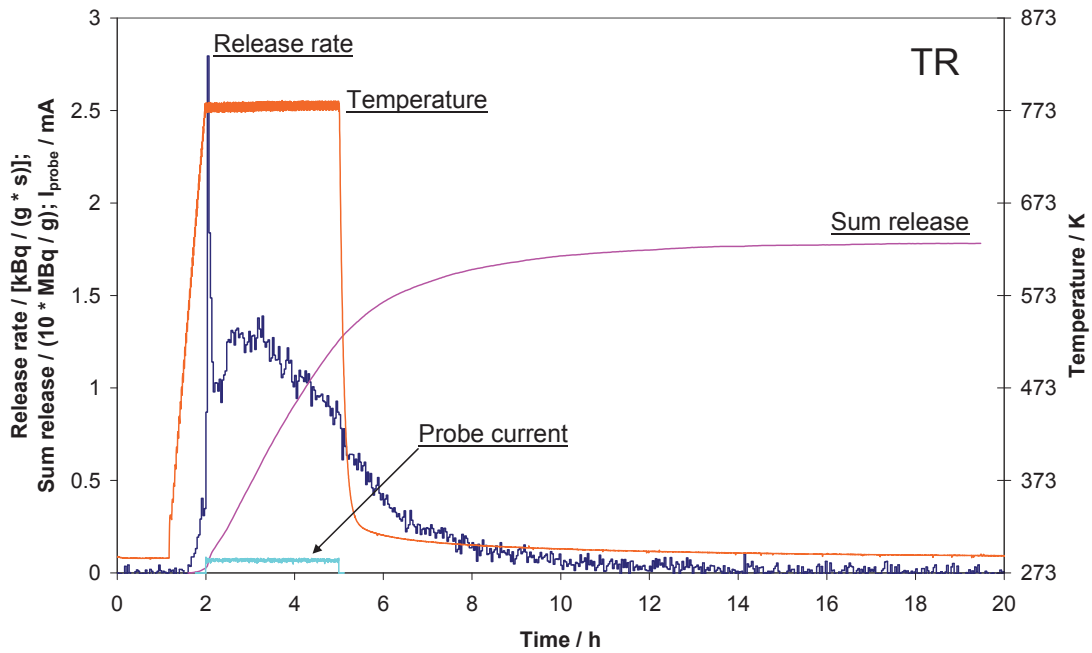


Fig. 10. Tritium release from pebble 46sPC/3/08. The maximum temperature: 784 K. The estimated dose of the electron irradiation 36.4 MGy (the average electron flux 1.072×10^{13} electrons $\text{cm}^{-2} \text{s}^{-1}$). The final tritium sum release: 17.8 MBq/g (0.093% of the estimated initial total tritium 19.2 GBq/g).

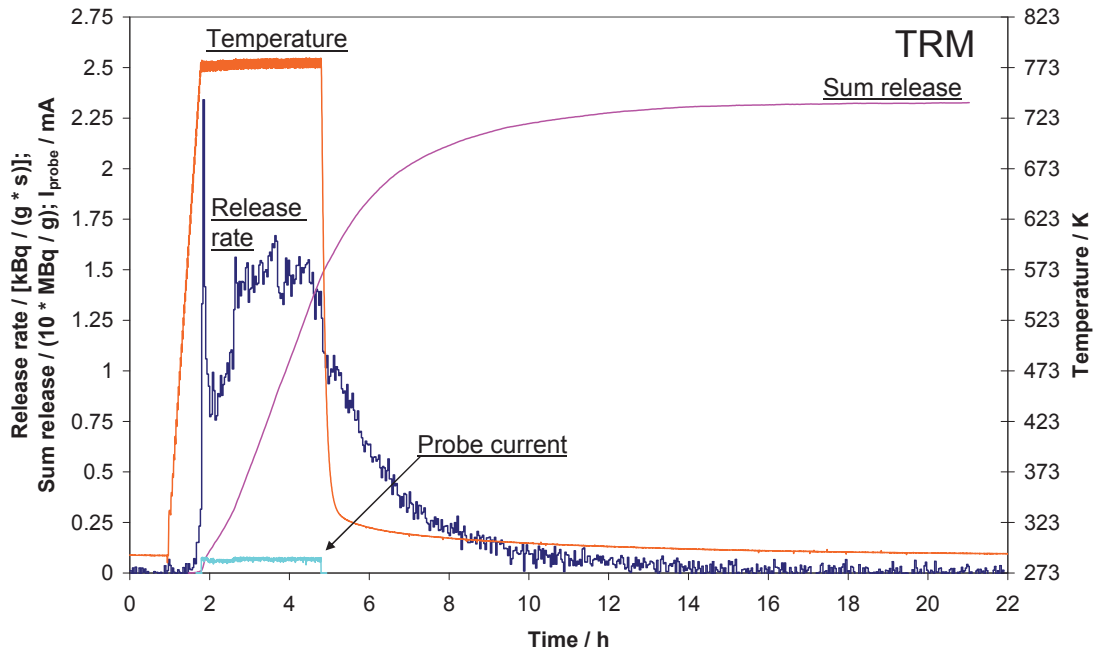


Fig. 11. Tritium release from pebble 46sPC/3/09. The maximum temperature: 782 K. The estimated dose of the electron irradiation: 35.2 MGy (the average electron flux 1.036×10^{13} electrons $\text{cm}^{-2} \text{s}^{-1}$). The final tritium sum release: 23.3 MBq/g (0.12% of the estimated initial total tritium 19.2 GBq/g).

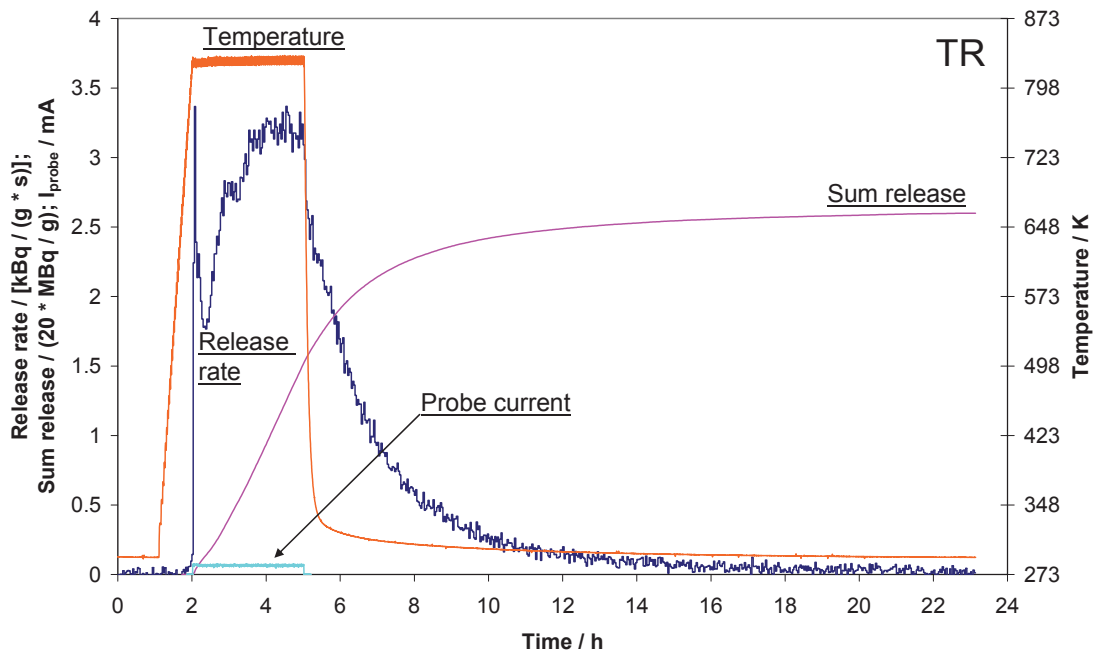


Fig. 12. Tritium release from pebble 46sPC/3/08. The maximum temperature: 833 K. The estimated dose of the electron irradiation: 34.9 MGy (the average electron flux 1.027×10^{13} electrons $\text{cm}^{-2} \text{s}^{-1}$). The final tritium sum release: 52.0 MBq/g (0.27% of the estimated initial total tritium 19.2 GBq/g).

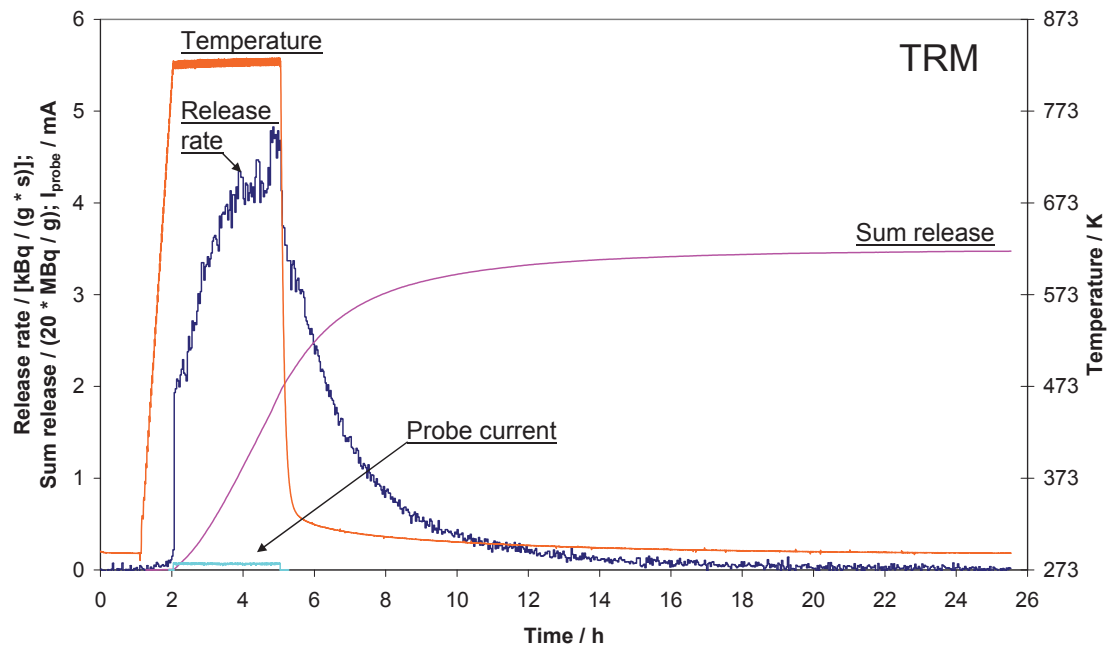


Fig. 13. Tritium release from pebble 46sPC/3/09. The maximum temperature: 831 K. The estimated dose of the electron irradiation: 35.5 MGy (the average electron flux 1.046×10^{13} electrons $\text{cm}^{-2} \text{s}^{-1}$). The final tritium sum release: 69.5 MBq/g (0.36% of the estimated initial total tritium 19.2 GBq/g).

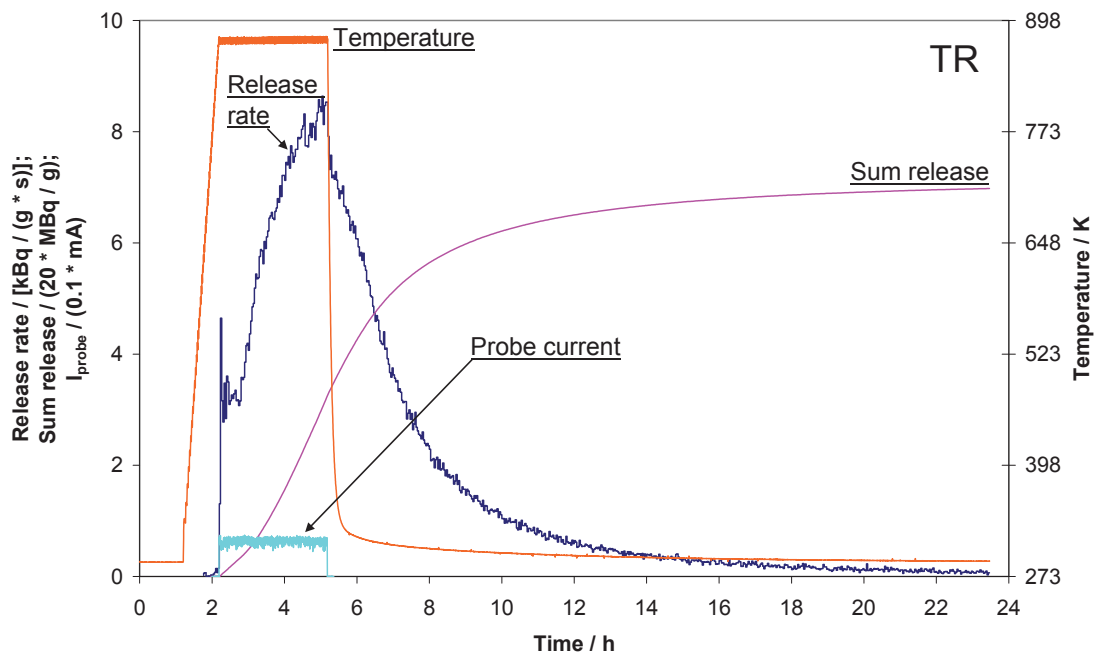


Fig. 14. Tritium release from pebble 46sPC/3/08. The maximum temperature: 880 K. The estimated dose of the electron irradiation: 33.3 MGy (the average electron flux 0.980×10^{13} electrons $\text{cm}^{-2} \text{s}^{-1}$). The final tritium sum release: 140 MBq/g (0.73% of the estimated initial total tritium 19.2 GBq/g).

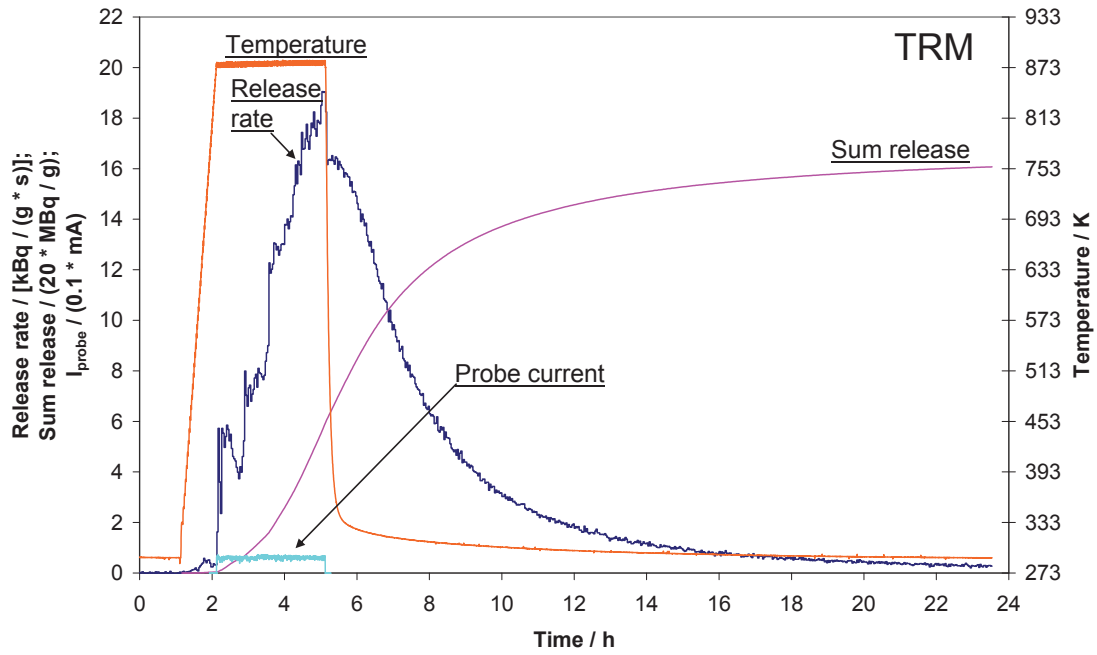


Fig. 15. Tritium release from pebble 46sPC/3/09. The maximum temperature: 882 K. The estimated dose of the electron irradiation: 31.9 MGy (the average electron flux 0.940×10^{13} electrons $\text{cm}^{-2} \text{s}^{-1}$). The final tritium sum release: 321 MBq/g (1.67% of the estimated initial total tritium 19.2 GBq/g).

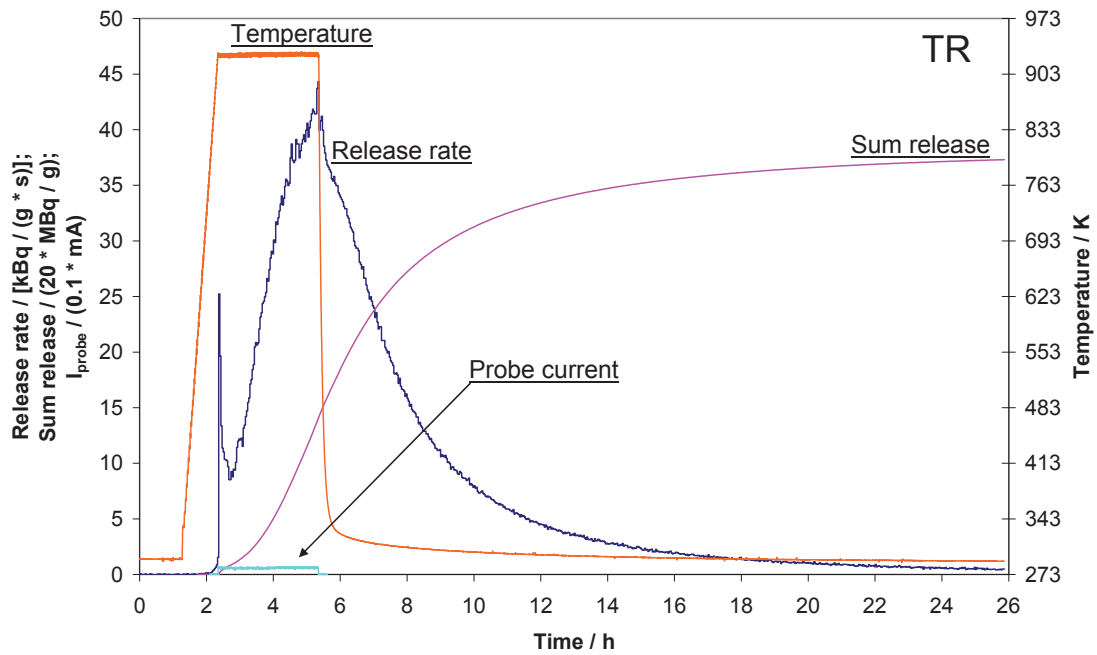


Fig. 16. Tritium release from pebble 46sPC/3/08. The maximum temperature: 930 K. The estimated dose of the electron irradiation: 31.6 MGy (the average electron flux 0.930×10^{13} electrons $\text{cm}^{-2} \text{s}^{-1}$). The final tritium sum release: 746 MBq/g (3.89% of the estimated initial total tritium 19.2 GBq/g).

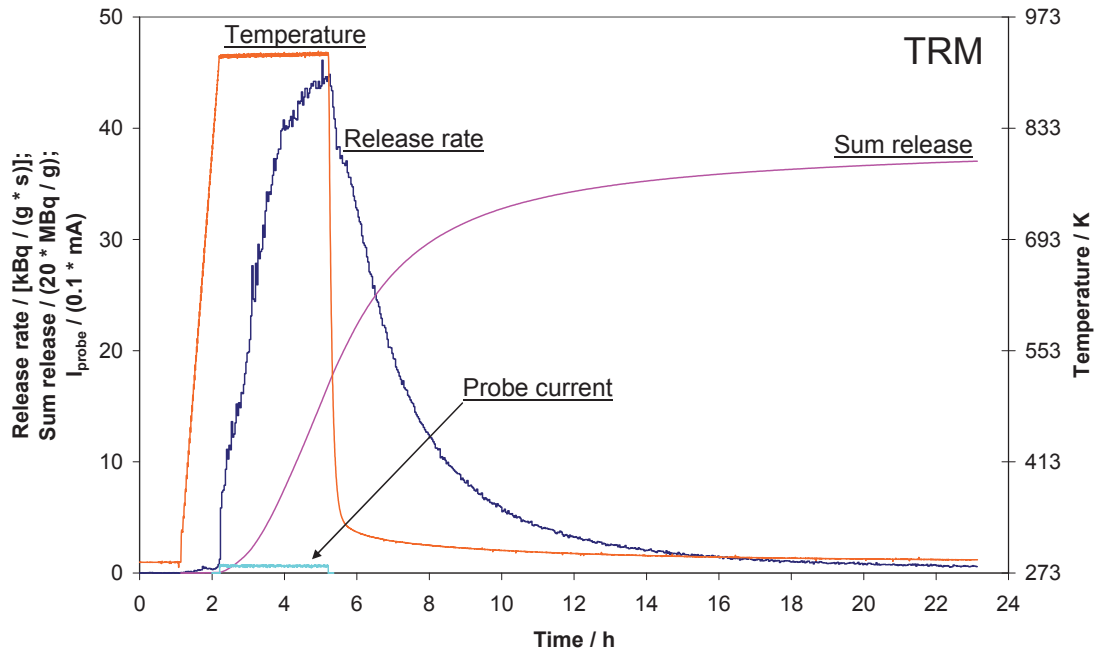


Fig. 17. Tritium release from pebble 46sPC/3/09. The maximum temperature: 930 K. The estimated dose of the electron irradiation: 33.8 MGy (the average electron flux 0.995×10^{13} electrons $cm^{-2} s^{-1}$). The final tritium sum release: 741 MBq/g (3.86% of the estimated initial total tritium 19.2 GBq/g).

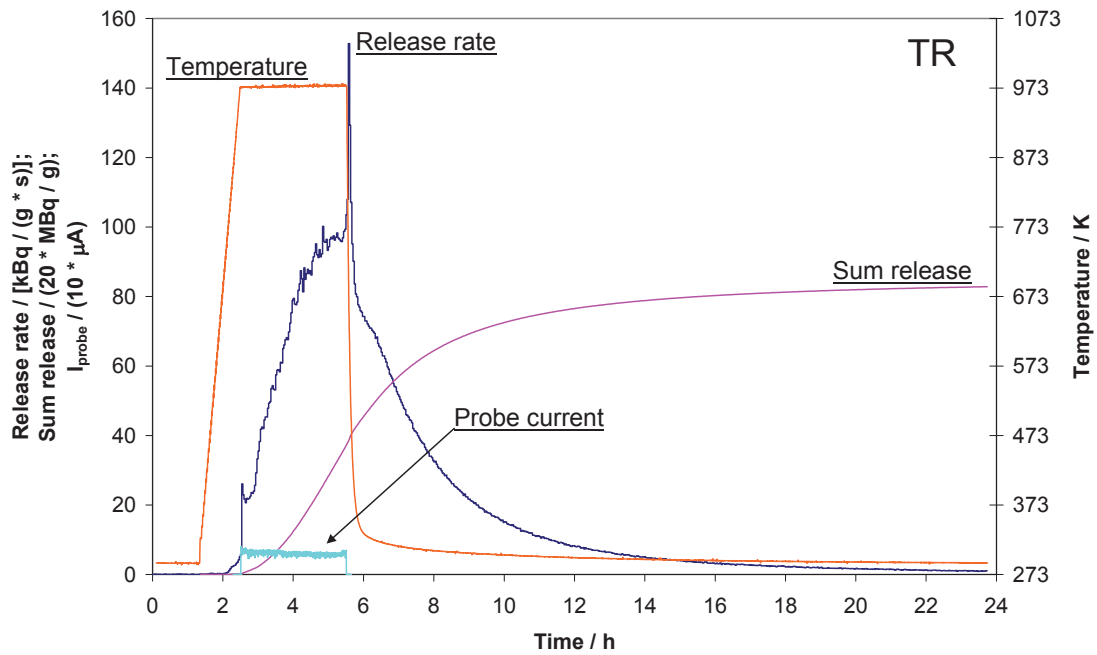


Fig. 18. Tritium release from pebble 46sPC/3/08. The maximum temperature: 979 K. The estimated dose of the electron irradiation: 31.8 MGy (the average electron flux 0.936×10^{13} electrons $cm^{-2} s^{-1}$). The final tritium sum release: 1.66 GBq/g (8.63% of the estimated initial total tritium 19.2 GBq/g).

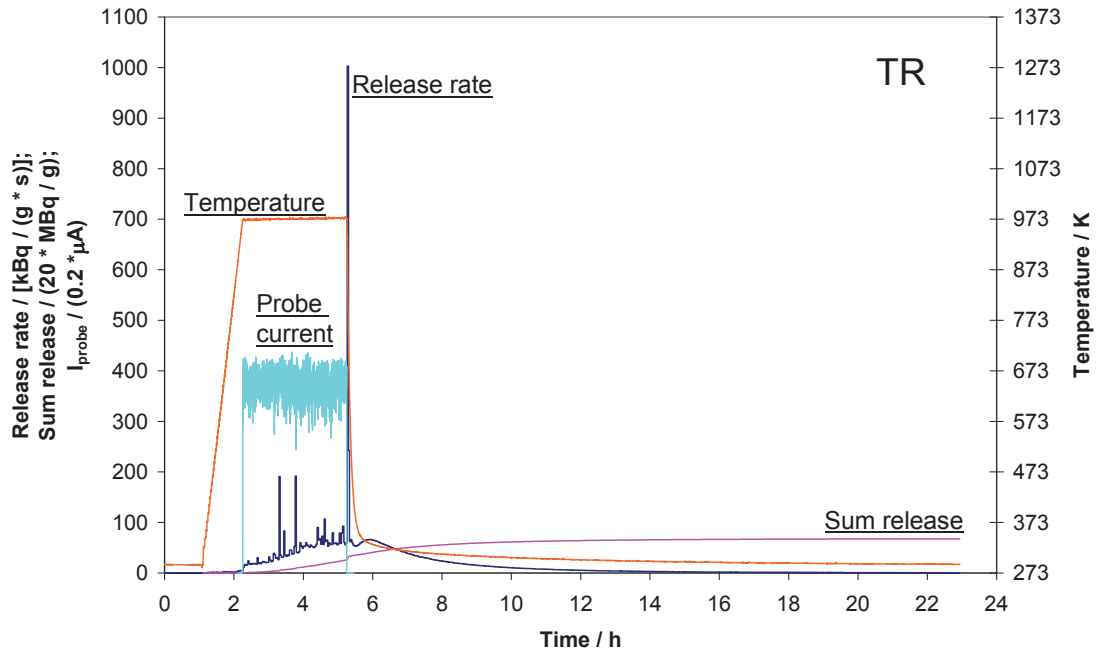


Fig. 19. Tritium release from pebble 46sPC/3/09. The maximum temperature: 978 K. The estimated dose of the electron irradiation: 39.3 MGy (the average electron flux 1.156×10^{13} electrons $\text{cm}^{-2} \text{s}^{-1}$). The final tritium sum release: 1.35 GBq/g (7.05% of the estimated initial total tritium 19.2 GBq/g).

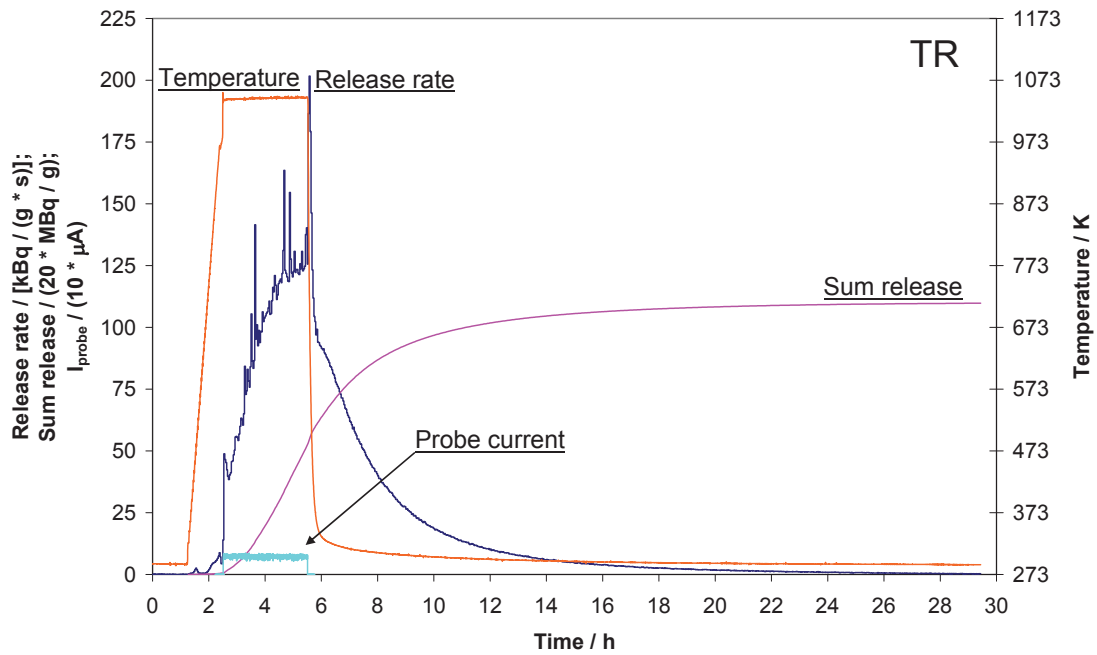


Fig. 20. Tritium release from pebble 46sPC/3/08. The maximum temperature: 1053 K. The estimated dose of the electron irradiation: 38.6 MGy (the average electron flux 1.135×10^{13} electrons $\text{cm}^{-2} \text{s}^{-1}$). The final tritium sum release: 2.20 GBq/g (11.5% of the estimated initial total tritium 19.2 GBq/g).

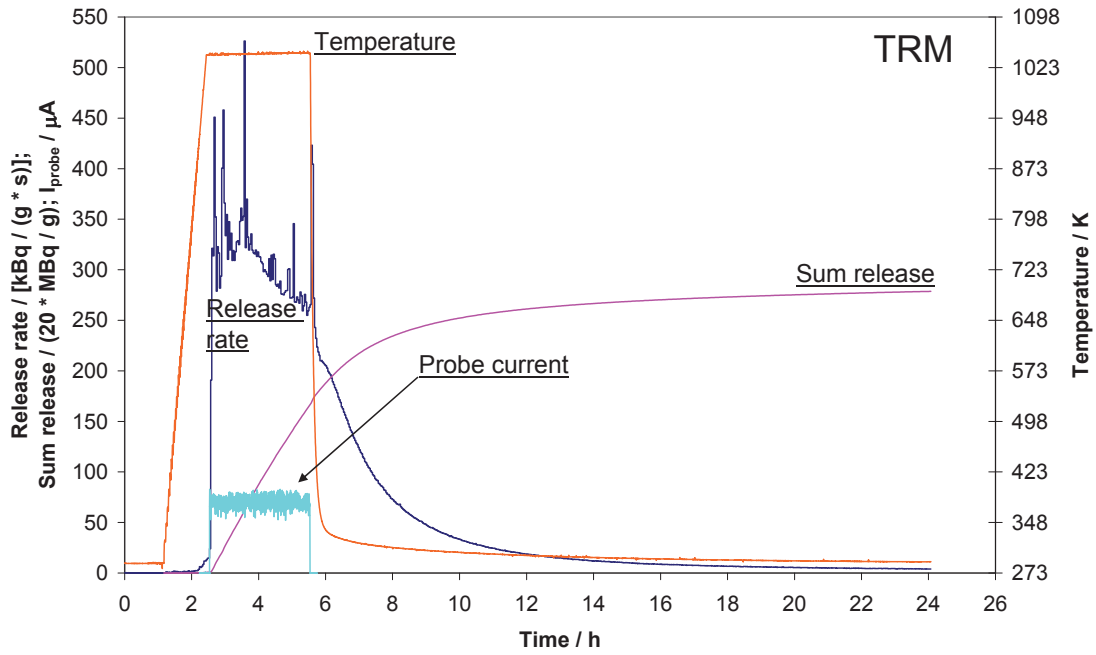


Fig. 21. Tritium release from pebble 46sPC/3/09. The maximum temperature: 1047 K. The estimated dose of the electron irradiation: 37.1 MGy (the average electron flux 1.093×10^{13} electrons $\text{cm}^{-2} \text{s}^{-1}$). The final tritium sum release: 5.57 GBq/g (29.0% of the estimated initial total tritium 19.2 GBq/g).

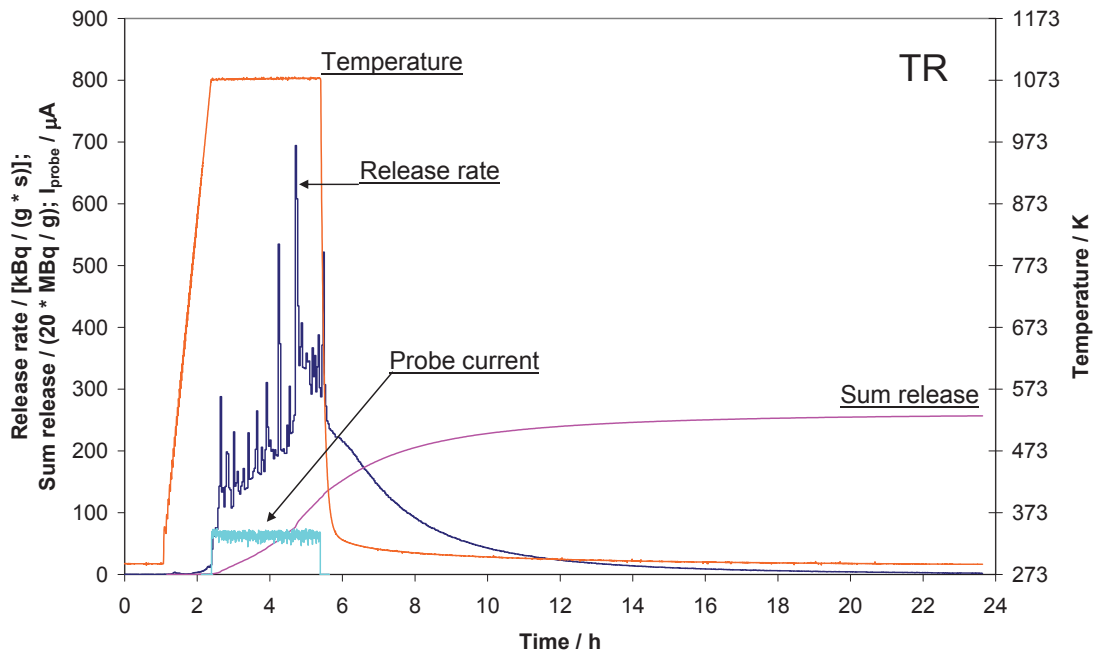


Fig. 22. Tritium release from pebble 46sPC/3/08. The maximum temperature: 1078 K. The estimated dose of the electron irradiation: 33.6 MGy (the average electron flux 0.990×10^{13} electrons $\text{cm}^{-2} \text{s}^{-1}$). The final tritium sum release: 5.14 GBq/g (26.8% of the estimated initial total tritium 19.2 GBq/g).

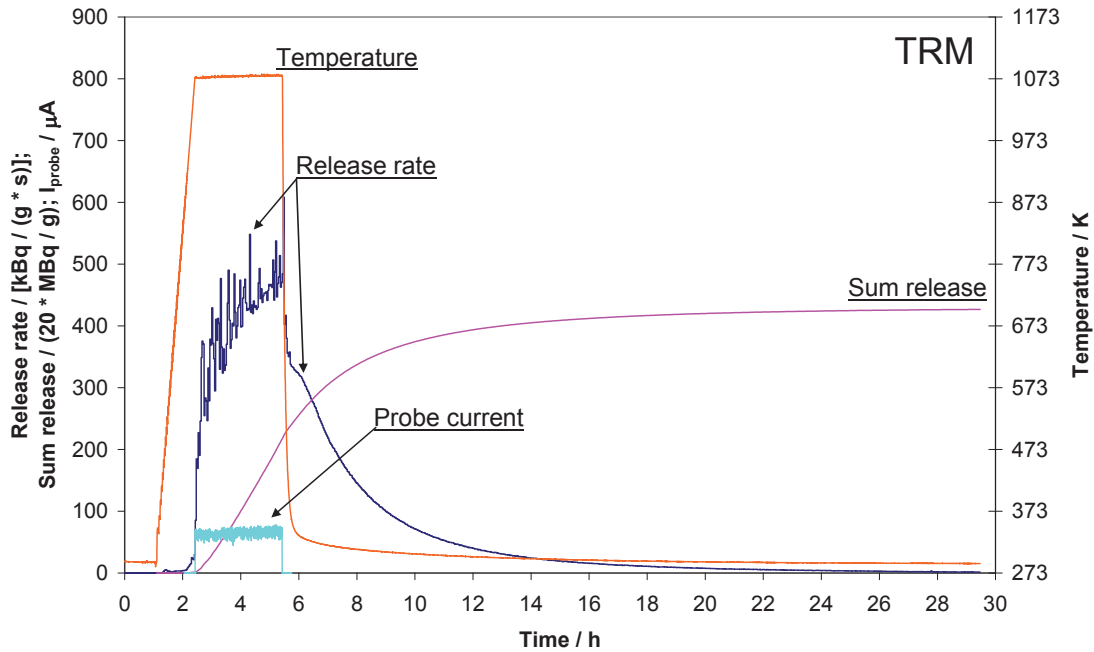


Fig. 23. Tritium release from pebble 46sPC/3/09. The maximum temperature: 1081 K. The estimated dose of the electron irradiation: 34.2 MGy (the average electron flux 1.007×10^{13} electrons $\text{cm}^{-2} \text{s}^{-1}$). The final tritium sum release: 8.53 GBq/g (44.4% of the estimated initial total tritium 19.2 GBq/g).

The tritium release rate in all the experiments of the series was not uniform. Most of the curves of the tritium release rate have a sharp maximum shortly after switching on the 5 MeV electron radiation. A sharp maximum is also present in all the curves of the tritium release rate on switching off the electron radiation and the temperature program in the temperature range 978-1081 K (Figs. 18-23). Sharp maximums of the tritium release rate occurred also during the electron irradiation with the external temperature program of 1047-1081 K (Figs. 20-23). Sharp maximums of the tritium release rate are indicative of the tritium burst release [27], however they had no large contribution in the final tritium sum release.

A common feature of most of the curves of the tritium release rate is a general ascending trend with time during the electron irradiation with the external temperature program of a constant temperature in a range of 831-1081 K (Figs. 12-23). The ascending trend of the tritium release rate indicates about activation of the tritium release under the given conditions of experiments. The activation is also evident from the fact that a considerable fraction of the final tritium sum release – up to 60% (Fig. 15) is released from a cooling pebble during 15 h after switching off the electron radiation and the temperature program. This type of activation of tritium release results in the fact that the time required for one experiment is about 24 h. As a practical significance of the activation of the tritium release, it is clearly visible from the curves of the tritium release rate (Figs. 12-23) that prolongation of the electron irradiation with the external temperature program 831-1081 K should considerably increase the degree of detritiation of the pebble under study.

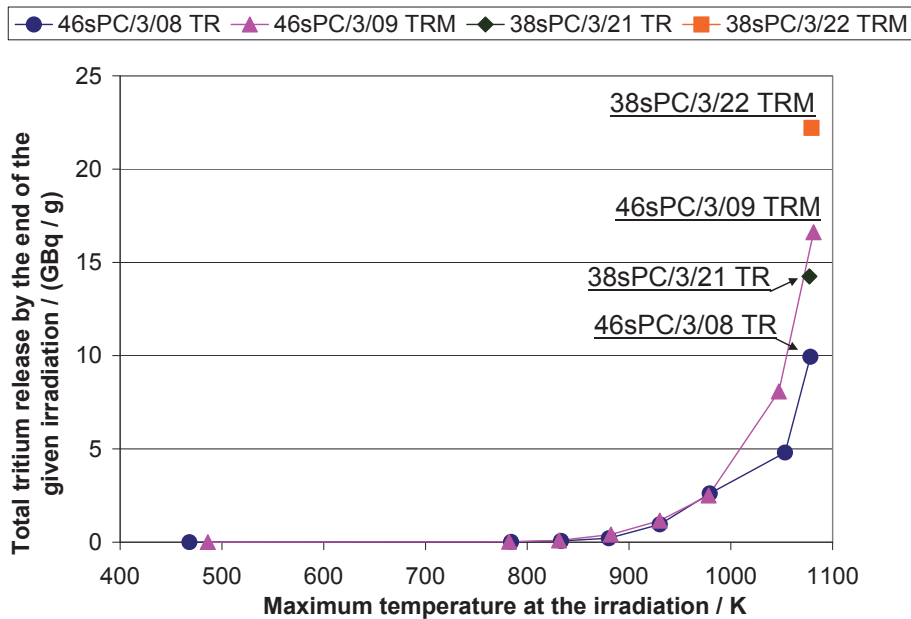


Fig. 24. Cumulative activity of the tritium released in successive anneals with electron irradiation for 3 h with increasing temperature without magnetic field (pebble 46sPC/3/08) and in a magnetic field of 1.5-1.7 T (pebble 46sPC/3/09) as a function of the maximum temperature in the given anneal. Values of the tritium cumulative release from pebbles 38sPC/3/21 and 38sPC/3/22 (Figs. 25 and 26, respectively) are given for comparison.

The curves of the total tritium release in Fig. 24 for pebbles 46sPC/3/08 and 46sPC/3/09 have been obtained by summing the values of the final tritium sum release in successive electron irradiation experiments with increasing temperature shown in Figs. 8-23. Up to 873 K the tritium release was little in comparison to the total amount of tritium in the pebbles estimated to be 19.2 GBq/g according to the data given in Section 2 above. Tritium release rate significantly increased above 873 K. This phenomenon is in line with the fact that a considerable tritium release was observed only at 923 K and 1023 K of the HIDOBE-01 neutron irradiation, rather than at 698 K and 798 K according to the results [11, 13] of out-of-pile measurements on samples that were irradiated at these temperatures. The curves of the total tritium release of pair of pebbles with \varnothing 1 mm 46sPC/3/08-46sPC/3/09 (Fig. 24) indicate a possible appreciable facilitating effect of a magnetic field of 1.5-1.7 T at temperatures above 973 K as by about 60% larger tritium release at 1040-1081 K.

6.2. Results of tritium release experiments with a pair of 0.5 mm pebbles

Only one post neutron-irradiation tritium release experiment at 1070-1079 K was performed with each pebble of pair 38sPC/3/21-38sPC/3/22. Their results are shown in Figs. 25 and 26 respectively. A sharp tritium release peak occurred on switching on the electron radiation. During the electron irradiation, the tritium release rate was not uniform; its curves have minor peaks. Also in the case of the 0.5 mm pebbles, the activation of the tritium release at temperatures 1070-1079 K is visible from the curves of the tritium release rate, and about 45% of the final tritium sum release was released from a cooling pebble during 15 h after switching off the electron radiation and the external temperature program. It is visible from the curves of the tritium release rate (Figs. 25 and 26) that prolongation of the electron irradiation with the external temperature program 1070-1079 K could increase the degree of detritiation of the pebbles. The comparison of the values of the tritium sum release of pebble pair 38sPC/3/21-38sPC/3/22 indicates a possible facilitating effect of a magnetic field of 1.5-1.7 T on the final tritium sum release by 56%.

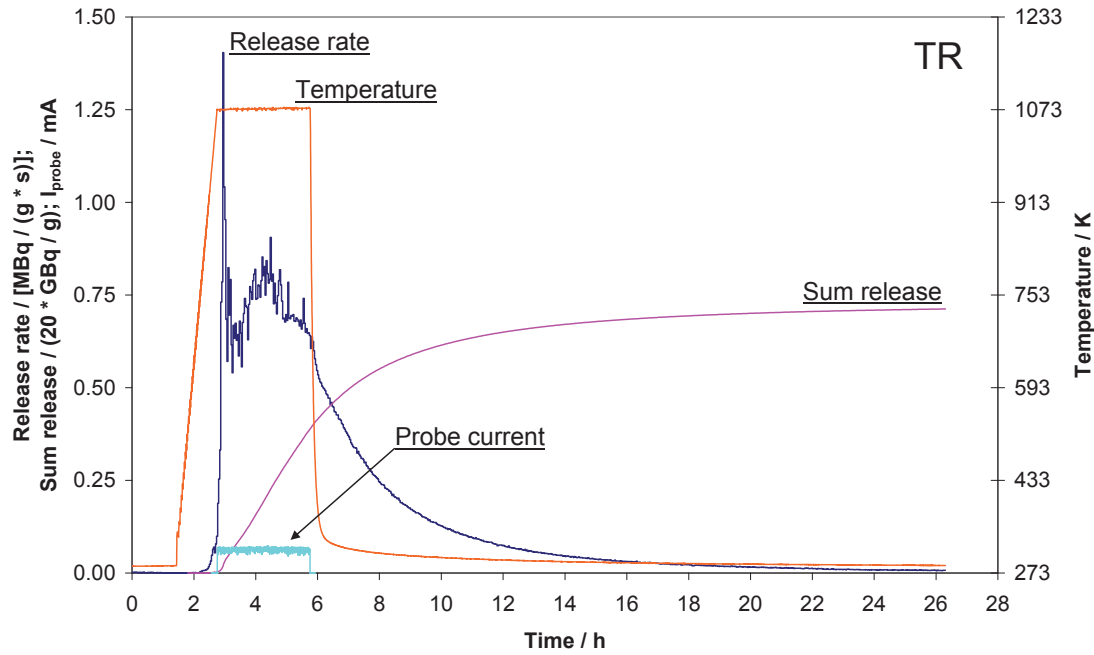


Fig. 25. Tritium release from pebble 38sPC/3/21 (798 K), $m=0.18$ mg, $\varnothing 0.54$ mm. The maximum temperature 1077 K; without magnetic field; an electron irradiation for 3 h with the estimated dose 33.1 MGy (the average electron flux 0.973×10^{13} electrons $\text{cm}^{-2} \text{s}^{-1}$). The final tritium sum release: 14.25 GBq/g (74.2% of the estimated initial total tritium 19.2 GBq/g).

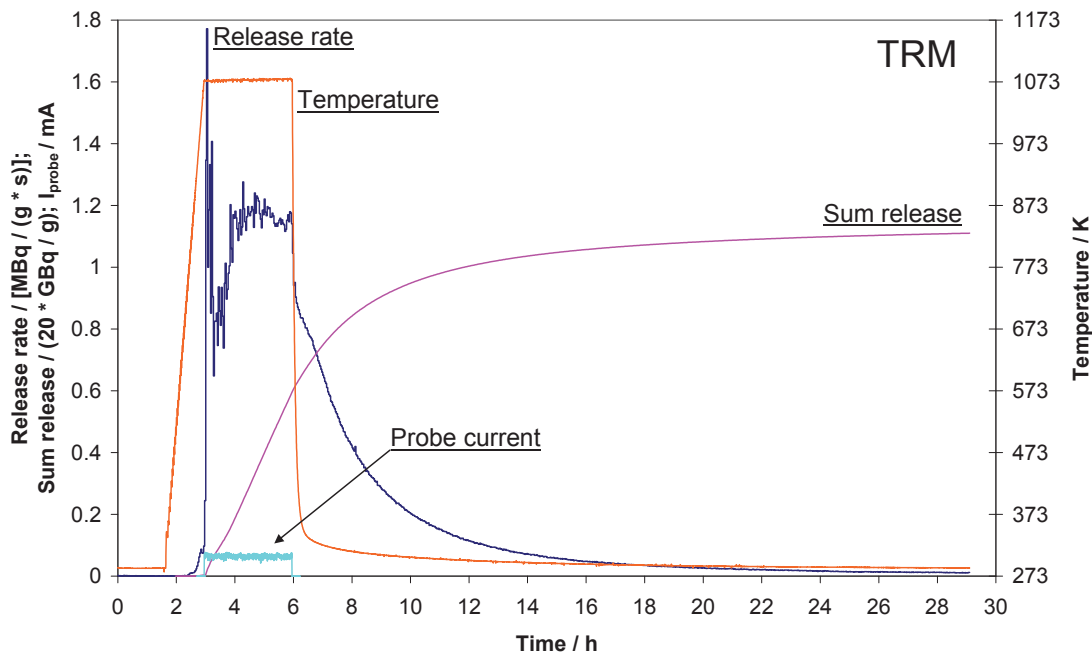


Fig. 26. Tritium release from pebble 38sPC/3/22 (798 K), $m=0.16$ mg, $\varnothing 0.53$ mm. The maximum temperature 1079 K; in a magnetic field of 1.5-1.7 T; an electron irradiation for 3 h with the estimated dose 34.0 MGy (the average electron flux 1.000×10^{13} electrons $\text{cm}^{-2} \text{s}^{-1}$). The final tritium sum release: 22.21 GBq/g (116% of the estimated initial total tritium 19.2 GBq/g).

7. DISCUSSION

The ascending trend of the curves of the tritium release rate on annealing at a constant temperature with simultaneous 5 MeV electron radiation (Figs. 12-23) indicates that the electron radiation produces structural changes in the neutron-irradiated Be pebble that facilitate tritium release. For comparison, descending curves of the tritium release rate at a constant temperature correspond to the tritium release controlled by atomic diffusion [15, 28]. Annealing of the pebbles under temperature programmes similar to those in Figs. 12-23 without electron radiation should determine the possible stimulating contribution of the electron radiation in the tritium release. Tritium release that is more complex than atomic-diffusion-controlled release was observed previously for the EXOTIC-8-3/13 beryllium pebbles [18]. Most of the tritium (about 90%) in the 0.5 and 1.0 mm pebbles irradiated with neutrons in the HIDOBE temperature zones 798 and 923 K respectively is reported to be molecular tritium [29], which is apparently localized in the helium bubbles in the pebbles. The 5 MeV electron radiation possibly produces microcrevices in the pebble, which facilitates tritium release during the annealing with the electron radiation and enables a following appreciable tritium release from a cooling pebble. Opening of the tritium-containing helium bubbles to the outer surface of the pebble may be a reason of the sharp tritium burst release peaks in the tritium release curves in the present study.

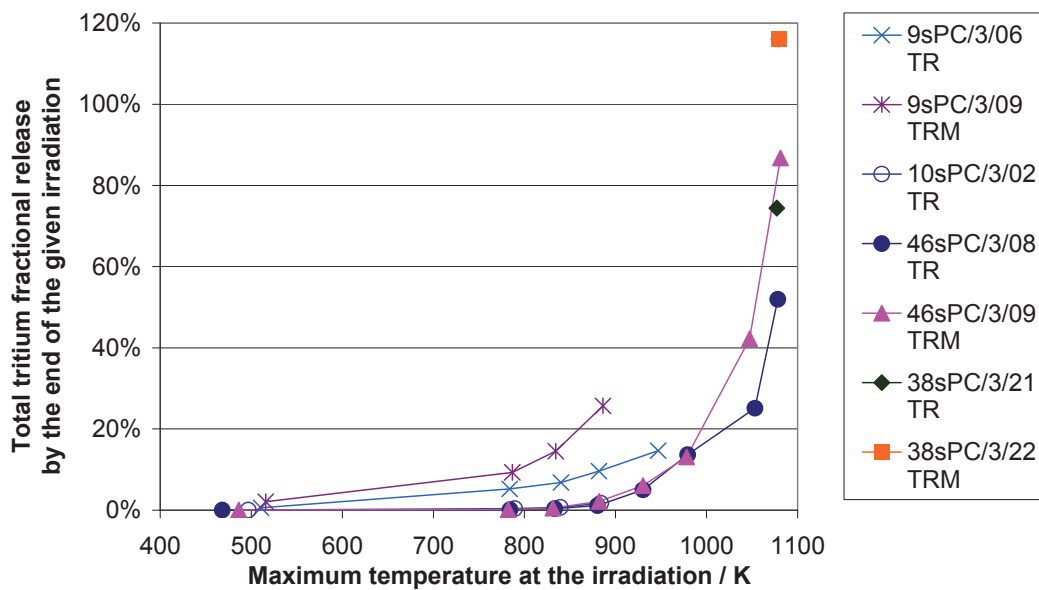


Fig. 27. Comparison of the estimated values of the total tritium fractional release from pebbles 46sPC/3/08, 46sPC/3/09, 38sPC/3/21 and 38sPC/3/22 determined in the present study on the grounds of the estimated value of the initial total tritium amount of 19.2 GBq/g (from the data in the section “2. Samples investigated”) with the previously reported [30] experimental values for pebbles 9sPC/3/06, 9sPC/3/09 and 10sPC/3/02. 1.0 mm (2001) pebbles 9sPC/3/06 (1.00 mg) and 9sPC/3/09 (1.34 mg) had been irradiated with neutrons in the HIDOBE-01 temperature zone 1023 K; their initial total tritium amount was found to be 1.03 and 0.29 GBq/g respectively. 1.0 mm (2001) pebble 10sPC/3/02 (1.28 mg) had been irradiated with neutrons in the HIDOBE-01 temperature zone 923 K; its initial total tritium amount was found to be 6.66 GBq/g. The dose rate of the 5 MeV electron radiation in the experiments with pebbles 9sPC/3/06, 9sPC/3/09 and 10sPC/3/02 is estimated to be 13-23 MGy/h.

The fractional tritium release estimated from the data in Fig. 24 of the present study is compared in Fig. 27 with the previously reported data [30] for 1.0 mm pebbles irradiated with neutrons in the HIDOBE-01 temperature zones 923 and 1023 K. Higher values of the

fractional release of pebbles 9sPC/3/06 and 9sPC/3/09 may be related to their higher porosity connected with the outer surface by a network of interconnected channels [11, 13-15].

The results of the post neutron-irradiation tritium release experiments in the present study indicate a facilitating effect of a magnetic field of 1.5-1.7 T with the simultaneous 5 MeV fast electron radiation at temperatures above 1040 K on the tritium release, but because of the fact that only one pair of pebbles was investigated on the magnetic field effect from each batch, the ability to draw general quantitative conclusions about the magnetic field effect is very limited by possible dissimilarity of the pebbles within the batch with respect to their initial total tritium amount and their tritium release properties.

8. CONCLUSIONS

1. The tritium release rate on annealing of HIDOBE-01 798 K neutron-irradiated beryllium pebbles with simultaneous 5 MeV fast electron radiation was not uniform – it had strong irregular oscillations particularly in the case of 1.0 mm pebbles. The sharp peaks of the release rate were indicative of burst release, which is characteristic to opening of tritium-containing gas inclusions.
2. The distinctive ascending trend of the tritium release rate on annealing at a constant temperature 830-1081 K with simultaneous 5 MeV fast electron radiation and a considerable following released fraction from a cooling pebble after the end of the annealing are indicative of activation of the tritium release by the electron radiation – possibly by production of structural changes, e.g. microcrevices, in the neutron-irradiated Be pebbles that facilitate the tritium release. The ascending curves of the tritium release rate at a constant temperature correspond to a release process that is different from the release determined by atomic diffusion, which is characterized by a descending tritium release rate at a constant temperature.
3. Up to 873 K the tritium release of the HIDOBE-01 798 K Be pebbles was less than 3% with respect to the total amount of tritium in the pebbles estimated to be 19.2 GBq/g. Tritium release rate significantly increased above 873 K. This phenomenon is in line with the fact that a considerable in-pile tritium release took place during the HIDOBE-01 neutron irradiation only from the beryllium pebbles at 923 K and 1023 K rather than from the pebbles at 698 K and 798 K.
4. A considerable facilitating effect (56-67%) of a magnetic field of 1.5-1.7 T with the simultaneous 5 MeV fast electron radiation on the tritium release from the HIDOBE-01 798 K 1.0 and 0.5 mm Be pebbles on annealing at temperatures above 1040 K was observed, but because of the fact that only one pair of pebbles was investigated on the magnetic field effect from each batch, the ability to draw general quantitative conclusions about the magnetic field effect is very limited by possible dissimilarity of the pebbles within the batch with respect to their initial total tritium amount and their tritium release properties.

ACKNOWLEDGEMENTS

This work, carried out by the University of Latvia, was financially supported by the European Communities within the framework of EFDA and by F4E, under contract F4E-2009-GRT030-A3. The views and opinions expressed herein do not necessarily reflect those of the European Commission.

The research reported in this paper was financially supported by ERDF Project 2010/0202/2DP/2.1.1.2.0/10/APIA/VIAA/013 “Support for the international cooperation projects and other international cooperation activities in research and technology at the University of Latvia” and by the Ministry of Education and Science of the Republic of Latvia, project No. ES-11-13 “EURATOM”.

The authors would like to express their gratitude to Sander van Til and Lida Magielsen (NRG, Petten, The Netherlands) for supplying data and samples within contract F4E-2009-GRT030-A3, and discussion of the results reported in this study.

REFERENCES

- [1] L.M. Giancarli, M. Abdou, D.J. Campbell, V.A. Chuyanov, M.Y. Ahn, M. Enoeda, C. Pan, Y. Poitevin, E. Rajendra Kumar, I. Rikapito, Y. Strebkov, S. Suzuki, P.C. Wong, M. Zmitko, Overview of the ITER TBM Program, *Fusion Eng. Des.* 87 (2012) 395-402.
- [2] M. Zmitko, Y. Poitevin, L. Boccaccini, J.-F. Salavy, R. Knitter, A. Möslang, A.J. Magielsen, J.B.J. Hegeman, R. Lässer, Development and qualification of functional materials for the EU Test Blanket Modules: Strategy and R&D activities, *J. Nucl. Mater.* 417 (2011) 678-683.
- [3] Y. Chen, U. Fischer, P. Pereslavitsev, F. Wasastjerna, The EU Power Plant Conceptual Study – neutronic design analyses for near term and advanced reactor models, *Wissenschaftliche Berichte FZKA 6763*, Forschungszentrum Karlsruhe, 2003, 53 pp.
- [4] A. Moeslang, G. Piazza, L.V. Boccaccini, A. Cardella, E. Rabaglino, L. Sannen, M. Scibetta, J. van der Laan, J.B.J.W. Hegeman, Status of the European R&D on beryllium as multiplier material for breeder blankets, in: H. Kawamura, S. Tanaka, E. Ishitsuka (Eds.), *Proceedings of the Sixth IEA International Workshop on Beryllium Technology for Fusion (BeWS-6)*, Miyazaki City, Japan, December 2-5, 2003, JAERI-Conf 2004-006, Japan Atomic Energy Research Institute, March 2004, p. 15.
- [5] E. Rabaglino, Helium and tritium in neutron-irradiated beryllium, *Wissenschaftliche Berichte FZKA 6939*, Forschungszentrum Karlsruhe, 2004, 127 pp.
- [6] A. Möslang, R.A. Pieritz, E. Boller, C. Ferrero, Gas bubble network formation in irradiated beryllium pebbles monitored by X-ray microtomography, *J. Nucl. Mater.* 386-388 (2009) 1052-1055.
- [7] J.B.J. Hegeman, J.G. van der Laan, A.J. Magielsen, A. Möslang, G. Piazza, J. Reimann, E. Rabaglino, M.A.G. Ooijevaar, M.P. Stijkel, The HFR Petten high dose irradiation programme of beryllium for blanket application, in: H. Kawamura, S. Tanaka, E. Ishitsuka (Eds.), *Proceedings of the Sixth IEA International Workshop on Beryllium Technology for Fusion (BeWS-6)*, Miyazaki City, Japan, December 2-5, 2003, JAERI-Conf 2004-006, Japan Atomic Energy Research Institute, March 2004, pp. 141-145.
- [8] J.B.J. Hegeman, J.G. van der Laan, H. Kawamura, A. Möslang, I. Kupriyanov, M. Uchida, K. Hayashi, The HFR Petten high dose irradiation programme of beryllium for blanket application, *Fusion Eng. Des.* 75-79 (2005) 769-773.
- [9] A. Sugonyako, S. van Til, HIDOBE: final report on irradiation up to 3000 appm He, NRG-20296/09.96239/P, EFDA subtask TW2-TTBB-004b D4b, 28 September 2009, 57 p.

- [10] R.K. Mutnuru, High DOse Irradiation of Beryllium – HIDOBE-01 (351-01). Neutron metrology in the HFR, NRG-20296.10/103521, 16 August 2010, 56 p.
- [11] S. van Til, HIDOBE PIE: Report on swelling, tritium retention and metallography. Final report F4E-GRT030-A3 T2-D6, NRG-22646/12.116032, 7 September 2012, 101 p.
- [12] S. van Til, J.B.J. Hegeman, H.L. Cobussen, M.P. Stijkel, Evolution of beryllium pebbles (HIDOBE) in long term, high flux irradiation in the high flux reactor, *Fusion Eng. Des.* 86 (2011) 2258-2261.
- [13] S. van Til, A.V. Fedorov, M.P. Stijkel, H.L. Cobussen, R.K. Mutnuru, P. v.d. Idsert, M. Zmitko, Tritium release from beryllium pebbles after high temperature irradiation up to 3000 appm He in the HIDOBE-01 experiment, *J. Nucl. Mater.* (2013), in press, 5 p.,
<http://dx.doi.org/10.1016/j.jnucmat.2013.02.055>
- [14] A.V. Fedorov, S. van Til, L.J. Magielsen, M.P. Stijkel, Analysis of tritium retention in beryllium pebbles in EXOTIC, PBA and HIDOBE-01 experiments, *J. Nucl. Mater.* (2013), in press, 6 p.,
<http://dx.doi.org/10.1016/j.jnucmat.2013.03.010>
- [15] V. Chakin, R. Rolli, A. Moeslang, M. Klimenkov, M. Kolb, P. Vladimirov, P. Kurinskiy, H.-C. Schneider, S. van Til, A.J. Magielsen, M. Zmitko, Tritium release and retention properties of highly neutron-irradiated beryllium pebbles from HIDOBE-01 experiment, *J. Nucl. Mater.* (2013), in press, 7 p.,
<http://dx.doi.org/10.1016/j.jnucmat.2013.03.032>
- [16] J. Tīliks, G. Ķizāne, A. Vītiņš, E. Kolodinska, E. Rabaglino, Magnetic field effects on tritium release from neutron-irradiated beryllium pebbles, *Nucl. Technol.* 159 (2007) 245-249.
- [17] A. Vītiņš, G. Ķizāne, J. Tīliks, J. Tīliks Jr., E. Kolodinska, Tritium release from breeding blanket materials in high magnetic field, *Fusion Eng. Des.* 82 (2007) 2341-2346.
- [18] J. Tīliks, G. Ķizāne, A. Vītiņš, E. Kolodinska, J. Tīliks Jr., I. Reinholds, Tritium release from beryllium articles for use in fusion devices, *J. Nucl. Mater.* 386-388 (2009) 874-877.
- [19] J. Tīliks, A. Vītiņš, G. Ķizāne, V. Tīlika, E. Kolodinska, S. Kalēja, B. Leščinskis, Effects of external energetic factors on tritium release from the EXOTIC 8-3/13 neutron-irradiated beryllium pebbles, *Fusion Eng. Des.* 84 (2009) 1842-1846.
- [20] E. Ishitsuka, H. Kawamura, N. Sakamoto, K. Nishida, M. Saito, Evaluation of beryllium pebble produced by rotating electrode method, JAERI-M Report JAERI-M 94-032, Japan Atomic Energy Research Institute, 1994, 34 p.
- [21] E. Ishitsuka, H. Kawamura, Thermal and mechanical properties of beryllium pebbles, *Fusion Eng. Des.* 27 (1995) 263-268.
- [22] T. Iwadachi, N. Sakamoto, K. Nishida, H. Kawamura, Production of various sizes and some properties of beryllium pebbles by the rotating electrode method, in: H. Kawamura, M. Okamoto (Eds.), *Proceedings of the Third IEA International Workshop on Beryllium Technology for Fusion (BeWS-3)*, Mito City, Japan, October 22-24, 1997, JAERI-Conf 98-001, Japan Atomic Energy Research Institute, January 1998, pp. 33-38.
- [23] E. Ishitsuka, H. Kawamura, N. Sakamoto, K. Nishida, Process for preparing metallic beryllium pebbles, US Patent No. 5958105, September 28, 1999, 8 p.
- [24] A.K. Pikaev, *Modern radiation chemistry. Basic principles, experimental technique and methods*, Nauka, Moscow, 1985, p. 74 (in Russian).

- [25] T. Ihli, T.K. Basu, L.M. Giancarli, S. Konishi, S. Malang, F. Najmabadi, S. Nishio, A.R. Raffray, C.V.S. Rao, A. Sagara, Y. Wu, Review of blanket designs for advanced fusion reactors, *Fusion Eng. Des.* 83 (2008) 912-919.
- [27] D.L. Baldwin, M.C. Billone, Diffusion / desorption of tritium from irradiated beryllium, *J. Nucl. Mater.* 212-215 (1994) 948-953.
- [28] A. Vītiņš, G. Kizāne, A. Matīss, E. Pajuste, V. Zubkovs, Tritium release behavior of beryllium pebbles after neutron irradiation between 523 and 823 K, *J. Nucl. Mater.* (2013), in press, 4 p.,
<http://dx.doi.org/10.1016/j.jnucmat.2013.03.037>
- [29] E. Pajuste, G. Kizane, S. van Til, A. Vitins, V. Zubkovs, O. Paskova, A. Matiko, Tritium bulk distribution and chemical state in beryllium pebbles irradiated in experiment HIDOBE01, Poster P3.118 presented at the 27th Symposium on Fusion Technology (SOFT 2012), Liège, Belgium, September 24-28, 2012. The abstract is available online at:
<http://sciconf.org/soft2012/ip/topic/h/session/p3/paper/118>
- [30] G. Kizane, A. Vitins, E. Pajuste, A. Matiss, B. Lescinskis, S. van Til, Tritium release under action of temperature, radiation and magnetic field from beryllium pebbles of HIDOBE-01 irradiation, Poster P4.168 presented at the 27th Symposium on Fusion Technology (SOFT 2012), Liège, Belgium, September 24-28, 2012. The abstract is available online at:
<http://sciconf.org/soft2012/ip/topic/h/session/p4/paper/168>

Tritium and helium release from constrained and unconstrained beryllium pebbles irradiated up to high neutron dose in the HIDOBE-01 experiment

V. Chakin, R. Rolli, P. Vladimirov, and A. Moeslang

*Karlsruhe Institute of Technology, Institute for Applied Materials,
Hermann-von-Helmholz-Platz 1, 76344 Eggenstein-Leopoldshafen, Germany*

*Corresponding author: Vladimir Chakin
Telephone number: +49 721 608 23639
Fax number: +49 721 608 24567
E-mail address: vladimir.chakin@kit.edu

ABSTRACT

Beryllium is the reference neutron multiplier material in the Helium Cooled Pebble Bed (HCPB) breeding blanket of fusion power plants. Significant tritium inventory accumulated in beryllium as a result of neutron-induced transmutations could become a safety issue for the operation of such blankets as well as for the nuclear waste utilization. To provide a related materials database, a neutron irradiation campaign of beryllium pebbles with diameters of 0.5 and 1 mm at 686-1006 K, the HIDOBE-01 experiment, has been performed in the HFR in Petten, the Netherlands, producing up to 3020 appm helium and 298 appm tritium. Thermal desorption tests of irradiated unconstrained and constrained beryllium pebbles were performed in a purge gas flow using a quadrupole mass-spectrometer (QMS) and an ionization chamber. Compared to unconstrained pebbles, constrained beryllium pebbles have an enhanced tritium release at all temperatures investigated. Small elongated sub-grains formed under irradiation in the constrained pebbles promote formation of numerous channels for facilitated tritium release.

KEYWORDS

neutron irradiation, beryllium pebble, tritium and helium release, retention, open porosity network.

1. INTRODUCTION

Beds of beryllium pebbles of 1 mm in diameter are considered as neutron multipliers in the Helium Cooled Pebble Bed (HCPB) breeding blanket of the European DEMO reactor concept [1] and will be tested in the dedicated tritium breeder module of the experimental fusion reactor ITER. In fusion reactor beryllium pebbles will be exposed to high-dose neutron irradiation resulting in severe radiation damage which includes swelling caused by radiation-induced accumulation of helium. Beta-radioactive tritium is also produced under neutron irradiation complicating handling of radioactive beryllium wastes after the end-of-life of fusion reactor. Thence, tritium release and retention characteristics are necessary for the breeder blanket design while tritium thermal desorption tests are mandatory tool within post-irradiation examinations of beryllium pebbles.

The long-term neutron irradiation of beryllium pebbles has been performed in the HIDOBE-01 experiment in the High Flux Reactor (HFR), Petten, the Netherlands on 2005-2007 [2, 3]. The investigated beryllium pebbles were irradiated at 686-1006 K up to 3000 appm helium and 300 appm tritium productions, accordingly. This is the first neutron irradiation experiment that provides relevant tritium concentrations at the fusion blanket specific operation temperatures in the reference beryllium material. The paper presents the results of thermal desorption (TD) tests and microstructure investigation of these irradiated pebbles. The TD tests were performed using a flow-through set with a quadrupole mass-spectrometer (QMS) and an ionization chamber located at Fusion Materials Laboratory (FML), Karlsruhe Institute of Technology, Germany.

2. EXPERIMENTAL

The investigated beryllium pebbles with diameters of 0.5 and 1 mm were fabricated by NGK Insulators Ltd., Japan using the rotating electrode method (REM) [4]. The 0.5 mm beryllium pebbles contain the following main impurities (in wt. %): 0.36 BeO, 0.088 Fe, 0.047 Al, 0.027 Si, 0.018 Mg. The 1 mm pebbles have similar chemical composition (in wt. %): 0.36 BeO, 0.094 Fe, 0.048 Al, 0.029 Si, 0.024 Mg.

Three different container types with beryllium pebbles were used in the HIDOBE-01 irradiation experiment [5]. Two of them (differing by height) imitate small constrained pebble beds with a diameter of 14.9 mm containing 0.5, 1, and 2 mm pebbles located at various heights of the irradiating facility. In this study, the 0.5 and 1 mm irradiated beryllium pebbles were investigated only. Before irradiation, the constrained pebble beds were filled with pebbles and closed by a screw-cap with a torque wrench. The height changes of the closed pebble beds are shown in Table 1. To prevent the chemical interaction of beryllium pebbles with stainless steel walls a thin platinum foil has been placed between beryllium and steel as a barrier. Nevertheless, the post-irradiation examinations have revealed significant interactions between beryllium pebbles and the foil which was accompanied by intensive pore formation and partial destruction of the materials in the intermediate contact layer [5]. The third container type with a diameter of 3.2 mm was used for the irradiation of beryllium pebbles after free filling (unconstrained pebbles).

Table 1. Parameters of the pebble bed (PB) deformation.

Type	Diameter of pebble, mm	Maximum T_{irr} , K	Height of PB, mm	Decrease of PB height, %
PB	0.5	686	~13	1.24
	0.5	1006		1.03
	1	753		0.41
	1	927		0.97

The irradiation parameters of the investigated beryllium pebbles are summarized in Table 2 [2, 3]. The temperatures during irradiation were measured by thermocouples located close to the containers with the beryllium pebbles. Table 2 shows the average irradiation temperatures in the HIDOBE-01 and also the maximum temperatures which were reached during the irradiation. For the analyses of the experimental results, the maximum irradiation temperatures were used as far as higher mobility of helium and tritium as well as beryllium atoms allows to form radiation defects which remain stable also at lower irradiation temperatures. The tritium contents are presented in Table 2 twice, i.e. to the end of irradiation on 2007 and to the moment of the TD tests on 2012.

Table 2. Irradiation parameters of constrained (PB – pebble bed) and unconstrained (P - pebbles) beryllium pebbles.

Type	D, mm	Average T_{irr} , K	Maximum T_{irr} , K	F, 10^{26} m ⁻² , E>1 MeV	D, dpa	⁴ He, appm	³ H to end of irradiation, <u>appm</u>	³ H to TD test, <u>appm</u>
P	0.5	641	686	5.69	11.3	1890	176	142
		702	753	6.94	13.9	2300	213	172
		802	861	8.07	16.3	2680	252	203
		909	968	8.92	18.1	2950	285	230
P	1	641	686	5.69	11.3	1890	176	142
		702	753	6.94	13.9	2300	213	172
		802	861	8.07	16.3	2680	252	203
		909	968	8.92	18.1	2950	285	230
PB	0.5	641	686	5.69	11.3	1890	176	141
	0.5	948	1006	8.92	18.1	2950	285	229
	1	740	753	8.29	17.0	2700	258	208
	1	873	927	9.21	18.9	3020	298	240

Fig. 1 shows the scheme of the TD flow-through setup with a quadrupole mass-spectrometer (QMS) and an ionization chamber (IC) which is located in a glove box filled by high-purity nitrogen. The gas mixture of high-purity argon with small addition of hydrogen (Ar+0.1 vol. % H₂) was used as a purge gas to transport the released species to the QMS and the IC. The TD setup consists of a furnace for heating of samples with different modes up to maximum temperature of 1373 K. In this study, the tritium and helium release rates are determined by temperature ramping at a constant rate of 7 K/min (0.117 K/s) from room temperature to 1373 K with final exposure at the maximum temperature for 3 h. The purge gas had a flow rate of 10 ml/min, that was optimized to facilitate tritium and helium desorption and subsequent transport through the manifold of the set. During the TD tests the released species first reach the QMS. The QMS includes two heads through which the purge gas with released species moves simultaneously in parallel ways. The Head 1 measures the partial pressures of released species with masses from 1 to 100 amu (atomic mass unit), while the Head 2 determines masses 1 to 6 amu with higher accuracy. Therefore, the Head 2 is more suitable for measuring hydrogen and helium isotope release rates with the detection limit of specie in the purge gas not lower than 4 appm. The ionization energy of 40 eV was used for this study. After QMS, the gas flow with released species moves to a Zn-bed heated to 663 K which transforms tritium water to tritium gas to avoid tritium water absorption in the pipes and in the IC. For the same reason, the gas pipes in the manifold are heated to 573 K during the TD tests.

During the TD tests, the helium atoms (mainly isotope ⁴He) escaping from gas bubbles [6] at a given temperature diffuse through the matrix and reach the external surface where they freely leave the pebble. It is assumed that the main part of tritium exists in bubbles in molecular form [7]. Therefore, to escape from the bubble, ³H₂ has to dissociate first. In the second step, ³H⁺ adsorbs at the internal surface of the bubble, penetrates into the bulk and diffuses to the external surface of the pebble. At the surface, ³H⁺ forms a molecule together with ¹H⁺ coming from the purge gas after dissociation of H₂ on the beryllium surface. ⁴He and ¹H³H have very close atomic masses, 4.0026 and 4.0239 amu, respectively [8]. This fact as

well as much lower inventory of tritium comparing to helium in irradiated beryllium pebbles (see Table 2) did not allow to divide reliably the QMS spectra to $^4\text{He}^+$ and $^1\text{H}^3\text{H}^+$ peaks while the $^1\text{H}^3\text{H}^+$ peak was in the noise of the $^4\text{He}^+$ signal. Thus, only the IC (which is located after QMS) allows to detect radioactive tritium in the form of $^1\text{H}^3\text{H}$. The total tritium release values were normalized to the weight of the pebbles tested in each test. For each TD test, 0.010-0.016 g of beryllium pebbles was used, corresponding to 60-90 pebbles with 0.5 mm and 8-12 pebbles with 1 mm in diameter, accordingly. Before TD tests with irradiated pebbles, the dummy release measurements were carried out to determine the background of tritium activity accumulated in the system.

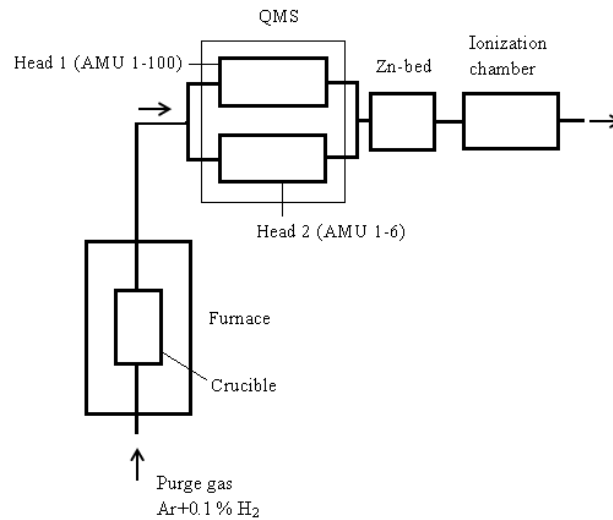


Fig. 1. Schematic draw of the flow-through setup for thermal desorption tests.

Microstructure examinations of cross sections of irradiated beryllium pebbles before TD tests were carried out by optical microscope (OM) Olympus GX51. Examples of general views of the pebbles after TD tests were earlier presented in [9]. The irradiated beryllium pebbles after the TD tests were covered by a thick surface layer of beryllium oxide (BeO) which was partially cracked and pill off. The most significant destructions of the surface film and even the pebbles occurred on pebbles exposed to the highest irradiation temperatures.

3. RESULTS AND DISCUSSION

3.1. Tritium and helium release

Fig. 2 shows release rates of tritium (Fig. 2a) and helium (Fig. 2b) versus time and temperature from 0.5 mm constrained beryllium pebbles irradiated at 753 K and tested with a heating rate of 7 K/min. In each graph, only one sharp high temperature peak occurs. The simultaneous release of tritium and helium was observed previously [10-13] and tentatively ascribed to formation of interconnected channels of bubbles along triple grain junctions and grain boundaries resulting in the so-called burst release peak. In our study, both tritium and helium release peaks have clear maximums that allow a determination of the release temperatures from the graphs with high accuracy. All release curves have universal shape with one major release peak. Fig. 2c shows release curves represented in Figs. 2a, b as a function of temperature allowing to observe the relative position of the tritium and helium release peaks. In this particular case, the helium peak is shifted to the right relative to the tritium peak by approximately 70 K.

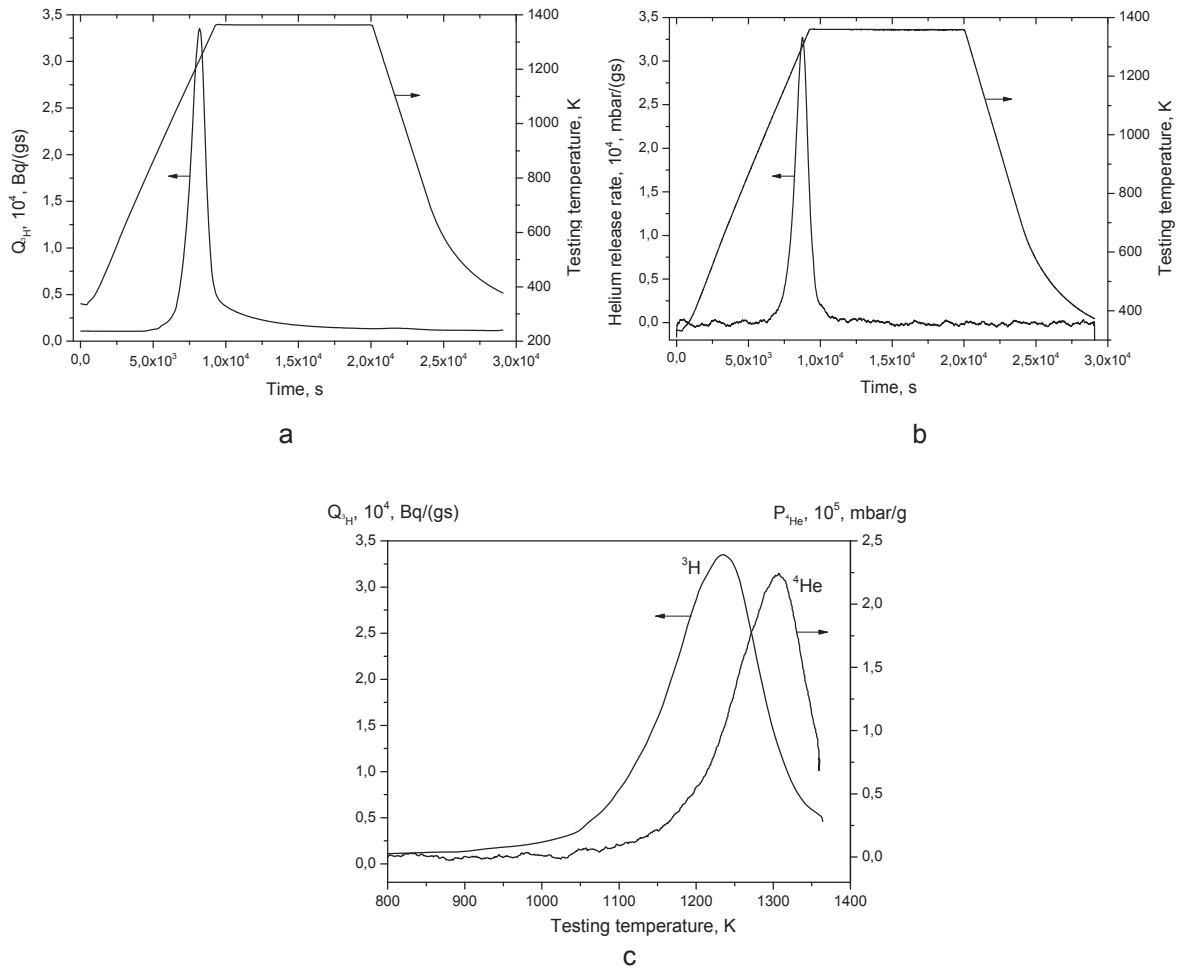


Fig. 2. Release rate of tritium (a) and helium (b) as well as temperature ramping versus time from the 0.5 mm unconstrained beryllium pebbles irradiated at 753 K. The same release curves plotted as a function of testing temperature (c). Heating rate is 7 K/min. Ionization energy is 40 eV.

The same behavior was observed for all irradiation temperatures both for constrained and unconstrained pebbles. The helium release peak is shifted by 40-130 K relative to the tritium one. Fig. 3 represents the temperatures of tritium release peaks for 0.5 mm and 1 mm (Fig. 3a) for unconstrained and constrained beryllium pebbles depending on irradiation temperature. The TD tests were performed for 0.5 mm pebbles irradiated at 686 K and 968 K, for 1 mm pebbles irradiated at two intermediate temperatures (753 and 861 K). It would be inappropriate to compare position of the release peaks for pebbles of different sizes. However, in all cases, the tritium release peak temperatures for constrained beryllium pebbles are lower than for unconstrained ones independent of the pebble diameter. The lowest peak temperature (1158 K) is observed for 0.5 mm constrained pebbles irradiated at 1006 K corresponding to the fact that these pebbles have shown the lowest tritium inventory due to a significant tritium loss already during irradiation [9]. Fig. 3b shows the dependence of helium release peaks on irradiation temperature. In contrary to the tritium release peaks, the helium peak temperatures for constrained pebbles are almost always higher than for unconstrained ones with exception of the irradiation at 753 K. Considering the form of the release peaks (see Fig. 2c) it can be recognized that the tritium release peak has an asymmetrical form with a longer shoulder at low temperatures that confirms previous results showing earlier release of tritium [11, 13].

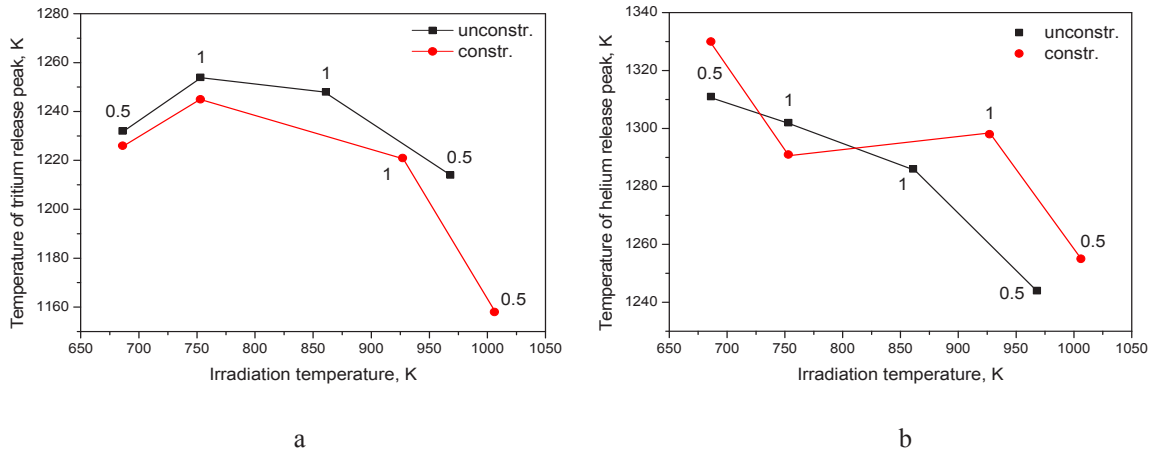


Fig. 3. Temperature of tritium (a) and helium (b) release peaks for 0.5 and 1 mm constrained and unconstrained beryllium pebbles versus irradiation temperature. For minimum and maximal irradiation temperatures the 0.5 mm beryllium pebbles were tested, while other temperature points are obtained for the 1 mm pebbles (marked as “0.5” and “1”, accordingly).

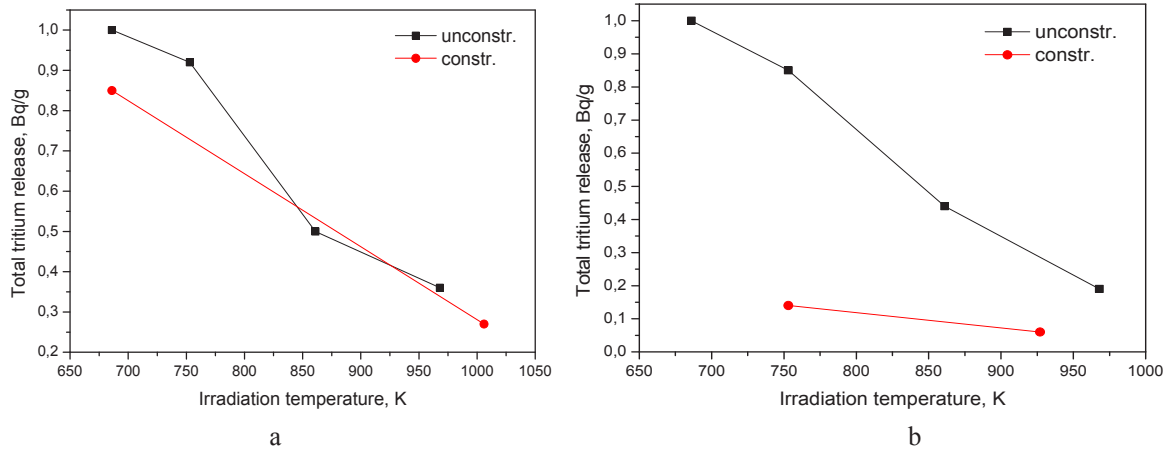


Fig. 4. Total tritium release from 0.5 mm (a) and 1 mm (b) beryllium pebbles versus irradiation temperature (normalized to the maximal tritium content accumulated in these pebbles in the HIDOBE-01 irradiation experiment).

Fig. 4 shows the fraction of tritium retained in the pebbles normalized to the amount of generated tritium as a function of irradiation temperature. It was found for both 0.5 mm (Fig. 4a) and 1 mm pebbles (Fig. 4b), that the total tritium release from constrained pebbles is always lower than from the unconstrained ones. The total helium release from 0.5 mm pebbles (Fig. 5a) follows this tendency, while for the 1 mm pebbles helium release from constrained pebbles is lower than that from unconstrained (Fig. 5b).

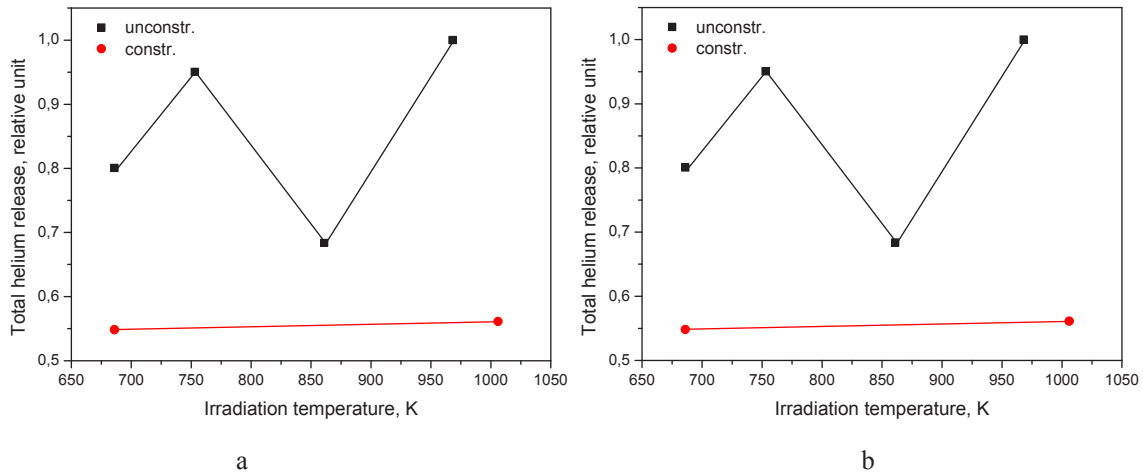


Fig. 5. Total helium release from 0.5 mm (a) and 1 mm (b) beryllium pebbles versus irradiation temperature (normalized to the maximal helium content accumulated in these pebbles in the HIDOBE-01 irradiation experiment).

3.2 Microstructure

Fig. 6 shows cross sections of unconstrained (Fig. 6a, b) and constrained (Fig. 6c, d) beryllium pebbles with a diameter of 0.5 mm irradiated at 686 K. The pebbles produced by REM have large coarse grains from 30 to 300 μm in size. The large-angle grain boundaries are clearly visible in polarized light (Figs. 6a-c). For unconstrained pebbles, there are no visible substructure features in the grains. For constrained pebbles, the large grains are subdivided into elongated sub-grains with an average size of $8 \times 60 \mu\text{m}$. In contrast to the large grains, the sub-grain boundaries are hardly visible by their contrast, even in polarized light. One can assume that they have a low misorientation (below 5°) [14, 15]. In the sub-grains, much smaller structural features can be additionally discerned (Fig. 6d). It is commonly assumed, that sub-grain walls consist of dislocations formed by plastic deformation at elevated temperatures [16]. In the case of constrained pebbles, they were tightly packed and stressed by thermal expansion and swelling under irradiation. Sometimes, the sub-grains are decorated by very small pores or bubbles (Fig. 6d). The pores line up in chains along grain and sub-grain boundaries coming sometimes to the pebble surface (see Fig. 6c) forming open channels for tritium and helium release. These channels decrease grain boundary cohesion and can provoke easy crack development under applied stress.

Fig. 7 represents microstructures of unconstrained (Fig. 7a, b) and constrained (Fig. 7c, d) beryllium pebbles with a diameter of 1 mm irradiated at 753 K. No sub-grain structure formation was expected to be observed in the unconstrained pebbles. However, in the regions close to the contact zones between pebbles the sub-grains are clearly visible (see Fig. 7b). Probably, the sub-grain formation was caused by internal stresses in the contact zones between pebbles under irradiation. No large pores visible by optical microscopy were found in the unconstrained pebbles, except the contact zones where remarkable loss of material can be detected. In contrast, the constrained beryllium pebbles reveal large pores localized near the contact zones [5]. The local stresses in contact zone might provoke the enhanced pore formation by stress-accelerated diffusion of vacancies to the compressed regions [17]. The formation of the sub-grains in the constrained pebbles occurs practically in the entire pebble volume. The elongated sub-grains are mainly oriented perpendicular to the applied stress direction. Sometimes, the pores are interconnected by cracks which are parallel to the sub-grain orientation (Fig. 7d).

The intensive pore formation occurs in the 1 mm unconstrained beryllium pebbles after irradiation at 861 K (Fig. 8a, b). The pores with an average size of 25 μm are uniformly distributed in the grain bulk, but sometimes also located at the grain boundaries. A completely different microstructure was observed in the 1 mm constrained pebbles irradiated at 927 K (Fig. 8c, d). The sub-grain walls are more visible in this case than at lower irradiation temperatures, probably, due to their decoration by denuded zones which are free of helium bubbles [18]. For this irradiation temperature, the thickness of the denuded zones is maximal in the bulk and decreases by approaching the pebble surface. We suppose that the small bubbles are seen as a grey contrast in the grain bulk. Opposite to the sub-grain walls, the large-angle boundaries of the grains existing before sub-grain formation are decorated with chains of bubbles. One can presume that tritium and helium atoms move to the external surface along the interconnected channels formed at the grain boundaries as well as at sub-grain walls which are notably longer. Thus, the developed network of interconnected channels formed on the former and newly created boundaries in the constrained beryllium pebbles can be considered as a precursor of the open porosity network [13, 19].

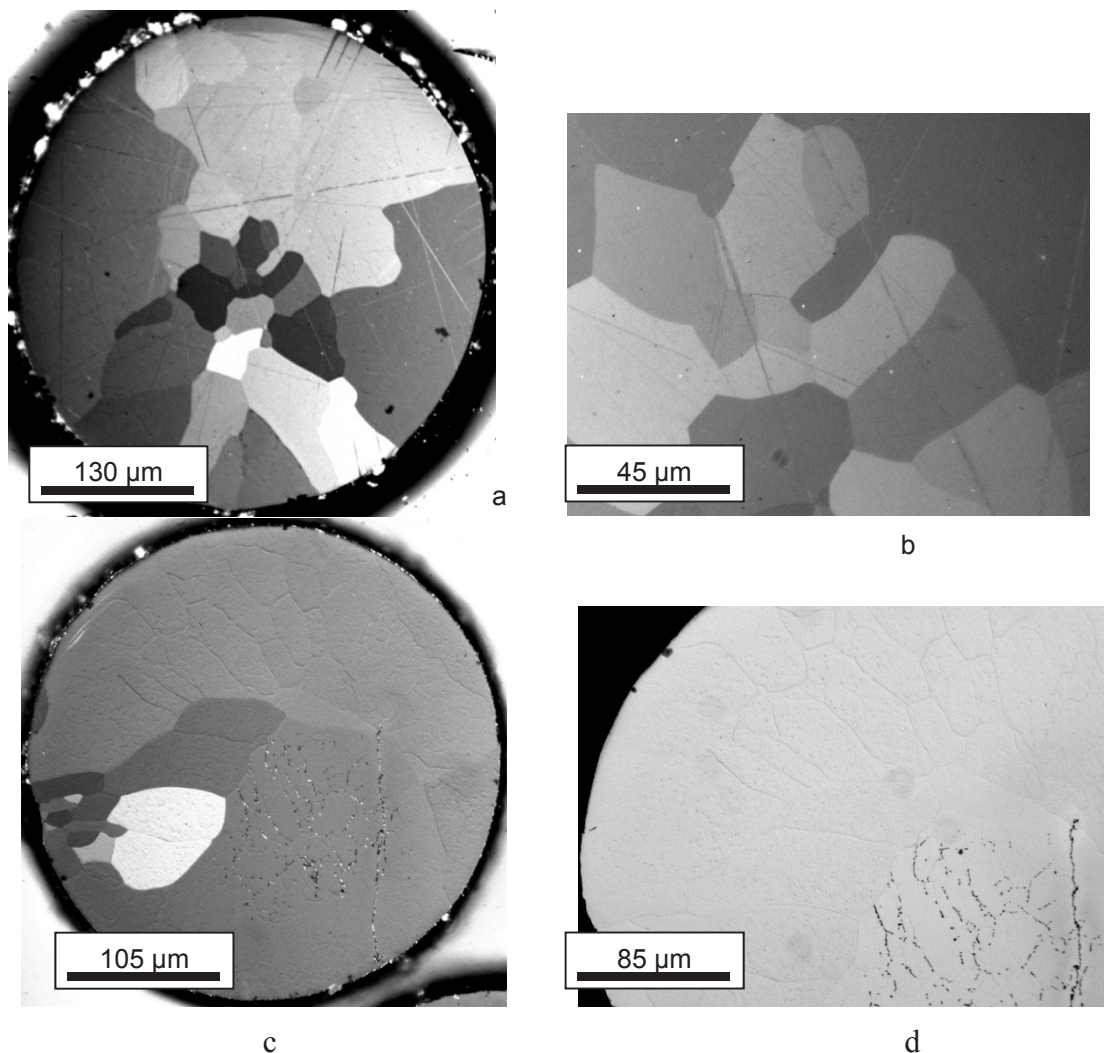


Fig. 6. Optical micrographs of cross sections of the 0.5 mm beryllium pebbles irradiated at 686 K: unconstrained (a, b) and constrained (c, d) pebbles.

Fig. 9 shows microstructures of 0.5 mm the unconstrained (Fig. 9a, b) and the constrained (Fig. 9c, d) beryllium pebbles irradiated at 968 and 1006 K, accordingly. In the unconstrained pebbles large pores ($\sim 40 \mu\text{m}$) are formed mainly on the grain boundaries, whereas in the constrained pebbles, the pores are distributed more homogeneously and have smaller sizes ($< 10 \mu\text{m}$). At this irradiation temperature, even in the unconstrained pebbles, the interconnected channels are sometimes visible in the regions close to the pebble surface (Fig. 9b). Considerable swelling ($\sim 12\%$) observed at this temperature [20] and previous X-Ray-absorption tomography studies [19, 21] suggest a possibility of the open porosity network formation which can explain the decrease of total tritium and helium release with increasing irradiation temperature (see Figs. 4, 5a).

Another interesting feature found for the first time in this study is pronounced apparent thickening of the grain boundaries in conjunction with protrusions of excess material observed at the external surface (see Fig. 9c, d). We suggest that the apparent thickening of the grain boundaries is, in fact, the thickening of the bubble denuded zone at elevated irradiation temperatures. We propose that the growth of denuded zone occurs due to vacancy emission by the grain boundary and is related to the material flow to the boundary. It is notable that the bubbles visible in the optical microscope are still present in a form of chains on the grain boundaries, i. e., within denuded zone.

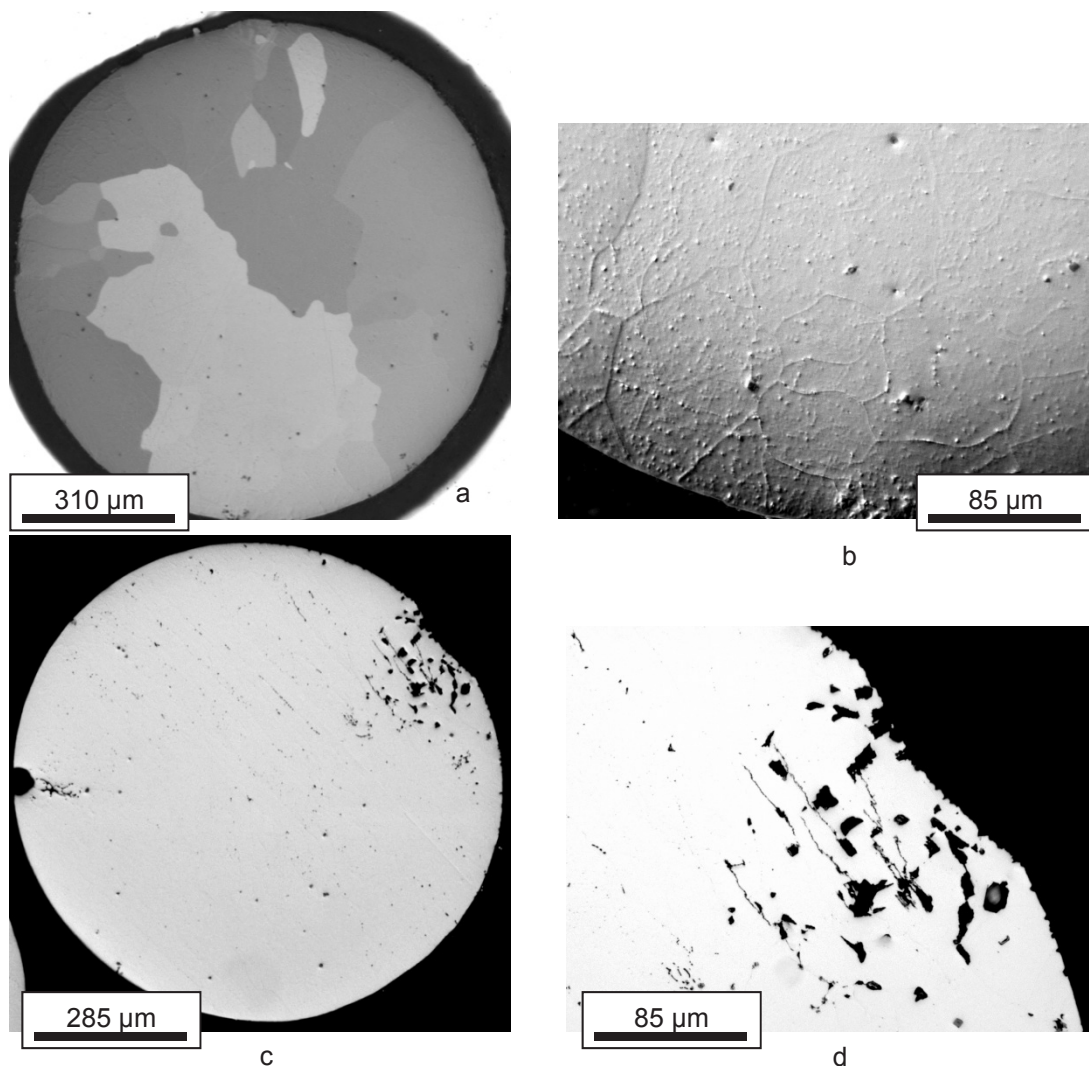


Fig. 7. Optical micrographs of cross sections of the 1 mm beryllium pebbles irradiated at 753 K: unconstrained (a, b) and constrained (c, d) pebbles.

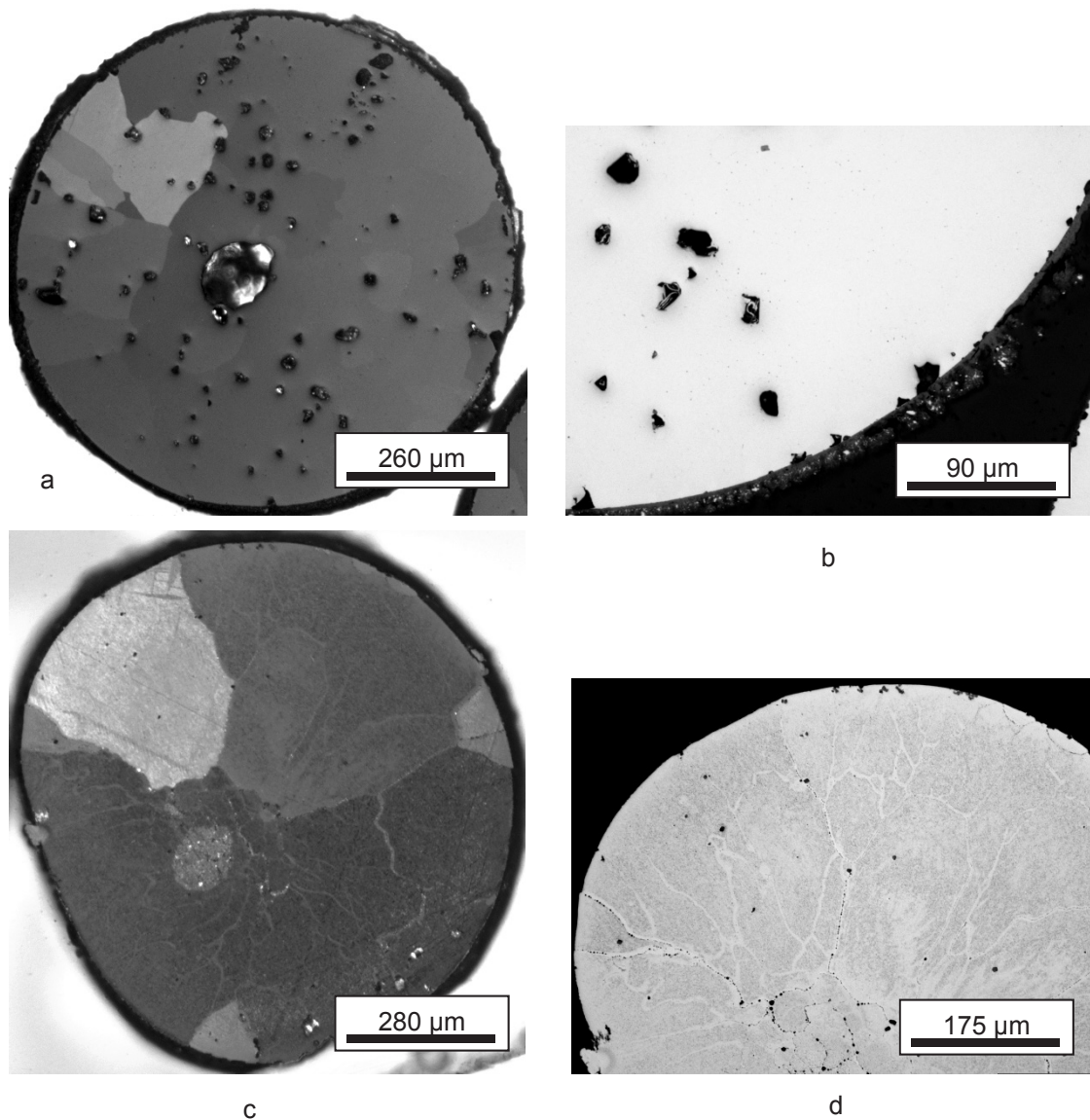


Fig. 8. Optical micrographs of cross sections of the 1 mm beryllium pebbles irradiated at 861 and 927 K: unconstrained (a, b) and constrained (c, d) pebbles.

It is interesting to note that the microstructures formed under irradiation in the constrained and unconstrained pebbles are significantly different. The external stresses due to thermal expansion and material swelling induce plastic deformation resulting in formation of the sub-grain walls. This feature drastically affects further microstructure development. At elevated temperatures, the large pores localized along grain boundaries are found in the unconstrained pebbles, whereas homogeneous distribution of small bubbles within grains with slightly large pores on the grain boundaries is revealed. Locally sub-grain formation occasionally occurs in the unconstrained pebbles near tentative contacts with other pebbles (see Figs. 7b and 9b). High temperature helium embrittlement of structural materials is related to formation of large helium bubbles along grain boundaries resulting in significant loss of cohesion and preferential intercrystalline fracture [22]. In the case of the constrained beryllium pebbles, the formation of the sub-grain structure provides additional sinks for helium and tritium thus reducing their concentrations at the boundaries. In this case, much smaller pores are formed at the grain boundaries (see Fig. 8c, d). Although at high temperatures, the increased mobility of helium-vacancy clusters leads to the loss of grain boundary cohesion and intergranular fragmentation even for constrained pebbles (see Fig. 9c, d).

Earlier tritium release with respect to helium release from the constrained pebbles (see Fig. 2c) can be explained by formation of dislocation walls as far as dislocation core is known to be an accelerated diffusion pathway for hydrogen isotopes. However, to comply with the obtained experimental results one has to assume that helium should be effectively captured by dislocation kinks so that it cannot escape from the material as rapid as tritium.

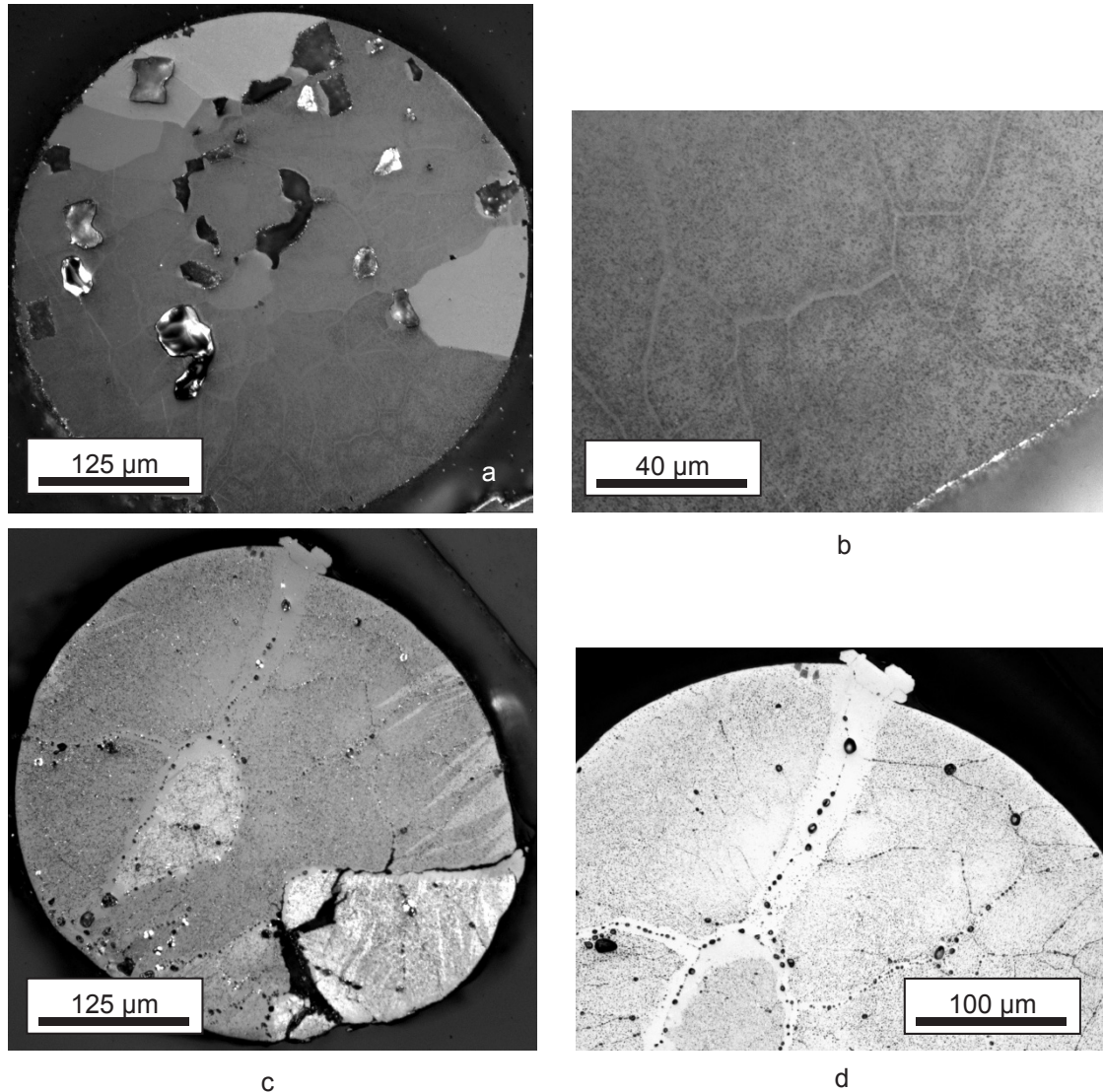


Fig. 9. Optical micrographs of cross sections of the 0.5 mm beryllium pebbles irradiated at 968 and 1006 K: unconstrained (a, b) and constrained (c, d) pebbles.

4. CONCLUSIONS

The study of tritium and helium release from the constrained and unconstrained beryllium pebbles with diameters of 0.5 and 1 mm after neutron irradiation at temperatures of 686-1006 K up to 176-298 appm tritium and 1890÷3020 appm helium productions, accordingly, was performed. All obtained tritium and helium release curves have universal shape with one major release peak while the helium release peak is always shifted to the higher temperatures of 40-130 K relative to the tritium one.

For the constrained pebbles, the tritium release peaks are always located at lower temperatures, and the total tritium release is lower than for the unconstrained ones for both 0.5 and 1 mm beryllium pebbles.

The tritium retention rapidly decreases with increasing irradiation temperature, in particular, for the 1 mm unconstrained beryllium pebbles being 19 % at the highest irradiation temperature and 44 % at the blanket operation temperature. For the 1 mm constrained beryllium pebbles, the tritium retention for the blanket operation temperature is 6 %, i.e. significantly lower than for unconstrained.

It was shown that external stresses applied to beryllium pebbles significantly affect microstructure evolution under irradiation. It is supposed that plastic deformation is induced by combined action of thermal expansion and irradiation swelling results in the development of the observed sub-grain structure. Another manifestation of the stress effect is formation of large pores near the contact zones between pebbles in the constrained pebble beds.

The formation of sub-grain structure elongated perpendicular to the stress direction, mainly, in constrained, but, sometimes, also near the surface of unconstrained pebbles was observed. The possible positive role of the sub-grain walls for accelerated tritium and helium release is discussed.

This work confirmed formation of open porosity network found previously [21] which can be formed either on the grain or sub-grain boundaries. Larger bubbles are formed on the large-angle grain boundaries, while chains of smaller bubbles are observed along small-angle sub-grain boundaries.

Pronounced thickening of the denuded zone along grain boundaries in conjunction with protrusions of excess material observed at the external surface was found for the first time in this study.

ACKNOWLEDGEMENTS

This work was supported by Fusion for Energy under the grant contract No. F4E-2009-GRT-030-03. The views and opinions expressed herein reflect only the author's views. Fusion for Energy is not liable for any use that may be made of the information contained therein.

REFERENCES

- [1] Y. Poitevin, L.V. Boccaccini, M. Zmitko, K. Schleisiek, I. Ricapito, J.-F. Salavy, E. Diegele, F. Magnani, H. Neuberger, R. Lässer, and L. Guerrini, *Fus. Eng. Des.* 85 (2010) 2340-2347.
- [2] J.B.J. Hegeman, J.G. van der Laan, H. Kawamura, A. Möslang, I. Kupriyanov, M. Uchida, and K. Hayashi, *Fus. Eng. Des.* 75–79 (2005) 769–773.
- [3] S. van Til, J.B.J. Hegeman, H.L. Cobussen, and M.P. Stijkel, *Fus. Eng. Des.* 86, 9–11 (2011) 2258-2261.
- [4] E. Ishitsuka, H. Kawamura, N. Sakamoto, and K. Nishida, Process for preparing metallic beryllium pebbles, US Patent No. 5958105, 1999.

- [5] V. Chakin, R. Rolli, A. Moeslang, P. Vladimirov, P. Kurinskiy, S. van Til, A.J. Magielsen, M. Zmitko, *Fus. Eng. Des.* 88 (2013) 2309-2313.
- [6] M. Klimenkov, V. Chakin, A. Moeslang, R. Rolli, *J. Nucl. Mater.* 443 (2013) 409-416.
- [7] E. Pajuste, A. Vitins, G. Kizane, V. Zubkovs, P. Birjukovs, *Fus. Eng. Des.* 86 (2011) 2125–2128.
- [8] Sreekumar, J., Hogan, T.J., Taylor, S., Turner P., Knott C., *Journal of the Society for Mass Spectrometry*, 2010. 21(8), 1364-1370.
- [9] V. Chakin, R. Rolli, A. Moeslang, M. Klimenkov, M. Kolb, P. Vladimirov, P. Kurinskiy, H.-C. Schneider, S. van Til, A.J. Magielsen, and M. Zmitko, *J. Nucl. Mater.* 442 (2013) 483-489.
- [10] F. Scaffidi-Argentina, H. Werle, Tritium release from neutron irradiated beryllium: kinetics, long-time annealing and effect of crack formation, in: *Proc. 2nd IEA International Workshop on Beryllium Technology for Fusion*, Jackson Lake Lodge, Wyoming, September 6-8, 1995.
- [11] F. Scaffidi-Argentina, *Fus. Eng. Des.* 58-59 (2001) 641-645.
- [12] F. Scaffidi-Argentina, G. Piazza, R. Rolli, *Fus. Eng. Des.* 69 (2003) 505-509.
- [13] E. Rabaglino, J.P. Hiernaut, C. Ronchi, F. Scaffidi-Argentin, *J. Nucl. Mater.* 307–311 (2002) 1424–1429.
- [14] I.I. Papirov, V.S. Shokurov, A.I. Pikalov, A.A. Nikolaenko, *PAST 1* (89) 2014, 3-8.
- [15] M.E. Kassner, *Fundamentals of creep in metals and alloys*, Elsevier, Oxford, UK, 2009, 28-37.
- [16] D. Hull and D.J. Bacon, *Introduction to Dislocations*, 3rd edn. Butterworth, Heinemann, Oxford, UK, 1984.
- [17] Ya.E. Geguzin, Ascending diffusion and the diffusion aftereffect, *Sov. Phys. Usp.* 29 (1986) 467–473.
- [18] G.A. Sernyaev, V.P. Goltsev, Z.I. Chechetkina, *Atomnaya Energiya*, Vol. 35, No, 3, September, 1973, 175-178.
- [19] R. Pieritz, J. Spino, P. Vladimirov, C. Ferrero, *Inter. J. Mater. Res.* 103 (2) (2012) 250-257.
- [20] S. van Til, J.B.J. Hegeman, H.L. Cobussen, M.P. Stijkel, *Fus. Eng. Des.* 86 (2011) 2258–2261.
- [21] E. Rabaglino, J. Baruchel, E. Boller, A. Elmoutaouakkil, C. Ferrero, C. Ronchi, T. Wiss, *Nuclear Instruments and Methods in Physics Research B* 200 (2003) 352–357.
- [22] H. Trinkaus, H. Ullmaier, *J. Nucl. Mater.* 212–215 (1994) 303-309.

Preliminary Synthesis of plasma-sintered binary beryllides

Jae-Hwan Kim, Masaru Nakamichi

*Fusion Research and Development Directorate, Japan Atomic Energy Agency,
2-166, Omotedate, Obuchi, Rokkasho, Kamikita, Aomori, 039-3212, Japan*

ABSTRACT

Binary beryllium intermetallic compounds have been extensively studied as the most promising candidate for advanced multipliers in demonstration fusion reactors because of its high temperature stability. The advanced neutron multiplier is being developed by Japan and the European Union (EU) in the demonstration reactor research and development (DEMO R&D) of the International Fusion Energy Research Centre (IFERC) project as part of Broader Approach (BA) activities from 2007 to 2016. However, it is no doubt that few study on synthesis and characterizations of the beryllides except for Be-Ti system found.

In the present study, we report on preliminary synthesis and microstructure observation of the binary beryllides, Be-Nb, Be-V, Be-Mo and Be-W fabricated by plasma sintering method. The beryllides were successfully fabricated with a majority of Be_{12}M phase. The microstructure images and electron probe micro-analysis of the beryllides demonstrated that Be-Nb compound was composed of Be, Be_{12}Nb , $\text{Be}_{17}\text{Nb}_2$ and Be_2Nb while Be-V compound Be, Be_{12}V , Be_2V and V. Additionally, in binary Be-Mo and Be-W, they are composed of Be, Be_{22}M , Be_{12}M , Be_2M and M (M = Mo and V). This is in good agreement with x-ray diffraction profiles of the beryllides.

1. INTRODUCTION

Beryllium intermetallic compounds (beryllides) have paid attention as an advanced neutron multiplier in fusion reactor. From viewpoints of stability and swelling property at high temperature, the beryllide is superior to beryllium. Many researches on titanium beryllide have been intensively reported in light of not only fabrication process [1] but characterizations [2]. In the present study, we report on the preliminary fabrication results of the binary beryllides, Be-Nb, Be-Mo, Be-V and Be-W using a plasma sintering method, which was newly suggested by our group [3].

2. EXPERIMENTAL

For the sake of clarity, plasma sintering which is consisted of an activation treatment to clean the surface of the powder by AC pulse and heating treatment by joule heat, was carried out under identical conditions as follows: temperature, time and pressure was 1000 °C, 20 min and 50 MPa, respectively while heating and cooling rate were 100 and 200 °C/min, respectively. Mixing ratio of beryllium and second elements (M:Nb, Mo, V and W) is Be-7.7at.%M which corresponds to stoichiometry of Be_{12}M . After synthesis of the beryllide, electron probe microscopy (EPMA, JXA-8530F, JEOL, Japan) was used for observation and qualitative analysis of the beryllide and additionally, XRD analysis was carried out.

3. RESULTS AND DISCUSSION

Fig.1 shows the SEM images with back-scattered electron of the plasma-sintered binary beryllides, (a) Be-Nb, (b) Be-Mo, (c) Be-V and (d) Be-W. In case of Be-Nb beryllide, it consisted of four phases, Be (black area), Be_{12}Nb , $\text{Be}_{17}\text{Nb}_2$ and Be_2Nb . This consolidation result is similar with that of Be-Ti binary beryllide, including phase composition formed as well as the area fraction for each phase. On the other hand, Be-Mo binary beryllide synthesized by plasma sintering, shows different tendency of phase composition with Be-Ti and Be-Nb. From not only SEM images observation but XRD analysis, Be_{22}Mo with area fraction of 10% was detected. This is caused by the fact that there co-exist Be_{22}Mo and Be_{12}Mo phase from 4.3 at.% to 7.7 at.% in Be-Mo binary phase diagram as shown in Fig. 2.

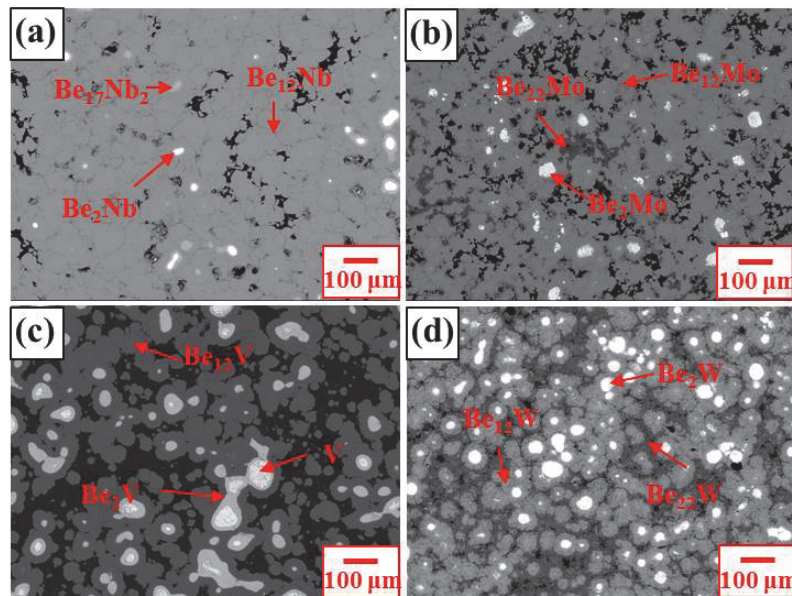


Fig.1 Binary beryllides plasma-sintered at 1273 K for 20 min.

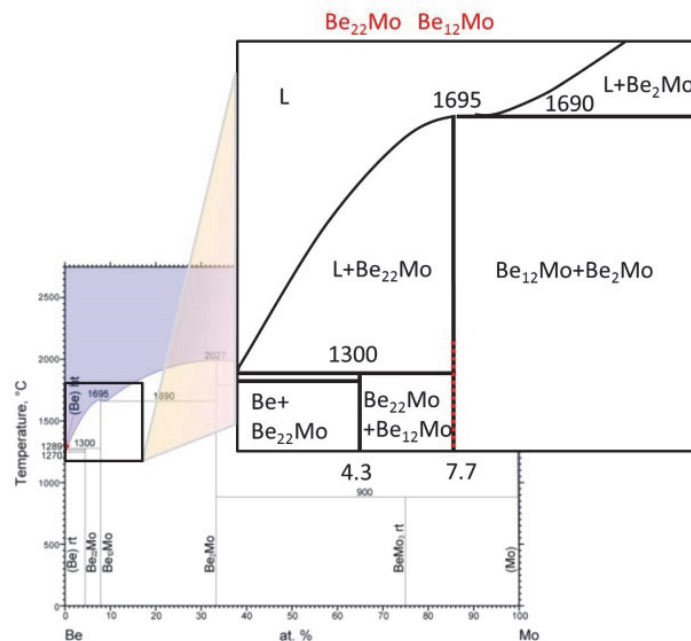


Fig.2 Be-Mo binary phase diagram.

In a SEM image of Be-V beryllide, the area fractions of Be, Be₁₂V, Be₂V and V are 26, 58, 13 and 3 %. As compared with Be-Ti beryllide, no Be₁₇V₂ detected while larger fraction of Be phase observed and some of V remained. Based on the Be-V diagram as shown in Fig.3, if it is granulated by rotating electrode method, it is expected that the peritectic reaction would not be occurred as follows: $L + Be_{17}M_2 \rightarrow Be_{12}M$, because the melting point of the Be₁₂V is higher than that of Be₁₇V₂.

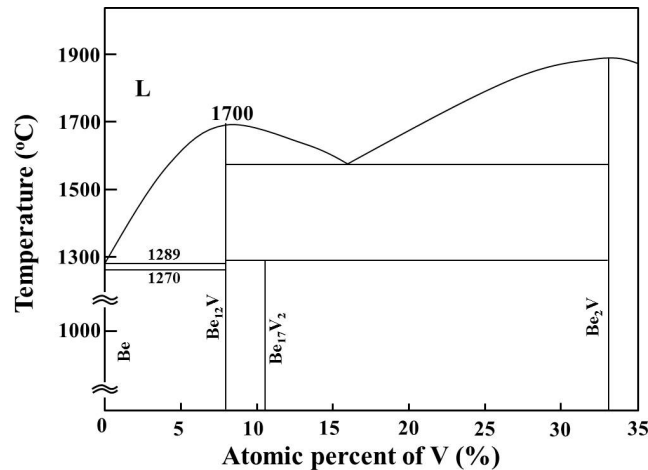


Fig.3 Be-V binary diagram.

Finally, Be-W binary beryllide shows the most complicated phase composition, consisting of Be, Be₂₂W, Be₁₂W and Be₂W phase. The area fraction of target composition, Be₁₂W was 59 % while those of Be₂₂W and Be₂W were 26% and 13%, respectively. Among secondary elements, the melting point of W is the highest (1750 °C). This might be associated with the lowest fraction of target composition to 59 %. On the surface of the Be-W beryllide, moreover, some cracks were observed although Be₁₂W phase was successfully synthesized. It may be due to larger fraction of Be₂₂W phase.

4. CONCLUSION

In order to investigate the applicability of the plasma sintering to synthesis the binary beryllide, Be₁₂Nb, Be₁₂Mo, Be₁₂V and Be₁₂W were plasma-sintered at 1000 °C for 20 min. SEM image observation and XRD analysis clarified that Be₁₂M was successfully synthesized and Be-Nb binary beryllide contains 92% of the Be₁₂Nb phase whereas that of Be-W beryllide does 59%. As a next step, thermal stability when annealed will be undergoing with fundamental properties.

REFERENCES

- [1] M. Nakamichi, J-H. Kim, D. Wakai, K. Yonehara, Fusion Engineering and Design, 87 (2012) 896-899
- [2] J.-H. Kim, M. Nakamichi, J. Nucl. Mater., In Press, (2012)
<http://dx.doi.org/10.1016/j.jnucmat.2012.10.013>
- [3] M. Nakamichi, K. Yonehara, Journal of Nuclear Materials, 417 (2011) 765-768

Characterisation of Be-Ti rod fabricated by extrusion at 900 °C

P. Kurinskiy^{1*}, A. Moeslang¹, H. Leiste¹, A.A. Goraieb², R. Rolli³, S. Mueller⁴

¹ - Karlsruhe Institute of Technology, Institute for Applied Materials- Applied Materials Physics (IAM-AWP), P.O. Box 3640, 76021 Karlsruhe, Germany

² - Karlsruhe Beryllium Handling Facility (KBHF GmbH), Herrmann-von-Helmholtz-Platz 1, 76344 Eggenstein-Leopoldshafen, Germany

³ – Karlsruhe Institute of Technology, Institute for Applied Materials- Materials Biomechanics (IAM-WBM), P.O. Box 3640, 76021 Karlsruhe, Germany

⁴ – Extrusion Research and Development Center, TU Berlin, Sekr. TIB 4/1-2, Gustav-Meyer-Allee 25, 13355 Berlin, Germany

author's email: petr.kurinskiy@kit.edu

ABSTRACT

Titanium beryllide Be₁₂Ti is one of the candidate materials for advanced neutron multiplier in the helium-cooled breeding blanket of DEMO reactor.

The process of fabrication of Be-Ti rods by hot extrusion of blended beryllium and titanium powders is very attractive from the point of view of production of long and high-dense rods.

The powder mixture having the composition of Be-30.8 wt.% Ti which corresponds to stoichiometric content of Be₁₂Ti intermetallic phase was milled down to few μm in size in decalin C₁₀H₁₈ and subsequently extruded at 900 °C in a double-walled container (outer jacket was made out of nickel-chromium steel and titanium inner jacket).

Produced Be-Ti rod was cut into discs for further density measurements and investigations of microstructure both in "as-extruded" state and after high-temperature annealing in vacuum at 1000 and 1100 °C.

KEYWORDS

titanium beryllide, Be-Ti rods, wet milling process, hot extrusion.

1. INTRODUCTION

The method of fabrication of Be-Ti rods by hot extrusion seems to be very promising from the point of view of production of long rods having the lengths up to a few meters and densities exceeding 90% of theoretical density. Fine Be-Ti powder having the composition of Be-30.8 wt.% Ti (corresponds to stoichiometric content of Be₁₂Ti intermetallic phase) was canned into a steel jacket and extruded in ambient atmosphere at 900 °C.

Annealing tests in vacuum at 1000 and 1100 °C followed by consequent X-Ray diffraction (XRD) analysis were performed for the evaluation of evolution of the phase composition of extruded Be-Ti rod. In parallel, density measurements of titanium beryllide samples cut out of Be-Ti rod were performed by immersing in decalin C₁₀H₁₈.

It should be noted that all works, excepting the extrusion process, were performed inside of different glove-box systems under argon atmosphere at KBHF (Karlsruhe Beryllium Handling Facility).

This work represents study of characteristics of microstructure of extruded Be-Ti rod as well as some issues which refer to a production of fine Be-Ti powder (particle sizes are in the range of few microns) by wet milling process.

2. EXPERIMENTAL

2.1 Initial materials

Coarse beryllium powder from Brush Wellman Inc. with the particle sizes ranging 100-200 μm and titanium powder with the sizes of particles not exceeding 44 μm delivered by Alfa Aesar GmbH were used as initial powders in this work.

2.2 Milling of Be-Ti powder

Be-30.8 wt.% Ti powder mixture was milled using NETZSCH milling machine in oxygen-free decalin $\text{C}_{10}\text{H}_{18}$. 2 mm beryllium pebbles produced by Company Brush Wellman Inc. were used as grinding bodies inside of the milling chamber. The use of decalin kept, from one hand, fine beryllium particles inside of milling chamber and, from another hand, prevented the milled powders from their oxidation. Fig. 1 shows Be-Ti powder after 12 h of milling at 1200 rpm which was used as initial material for the production of Be-Ti rod by hot extrusion.

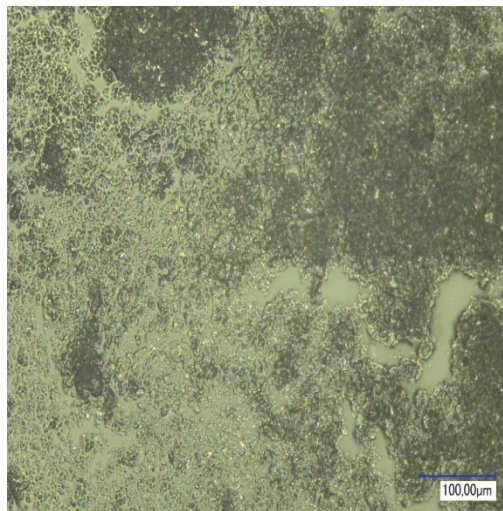


Fig. 1 Be-30.8 wt.% Ti powder after 12 h of milling at 1200 rpm using NETZSCH machine

Besides analysis of the particle sizes of the milled Be-Ti powder, the optical inspection of the grinding bodies using KEYENCE digital microscope was performed. During the milling process, 2 mm beryllium pebbles were often split into 2-5 pieces what is determined by very low values of fracture toughness of pure beryllium (approx. $9\text{-}13 \text{ MN}\cdot\text{m}^{-3/2}$) [1]. Fig. 2 represents a typical view of beryllium pebble after its using in the milling process. Therefore, a certain quantity of pure beryllium moved into Be-Ti powder mixture. From another hand, it is expected that titanium powder originated from the mill's stator during its operation compensates the excess of beryllium powder.

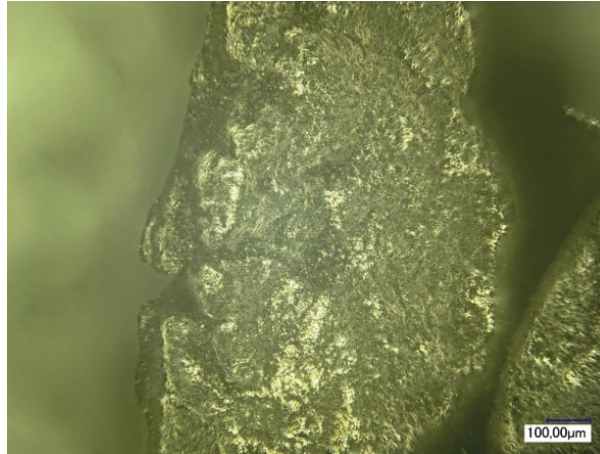


Fig. 2 Beryllium pebble after using in the NETZSCH milling machine

2.3 Encapsulation of Be-Ti powder and extrusion process

After the milling process, fine Be-Ti powder was dried at 120 °C for 4 hours at about 2-5 mbar of residual pressure and, then, was additionally sieved through -63 μm (-230 mesh) sieve in order to get rid of bigger particles which were split off, mainly, from the grinding bodies.

Jackets out of nickel-chromium steel with outer and inner diameters of 80 and 46 mm, respectively, were used for Be-Ti powder canning before an extrusion process. Milled powder was compacted inside of jacket's cylindrical cavity having a height of 100 mm by tapping with a hammer. Titanium sheet having the thickness of 1 mm was used as a diffusion barrier in order to prevent interaction between steel outer capsule and Be-Ti powder. Afterwards, the capsule was sealed by welding and the pre-compacted powder was additionally outgassed at 120 °C using a vacuum pump.

Before the extrusion, the welded steel jacket with Be-Ti powder inside was heated in a furnace in air up to 900 °C and held for 4 h at this temperature while the process tools (extrusion die, etc.) were heated up to 500 °C in ambient atmosphere in another furnace. The process of extrusion has been performed using 8 MN extrusion press in ambient atmosphere. The velocity of the ram displacement was constant during the process and equaled to 10 mm/s.

Fig. 3 depicts the cross-section of the extruded at 900 °C Be-Ti rod right after cutting by a disc saw in a glove-box. The diameter of fabricated rod (including steel jacket) is 32 mm. The achieved extrusion ratio was 7:1.



Fig. 3 Hot-extruded Be-Ti rod inside of a steel jacket

3. STUDY OF MICROSTRUCTURE OF EXTRUDED BE-TI ROD

3.1 Optical microscopy

Disc cut from Be-Ti rod was embedded and then the surfaces of its segments were polished in two mutually perpendicular directions – along and transverse with the respect to an extrusion axis. Fig. 4 depicts microstructure of Be-Ti rod in direction parallel to an extrusion axis and fig. 5 shows the polished cross-section which is transverse to an extrusion axis. One could observe the preferred grain orientation (texture) coinciding with the direction of extrusion (Fig. 4). It is notable that texture became more pronounced in the vicinity of the steel jacket.

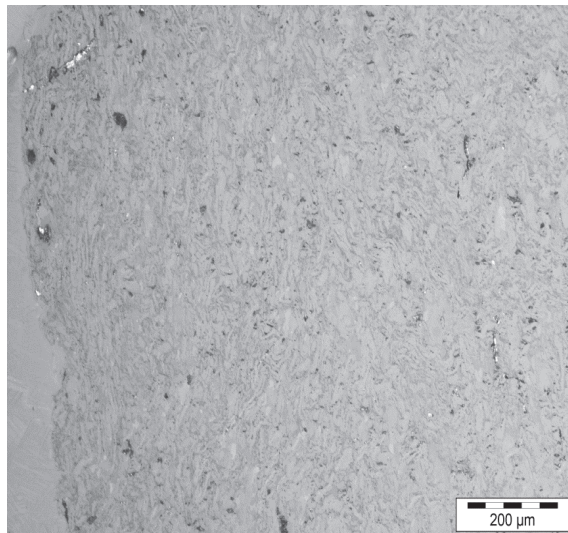


Fig. 4 Microstructure of Be-Ti rod in direction parallel to an extrusion axis

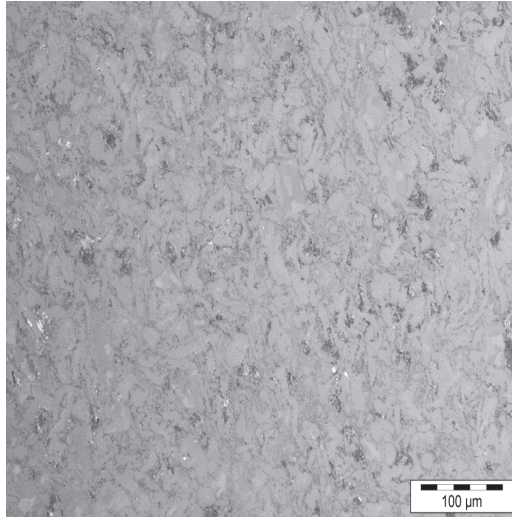


Fig. 5 Polished cross-section of Be-Ti rod in the transverse direction with the respect to an extrusion axis

Homogeneously distributed pores were observed within the whole rod volume what could be determined by the difference in diffusion rates of Be in Ti and, on the contrary, of Ti in Be (Kirkendall effect). On the other hand, residual porosity could refer to "pure" technological defects and can be explained, presumably, by a need for preliminary compaction of initial Be-Ti powder using higher loadings. Noteworthy, theoretical density of extruded Be-Ti rod was 0.912 of fully dense Be₁₂Ti phase (2.26 g/cm³) [2].

3.2 High-temperature annealing tests and X-Ray diffraction (XRD) analysis

In order to study the influence of temperature on the evolution of the phase composition of Be-Ti samples, heat treatment at 1000 and 1100 °C was performed. Be-Ti discs were annealed in vacuum (residual pressure in the range of 10⁻⁵...10⁻⁴ mbar) with the duration of each test of 2 h.

After performing of the annealing tests, several specimens having diameters of 3 mm and heights of a few mm were cut out of Be-Ti discs in as-received and annealed states for further XRD investigations (Fig. 6). This operation was done to exclude the possibility of X-Ray beam interaction with material of the encapsulation.



Fig. 6 Be-Ti sample for XRD investigations

Fig. 7 shows XRD patterns corresponding to Be-Ti rod in "as-extruded" (initial) state and after high-temperature annealing tests at 1000 and 1100 °C.

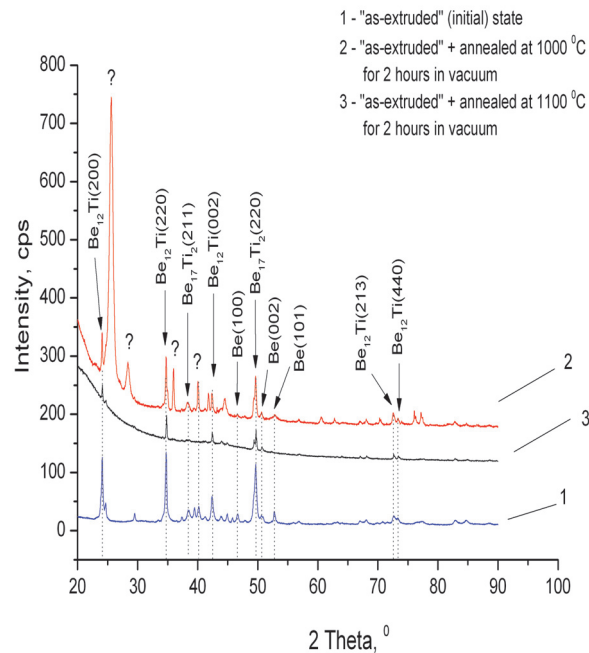


Fig. 7 XRD patterns of Be-Ti rod in initial and annealed states

The phase composition of Be-Ti rod in "as-extruded" state is presented, mainly, by pure Be, Be_{12}Ti and $\text{Be}_{17}\text{Ti}_2$. The presence of unidentified phase was detected after heat treatment at 1000 °C. This phase corresponds, probably, to Be_xTi_y compound with low Be content. One can observe the tendency of pure Be peaks to disappear after high-temperature heat treatments. While performing the annealing tests, diffusion rates of Be increase with increasing temperature. Thus, beryllium dissolves in complex Be-Ti matrix and forms Be-rich phases ($\text{Be}_{17}\text{Ti}_2$, Be_{12}Ti). It should be emphasized that in spite of high signal-to-noise ratio observed during XRD measurements of specimen annealed at 1100 °C, pure Be_{12}Ti phase was detected.

Obtained results are in a good agreement with data from M. Nakamichi and J.-K. Kim [3-5] who observed the formation of nearly pure $\text{Be}_{17}\text{Ti}_2$ and Be_{12}Ti phases after high-temperature homogenization of Be-Ti specimens containing, before the annealing tests, both – pure Be, Ti and Be_2Ti phase.

4. SUMMARY

Experimental results obtained in this work allow to make following conclusions:

- Extrusion can be considered as perspective method of obtaining of Be-Ti rods,
- Observed texture of Be-Ti rod can lead to a certain anisotropy of material properties,
- Pure Be_{12}Ti phase was formed after annealing of extruded Be-Ti at 1100 °C for 2 h in vacuum,
- Some process parameters (temperature, material of jackets, particle sizes of initial Be and Ti powders) still need to be specified.

REFERENCES

- [1] D. Webster, G.J. London (editors), Beryllium Science and Technology (in Russian), p. 493, Metallurgija, Moscow, 1984.
- [2] Ch. Dorn, W. Haws, E. Vidal, A review of physical and mechanical properties of titanium beryllides with specific modern application of TiBe₁₂, Fusion Engineering and Design 84 (2009) 319-322.
- [3] J.-K. Kim, M. Nakamichi, Optimization of synthesis conditions for plasma-sintered beryllium-titanium intermetallic compounds, Journal of Alloys and Compounds 577 (2013) 90-96.
- [4] J.-K. Kim, M. Nakamichi, Oxidation property and homogenization treatment of plasma sintered beryllides, Fusion Engineering and Design 2013, in Press.
- [5] M. Nakamichi, K. Yonehara, D. Wakai, Trial fabrication of beryllides as advanced neutron multiplier, Fusion Engineering and Design 86 (2011) 2262–2264.

Optimization of beryllide electrode fabrication as raw material for granulation by the rotating electrode method

Masaru Nakamichi, Jae-Hwan Kim, D. Wakai

*Fusion Research and Development Directorate, Japan Atomic Energy Agency,
2-166, Omotedate, Obuchi, Rokkasho, Kamikita, Aomori, 039-3212, Japan*

ABSTRACT

It should be clear that the granulation process of the beryllide is available with low cost and high efficiency. In order to fabricate the beryllide pebbles, a new granulation process has been established, combined by a plasma sintering method for beryllide synthesis and a rotating electrode method using plasma-sintered electrode for granulation. The fabrication process of the beryllide electrode was investigated in light of the mass production. From the optimization results, because the optimized beryllide electrode indicated higher ductility and was sintered at lower temperature for shorter time, this beryllide electrode were more suitable not only to withstand the thermal shock by arc-discharge during granulation but to produce the beryllide pebble on a large scale. Accordingly, the optimization result could lead to expectation of the time reduction and cost saving for pebble mass production because this result can reduce the time of electrode fabrication by 40%.

KEYWORDS

Fusion Blanket, Neutron multiplier, Beryllium intermetallic compound, Beryllide

1. INTRODUCTION

Beryllium intermetallic compounds (beryllides) such as Be_{12}Ti are the most promising material as advanced neutron multipliers [1–2]. However, few studies on developments of mass production reported. It should be considered that the beryllide granulation is available with low cost and high efficiency owing to requirement of 200-400 tons of neutron multiplier for its breeder blanket.

We suggested a new beryllide granulation process, which was combinational process with a plasma sintering method and a rotating electrode method (REM). A new granulation flow scheme for the Be-Ti beryllide is shown in Fig. 1. The plasma sintering is simple, easy to control and can reduce the time of beryllide electrode fabrication by 30% shorter time than the hot isostatic pressing method as conventional methods. To fabricate the beryllide pebbles, the REM was selected because of the broad experience base for its use, not only for beryllium pebbles but also metallic pebbles in industry in general. This study describes the effect of plasma sintering conditions on the thermal shock resistivity of beryllide electrode.

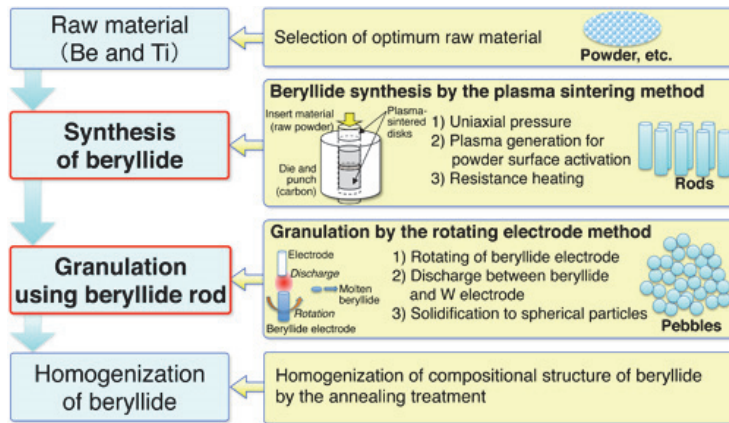


Fig. 1 Process flow scheme of beryllide granulation.

2. TRIAL FABRICATION OF BERYLLIDE PEBBLES

2.1 Beryllide electrode fabrication by the plasma sintering method

Beryllide disks as a Be–Ti intermetallic were synthesized from mixed pure Be and Ti powders. Thirty grams each of beryllium powder (Materion Brush Inc., 99.4 wt.%) and titanium powder (Kojundo Chemical Laboratory Co. Ltd., 99.9 wt.%) were mixed for 60 min with an automatic mortar (RM200, RETSCH, Co. Ltd.) made of Al_2O_3 . The size of the Be and Ti powders was less than $45\ \mu\text{m}$. The mixed powder composition was 92.3 at.% Be and 7.7 at.% Ti, which is the stoichiometric composition of Be_{12}Ti .

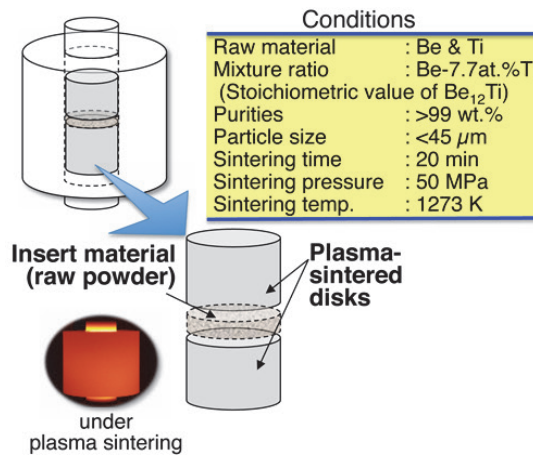


Fig.2 Plasma sintering condition for fabrication of beryllide block.

The powder was loaded into a graphite die, and uniaxial pressure was applied for cold compaction. Electric current was applied to create the plasma environment and to activate the particle surfaces (see Fig.1). The powder compact was resistance-heated while uniaxial pressure was still being applied to the material in the sintering mold. In the present study, a plasma sintering apparatus (KE-PasIII, KAKEN Co. Ltd.) was used. The plasma sintering was conducted at any given sintering temperature of 1273 K and sintering time of 20 min under a pressure of 50 MPa while heating and cooling rates were approximately 100 and 200 K/min, respectively. The plasma-sintered beryllide disks were 20 mm in diameter and 45 mm in thickness.

To fabricate the beryllide electrode for the REM, joining process to fabricate a beryllide block was performed by use of two plasma-sintered beryllide disks (see Fig.1 and 2). For the joining, three grams of powder (i.e., the same raw material used to fabricate the beryllide disks) was inserted between the plasma-sintered disks. The plasma sintering conditions for joining were the same as those for fabrication of the beryllide disk. The size of the joined beryllide block was 20 mm in diameter and 60 mm in length. Using the beryllide electrode with 10 mm in diameter and 60 mm in length machined by the wire electric discharge method from this plasma-sintered beryllide block, trial fabrication of prototypic beryllide pebbles was performed by the REM (see Fig.3).

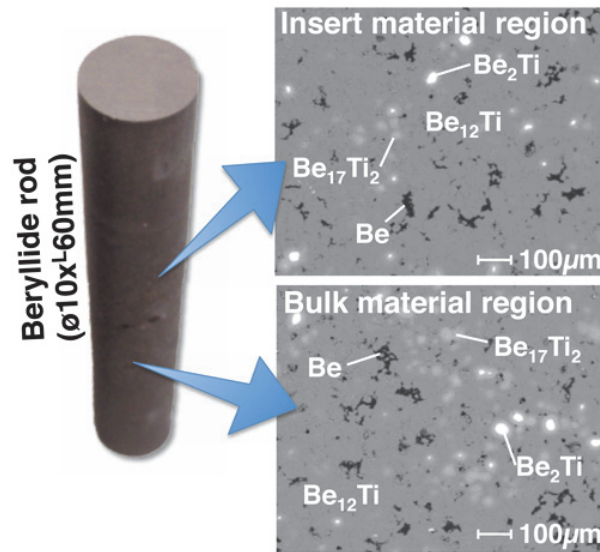


Fig.3 Photographs of the plasma-sintered beryllide electrode.

2.2 Beryllide pebble fabrication by the rotating electrode method

With these plasma-sintered beryllide electrodes, trial fabrication of prototypic beryllide pebbles was performed by the REM, in which a metal particle is produced as the end of a metal rod is melted while being rotated along its longitudinal axis. The melted metal is centrifugally ejected and forms droplets that solidify to spherical particles (see Fig.1).

The beryllide pebbles were fabricated in a REM apparatus that has a granulation chamber 1000 mm in diameter, using a current of 80 A, a rotating speed of 6000 rpm, and the plasma-sintered beryllide rod as an electrode. The pressure of the granulation vacuum chamber with replacement of pure He gas was approximately 0.1 MPa.

From the plasma-sintered beryllide electrode, prototypic beryllide pebbles of 1 mm average diameter were successfully fabricated, although the pebbles were composed of Be, $\text{Be}_{17}\text{Ti}_2$, and Be_{12}Ti phases due to a peritectic reaction caused by re-melting [3] (see Figs.4 and 5). Subsequently, a procedure using annealing treatments to homogenize to the Be_{12}Ti phase was evaluated. From the results of the annealing treatments on the prototypic pebbles, the pebble phase was homogenized to a single phase of Be_{12}Ti by annealing either at 1473 K for more than 8 h or at 1673 K for 1 h [4].

However, it revealed that an electrode with a high beryllide content breaks easily by the thermal shock at arc-discharge in granulation process of REM, because beryllide is so brittle (Fig.5). The electrode as a raw material for granulation by REM should have a higher ductility. Therefore, in light of the mass production of beryllide pebbles, the optimization of beryllide electrode fabricated by the plasma sintering method is a key issue.

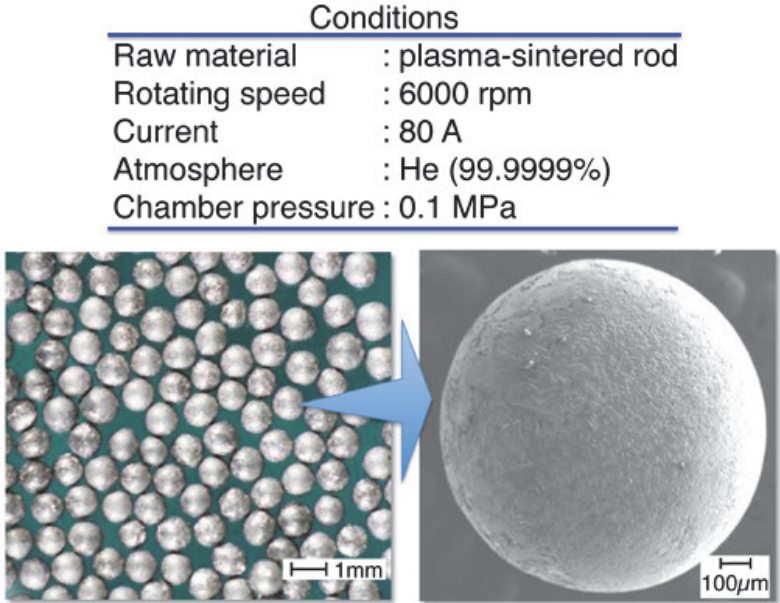


Fig.4 Granulation condition of the rotating electrode method and photographs of prototypic beryllide pebbles.

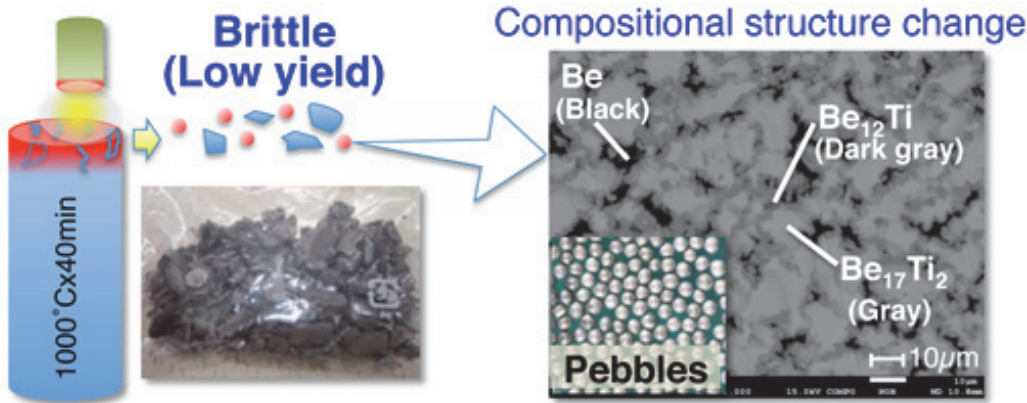


Fig.5 Compositional structure change in beryllide pebble by re-melting during granulation by the REM.

3. RELATIONSHIP OF COMPOSITIONAL STRUCTURE BETWEEN PLASMA-SINTERED ELECTRODES AND PROTOTYPIC PEBBLES

3.1 Compositional structure changes in the plasma-sintered beryllide electrode and in beryllide pebbles using these electrodes

The effect of the compositional structure of the plasma-sintered beryllide electrodes on that of prototypic beryllide pebbles granulated by REM was evaluated. First of all, to evaluate the effect of the plasma sintering conditions on compositional structure, the plasma sintering was performed at 1073, 1173, and 1273 K for 5 and 40 min. And then, the compositional structures in prototypic beryllide pebbles by the REM were evaluated using these plasma-sintered beryllide electrodes. The area fractions of each element or composition were determined from the cross-sectional micrographs of samples with an electron probe micro-analyzer (EPMA; JXA-8530F by JEOL Co. Ltd.).

3.2 Results and discussion

Compositional structure changes in the plasma-sintered beryllide electrodes were shown in Fig.6. The elemental state fraction of Be in the plasma-sintered material decreased by consolidation enhancement as the sintering time increased, with only approximately 6% of the elemental phases remaining in 94% beryllide from processing at 1273 K for 40 min. Not only Be but also Ti phase in the plasma-sintered material were identified as un-consolidated element from plasma sintering at 1073 K for 5 min. The fraction of Be in the plasma-sintered material decreased by consolidation enhancement as the sintering temperature increased.

The compositional structures in the prototypic beryllide pebbles by the REM were evaluated using three kinds of plasma-sintered beryllide electrodes. This granulation examination was performed using the plasma-sintered beryllide electrode from plasma sintering at 1073 K for 5 min, at 1273 K for 5 min and at 1273 K for 40 min. Compositional structure changes in the plasma-sintered beryllide electrodes and the prototypic beryllide pebbles using each plasma-sintered beryllide electrode are shown in Fig.7.

The area fractions of each phase in the prototypic beryllide pebbles by the REM were considerably different from those in the plasma-sintered beryllide electrode used for the REM. On the other hand, microstructural observation showed no difference in compositional structures in each prototypic beryllide pebbles using three different plasma-sintered beryllide electrodes. From the results of these granulation examinations, it was revealed that the compositional structure of the pebble was changed due to re-melting during the granulation process.

Accordingly the plasma-sintered beryllide electrode sintered at lower temperature for shorter time seems to be more suitable to withstand the thermal shock by arc-discharge during granulation by the REM as well as to cut down the production cost. It was supposed that this electrode contains high Be with ductility.

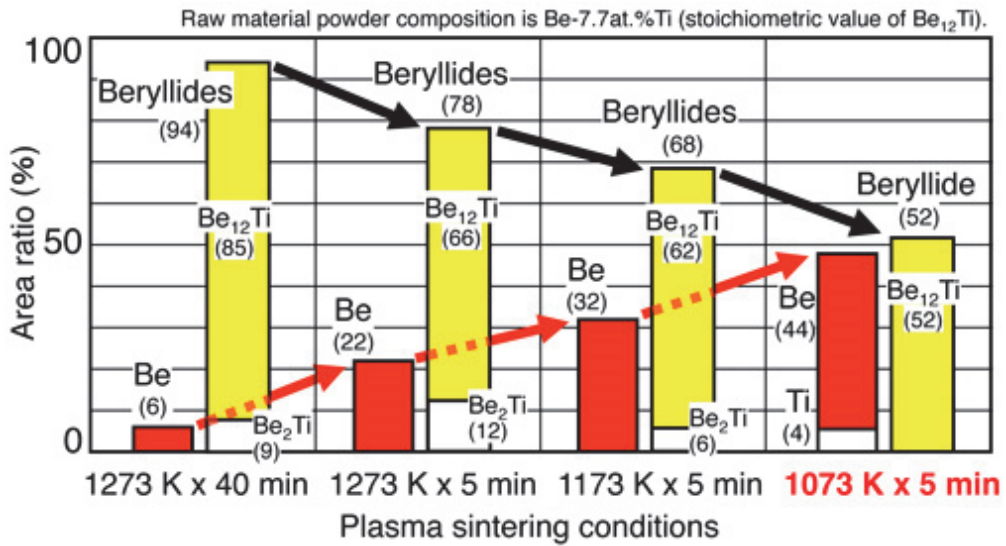


Fig.6 Compositional structure changes in the plasma-sintered beryllide electrodes.

Plasma sintering conditions	Plasma-sintered electrode	Pebbles* by REM**
	(%)	(%)
1073 K x 5 min	Be_{12}Ti : 52	Be_{12}Ti : 32
	$\text{Be}_{17}\text{Ti}_2$: 0	$\text{Be}_{17}\text{Ti}_2$: 58
	Be_2Ti : 0	Be_2Ti : 0
1273 K x 5 min	Be : 44	Be : 11
	Ti : 4	
1273 K x 40 min	Be_{12}Ti : 66	Be_{12}Ti : 36
	$\text{Be}_{17}\text{Ti}_2$: 0	$\text{Be}_{17}\text{Ti}_2$: 53
	Be_2Ti : 12	Be_2Ti : 0
1273 K x 40 min	Be : 22	Be : 11
1273 K x 40 min	Be_{12}Ti : 85	Be_{12}Ti : 35
	$\text{Be}_{17}\text{Ti}_2$: 0	$\text{Be}_{17}\text{Ti}_2$: 55
	Be_2Ti : 9	Be_2Ti : 0
1273 K x 40 min	Be : 6	Be : 10

*) without annealing for homogenization
 **) REM: rotating electrode method

Fig.7 Compositional structure changes in the plasma-sintered beryllide electrodes and the prototypic beryllide pebbles using each plasma-sintered beryllide electrode.

4. CONCLUSION

A new beryllide granulation process that was combinational process with a plasma sintering method and a rotating electrode method (REM) was suggested. The plasma sintering is simple, easy to control and can reduce the time of beryllide electrode fabrication by 30 % shorter time than the hot isostatic pressing method as conventional methods. The prototype pebbles were successfully fabricated by the REM using the plasma-sintered beryllide electrode.

The beryllide electrode fabrication process was investigated in light of the mass production. From the optimization results, it was revealed that the beryllide pebbles with identical phase composition could be fabricated regardless of the difference of the phase compositions in the beryllide electrodes sintered for different temperature and time. Because this optimized beryllide electrode indicated higher ductility and was sintered at lower temperature for shorter time, this beryllide electrode seems to be more suitable not only to withstand the thermal shock by arc-discharge during granulation but also to produce the beryllide pebble on a large scale. Furthermore, the optimization result could lead to expectation of the time reduction and cost saving for pebble mass production because this result can reduce the time of electrode fabrication by 40 %.

REFERENCES

- [1] M. Nakamichi, K. Yonehara, Sintering properties of beryllides for advanced neutron multiplier, *J. Nucl. Mater.* 417, 1-3, (2011) 765-768.
- [2] M. Nakamichi, K. Yonehara, D. Wakai, Trial fabrication of beryllides as advanced neutron multiplier, *Fusion Eng. Des.*, 86, 9-11, (2011) 2262-2264.
- [3] M. Nakamichi, J. H. Kim, K. Yonehara, Novel granulation process of beryllides as advanced neutron multipliers, *Fusion Eng. Des.*, In Press Corrected Proof, Available online 26 March 2013.
- [4] M. Nakamichi, J. H. Kim, Homogenization treatment to stabilize the compositional structure of beryllide pebbles, *Journal of Nuclear Materials*, In Press, Corrected Proof, Available online 13 March 2013.

Prototypic pebbles Fabrication of Titanium beryllide with different chemical composition

Jae-Hwan Kim, Kazuo Yonehara, Masaru Nakamichi

*Fusion Research and Development Directorate, Japan Atomic Energy Agency,
2-166, Omotedate, Obuchi, Rokkasho, Kamikita, Aomori, 039-3212, Japan*

ABSTRACT

Beryllium-Titanium intermetallic compounds have been paid attention as the most promising candidate for advanced multipliers in demonstration fusion reactors. The advanced neutron multiplier is being developed by Japan and the European Union (EU) in the demonstration reactor research and development (DEMO R&D) of the International Fusion Energy Research Centre (IFERC) project as part of Broader Approach (BA) activities from 2007 to 2016.

In this study, the preliminary granulation and analysis of beryllide pebbles with different chemical composition of Ti was reported. In order to clarify the effect of the content of Ti on the fabrication of beryllide pebbles, plasma-sintering method and rotating electrode method were applied for fabrication of beryllide electrode and granulation, respectively. It was clearly confirmed that the beryllide pebbles were successfully fabricated accompanied by phase changes induced by re-melting during the rotating electrode method. The SEM observation of the rods and the cross-section of the pebbles demonstrated that the phases of the electrodes and pebbles were changed due to re-melting during the granulation process. At the edge and center area of the cross-sectional images, moreover, a remarkable difference of the phase size was observed. It may be due to the dissimilarity of the cooling rate at inside and outside of the pebble.

1. INTRODUCTION

Beryllium metals have been extensively investigated as a neutron multiplier of fusion reactor blankets. This neutron multiplier is supposed to be loaded in the blanket as pebble type because of higher packing density as well as reduction of cracking due to thermal stress. For granulation of beryllium, conventional methods such as the rotating electrode method (REM), Mg reduction method (MRM), and gas atomization method have been suggested [1]. In the present study, we investigated the effect of the content of Ti on the synthesis of beryllide pebbles using plasma-sintered beryllide rods and the rotating electrode method.

2. EXPERIMENT

To investigate the effect of the content of Ti on the fabrication of beryllide pebbles, the powder composition was varied among 3 at.%, 5 at.%, 6 at.%, 7 at.%, and 7.7 at.% Ti. The plasma sintering temperature used in the experiments was 1,073 K while the sintering times were 2 min and 30 sec with heating and cooling rates of 100 and 200 K/min, respectively (refer [2] for details).

The conditions of the REM are given in Table 1. To compare the phase compositions before and after the granulation, scanning electron microscope images of the surfaces and cross-sections were obtained by using an electron probe micro analyzer (EPMA, JXA-8530F, JEOL, Japan). Additionally, x-ray diffraction measurements (XRD, Rigaku, UltimaIV, Japan) were carried out for qualitative analysis.

Table 1. Conditions applied in the rotating electrode method

Classification	Conditions
Arc current	80 A
Atmosphere	He gas (0.1MPa)
Rotational speed	6000 rpm
Rod diameter	10 mm

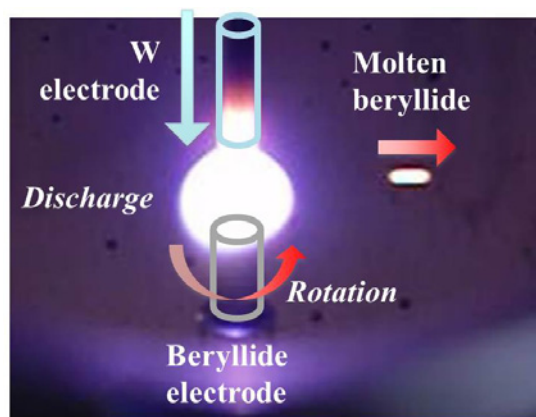


Fig.1 REM (Rotating Electrode Method) process.

3. RESULTS AND DISCUSSION

In granulation process by the REM, the edge of the beryllide electrode is melted while it is rotated toward its longitudinal axis. The molten beryllide is ejected centrifugally and recrystallized, becoming pebbles that solidify with a spherical shape with diameters of about 1 mm.

Fig.2 shows the surface SEM images of the pebbles fabricated by the rotating electrode method, indicating that all pebbles morphology was spherical. It was obvious that in the case of beryllide with 3 at.% Ti, a large portion of the Be phase was confirmed at the surface. For the beryllide pebbles with 5 at.%, 6 at.%, 7 at.%, and 7.7 at.% Ti, on the other hand, beryllide structures growing with a random columnar type was detected without a Be phase. There was no tendency for growth of the beryllide phase in terms of crystallography.

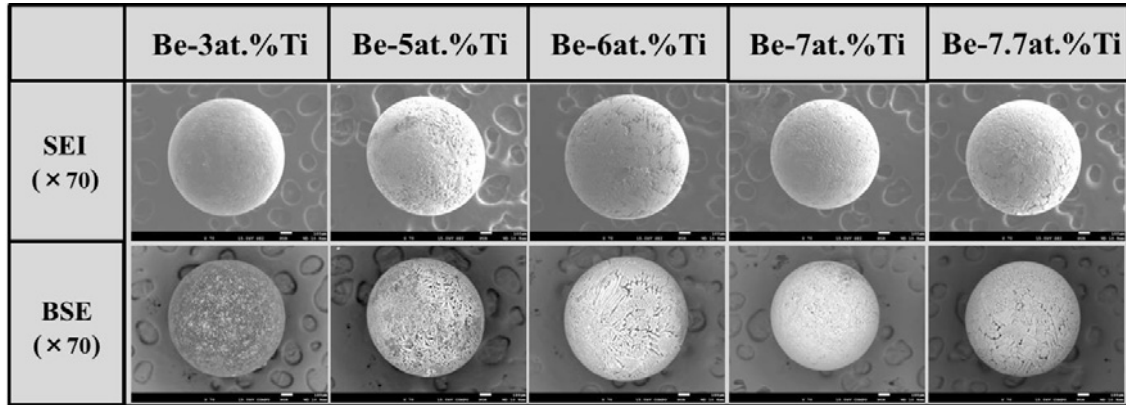


Fig.2 Surface SEM images of the pebbles

In order to evaluate the phase composition in detail, cross-sections of the pebbles with 3, 5, 6, 7 and 7.7 at.%Ti were observed (see Fig. 3). Although the surfaces of the pebbles seemed to be porous without the detection of Be, the cross-sectional images infer that the Be phase exists in all beryllide pebbles and that with increasing content of Ti, the area fraction of the Be phase decreased. Based on the Be-Ti binary phase diagram, the Be_{12}Ti and Be phases were detected in the 3 and 5 at.% Ti beryllides. However, the $\text{Be}_{17}\text{Ti}_2$ phase was formed in the beryllides with 6, 7 and 7.7 at.% Ti as following peritectic reaction, $\text{L} + \text{Be}_{17}\text{Ti}_2 \rightarrow \text{Be}_{12}\text{Ti}$. This might be caused by with re-melting and recrystallization with the peritectic reaction. Although re-melting of the beryllide occurred, the stoichiometry of the beryllide pebbles was the same as the rods. Accordingly, the phase compositions of the pebbles were changed, following the phase diagram.

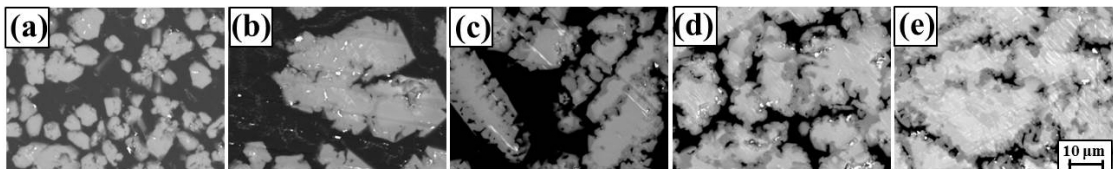


Fig.3 Cross sectional SEM images of the pebbles

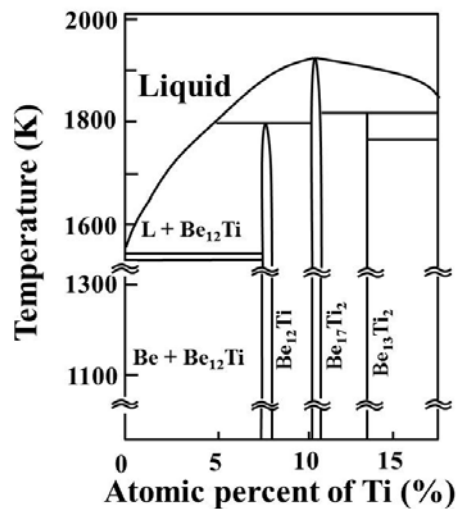


Fig. 4 phase diagram of Be-Ti

4. CONCLUSION

Prototypic pebbles of titanium beryllide with different chemical composition were successfully fabricated. SEM images of the pebble clarified that the $\text{Be}_{17}\text{Ti}_2$ phase was formed in the beryllides with 6, 7 and 7.7 at.% Ti as following peritectic reaction, $\text{L} + \text{Be}_{17}\text{Ti}_2 \rightarrow \text{Be}_{12}\text{Ti}$, while the Be_{12}Ti and Be phases were detected in the 3 and 5 at.% Ti beryllides.

REFERENCES

- [1] Etsuo Ishitsuka, Hiroshi Kawamura, Fusion Engineering and Design 27 (1995) 263-268
- [2] Masaru Nakamichi, Jae-Hwan Kim, Fusion Engineering and Design, to be submitted, (2013)

Environmental Control of Beryllium in NGK

Keigo NOJIRI¹

¹ *Process Engineering Department, New Metals Division, NGK INSULATORS, LTD.
1 Maegata, Handa, Aichi 475-0825, Japan
TEL: +81-569-23-5868, FAX: +81-569-23-5856, e-mail: nojiri@ngk.co.jp*

ABSTRACT

Beryllium will be used as neutron multiplier in ITER. The Test Blanket Modules with beryllium will be fabricated. Beryllium neutron multiplier will be used in form of pebble, small sphere, of high quality. NGK had developed the beryllium pebble fabrication technology with JAEA. At the start of the mass production of the pebbles, the beryllium hygiene and safety issues should be reviewed.

1. INTRODUCTION

Beryllium is categorised as a substance which needs some precautions against occupational diseases. Especially in process generating airborne fume or dust, we should be careful. Everyone who treats beryllium is controlled by law or regulation of each country. NGK, unique processor of beryllium in Japan, has worked hard in this issue for a long time. Although this issue is never-ending, NGK rises to certain control level. Japanese law obliges us to keep the beryllium concentration in workplace within $1.0\mu\text{g}/\text{m}^3$. NGK complies with this value, focuses on the internal standard with tougher criteria. Assessment of airborne beryllium concentration and improvement of machines and local exhaust ventilation system according to the results are absolutely necessary to meet the internal standard. Respiratory protective equipment and careful medical check are also important for operators.

2. NGK'S POLICY

NGK's policy of beryllium environmental issue is simple as « No CBD any more ». NGK unfortunately has some examples of CBD, chronic beryllium disease, in the past. We strongly declare not to have it any more.

3. HOW TO CONTROL

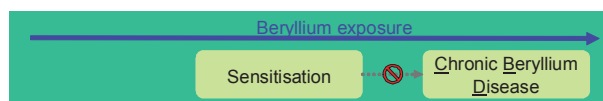


Fig.1 Process to CBD

Fig.1 simply shows the process to CBD. At first, sensitisation comes under beryllium exposure. Then CBD could be possible if the exposure continues. To prevent CBD completely,

it's very important to stop exposure when the sensitisation is detected. It's also important to minimise the possibility of beryllium sensitisation.

To minimise the risk of sensitisation, we need very low concentration of beryllium and also the selection of operators who aren't sensitive.

3.1 Beryllium concentration in workplace

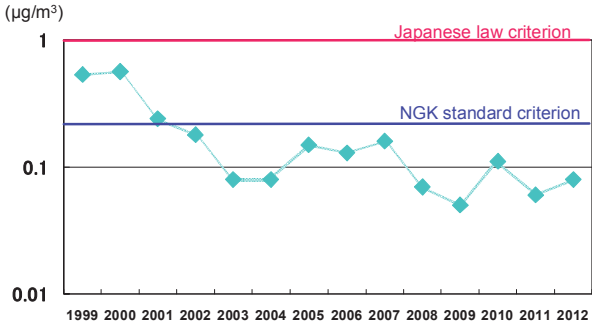


Fig.2 One example of Be concentration evolution in NGK

Fig. 2 shows an example of monitoring data of beryllium concentration of a workplace. The Japanese criterion is 1 µg/m3. NGK is actually largely lower than the criteria. Another internal criterion is, however, set to improve more.

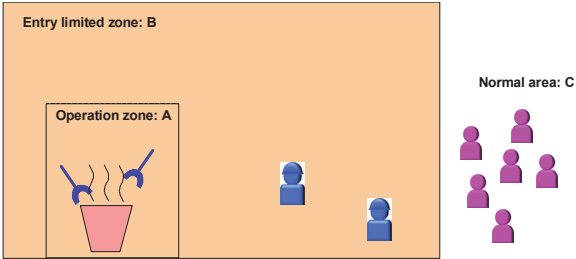


Fig.3 Zone control by machine and exhaust ventilation system

Fig. 3 shows NGK's zone control way schematically. There are three zones, operation zone A, entry limited zone B and normal area C. Firstly, maximum automation of process is necessary to for have minimum access to Zone A where the beryllium dust source exists. Then carefully designed exhaust ventilation system provides us the airflow from zone C, B to A. By this ventilation system, NGK practically has same level of beryllium concentration for Zone B as the normal zone C.



Fig.4 Respiratory protective equipment

Fig. 4 shows the respiratory protective equipment for operators. The operators almost spend their working time in the Zone B. It means that they are already in the safe atmosphere during the operation. However, NGK strictly requires them to put the respiratory protective equipment when they enter the limited zone B. This provides the high level of security. The respiratory protective equipment has a speaking assistance system. The operators are very satisfied with this system because it was difficult to hear what other people are saying without this system in noisy environment. That caused some operators to put out the equipment for easier communication.

3.2 Medical check

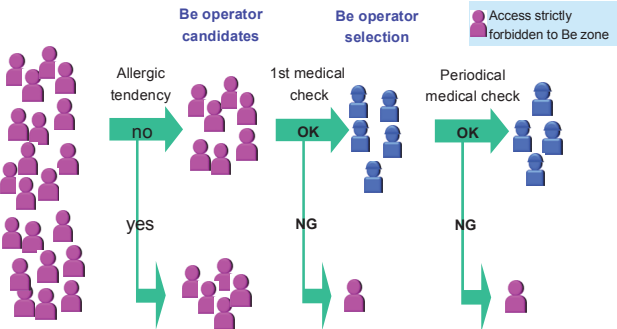


Fig.5 Screening and selection of operators for beryllium process

The medical check is very important to reduce the number of case of sensitisation. Fig.5 shows schematically what NGK is doing. At first, the persons who have a tendency of allergy like eczema or asthma aren't selected as candidate of beryllium operators because the beryllium sensitisation is considered as some kind of allergy. This pre-screening is very useful. When a new beryllium operator is needed, a candidate must take a medical check. This check includes general test like X-ray photo and pulmonary function test. He is also applied BeLTT, Beryllium Lymphocyte Transformation Test, as screening. NGK takes a very severe criterion of BeLTT to detect the sensitisation of beryllium. It should be called "possible-sensitisation". This criterion sometimes judges "positive" for a person who never exposed to beryllium. Selected operators must take periodical medical check including BeLTT.

Operators judged sensitisation must leave from the beryllium operation team immediately. It isn't easy to keep enough number of operators with this system. However, the policy as No CBD is more important.

It's necessary to have a total management of operation exposure risk.

4. CONCLUSION

- Not to have any case of CBD, it's very important;
- to minimise the risk of sensitisation with beryllium airborne concentration management
 - to stop the exposure of beryllium by changing the job when an operator is sensitised

Preliminary results of a X-ray photoemission study on the interaction of energetic nitrogen ions with clean beryllium

M. Köppen, T. Phan & Ch. Linsmeier

*Forschungszentrum Jülich GmbH, Institut für Energie- und Klimaforschung – Plasmaphysik,
52425 Jülich, Germany
m.koeppe@fz-juelich.de*

INTRODUCTION

Beryllium and tungsten are among the proposed armour materials for ITER. Be is going to cover with 690 m² most of the inner wall. (1) During plasma operation temperatures of up to 570 K are expected at the first wall, while in the divertor region temperatures up to 1770 K can occur. (2) In order to control the heat flux to first wall and divertor materials, injection of seeding gases into the plasma has been tested successful in fusion experiments. In experiments at ASDEX Upgrade (3) and JET within the ITER-like wall project (4), nitrogen has proven its beneficial properties as seeding gas. After injection nitrogen ions are produced and can be transported along the magnetic field lines. When they finally leave the plasma they can impinge on the beryllium first wall material. Here, chemical reactions are induced by the elevated temperatures and the kinetic energy of the N-particles. These chemical reactions can severely alter the physical and chemical properties of the first wall surface. For this reason, the investigation of the interaction of nitrogen ions with beryllium is crucial in order to predict properties of the first wall under operational conditions.

In this study the interaction of energetic nitrogen ions with beryllium is investigated by X-ray photoelectron spectroscopy (XPS). The first part of the experiment covers the fluence dependence of the formation of Be-N-species. Therefore, nitrogen ions are implanted in a pristine Be-sample with an acceleration voltage of 3 kV in three fluence steps of $6.0 \times 10^{16} \text{ cm}^{-2} \text{ N}$, $3.0 \times 10^{17} \text{ cm}^{-2} \text{ N}$ and $5.5 \times 10^{17} \text{ cm}^{-2} \text{ N}$. In the second part of the experiment the compound formation of the implanted Be-sample is studied as a function of temperature. The Be-sample is heated in 100-K-steps from room temperature (r.t.) to 870 K for 30 min at each temperature step. After each experimental step survey spectra and high-resolution core level spectra of the Be 1s-, N 1s- and O 1s-levels are recorded.

EXPERIMENTAL PROCEDURE

Experimental Setup

Experiments were carried out in a customised PHI ESCA 5600 XPS-system. Base pressure of the system is 5×10^{-11} hPa. Excitation source of the system is a monochromatic Al K_α-X-ray source. The system is equipped with a hemispherical analyser. The energy axis is calibrated with the Au 4f_{7/2}-peak at 84.0 eV and Cu 2p_{3/2}-peak at 932.7 eV. Linearity of the energy scale is verified with the Ag 3d_{5/2}-signal at 368.3 eV. The reproducibility of the energy scale is ± 0.1 eV.

A *SPECS IQ 12/38* ion source is used for sample cleaning and implantation experiments. The pressure in the ioniser chamber of the source is in the range of 5×10^{-6} hPa, resulting in a N_2 -pressure of 2×10^{-7} hPa in the analysis chamber. The ions are ionised by electron impact with an electron energy of approximately 100 eV. Furthermore the system is equipped with a sample heater for sample temperatures up to 1270 K.

Deconvolution of the spectra is performed with the software package *MultiPak* (5). Background is subtracted by using a Shirley-type background (6). Pseudo-Voigt functions are used for deconvolution of the signals in the core-level spectra.

EXPERIMENTS

Sample cleaning

A polished Be-sample from *MaTecK* with a diameter of 15 mm and a bulk purity of at least 99 % is used. To remove surface contaminations and remaining impurities the sample is cyclically cleaned by sputtering with Ar^+ at 5 kV and annealing at 770 K for 30 min. The survey spectrum of the cleaned sample is shown in

Figure 1. Small remains of implanted argon from the cleaning procedure are visible. The amount of oxygen is negligible since the area of the O 1s signal is very low and no beryllium oxide signal can be identified, even in the high resolution core level spectrum of the Be 1s region (s. spectrum of the clean Be precursor in Figure 3).

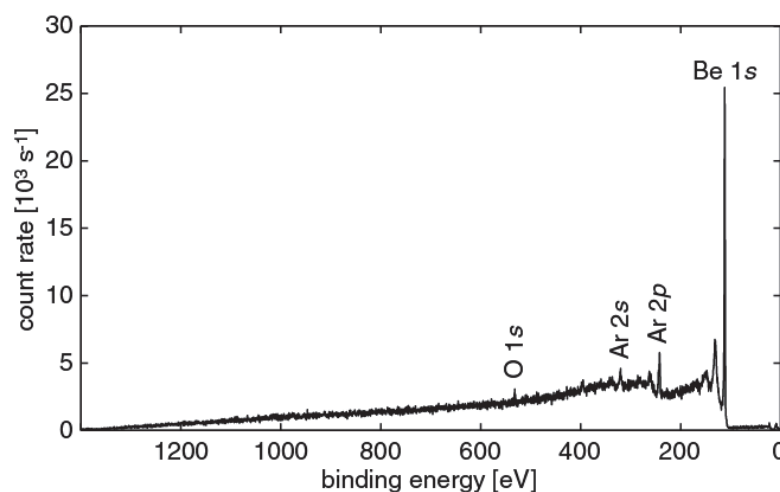


Figure 1: Survey spectrum of the clean Be sample: Small remains of argon from the cleaning procedure are visible. The amount of oxygen is negligible since the area of the O 1s signal is very low and no beryllium oxide signal can be identified, even in the high resolution core level spectrum of the Be 1s-region (s. spectrum of the clean Be sample in Figure 3)

N-Implantation

In the previously cleaned Be-sample nitrogen ions are implanted with an acceleration voltage of 3 kV. It is not possible to determine the exact beam composition in this experiment, but according to NIST electron impact ionisation of nitrogen leads to the two ionic species N^+ and N_2^+ . The resulting ionisation pattern is 12.1 % for N^+ and 87.9 % for N_2^+ . (7) Since the same ionisation method is used in this experiment, these values are considered as a valid

approximation. That the majority of the ion beam consists of the molecular ion N_2^+ seems also viable considering the strong chemical bond in N_2 . Oberkofler & Linsmeier have discovered, that the saturation limit for the N-implantation in Be is at an upper estimate of $1.8 \times 10^{18} \text{ N cm}^{-2}$. (8) Considering this saturation limit, the three fluence steps $6.0 \times 10^{16} \text{ cm}^{-2} \text{ N}$, $3.0 \times 10^{17} \text{ cm}^{-2} \text{ N}$ and $5.5 \times 10^{17} \text{ cm}^{-2} \text{ N}$ are chosen in order to investigate the difference in phase formation as a function of N-fluence.

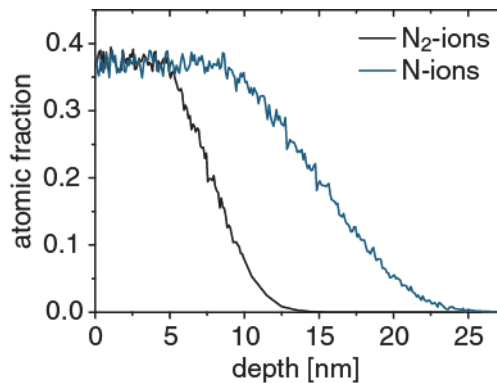


Figure 2: Simulated N-implantation profile: In this graph the simulated depth-profile calculated with SDTrim.SP (9) (10) for N-fluences of $6 \times 10^{16} \text{ N cm}^{-2}$ is shown. The black curve is a simulation for N-ions with an energy of 1.5 keV. This is the resulting depth-profile for the implantation of molecular N_2^+ -ions with an acceleration voltage of 3.0 kV. The blue curve shows the implantation profile of pure atomic N^+ -ions with an energy of 3.0 keV. For these depth profiles the maximum atomic fraction of N is in both simulations artificially constrained to 0.4, which is the N-fraction in Be_3N_2

Implantation profiles for these three fluences are calculated with SDTrim.SP (9) (10). The simulated depth-profiles for a N-fluence of $6 \times 10^{16} \text{ cm}^{-2}$ are shown in Figure 2. The black curve is a simulation for N-ions with an energy of 1.5 keV. This is the resulting depth-profile for the implantation of molecular N_2^+ -ions with an acceleration voltage of 3.0 kV. The blue curve shows the implantation profile of pure atomic N-ions with an energy of 3.0 keV. For this depth profiles the maximum atomic fraction of N is constrained to 0.4 in the simulations, which is the N-fraction in Be_3N_2 . The simulated depth-profiles for the other two used fluences are very similar and therefore not shown.

In Figure 3 the Be 1s- and N 1s-spectra are shown. The black spectrum of the Be 1s-region is recorded directly after the cleaning procedure. Only one peak originating from metallic Be at a binding energy (BE) of 111.9 eV is visible and in agreement with literature (e.g. (11), (12), (13), (14), (15))). No BeO or other Be-containing compounds can be seen in this spectrum. The sample is oxygen free within the analysis region.

After irradiation with a N-fluence of $6.0 \times 10^{16} \text{ cm}^{-2}$ a second peak emerges in the Be 1s-region. This peak can be clearly assigned to a Be-N species. The maximum of this peak is located at a BE of 113.4 eV. The signal of elemental Be becomes smaller, but is still clearly visible. In the spectrum of the N 1s-region one peak is visible at its maximum at a BE of 397.3 eV.

Increasing the N-fluence to $3.0 \times 10^{17} \text{ cm}^{-2}$ leads to a shift of the main signal in the Be 1s-spectrum by -0.3 eV to 113.1 eV. The Be(0)-signal is further reduced and only visible as a small shoulder on the low-BE-side of the main signal. In the N 1s-spectrum the signal is also shifted towards lower binding energies to 396.9 eV. The shift of the signals strongly suggests formation of a different Be-N phase.

After the last N-irradiation step, positions of the main signals in the Be 1s- and N 1s-spectra stay the same. In the Be 1s-spectrum the signal originating from elemental Be cannot be identified without spectral deconvolution anymore.

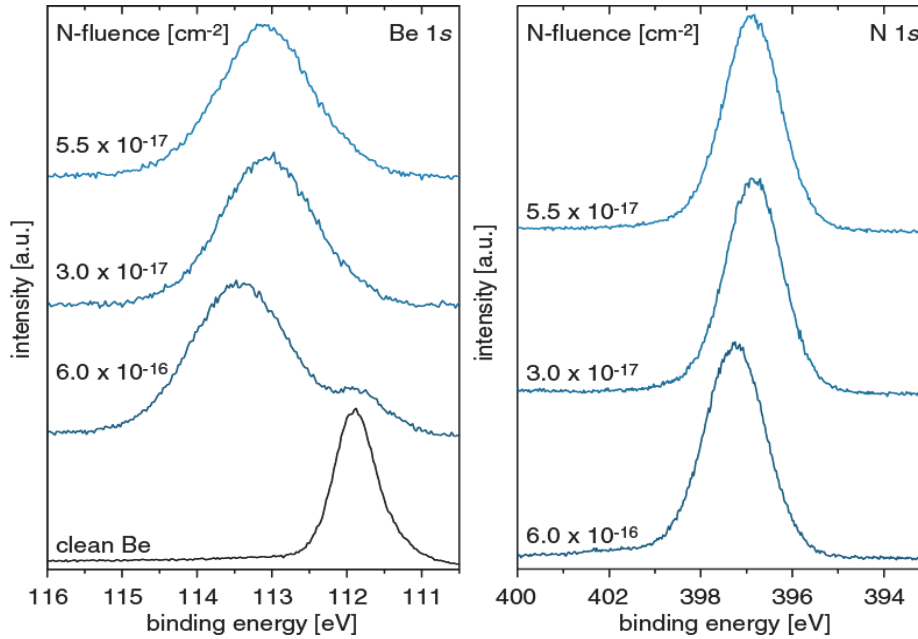


Figure 3: Spectra of the fluence series: In the left panel the Be 1s-spectra are shown and in the right panel the spectra of the N 1s-regions are shown. The numbers on the left denote the applied N-fluence. For better readability all spectra are normalized to one.

Deconvolution of the Be 1s-spectra of the implanted sample reveals three signal contributions after every implantation steps. The peak fitting procedure is shown in Figure 4 and the signal contributions are compiled in Figure 2. In order to reproduce all three Be 1s-spectra with the same set of parameters, three fit functions are necessary: One fit function represents the signal contribution of elemental Be at a BE of 111.9 eV. The second fit function is determined by the spectra at the highest N-fluence to reproduce the main peak. This fit function has its maximum at a BE of 113.1 eV and it is assigned to the second identified Be-N phase (Be-N II). To reproduce the spectrum at the lowest N-fluence of $6 \times 10^{16} \text{ cm}^{-2}$, a third function at a BE of 113.8 eV must be introduced. This signal contribution is assigned to a low fluence phase of Be-N (Be-N I). By peak fitting of the N 1s-region, the BE for N of Be-N I is determined to 396.9 eV, while the N 1s-signal originating from Be-N II is 397.4 eV.

Table 1: Signal contributions of the deconvoluted Be 1s-spectra of the fluence-series

N-Fluence	Be (119.9 eV)	Be-N I (113.8 eV)	Be-N II (113.1 eV)
$6.0 \times 10^{16} \text{ cm}^{-2}$	15.1 %	54.5 %	30.4 %
$3.0 \times 10^{17} \text{ cm}^{-2}$	3.4 %	4.7 %	91.9 %
$5.5 \times 10^{17} \text{ cm}^{-2}$	2.2 %	3.1 %	94.7 %

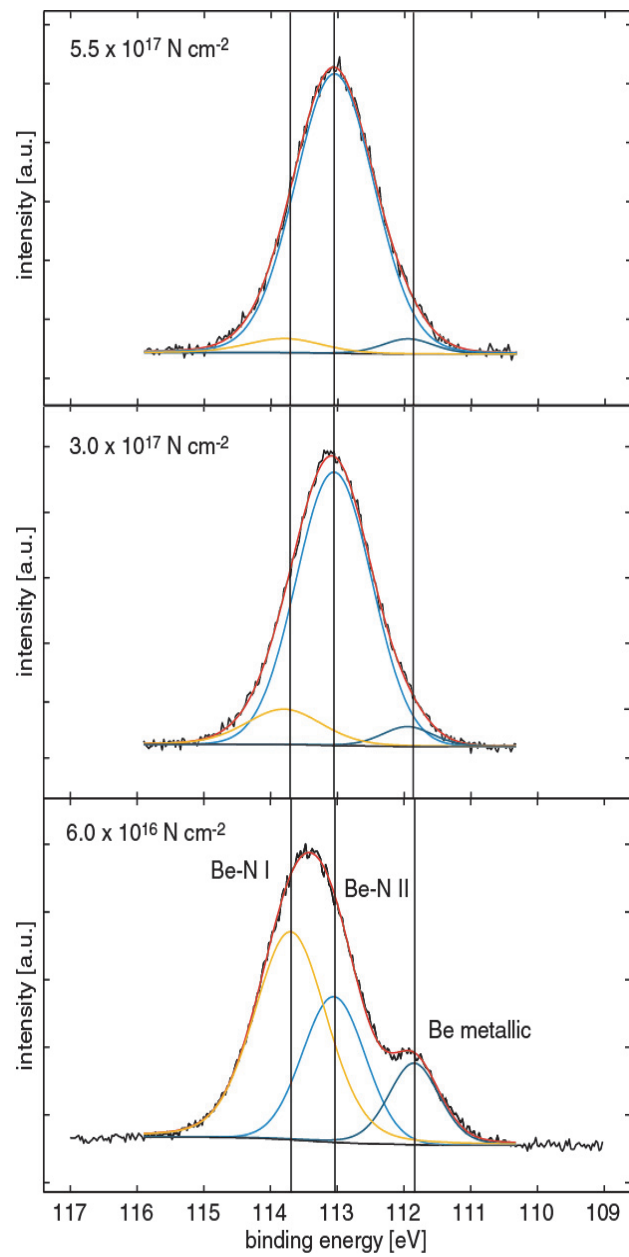


Figure 4: Peak fitting of the Be 1s-spectra of the fluence series: The applied N-fluence is written in the upper left corner of each spectrum. The lines mark the positions of the fitted compounds. The red curve is the resulting envelope of the fitting procedure.

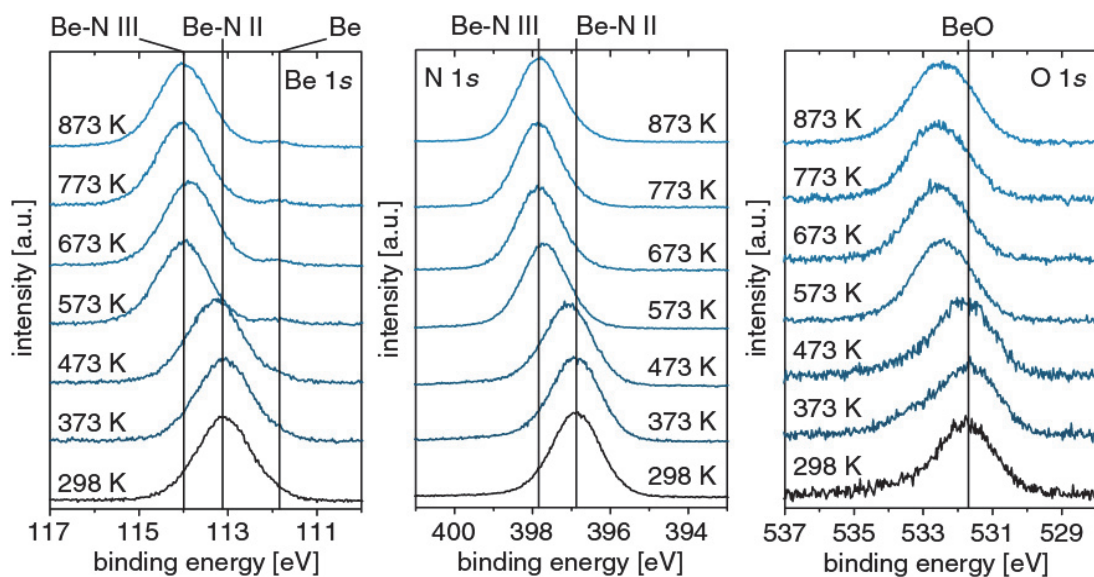


Figure 5: Spectra of the temperature series: The three tables show the core level spectra of the temperature series. The left panel shows the spectra of the Be 1s-region, while the middle & the right panel show the spectra of the N 1s- and the O 1s-core levels. The lowest spectra in each panel show the sample at r.t. directly after the N-implantation. Numbers above the spectra denote the temperature steps. The black lines mark BEs of the compounds identified by peak fitting.

TEMPERATURE SERIES

In the next experimental series, the thermal behaviour of the Be-N II phase is investigated. The sample is heated in 100-K-steps for 30 min from r.t. up to 873 K. After each temperature step, high resolution spectra of the relevant core levels Be 1s, N 1s and O 1s are recorded as well as a survey spectrum. The core level spectra are shown in Figure 5. The O-content in the sample never exceeded 4.6 % under the assumption of a homogenous distribution over the analysis depth. Since oxygen is assumed to be located at the sample surface and therefore has a lower attenuation by the material itself, this value can be considered as upper estimate. At r.t. the signal in the O 1s-spectrum is located at 531.6 eV, Which is attributed to BeO (16).

At a temperature of 373 K no changes are visible in the spectra. At 474 K in the spectra of the Be 1s- and N 1s-region (s. Figure 5) a very small shift towards higher BEs is visible, pointing into the direction of a beginning phase transition. After heating the sample to 573 K in all three regions changes in the peak positions are visible. In the Be 1s-spectrum, we find the main peak located at 114.0 eV. Also the signal of the remaining Be(0) is visible again. In the N 1s-spectra also a shift to a higher BE is visible. The maximum of the signal is now located at 397.9 eV. In the spectrum of the O 1s-region the signal also shifts to a higher BE of 532.5 eV. Increasing the temperature does neither affect the BE nor the peak shapes in all three core levels anymore. This means, that the phase transition is already completed at 573 K and no new reactions take place in this particular system.

The newly found BE in the Be 1s- and N 1s-spectra confirm a new phase in this system. The BE of 114.0 eV in the Be 1s-spectra from 573 K to 873 K corresponds to binding energies reported by Soto et al. for Be₃N₂ (17). The binding energy in the N 1s-spectra is 397.9 eV. Irritating is the fact, that also in the O 1s-region a shift of the signal is visible which points into the direction of a interaction of oxygen with the newly formed Be₃N₂. Since the amount of oxygen is very low, a possible explanation for this behaviour might be that oxygen replaces some N-atoms in the Be₃N₂-structure.

SUMMARY

In the first series of experiments, a Be sample is irradiated with three different fluences of N-ions. In the spectra two different phases can be seen. The intermediary low fluence phase Be-N I is identified at a BE of 113.8 eV in the Be 1s-region. The corresponding N 1s-signal is located at 396.9 eV. The second phase Be-N II is identified at a BE of 113.1 eV in the Be 1s-regions and 397.4 eV in the N 1s-region. For low fluences (here: $6 \times 10^{16} \text{ N cm}^{-2}$) the spectrum is dominated by the signal originating from Be-N I, while for higher fluences (here: $3 \times 10^{17} \text{ cm}^{-2}$ and above) the signal almost exclusively originates from Be-N II.

In the annealing experiment it is shown, that the Be-N II phase is stable to temperatures of 373 K. The small shift in the spectra observed at 473 K points into the direction of a beginning phase formation. At 573 K the phase formation is completed. Comparison of the BE of 114.0 eV in the Be 1s-region with literature (17) suggests formation of stoichiometric Be_3N_2 . The observed shift in the O 1s-spectra points into the direction of participation of O in the new phase. Further experiments have to be carried out, to determine the role of O in this reaction. The formed Be_3N_2 is stable in the investigated temperature range.

In conclusion the reported experiments show the complex behaviour of clean Be under N-irradiation. The reported results will serve as starting point for further investigations of the system Be-N. To understand the mechanisms and reactions in this system to full extend further dedicated experiments are necessary.

ACKNOWLEDGEMENTS

The work of Tony Phan on this subject is highly appreciated (18). All experiments have been carried out at the Max-Planck-Institut für Plasmaphysik in Garching near Munich.

BIBLIOGRAPHY

1. **Pitts, R.A., et al., et al.** *J. Nucl. Mater.* 2011, Vol. 415, pp. S957 - S967.
2. **Bolt, H., et al., et al.** *J. Nucl. Mater.* 2002, Vols. 307 - 311, pp. 307 - 311.
3. **Schweitzer, J., et al., et al.** *Nucl. Fusion.* 2011, Vol. 51, p. 113003.
4. **Giroud, C., et al., et al.** *Nucl. Fusion.* 2013, Vol. 53, p. 113025.
5. **Physical Electronics.** *MultiPak 6.1A.* 1999.
6. **Shirley, D.A.** *Phys. Rev. B.* 1972, Vol. 5, pp. 4709 - 4714.
7. **NIST Mass Spec Data Center, S.E. Stein (director).** Mass Spectra. [ed.] P. J. Linstrom and W. G. Mallard. *NIST Chemistry Webbook, NIST Standard Reference Database Number*
69. Gaithersburg MD : National Institute of Standards and Technology.
8. **Oberkofler, M. and Linsmeier, Ch.** *Nucl. Fusion.* 2010, Vol. 50, 12.
9. **Eckstein, W., et al., et al.** *SDTrimSP: A Monte-Carlo Code for Calculating Collision Phenomena in Randomized Targets.* Garching bei München : Max-Planck-Institut für Plasmaphysik, 2007. Vols. IPP-Report 12/3.
10. **Eckstein, W.** *Computer Simulation of Ion-Solid Interactions.* Berlin : Springer, 1991.
11. **Köppen, M., et al., et al.** *Phys. Scr.* 2011, Vol. T145, p. 014015.
12. **Wiltner, A., et al., et al.** *Phys. Scr.* 2007, Vol. T128, pp. 133 - 136.
13. **Goldstraß, P., Klages, K.U. and Linsmeier, Ch.** *J. Nucl. Mater.* 2001, Vols. 290 - 293, 76 - 79.

14. **Powell, C.J.** *Appl. Surf. Sci.* 1995, Vol. 89, pp. 141 - 149.
15. **Moulder, et al., et al.** *Handbook of X-Ray Photoelectron Spectroscopy*. [ed.] Jill Chastain. s.l.: Perkin-Elmer Corporation, 1992.
16. **Nefedov, V.I., Firsov, M.N. and Shaplygin, I.S.** *J. Electron Spectrosc. Relat. Phenom.* 1982, Vol. 26, pp. 65 - 78.
17. **Soto, G., et al., et al.** *Mater. Lett.* 2002, Vol. 52, 1 - 2, pp. 29 - 33.
18. **Phan, T.** *Compound formation at the beryllium surface during nitrogen ion implantation*. Paris : Ecole Nationale Supérieure de Chimie de Paris, 2010.

Packing Experiments of Beryllium Pebble Beds for the Fusion Reactor HCPB Blanket

Joerg Reimann^{a*}, Ali Abou-Sena^a, Emmanuel Brun^{b,c}, Benjamin Fretz^d,

^a Karlsruhe Institute of Technology, P.O. Box 3640, 76021 Karlsruhe, Germany

*joerg.reimann@partner.kit.edu

^b European Synchrotron Radiation Facility, B.P. 220, F-38043 Grenoble Cedex, France

^c Ludwig Maximilians University, Faculty of Physics, 85748 Garching, Germany

^d KBHF GmbH, Herrmann-von-Helmholtz-Platz 1, 76344 Eggenstein-Leopoldshafen, Germany

ABSTRACT

Packing factors results are presented for different grades of spherical and non-spherical beryllium pebbles in cavities dominated by flat walls and small bed heights in combination with blanket relevant filling conditions.

For cavities with a movable piston on the top the packing factors increase slightly with decreasing bed heights because the development of structured packings close to the flat walls is favored.

The experiments with fixed prismatic cavities show that for small heights the values are smaller than for the cavity with a movable wall; however, it is expected that for blanket relevant bed heights, the reference packing factor values will be also achieved.

The packing factor does not remarkably change for the different beryllium grades although pebble shapes, and surface roughnesses differ significantly.

First results from recent tomography investigations are presented using spherical beryllium pebbles in a cavity with concave and convex cylindrical walls. Regular packing structures close to walls are observed.

KEYWORDS

granular material, pebble bed, packing factor fusion reactor blanket, tomography.

1. INTRODUCTION

In the European Helium-cooled Pebble Bed (HCPB) breeder blanket [Her03], both the ceramic breeder material and the beryllium are used in form of pebbles. For beryllium, rather spherical pebbles with a diameter of about 1mm, produced by the company NKG by the rotating electrode process (REP) are considered as candidate material, designated in the following as Be-1. Non-spherical particles could be produced in a much cheaper way; the first step to characterize such granular materials is the performance of packing experiments. Therefore, packing experiments with four different grades of non-spherical pebbles and Be-1 were carried out.

For filling HCPB blankets, the pebbles will be poured through small pipes in interconnected cavities in a way that high packing factors γ (ratio of pebbles volume to total cavity volume) will be achieved. The packing factor is an important design parameter, however, is not sufficient for the understanding of heat transfer mechanisms. For this, a detailed view into the pebble bed is very helpful, obtained by computer-aided microtomography (CMT) as outlined below.

In the HCPB blanket, pebble beds are contained in quasi-square cavities where one dimension, the pebble bed height H is much smaller than the other two dimensions, thus resulting in shallow pebble beds. Experiments with 1mm glass spheres in blanket relevant cavities combined with a relevant filling procedure resulted in maximum values of $\gamma = 63.5\%$ [Abo09].

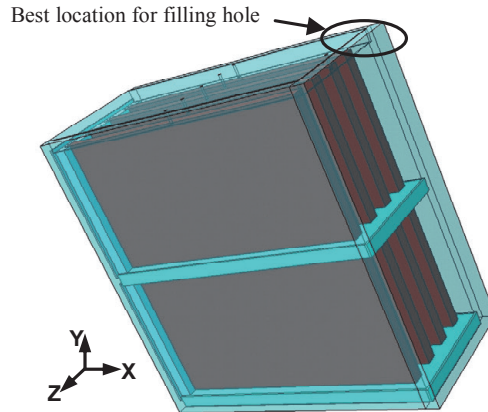


Fig.1. Packing experiments with Breeder Unit Mock-up [Abo09].

Most of the previous packing experiments concentrated on spherical pebbles in cylindrical cavities (axis length $L \gg$ cavity diameter D) with a piston at the top, which could move during the densification of the pebble bed by vibration and/or hammering. Both mono-sized (one nominal sphere diameter d) and multi-sized systems (different diameters) were investigated. For mono-sized systems, γ values between 62 and 64% were obtained for large cavities whereas for multi-sized systems γ can be much larger, depending on the pebble diameter ratios and volume fractions and the filling technique, see e.g. [McG63].

In the present experiments, using different beryllium pebble grades, the cavities had to be much smaller compared to the HCPB ones because only small amounts of non-spherical beryllium grades were available. However, the container geometries were chosen in such a way that conclusions for HCPB relevant cavities could be drawn. In order to broaden the database, experiments with spherical glass and steel particles were also performed, for details see [Rei12,13].

It is well known, that within the pebble bed, structured pebble packing occurs close to walls, whereas in the bulk, the pebbles are fairly homogeneously distributed. This results in characteristic void fraction (ratio of empty volume to total volume) fluctuations close to the wall determined most accurately in the last years by 3d CMT investigations [Rei06, 08, Pie11]. This technique can reveal even more details, such as contact numbers and contact angle distributions.

Figure 2 presents recent CMT results from the European Synchrotron Radiation Facility (ESRF) in Grenoble, France, using 2.3 mm aluminum spheres in a 49 mm diameter cavity [Rei12, 13]. The upper part of Fig. 2 shows axial and radial void distributions evaluated with the total cavity volume, all wall distances were normalized with the sphere diameter. The axial distribution is characteristic for a plain wall, $D/d = \infty$, whereas the fluctuations close to the curved wall are more regular than those for the plain wall and die down faster because regular structures can develop to a smaller degree at curved walls.

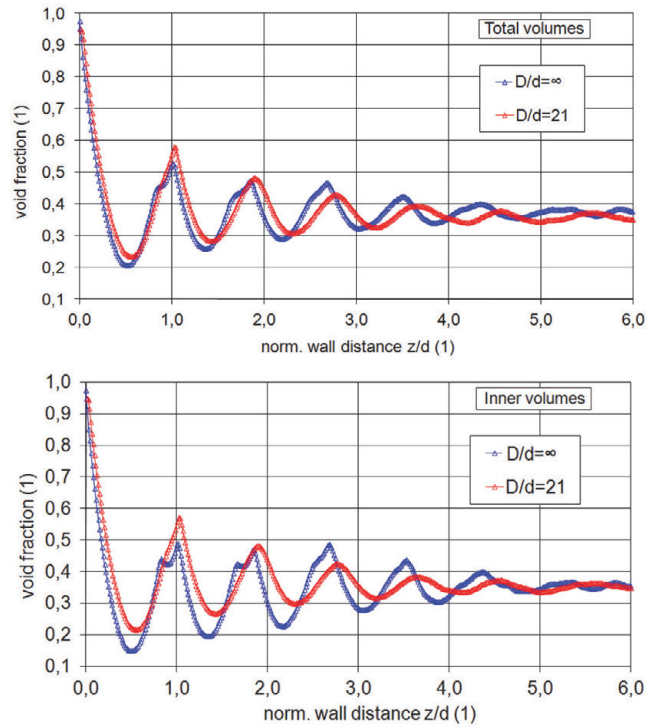


Fig. 2. Void fraction profiles for $D/d=21$ and $D/d = \infty$ determined with total (above) and inner (below) cavity volumes.

The influence of wall curvature, however, is evaluated more sensitively if for the radial distribution the axial wall zones close to the top and bottom plates are excluded, and if for the axial distribution the cylindrical wall zone is not included, compare Fig. 3. The lower part of Fig. 2 shows that the differences are small for the radial distributions, however, the void fraction values for $D/d = \infty$ are distinctively smaller in the wall zone using the inner volume because close to flat walls structured packings are the most expressed.

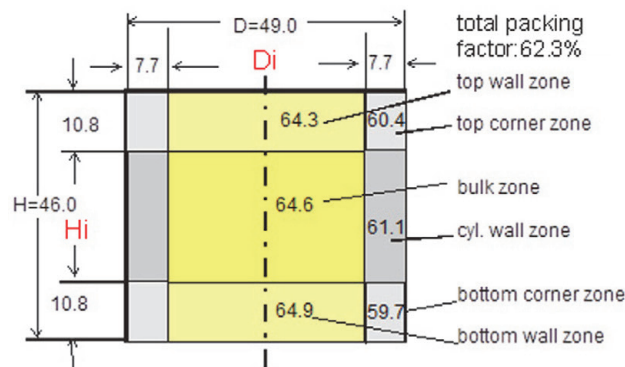


Fig. 3. Packing factors for characteristic cavity zones.

These detailed tomographic analyses depict that close to flat walls regular structures occur within a normalized distance z/d of about 4 (corresponding to about 5 pebble layers). With decreasing D/d , this thickness decreases and the void fraction increases.

The integration of axial and radial void fraction distributions for the different volumes allows also the determination of void fractions, respectively, packing factors, in characteristic zones, see Fig. 3. The packing factor for the total cavity was 62.3%. The packing factors of the bulk, inner bottom and top zones, however, are larger than 64%, whereas γ in the inner cylindrical zone is $\approx 61\%$, and in the corner regions $\gamma \approx 60\%$.

The important conclusion from the present result is that the packing factor in cylindrical wall zones decreases with decreasing D/d . For flat walls, the value is about the same or even higher as in the bulk. For shallow pebble beds in prismatic cavities a bulk zone no longer exists for $H/d < 10$. Depending on the possibility to develop regular packings during the filling process quite high packing factors are expected occur also in shallow cavities, see next Section.

The tomography results shown above were obtained with smooth aluminum spheres with a negligible diameter variation and cannot be extrapolated quantitatively e.g. to pebble beds consisting of particles varying in size and shape or surface condition.

2. FIRST CMT RESULTS FROM NEW BERYLLIUM EXPERIMENTS

Very recently, extensive CMT investigations have been performed in the ESRF in order to investigate in detail the influence of D/d on void fraction distributions, respectively local packing factors, both for concave and convex walls. The latter was realized by the use of centric cylinders (diameter D_i) within the cylindrical cavity (diameter D_o). Both ratios, D_i/d and D_o/d , were varied in a wide range by using different cavity, inner cylinder and aluminum sphere dimensions. A single experiment was performed with NGK beryllium pebbles with a nominal diameter of 1mm in a cavity with $D_o = 49\text{mm}$ and $D_i = 10\text{mm}$. At present, only first cuts through the cavity have been evaluated.

Figure 4 shows a horizontal cut at a distance $z = 0.5\text{mm}$ above the bottom plate, that is, a cut through the pebble centers of the first bottom layer. Many details are detectable: e.g. voids at the pebble centers, resulting from the solidification process, diameter variations, and deviations from sphericity for some pebbles. At the concave and convex walls, an ordered structure in form of pebble rows is partly observed; in between there are small isles with a hexagonal packing structure. Figure 5 show a horizontal cut at a larger distance from the bottom plate and a vertical cut: close to walls, regular structures are clearly visible whereas in the pebble bed bulk this is not the case.

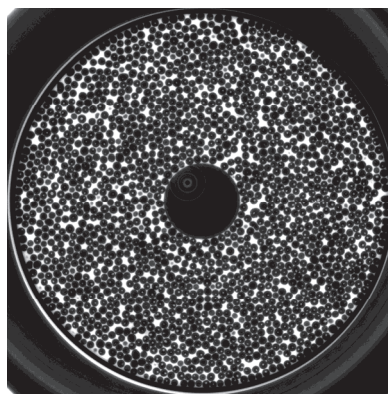


Fig. 4. CMT cut through beryllium pebble bed at $z/d=0.5$; $d=1\text{mm}$, $D_o=49\text{mm}$, $D_i=10\text{mm}$.

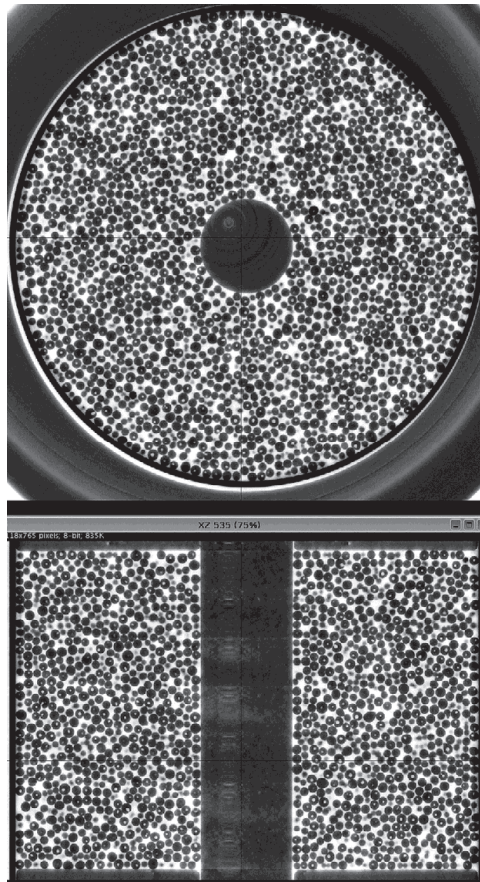


Fig. 5. CMT images; upper part: horizontal cut at $z/d = 15$; lower part: vertical cut.

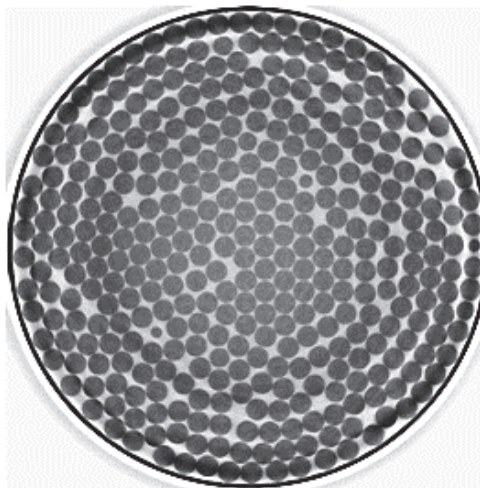


Fig. 6. CMT image through aluminum pebble bed at $z/d=0.5$; $d=2.3\text{mm}$, $D_o=49\text{mm}$.

Figure 6 shows a cut through the center of the bottom layer for mono-sized aluminum spheres: compared to Fig. 4, the row structure close to the cylindrical wall is more developed, as well as the hexagonal structure outside of this wall zone. The degree of packing regularity, therefore, is expected to become smaller with increasing diameter variation and non-sphericity. Future evaluations of the void fraction distributions will be able to quantify this tendency.

3. INVESTIGATIONS ON PACKING STRUCTURE AND PACKING FACTORS

3.1 Experimental

Pebble characteristics: The experiments were performed in the Karlsruhe Beryllium Handling Facility, KBHF, for details see [Kur09]. Five different beryllium batches were investigated, see Fig. 7.

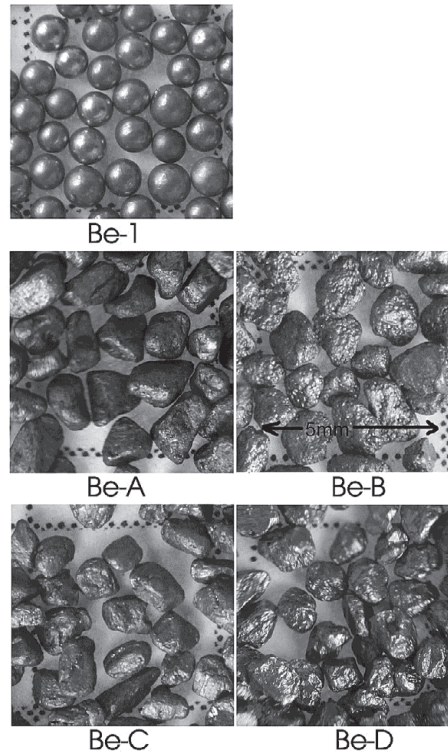


Fig. 7. Pebble photographs

Be-1 consists, as mentioned before, of the rather spherical pebbles with diameters of 1 ± 0.15 mm, see also Figs. 4 and 5. The other grades were manufactured by crushing sintered beryllium blocks and subsequent grinding. As a result, non-spherical scrap-type pebbles were obtained with values of the largest pebble dimension up to 2.5 mm. As a characteristic diameter, a value of 1.5 mm is assumed. The batches Be-A, B, and C were produced by Bochvar Institute, Russia, and differed in grain size. The batch Be-D originates from Materion, USA.

Cavity characteristics: The limited amounts of non-spherical beryllium grades dictated the dimensions of the Plexiglas containers: the cylindrical container with $D = 50$ mm, $H_{\max} = 65$ mm and the square one with a volume of $100 \times 100 \times 10$ mm. For Be-1 and Be-D, a square container with $100 \times 100 \times 20$ mm could also be used. The cylindrical container was operated either by using a moveable piston at the top of the pebble bed (Type A cavity), or by fixing its dimensions (Type B cavity), see Fig. 8. With the arrangement of Type A, conventionally used in previous investigations, experiments with different bed heights H were performed. The Type B cavities are more representative for technical applications; both the cylindrical and square cavities were filled and vibrated in tilted positions through a 4mm opening at the top corner.

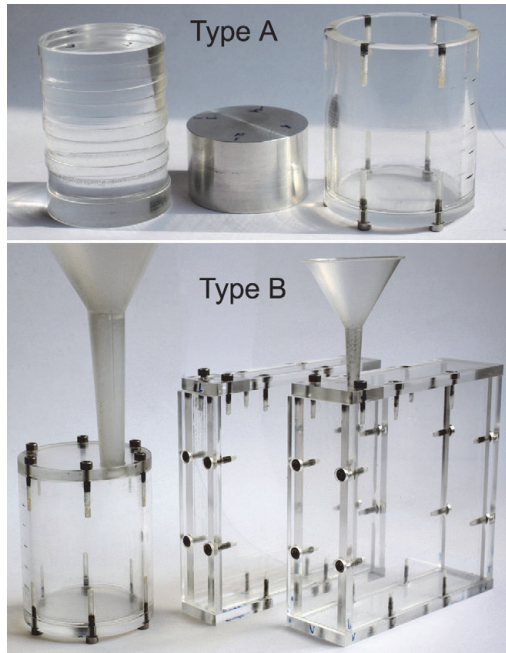


Fig. 8. Pebble bed containers.

Figure 9 displays results of the repose angle of some batches, measured after pouring the granular materials in the square cavity (100x 100x20mm). The repose angle is a measure of the pebble friction and is expected to influence the pebble bed packing. The repose angle β generally increases with increasing surface roughness, irregular shape, and particle size. The smooth spherical glass spheres show values between 23.5-26°, a value of $\beta \approx 28^\circ$ for the rather spherical 1 mm Be pebbles was found and the strongly irregular pebble shapes of Be-A, B, and C resulted in values of about 40°.

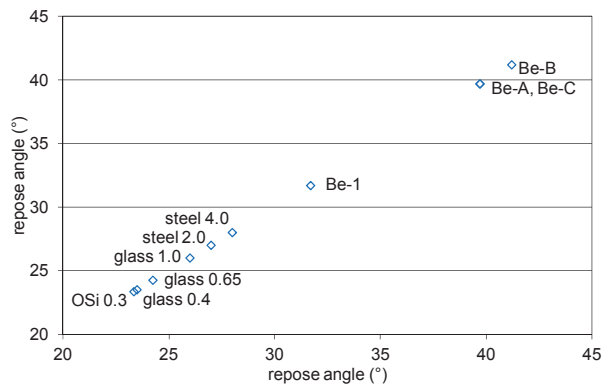


Fig. 9. Repose angles of the different granular materials.

Filling and densification procedure: In order to obtain dense packings, energy must be introduced into the system by knocking the container walls or vibrating the containers to such an extent that pebbles can overcome frictional forces with neighboring pebbles in order to find positions with the smallest potential energy. For vibration, a vibration table (Renfert Vibrax Vibrator M-13295) was operated at (230 V / 50 Hz) with different amplitudes.

Filling efficiently containers with a movable top plate (Type A cavity) is relatively simple because the densification parameters are varied in such a way that the lowest position of the top plate is achieved.

Filling efficiently Type B cavities is more difficult, especially if the packing cannot be visually controlled. Details of the filling/densification procedures (initial complete filling versus stepwise filling with subsequent densification, the role of granular convection flows, etc) are described in [Rei12b]. In the present experiments, stepwise filling and a combination of vibration and knocking were generally applied. The values obtained are probably at the upper limit of values achievable in large blanket components.

It should be noted that it is not possible to recommend unique densification parameters for large pebble bed containers. Even for a given container, the parameters depend on the filling level, and relevant pretests are required.

3.2 Results on pebble bed packing characteristics

Figures 10 and 11 show the packing structures for Be-1 pebbles and 2mm steel spheres.

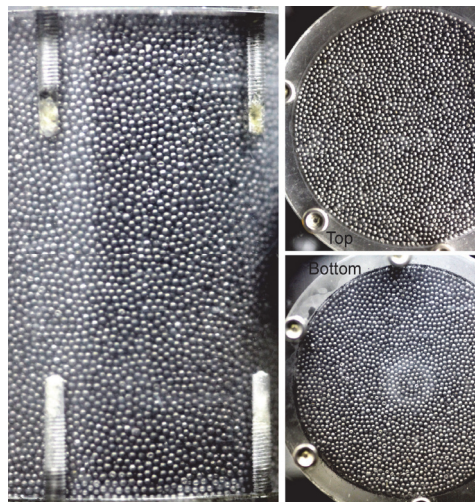


Fig. 10. Type B cavity, $H = 65\text{mm}$, Be-1, $\gamma = 61.85\%$.

Regular structures are much less developed for Be-1 compared to the pebble bed consisting of mono-sized spheres, as already observed in Figs. 4-6.

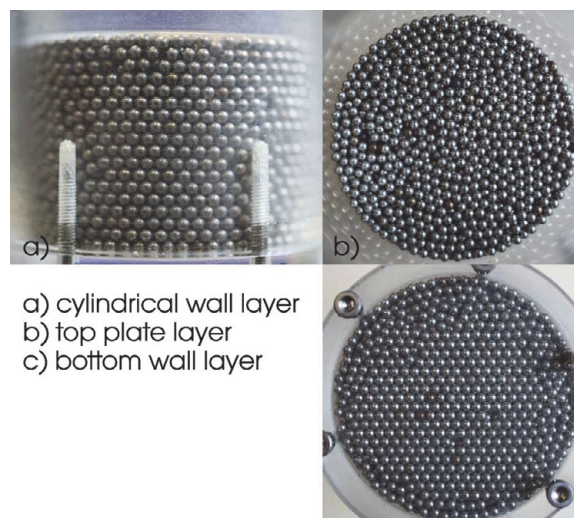


Fig. 11. Type A cavity, $H = 32.5\text{mm}$, 2mm steel spheres, $\gamma = 63.85\%$.

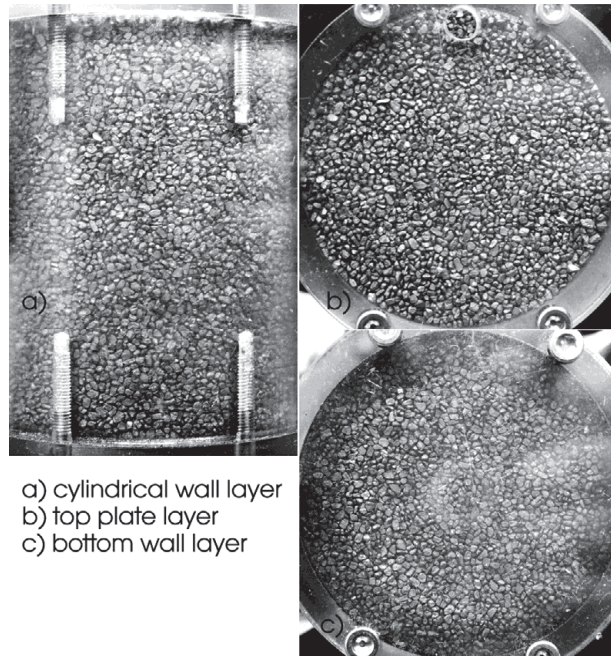


Fig. 12. Type A cavity, $H = 65\text{mm}$, Be-C, $\gamma = 62.17\%$.

Figure 12 shows the non-spherical Be-C particles in the Type B cavity. Hexagonal structures are not observed, however, a structured packing exists because the particles tend to align their largest side along the wall. Tomography experiments could answer the question to which extent this tendency also exists in the next inward layers. It should be noted that the largest particle size preferentially being in contact with the wall is expected to be beneficial for heat transfer.

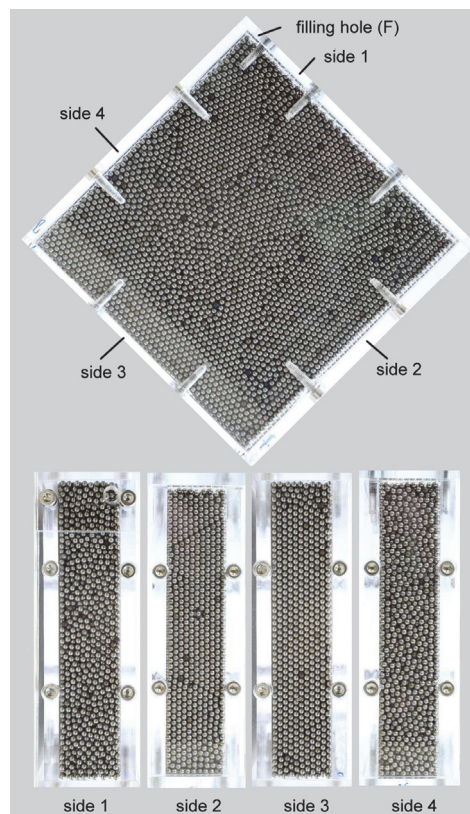


Fig. 13. Square cavity, $H = 20\text{mm}$, 2mm steel spheres, $\gamma = 64.19\%$.

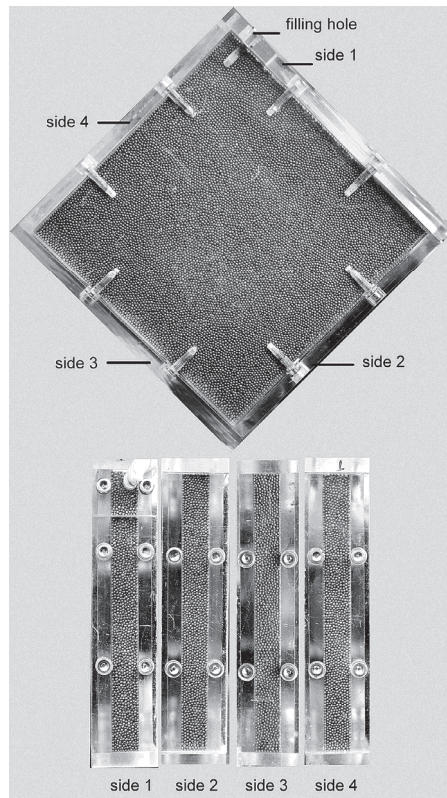


Fig. 14. Square cavity, $H = 10\text{mm}$, Be-1, $\gamma = 62.19\%$.

Figures 13-15 contain corresponding results for the square cavities. Again, large zones with regular packing are observed for mono-sized spheres and non-spherical pebbles tend to align the largest side along the wall.

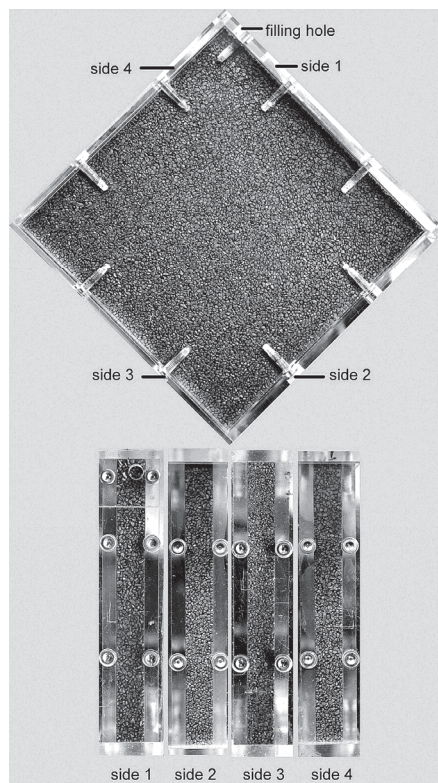


Fig. 15. Square cavity, $H = 10\text{mm}$, Be-A, $\gamma = 62.0\%$.

3.3 Results on packing factors

The packing factor γ , defined as the ratio of volume occupied by the pebbles, V_{pebbles} , to volume of the cavity, V_{cavity} , is given by

$$\gamma(1) = V_{\text{pebbles}}/V_{\text{cavity}} = m_{\text{pebble bed}}/((1-P)\rho V_{\text{cavity}}),$$

where $m_{\text{pebble bed}}$ is the total mass of pebbles, ρ is the density of the pebble material, and P is the porosity of the pebbles. For beryllium, $\rho = 1.85\text{g/cm}^3$; $P = 0.003$ was measured previously for the NGK pebbles (Be-1). This value was also assumed for the other batches.

Fig. 16 shows packing factor versus pebble bed height results for spherical pebbles of different materials in a cylindrical cavity. As mentioned before, all experiments were performed with a piston on top of the pebble bed (Type A cavity) except for $H = 65\text{mm}$, where the top plate was fixed (Type B cavity). For pebble diameters $d \leq 1\text{mm}$, the ratio D/d is ≥ 50 . For small bed heights which are of special interest, the cavities are dominated by the flat top and bottom plate and with this, the data are representative for shallow pebble beds and the relevant parameter is the ratio H/d (and not D/d).

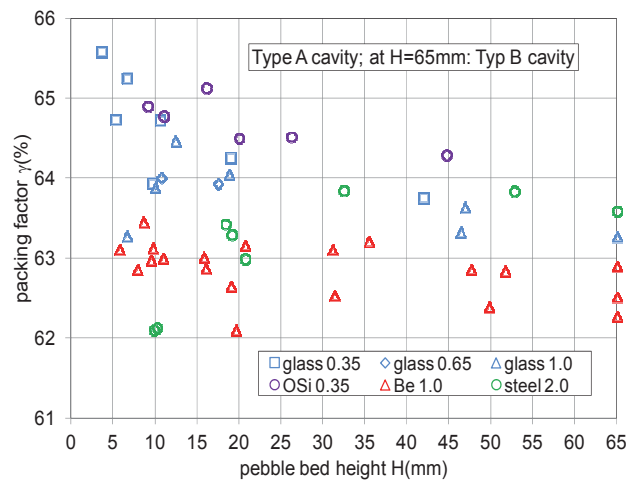


Fig. 16. Packing factors for spherical pebbles in cylindrical cavities.

For pebble diameters $d \leq 1\text{mm}$, there is a weak tendency that γ increases with decreasing H . This tendency differs characteristically from that found in long cylinders where D/d is the characteristic parameter and where it is observed that below $D/d \approx 20$, γ decreases with decreasing D/d .

For cavities dominated by plane walls, the packing factor of the structured packing in the wall zone can be larger than that in the bulk zone, compare Fig. 3. The movable top plate favors also the development of a structured packing at the top wall.

Packing factors of the OSi pebble bed and the 0.35mm glass sphere bed are about the same. Both pebble batches have a similar diameter spread and small repose angles, see Figs. 9. For Be-1, γ is about 63%. This value is about 1% smaller than for the comparable 1mm glass pebble bed. The difference is attributed to the rougher surface of the Be pebbles, the smaller sphericity and larger diameter variation.

The maximum height $H = 65\text{mm}$ belongs to the Type B cavity. The packing factors are similar to those for large bed heights with the piston on the top.

Fig. 17 shows results for the different beryllium grades in the cylindrical cavity. The mean packing factors for all materials, except Be-B, are very similar although repose angles differ considerably between Be-1 and the other grades. One reason might be the formation of dense wall layers by the irregularly shaped pebbles owing to the fact that these particles tend to align their largest side along the wall, see Fig. 12. As mentioned before, densification with the movable piston might favor this formation. The low values for Be-B can be caused by a considerably rougher surface than the other grades, confirmed by the largest repose angle, see Fig. 9. This large roughness was probably caused by a non-perfect sintering process [Kur12] which also could result in pebble porosities significantly larger than the assumed value.

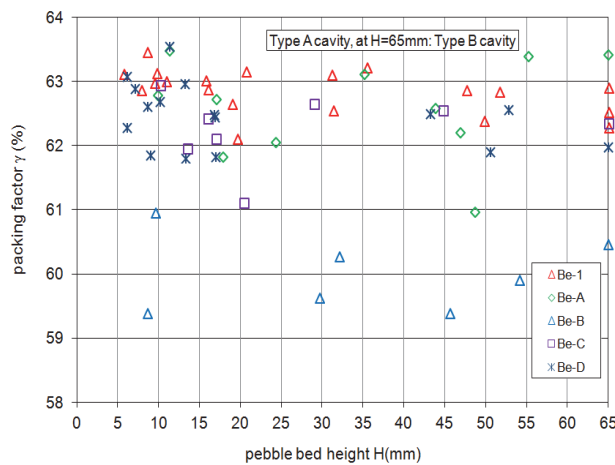


Fig. 17. Packing factors for different granular beryllium materials in cylindrical cavities.

Fixed cavity walls partly render it more difficult to generate dense packings close to walls, especially for shallow pebble beds, thereby lower total packing factors are expected in the prismatic Type B cavities. This is generally observed for the $H = 10\text{mm}$ cavity but to a much smaller extent for the 20mm cavity, see Fig.18.

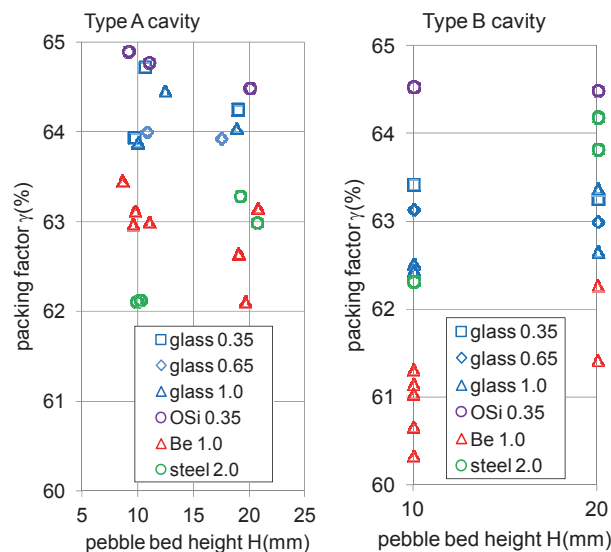


Fig.18. Packing factors for spherical pebbles in Type A and Type B cavities.

Fig.19 shows the results for the beryllium grades. Again, the values for $H = 10\text{mm}$ are smaller than the corresponding values for the cavity with the movable wall, Fig. 17.

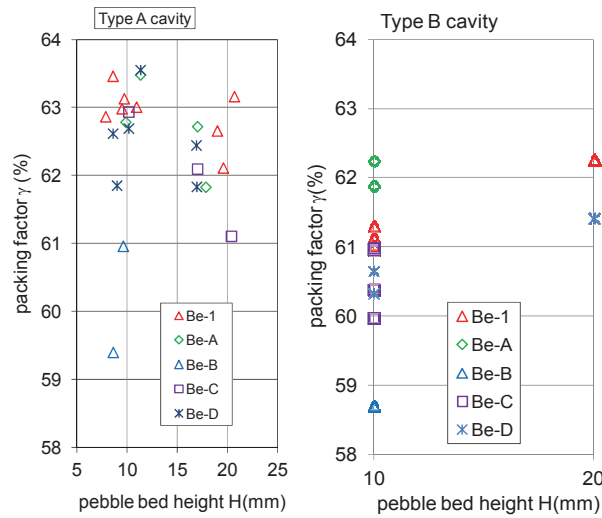


Fig. 19. Packing factors for different beryllium grades in Type A and Type B cavities.

In the present HCPB blanket designs, square cavities with beryllium pebble beds heights in the range of 30mm are foreseen and it is expected that values close to the reference value $\gamma = 63.5\%$ will be achieved.

CONCLUSIONS

Packing factors results were presented for different grades of beryllium pebbles in cavities dominated by flat walls and small pebble bed heights in combination with blanket relevant filling procedures.

Previous packing experiments focused on cylindrical cavities and a decrease of the packing factor with decreasing ratio of cavity cylinder diameter to pebble diameter was observed. In cavities with flat walls and small widths (bed heights H), the ratio H/d is the relevant parameter.

Recently performed tomography investigations proved quantitatively that for flat walls packing factors in the wall zone are as high as in the bulk zone, in contrast to the smaller values obtained near cylindrical walls and corner zones.

The present packing experiments with a movable piston on the top of the cavities show that the packing factor increases slightly with decreasing bed height. This is attributed to the fact that for this experimental condition, the development of structured packings close to the flat walls is favored.

For fixed square cavities the packing factors are smaller for small pebble bed heights than for the cavity with a moveable wall; however, it is expected that for larger blanket bed heights, the reference packing factor value will be also achieved.

Comparing the packing factors for the rather spherical beryllium pebbles with those for the non-spherical pebbles, it is surprising how small the differences are regarding the different pebble shapes and friction angles. Tomography experiments with non-spherical pebbles

would increase considerably the understanding of the packing structure and would enable the determination of packing factors in different characteristic zones.

Further experiments with the non-spherical materials are required in order to judge if these materials could become attractive for fusion reactor blankets; next steps should be uniaxial compression tests and thermal conductivity measurements, followed by irradiation experiments.

REFERENCES

- [Abo09] A. Abou-Sena et al., *Fus. Eng. Des.* 84 (2009) 355-358.
- [Ben 62] R. F. Benenati and C. B. Brosilow, *A.I. Ch. E. Journal*, Vol. 8, No. 3, (1962) 359-361.
- [Her03] S. Hermsmeyer et al, *Proc. 20th SOFE*, San Diego, USA, Oct. 14-17, (2003) 440-445.
- [Kur09] P. Kurinskiy et al., *Fus. Eng. Des.* 84 (2009) 1136-1139
- [McG63] R. K. McGeary, *J. Am. Ceram. Soc.* Vol. 44, No 10 (1963) 514-522.
- [Pie11] R. A. Pieritz et al., *Adv. Eng. Mat.*, 13, No.3, (2011) 145-155.
- [Rei06] J. Reimann et al., *Fus. Eng. Des.* 81(2006) 653-658.
- [Rei08] J. Reimann et al., *Fus. Eng. Des.*, 83,(7-9) (2008) 1326-1330.
- [Rei12] J. Reimann et al., *KIT-SR*, 2012.
- [Rei13] J. Reimann et al., *Fus. Eng. Des.*, in press.
- [Rid68] K. Ridgway et al., *Chem. Eng. Science*, Vol. 23 (1968) 1147-1155.

Some Thoughts about Beryllium Resources, Impurities in It and Necessity of Its Detritiation after Irradiation

B.N. Kolbasov*, V.I. Khripunov, A.Yu. Biryukov

NRC “Kurchatov Institute”, Moscow, Russia

**Corresponding author.*

E-mail address: kolbasov@nfi.kiae.ru (B.N. Kolbasov).

ABSTRACT

World identified resources of beryllium somewhat exceed 80 000 t. Beryllium production all over the world in 2012 was about 230 t. At the same time, some conceptual designs of fusion power reactors envisage application of several hundreds tons of this metal. Therefore return of beryllium into production cycle (recycling) will be necessary. Some preliminary developments of radiochemical technology for beryllium recycling were carried out in Russia. They were stopped due to suspension of financing. Beryllium ore from some major deposits has uranium content inadmissible for a fusion reactor. This raises the question on the necessity to develop and apply an economically acceptable technology for beryllium purification from uranium. Practically any technological procedure involving beryllium requires its detritiation. A study of tritium and helium release from irradiated beryllium at different temperatures and temperature increase rates was performed in Kurchatov Institute.

KEYWORDS:

beryllium, beryllium resources, impurities in beryllium, beryllium management, beryllium detritiation.

1. INTRODUCTION

1.1 Beryllium resources

Beryllium is considered as a material that holds promise for application in fusion power engineering, but there are some problems in this respect. First of all its resources are very restricted. According to the U.S. Geological Survey's 2013 report [1], the world natural resources of Be exceed 80 kt, of which about 65% are in the USA.

At the same time, the N.M. Fedorovskij All-Russian Mineral Research and Development Institute states that total reserves of Be ores in the Russian Federation amount to 49.8% of world resources. Beryllium is found in 27 deposits located in four federal districts: Siberian (46.5%), Ural (22.4%), Far-Eastern (17.1) and North-Western (13.9%) [2].

Beryllium production in all the world countries in 2012 was about 230 t. The main extractive countries in 2012 were the USA (88%), China (9%) and Mozambique (1%) [1]. At present, only three countries, USA, Kazakhstan and China, process beryllium containing ores and concentrates into Be metal and produce Be products on an industrial scale [3].

It would be interesting to compare annual global Be production value cited above (230 t) with the estimated amount of Be (~560 tons) required for neutron multiplication in the blanket of the PPCS-B fusion power reactor (FPR) that has a fusion power of 3.6 GW [4]. Experience gained under operation of Be in nuclear (fission) research reactors has shown that its lifetime in those reactors is about 8-10 years due to swelling [5]. Beryllium lifetime in FPRs is expected to be around 5 years [6]. Thus, recycling of Be irradiated in FPRs seems inevitable.

1.2 Beryllium for ITER

According to the ITER design developed in 2001, the armor of the ITER first wall should be made of S-65C vacuum hot pressed (VHP) beryllium grade produced by Brush-Wellman Inc. (USA) or Russian DShG-200 Be grade (distilled, stamped from hot-pressed billets) [7]. Both these Be grades are manufactured using vacuum hot-pressing. They were chosen owing to their good functional qualities, above all against thermal fatigue and shock loads.

Later China proposed to add Chinese beryllium grade CN-G01 to the list of materials approved for manufacturing of the first wall armor, and Russia suggested to replace in this list Be grade DShG-200 with another Russian grade TGP-56PS (technical, hot-pressed for the first wall armor). The main advantages of TGP-56PS over DShG-2900 are higher breaking point and plastic limit as well as constancy of physical and engineering properties both in transverse and lengthwise directions relative to axes of beryllium pressing. International tests have shown that these Be grades meet the ITER material requirements [8, 9].

2. PROSPECTS OF BERYLLIUM PRODUCTION IN RUSSIA

In 1964 a team of geologists led by G.A. Ermakov discovered one of the world's best deposits of the beryllium ore in the Republic of Buryatiya in eastern Siberia. The deposit, called Ermakovskoye [10], contains ~5700 t of Be [11]. In 1979-1989 the deposit was mined by open pit methods. High-grade Be concentrates were supplied to the Ulba Metallurgical Plant (UMP) in Ust-Kamenogorsk, the East Kazakhstan Province of Kazakhstan. UMP is the only enterprise in Eurasia producing a wide range of beryllium products from rough ingots to various finished items.

The year 1989 saw the cessation of mining at all but two Russian beryllium mines, namely the Zavitinskoye in Chita Oblast and the Pogranichnoye in the Far East [12], as well as the suspension of Be ore concentrate production [2, 13]. According to the U.S. Geological Survey's estimates [14], beryllium concentrate inventories in the USSR by that time were sufficient to meet the country's needs in the coming 30 years. UMP used available concentrates and exported Be products to the USA, Russia, China and other countries [13]. During 2008-2011, the USA imported 457 t of beryllium; mostly coming from Russia (201 t; 44%) and Kazakhstan (122 t; 26%), and the rest from Japan, Kenya and other countries. In 2012, Be import to the USA, including alloys and finished products, came to 106 t. Average Be price was US\$468 per kg [1].

In 2005, "Metals of Eastern Siberia" corporation (a member of Metropol Group) obtained a licence to resume operations at the previously abandoned Ermakovskoye deposit and mine it until 2025. Together with UMP the corporation developed an engineering design of an ore-dressing and processing enterprise with a production capacity of up to 400 t/yr of Be(OH)₂ (80 t/yr of Be) in the next 50 years. One part of Be hydroxide is expected to be shipped to

Kazakhstan, China and Japan for processing into a beryllium metal and alloys and another part — to be used for the manufacturing of Be nano-materials and alloys in Buryatiya. The total cost of the project is about RUR7 billion (US\$200 million). The project is financed by Metropol and state corporation Rosnano. The construction of the ore-dressing and processing complex is to start in 2013. The mine is expected to reach the design production capacity in 2016 [15].

3. CONTENT OF URANIUM IN BERYLLIUM

The main difference between beryllium provided by U.S., Chinese and Russian-Kazakhstan producers is the level of U impurity.

3.1 Uranium in U.S. beryllium

The concentrations of U in the Be blocks procured for Advanced Test (fission) Reactor (ATR) Core VI at the Idaho National Laboratory in 2002 ranged from 23 to 105 wppm with an average concentration of ~71 wppm, according to chemical assay data provided by vendor, Brush-Wellman [16].

At the 7th IEA Be Workshop in 2005 E. Alves (Portugal) said that the average U content in Be-5at%Ti alloy which he obtained from JAERI was 200 ± 12 wppm [17].

According to Brush-Wellman's specification for the S-65C VHP beryllium to be delivered for ITER, a typical average U content is 32 wppm, the lowest content is <30 wppm, and the highest value is 85 wppm [18]. One of the ITER Organization requirements is that uranium impurity levels in grade S-65C VHP beryllium and beryllium pebbles to be used in ITER are within 30 wppm [18]. Brush Wellman has identified the possibility of supplying beryllium with U impurity levels in the vicinity of 1 appm (26 wppm). This material would be furnished at a necessary cost premium, but its other properties would be essentially the same as those of the regular beryllium [16].

3.2 Uranium in Chinese beryllium

The designers of the Chinese ITER test blanket module (TBM) have informed that U content in beryllium to be used in the module as neutron multiplier is 100 wppm [19].

3.3 Uranium in Russian-Kazakhstan beryllium

Measurements of U content in Russian-Kazakhstan Be were performed with 35 samples. There were 20 samples of commercial Be produced by vacuum casting and 15 samples after vacuum distillation. The samples were fabricated from powders with different particle size distribution. Different compacting methods were used for the fabrication of final Be products: vacuum hot pressing, hot isostatic pressing, hot extrusion and upsetting. Measurements have shown that uranium concentration in commercial Be grades is within 0.16-18.0 wppm and averages 5.2 wppm, while in distilled Be it goes down to 0.05—0.92 wppm and averages 0.24 wppm (Fig. 1) [20, 21].

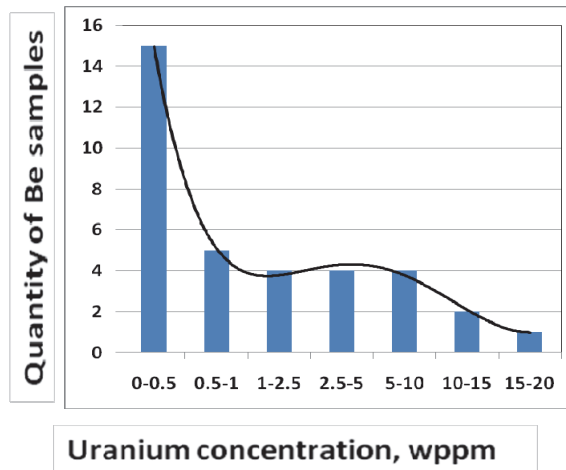


Fig. 1. Uranium content in Russian-Kazakhstan beryllium.

4. CONSEQUENCES OF BE CONTAMINATION WITH U

Uranium contamination of beryllium is of no concern in "neutron free" applications such as aerospace engineering or electrical technology.

For fusion reactors, the situation is different. Due to the presence of natural U in Be armor of the first wall and in Be neutron multiplier in four from six TBM in ITER, these Be components can be considered as combination of fertile (^{238}U) and fissile (^{235}U) uranium isotopes with beryllium as the fine neutron multiplier and moderator that is typical for blankets of fusion-fission hybrid systems. Interaction of neutrons with U in such systems will result in fissile isotopes enrichment (Fig. 2) and in their fission with fission neutron yield.

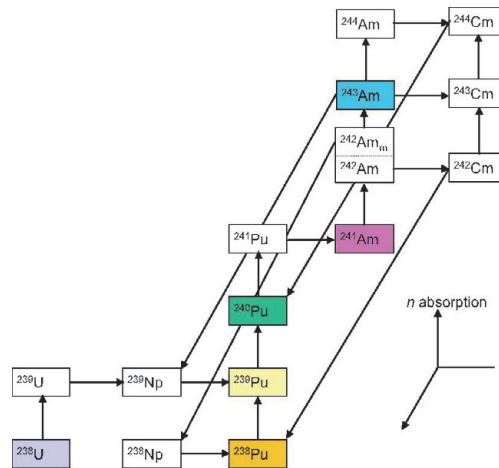


Fig. 2. Activation processes for U impurity in Be.

At initial concentration of U in ITER Be equal to 30 wppm, there will be $U_{\text{tot}} = \sim 370$ g of natural U, including about 2.7 g of ^{235}U , in 12.3 t of the ITER first wall Be. By the end of ITER 20-years operation period (at fluence of fusion neutrons through the first wall of $0.3 \text{ MW}\cdot\text{yr}/\text{m}^2$) $\sim 2\%$ of ^{238}U and $\sim 10\%$ of ^{235}U will burn up, ~ 8 g of ^{239}Pu and other fissile transuranic nuclides and ~ 180 mg of fission products will accumulate. Enrichment of fissionable fuel equal to $^{235}\text{U} + ^{239}\text{Pu} + ^{241}\text{Pu} / U_{\text{tot}}$ will be $\sim 2.5\%$ [22].

Besides, about 1 t of Be will be contained in the four ITER TBMs [23]. Chinese designers are going to use a Be grade containing 100 wppm of U in their TBM [19].

One can expect that similar assessments for demonstration and power fusion reactors will be more impressive. Russia's design of DEMO-S reactor with fusion power of 2.4 GW envisages the use of 215 t of beryllium (as neutron multiplier and the first wall armor) [24, 25]. In the European FPR MINERVA-H design the required Be amount is 865 t [6].

The European FPR PPCS-B requires ~560 t of Be [4]. At U concentration in Be of 30 wppm, the contents of natural U and ^{235}U in this reactor will amount to 17 kg and 123 g, respectively. In a day after the reactor shutdown for blanket replacement after 5 years of full power operation (i.e. for fusion neutron fluence through the first wall of $10 \text{ MW}\cdot\text{yr}/\text{m}^2$), the total content of Pu and other fissile isotopes will be of about 4.4 kg. Total activity of all the α -emitters in 1 kg of Be will amount to 525 MBq [6].

Thus, the difference between “pure” fusion reactors and fusion-fission hybrid reactors seems to be rather conditional. At the presence of U in Be of a so called “pure” fusion reactor we have the whole bouquet of different transuranic elements (actinides): from Pu to Am and Cm weighing several kilograms.

In May 2012, the ITER TBM Program Committee approved Korean proposal for the application of graphite neutron reflector decreasing amount of beryllium in their TBM. Commenting this decision Chief Technical Officer of the TBM Program L. Giancarli commented: “The innovative He-Cooled Ceramic Reflector concept uses graphite as neutron reflector, opening the possibility of avoiding the use of a Be neutron multiplier” [26].

4.1 Specific activity, classification of irradiated beryllium

Specific activity of the ITER beryllium, at initial U concentration in it of 30 wppm and fusion neutron fluence through the first wall of $0.3 \text{ MW}\cdot\text{yr}/\text{m}^2$ at ITER shutdown will be on the level of ~20 GBq/g, mainly due to the presence of the ^9He and other short-lived isotopes, [22]. In a day after the reactor shutdown the Be specific activity will come down to ~533 kBq/g (97% owing to ^3H and 3% due to transuranic isotopes and Co-60). After 100 years cooling the specific activity will be ~10 MBq/g, including 82% due to transuranic isotopes, [22, 6]. The corresponding specific activity of the DEMO-S beryllium at the fusion neutron fluence through the first wall of $10 \text{ MW}\cdot\text{yr}/\text{m}^2$ and under the same other conditions will be ~180 MBq/g (without detritiation) [25].

Under Russian regulations [27], such a beryllium in both cases is medium-active material, since these regulations determine a material containing transuranic radionuclides as low-active only if their specific activity does not exceed 10 Bq/g.

As to the U.S. regulations, if the total specific activity of α -emitting isotopes with atomic numbers greater than 92 and half-lives greater than 20 years exceeds 100 nCi/g (3.7 kBq/g), the corresponding material is transuranic (TRU) [16]. Specific activity of the irradiated ITER beryllium at the initial U concentration of 30 wppm is lower than this threshold, but the specific activities of spent Be from DEMO and power fusion reactors noticeably exceed it.

4.2 Consequences of possible ITER accident

Consequences of a possible ITER accident at the end of its lifetime, involving a Be dust release, were considered in [22] for the initial U concentration in Be of 85 wppm. In this case the Be dust specific activity would be ~20 GBq/g, due to the short-lived isotopes. The Be specific activity originated from Np, Pu and Am would be ~44 MBq/g.

A contact dose rate from the Be dust is 3.4 mSv/(h·g). About 54% of it is originated from transuranic elements and fission products.

The long-term ingestion and inhalation doses from Be dust were calculated on the basis of the European Activation System [28]. Concentrations of transuranic nuclides, tritium and ⁶⁰Co in Be dust and aerosols were assumed to be the same as in beryllium metal. The inhalation dose was ~1 Sv/g, and the ingestion dose — 94 mSv/g (owing to actinides: 66 and 39%, respectively).

According to Russian regulations [29], if the irradiation dose during the first 10 days after a radiation accident amounts to 50 mSv, it is necessary to come to decision on evacuation of population where appropriate. It means that evacuation of population should be considered in the cases when inhaled air during the first 10 days after an accident can contain 50 mg of the beryllium aerosols or meal can contain 530 mg of the beryllium dust.

4.3 Burial

Apparently, the highest difficulties resulted from Be contamination with U will be met at burial of irradiated Be.

Specific activity of Be by the end of the ITER life time due to ³H, actinides, ⁹⁴Nb and ¹⁴C will essentially exceed limits specified by European and American regulations for burial of radioactive waste in sub-surface disposal sites.

Under French classification of radioactive waste Be, containing transuranic α -emitters, is MAVL (intermediate level long-lived waste with half-life exceeding 31 years). Criteria for burial of such waste for the time being are not determined, except the requirement that energy-release in containers with waste of this category should not exceed 13 W. The opportunity of such a waste burial in geological repositories is under study [6, 30].

In this connection we would like to quote G. Longhurst and R. Rohe [16], who wrote: “No existing waste repositories could be found that would accept ATR’s transuranic waste Be. Even the Waste Isolation Pilot Plant in New Mexico, which accepts transuranic waste from defense programs, could not accept ATR Be, in part because of its large ³H inventory”.

4.4 Impossibility of clearance

According to the IAEA recommendations [31], clearance (unrestricted release from regulatory control) of irradiated materials containing transuranic radioactive nuclides and its subsequent unrestricted use require, at the least, to have the total specific activity of ²³⁸Pu, ²³⁹Pu, ²⁴⁰Pu, ²⁴¹Am, ^{242m}Am and ²⁴³Am contained in any material < 0.1 Bq/g. These recommendations, already as requirements, are included in the Russian Regulations [27]. Thus, clearance of Be extracted from ITER after its operation up to equivalent fusion neutron

fluence through the first wall of $0.3 \text{ MW}\cdot\text{yr}/\text{m}^2$ is possible only if initial U concentration in Be is $<1 \text{ ng/g}$. For reactor PPCS-B [4] a corresponding U content should be $<0.03 \text{ ng/g}$.

Russia's Radiation Safety Regulations [29] and relevant guideline of the EC [32] provide for an eventuality to use materials with specific activity of transuranic α -emitters from 0.1 to 1 Bq/g if forthcoming individual effective irradiation dose does not exceed $10 \mu\text{Sv}/\text{year}$. However, Russian regulations require in this case radiation control without fail. The initial U concentration in Be in this case should not exceed 10 and 0.3 ng/g Be, respectively for ITER and PPCS-B. We would like to remind, that a minimal U concentration in Russian beryllium after vacuum distillation is 50 ng/g .

4.5 Contact dose rate

Designers of China ITER TBM estimated a contact dose rate from the TBM, as a whole, and from the beryllium neutron multiplier, particularly. The uranium concentration in the Chinese beryllium is 100 wppm [19]. During the TBM cooling up to 10^5 years the main contribution to the module contact dose rate is from steel, even if it is low-activated eurofer-97.

The contact dose from Be, permissive hands-on handling of the metal without any protector ($10 \mu\text{Sv}/\text{h}$) is reached after 100 years of cooling. By this time it is determined by ^{239}Pu [19, 21], remaining less than contact dose rate from steel [19].

A shielded hands-on handling (using simple protectors, like glove boxes) is possible in respect to a material producing contact dose rate less than $2 \text{ mSv}/\text{h}$ [30]. Such a dose rate from the beryllium in the Chinese TBM is reached after 30 years of cooling [19].

5. POSSIBLE COMBINATIONS

Brush-Wellman and UMP representatives gave a joint report at the 6th IEA Workshop on beryllium Technology for Fusion [33]. The authors of the report considered strong and weak features of their enterprises and proposed the following plan of beryllium elements for ITER manufacturing:

- UMP makes the high-grade vacuum cast Be ingots with low content of U and sends them to Brush-Wellman;
- Brush-Wellman produces tiles for the ITER first wall armor with a small overdimension from these ingots and sends them back to UMP;
- UMP carries out the final mechanical working of the tiles and, possibly, solders them to substrate, and then sends the tiles to the USA;
- Brush-Wellman performs the final inspection of tiles and sends them to the ITER Organization.

6. BERYLLIUM RECYCLING NECESSITY

Given the sizes of total world beryllium resources (somewhat more than 80 kt) [1], the annual world beryllium production (230 t in 2012), the fusion power engineering demand for this metal ($\sim 560 \text{ t}$ for PPCS-B, $\sim 865 \text{ t}$ for MINERVA-H [6]), to say nothing about other needs, we regard beryllium as a scarce metal. Therefore the necessity of a beryllium recycling (return to the production cycle) with its purification from U, transuranic α -emitters, fission and activation products seems to be inevitable.

A laboratory radiochemical technology for reprocessing, purification from activation products and return to production cycle of scarce and expensive components of vanadium-chromium-titanium alloy was developed in V.G. Khlopin Radium Institute, in Saint-Petersburg. This technology is similar to PUREX (Plutonium-URanium Extraction) technology, which is the only industrial method of spent nuclear fuel reprocessing used in all the radiochemical plants in the world. It reliably serves for separation of Pu from U and their purification from fission products. As a result the fission product concentration in alloy components can be reduced by a factor of 10^7 — 10^8 [34].

The only restriction for this technology application is the requirement that the specific activity of the fuel solution should not exceed 4 TBq/l, since already at 6 TBq/l radiolysis of organic reagents is badly increased, degrading functional quality of extractor [35].

The technology developed for recycling of V alloy components was tested in laboratory conditions with activated samples. The Co and Nb contents in V were reduced by three orders of magnitude. The calculations have shown that the purification of V5Cr5Ti alloy components using 50-stage extraction cascade ensures a hands-on handling (at contact dose rate < 10 μ Sv/hour) up to 95% of alloy [34].

Preliminary development work on a beryllium purification and recycling was carried out basing on previous experience gained with a vanadium alloy [36], But this work stopped because of the funding cut-off.

7. OTHER IMPURITIES

Besides U and ^3H , some other isotopes play an important role in safety and environmental characteristics of Be. They are ^{14}C , forming in Be mainly from N impurity, ^{94}Nb , ^{60}Co , and to a lesser degree $^{108\text{m}}\text{Ag}$. If U in Be is lacking and Be detritiation is effective, these nuclides become the main obstacle for Be clearance.

Cobalt-60 determines the contact dose rate level from beryllium during several decades of cooling. Its contribution to the contact dose rate in a month after reactor shutdown of the Russian demonstration reactor DEMO-S is 86.5%, and in 10 years — 99.8% [26].

Without U in beryllium a contribution of ^{94}Nb to the contact dose rate from Be becomes dominating in 100 years after reactor shutdown. For example, this contribution in the beryllium neutron multiplier of the DEMO-S outer blanket by this time is about 86% [26].

Enhanced content of Nb in Be (it had a place at deliveries) results in additional normative difficulties at permitting for a beryllium handling.

8. EXPERIMENTS ON THERMAL DESORPTION OF TRITIUM AND HELIUM

Tritium formed in Be through the reactions $^9\text{Be}(n;\alpha)^6\text{Li}(n;\alpha)\text{T}$ badly decreases opportunities for the irradiated beryllium burial. The specific activity of the irradiated beryllium during decades of its cooling is determined by the accumulated tritium. For example, the contribution of tritium to the beryllium specific activity in the DEMO-S outer blanket in a month after reactor shutdown is 99.6% and in 100 years it is 99.75% [26].

A contribution of tritium to energy release in the nearest to plasma layers of the beryllium neutron multiplier in the DEMO-S outer blanket after 10 years of cooling is 81% and after 100 years it is 98% [26].

Practically all the technological operations with irradiated beryllium require latter's detritiation. A basic procedure for tritium removal from beryllium could be the thermal desorption (may be using tritium replacement with protium).

Studies of ^3H and He release from the TShG-200 beryllium grade irradiated in the 40-MW material test nuclear reactor MR to the fluences of fast neutrons (with energy >500 keV) of $\sim 3 \cdot 10^{21}$ and $\sim 1 \cdot 10^{22}$ n/cm^2 were carried out in Kurchatov Institute by A.Yu. Biryukov. The highest ^3H and He content in samples was respectively ~ 785 and 4400 appm. Preliminary results of these studies were reported at the 4th International Symposium on Fusion Nuclear Technology [37].

The experiments have shown that tritium and He release from samples has a non-diffusive (explosive) nature. Under small temperature rise rates (of about 10 $^{\circ}\text{C}/\text{min}$.) and the fast neutron fluence of $\sim 3 \cdot 10^{21}$ n/cm^2 tritium goes out of samples at temperature of about 810°C . Temperature of He release was around 1200°C (Fig. 3). Under a neutron fluence increase to $1 \cdot 10^{22}$ n/cm^2 the temperatures of tritium and He explosive release peaks have decreased to 740 and 1050 $^{\circ}\text{C}$ respectively (Fig. 4). The temperatures of tritium and He release and width of spectral peaks decrease also with increase of temperature growth rate (Figs. 5, 6, 7).

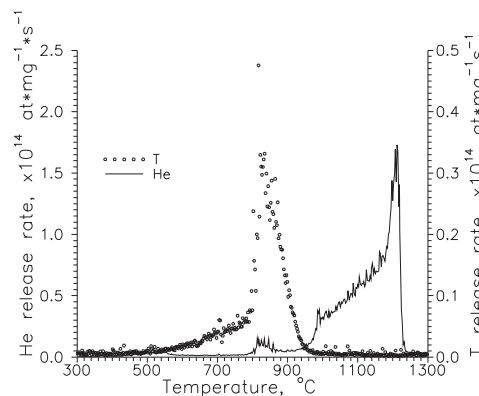


Fig. 3. Thermodesorption spectra of beryllium irradiated to fast neutron fluence of $3 \cdot 10^{21}$ n/cm^2 ; linear temperature rise rate is 10 $^{\circ}\text{C}/\text{min}$.

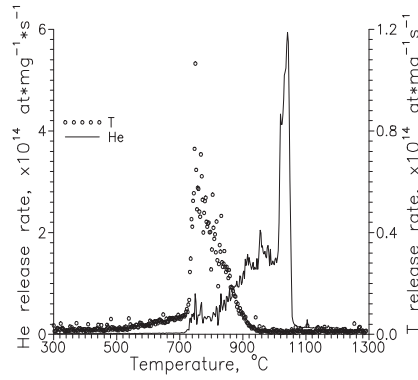


Fig. 4. Thermodesorption spectra of beryllium irradiated to fast neutron fluence of $1 \cdot 10^{22} \text{ n/cm}^2$; linear temperature rise rate is 10 oC/min .

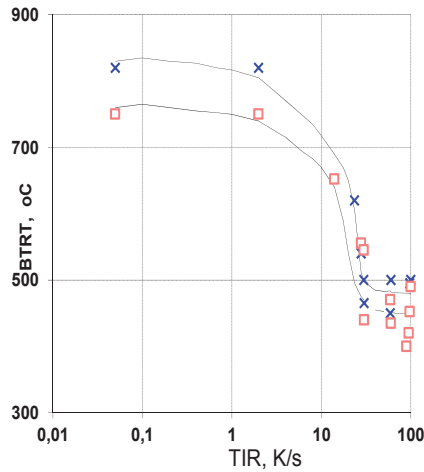


Fig. 5. Burst tritium release temperature (BTRT) versus temperature increase rate (TIR) of a beryllium sample for two values of fast neutron fluence: $3 \cdot 10^{21} \text{ cm}^{-2}$ (x) и $1 \cdot 10^{22} \text{ cm}^{-2}$ (□).

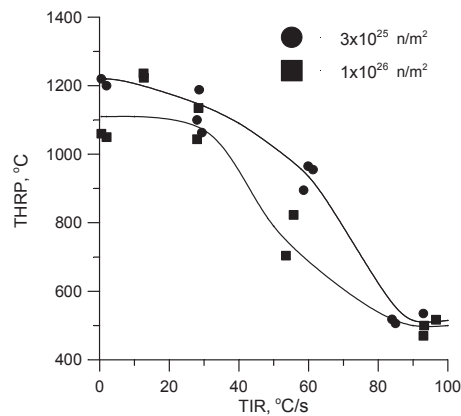


Fig. 6. Temperature of He release peaks (THRP) for neutron irradiated beryllium versus temperature increase rate (TIR) of a sample for two values of fast neutron fluence.

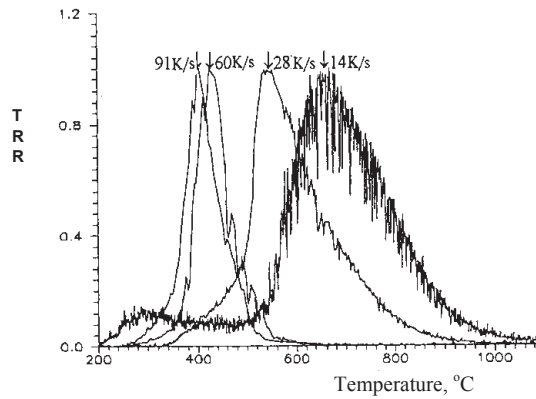


Fig. 7. Evolution of thermodesorption spectra for tritium release from neutron irradiated Be; fast neutron fluence $\sim 1 \cdot 10^{22}$ n/cm² at different temperature growth rates. TRR — tritium release rate (relative units).

It is appropriate mention here that tritium, co-deposited with Be under interaction of plasma with surface of vacuum chamber, can be removed at appreciably lower temperature (about 350°C) [38, 39].

The reason that tritium and He, formed through the reactions ${}^9\text{Be}(n,\alpha){}^6\text{Li}(n,\alpha)\text{T}$, are released at different temperatures, apparently, can be explained by the fact that tritium, as more mobile nuclide, migrates to grain boundaries, while He, for the most part, remains inside the grains, where it was formed. The sample destruction due to swelling under temperature rise begins along the grain boundaries. This results in explosive release of tritium accumulated there. Destruction of Be grains themselves, causing helium release, occurs at higher temperature and bigger swelling (Fig. 8).

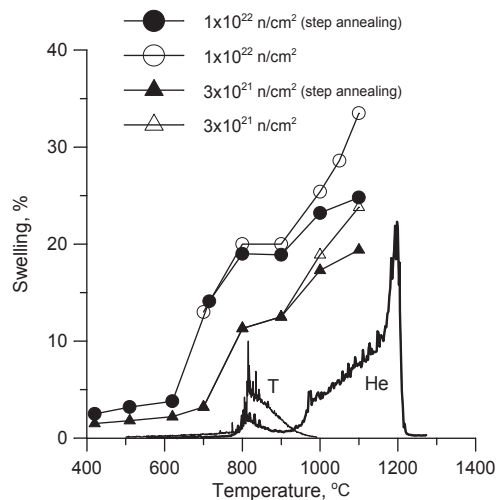


Fig. 8. Swelling of irradiated Be versus postreactor annealing temperature in comparison with thermodesorption spectra of tritium and He for samples irradiated with fast neutron fluence of $3 \cdot 10^{21}$ n/cm².

7. CONCLUSIONS

Potential needs in beryllium for fusion power engineering may exceed its resources if beryllium recycling is not realized.

It is necessary to develop an economically viable technology for the removal of uranium from beryllium intended for fusion applications.

Also it is necessary to develop and apply in industry an optimal technology for irradiated beryllium detritiation.

REFERENCES

- [1] **Minerals Information: Beryllium Statistics and Information: Mineral Commodity Summaries.** — US Geological Survey. Retrieved 11 March 2013.
<http://minerals.usgs.gov/minerals/pubs/commodity/beryllium/mcs-2013-beryl.pdf>
- [2] **Federal State Unitary Enterprise “N.M. Fedorovskij All-Russian Scientific Research Institute of Minerals”.** Review of Sources of Be Raw Materials. 2013.
<http://www.vims-geo.ru/elements/beryllium.aspx> (in Russian).
- [3] **Materion Brush Inc.** Sources of Beryllium. 2013. <http://www.beryllium.com/sources-beryllium>
- [4] **D. Maisonnier, I. Cook, P. Sardain, R. Andreani, L. Di Pace, R. Forrest et al..** A Conceptual Study of Commercial Fusion Power Plants. — Final Report of the European Fusion Power Plant Conceptual Study, EFDA (05)-27/4/10, revision 1 April 2005, EFDA-RP-RE-5.0.
- [5] **D.E. Sebo, C.K. Mullen, G.R. Longhurst, M.L. Carboneau, J.W. Sterbentz.** Beryllium Waste Transuranic Inventory in the Subsurface Disposal Area, Operable Unit No. 7-13/14. — INEEL/EXT-01-01678. Revision 3. August 2005.
- [6] **G. Cambi, D.G. Cefruga, L. Di Pace, E. Druyts, V. Massaut.** The potential presence and minimization of plutonium within the irradiated beryllium in fusion power reactors. — Fusion Eng. Des. 85 (2010) 1139-1142.
- [7] **ITER Technical Basis** —ITER EDA Documentation Series No. 24, International Atomic Energy Agency, Vienna, 2002.
- [8] **V. Barabash, R. Eaton, T. Hirai, I. Kupriyanov, G. Nikolaev, Zhanhong Wang, Xiang Liu, M. Roedig, J. Linke.** Beryllium qualification activity for ITER first wall applications. —13th International Workshop on Plasma-Facing Materials and Components for Fusion Applications/ 1st International Conference on Fusion Energy Material Science, Rosenheim, Germany, 09 May - 13 May, 2011. https://www.ipp.mpg.de/ippcms/eng/for/veranstaltungen/konferenzen/archiv/2011/03pfmc-13/internal/presentations/I-18_Barabash.pdf.
- [9] **V. Barabash, R. Eaton, T. Hirai, I. Kupriyanov, G. Nikolaev, Zhanhong Wang, Xiang Liu, M. Roedig, J. Linke.** Summary of beryllium qualification activity for ITER first-wall applications. — Physica Scripta, 2011, vol. 2011, T145, 014007; <http://iopscience.iop.org/1402-4896/2011/T145/014007>.
- [10] **Novokizhiginsk Secondary Education School.** Ermakov Gennadij Alexeevich — the State Prize laureate. 2012 г. <http://selorodnoe.ru/vid/show/id3632943/11> (in Russian).
- [11] **VostokTele Inform.** Group of companies “Metropol” will construct a plant in deposit Ermakovskoye in Buryatiya. June 12, 2013. <http://vt-inform.ru/vti/142/53950.php> (in Russian).
- [12] **Encyclopedia Krugosvet (Round-the-World).**
http://www.krugosvet.ru/enc/nauka_i_tehnika/himiya/BERILLI.html?page=0,1 (in Russian).

- [13] **Corporation «Metals of Eastern Siberia».** Ermakovskij Ore Mining and Smelting Industrial Complex. 2013. <http://mbc-corp.ru/activity/gorsector/ermak/index.wbp> (in Russian).
- [14] **Minerals Information: Beryllium Statistics and Information: 2011 Minerals Yearbook: Beryllium (Advance Release).** — United States Geological Survey. February 2013. <http://minerals.usgs.gov/minerals/pubs/ommodity/beryllium/myb1-2011-beryl.pdf>
- [15] **Beryllium: Creation of the Production Complex for High-Tech Manufacturing Beryllium Products for Telecommunicational Engineering, Nanoelectronics and Other Applications in Nanoindustry.** — Project of group of companies “Metropol”, corporation «Metals of Eastern Siberia», state corporation ROSNANO and Moscow Physicotechnical Institute, 2011. <http://drec.mipt.ru/faculty/report2011/Beryllium-arpgyh9lgzh> (in Russian).
- [16] **G.R. Longhurst and R.D. Rohe.** Beryllium use in the Advanced Test Reactor. — 8th IEA International Workshop on Be Technology, Lisbon, Portugal, 2007.
- [17] **E. Alves, L.C. Alves, N. Franco, M.R. Da Silva, and A. Paúl.** Structural and oxidation studies of titanium beryllides. — Proceedings of the 7th IEA International Workshop on Beryllium Technology, Santa Barbara, CA, USA, 2005, INL/EXT-06-01222, 2006, Ed. G. R. Longhurst. pp. 43-46.
- [18] **V. Barabash.** Chemical composition and some properties of materials for the ITER in-vessel components for type B radioactive waste assessment. — Internal ITER document, ITER Document Management (IDM) Number: ITER_D_2DKPK7 v1.3, 24.05.2010, unpublished.
- [19] **J.R. Han, Y.X. Chen, R. Han, K.M. Feng, R.A. Forrest.** Activation analysis and waste management of China ITER helium cooled solid breeder test blanket module. — *Fusion Eng. Des.* 85 (2010) 761-765.
- [20] **I.B. Kupriyanov, A.M. Khomutov, G.N. Nikolaev, V.V. Gorlevsky, Yu.E. Markushkin, V.P. Chakin, A.A. Gervash, A.N. Kalashnikov, B.N. Kolbasov.** Status of beryllium R&D activities in Russian Federation. — Proceedings 7th IEA International Workshop on Be Technology, Santa Barbara, CA, USA, 2005, INL/EXT-06-01222, 2006, Editor Glen R. Longhurst. pp. 8-16.
- [21] **I.B. Kupriyanov, A.A. Borisov, N.G. Gorlevskaja.** Investigation of uranium content in Russian Federation beryllium. — *Fusion Science and Technology*, 62 (2012) 180-184.
- [22] **V.I. Khripunov.** 3-D study of PFC and dust activation in ITER. — 22th IAEA Fusion Energy Conference, October 13—18, 2008, Geneva, Switzerland.
- [23] **L.V. Boccaccini, S. Ciattaglia, R. Meyder and X. Jin.** Review of accidental safety studies for the European HCPB test blanket system. — *Nucl. Fusion* 47 (2007) S436-S441.
- [24] **B.N. Kolbasov, V.A. Belyakov, E.N. Bondarchuk, A.A. Borisov, I.R. Kirillov, V.M. Leonov, G.E. Shatalov, Yu.A. Sokolov, Yu.S. Strebkov, N.N. Vasiliev.** Russian concept for a DEMO-S demonstration fusion power reactor. — *Fusion Eng. Des.*, 83 (7-9) (2008) 870-876.
- [25] **Concept Basics for Demonstration Fusion Reactor DEMO-S.** Part V. Reactor site. Outside systems. Cost estimation for construction of the plant with reactor DEMO-S. Safety of plant operation and environmental impacts. — Design of Russian Federation DEMO. Russian Research Centre «Kurchatov Institute», Institute of Nuclear Fusion, Moscow, 2001 (in Russian).
- [26] **L. Giancarli.** Major step forward for the Test Blanket Modules Program. — ITER Newline, No. 223, 18 May 2012.

- [27] **Basic Sanitary Regulations of Radiation Safety Assurance** (OSPORB-99/2010), Sanitary regulations and standards (SP 2.6.1.2612-10). — Moscow: Federal Service for Supervision in the Field of Protection of Consumers and Well-Being of People of Russian Federation, 2010. <http://nucloweb.jinr.ru/nucloserv/inform/instructions/osprb-99-2010.pdf> (in Russian).
- [28] **R.A. Forrest**. The European Activation System: EASY-2003, Overview, EASY Documentation Series, UKAEA Fus484, EURATOM/UKAEA Fusion Association (2002).
- [29] **Radiation Safety Regulations** (NRB-99/2009). Hygienic regulations and Standards (SanPin 2.6.1.2523-09/2009). — Moscow: Ministry of Health of Russia, 2009. <http://www.complexdoc.ru/ntd/534510> (in Russian).
- [30] **M. Zucchetti, L. Di Pace, L. El-Guebali, B.N. Kolbasov, V. Massaut, R. Pampin, P. Wilson**. The back end of the fusion materials cycle. — *Fusion Sci.Technol.*, 55 (2009) 109-139.
- [31] **IAEA**. Application of the Concepts of Exclusion, Exemption and Clearance. — Safety Standards Series, No. RS-G-1.7, International Atomic Energy Agency, Vienna, (2004). http://www-pub.iaea.org/MTCD/publications/PDF/Pub1202_web.pdf
- [32] **EC-RP**. Radiation Protection 122 - Practical Use of the Concepts of Clearance and Exemption, Guidance on General Clearance Levels for Practices. — European Commission, Directorate General for the Environment. 2000. http://ec.europa.eu/energy/nuclear/radioprotection/publication/doc/122_part1_en.pdf
- [33] **D. Kaszynski, K. Sato, V.V. Savchuk, V.P. Shestakov**. Reducing the cost of S-65C grade beryllium for ITER first wall applications. — Proceedings of the 6th IEA International Workshop on Be Technology for Fusion, 2003, Miyazaki, Japan, pp. 90—94.
- [34] **B.N. Kolbasov, S.A. Bartenev, V.T. Gotovchikov, V. Massaut, M. Zucchetti, L. Di Pace, L. El-Guebali, A. Robinson**. Some technological problems of spent fusion materials management. — *Problems of Atomic Science and Engineering, Ser.: Thermonuclear Fusion*, 2011 (3) pp. 38-53, http://vant.iterru.ru/vant_2011_3/3.pdf (in Russian).
- [35] **V.I. Zemlyanukhin, E.I. Il'yenko, A.N. Kondrat'yev**. Radiochemical Reprocessing of Nuclear Fuel. — Moscow: Energoatomizdat, 1989. (in Russian).
- [36] **S.A. Bartenev, A. Ciampichetti, N.G. Firsin, R. Forrest, B.N. Kolbasov, P.V. Romanov, V.N. Romanovskij, M. Zucchetti**. Activation and clearance of vanadium alloys and beryllium multipliers in fusion reactors. — *Fusion Eng. Des.* 82 (15-24) (2007) 2885-2890.
- [37] **D.V. Andreev, A.Yu. Biryukov, L.S. Danelyan, N.G. Elistratov, V.M. Gureev, M.I. Guseva, B.N. Kolbasov, Yu.Ya. Kurochkin, V.N. Nevzorov, O.V. Stativkina, A.M. Zimin**. Studies of tritium desorption from beryllium and characterization of erosion products under plasma—beryllium interaction. — *Fusion Eng. Des.* 39-40 (1998) 465-475.
- [38] **R.A. Pitts, S. Corpentier, F. Escourbiac, T. Hirai, V. Komarov, A.S. Kukushkin et al**. Physics basis and design of the ITER plasma-facing components. — *J. Nucl. Mater.* 415 (2011) S957-S964.
- [39] **R.P. Doerner et al**. — *Nucl. Fusion* 49 (2009) 035002.

X-ray tomography study of porosity in neutron irradiated beryllium after post irradiation annealing

P. Vladimirov¹, C. Ferrero², V. Chakin¹, P. Kurinskiy¹, A. Moeslang¹, R. Pieritz³,
T. Weitkamp⁴, E. Brun^{2,5}

¹*Karlsruhe Institute of Technology, Karlsruhe, Germany*

²*European Synchrotron Radiation Facility, Grenoble, France*

³*AR4DA – Applied Research Solutions, Chirens, France*

⁴*Synchrotron SOLEIL, Gif-sur-Yvette, France*

⁵*Ludwig Maximilian University, Munich, Germany*

pavel.vladimirov@kit.edu

ABSTRACT

In fusion reactors, hydrogen isotopes, i.e., tritium and deuterium, will be used as fuel producing energetic neutrons and helium atoms. Whilst deuterium is a stable nuclide frequent in nature, tritium is beta-radioactive. Its half-life time is about 12 years, requiring constant renewal via tritium generation in nuclear reactions. Neutrons produced in fusion reactions should therefore be effectively multiplied. To this end, beryllium is planned to be used in form of pebble beds in the blanket of a fusion reactor. Unfortunately, helium and tritium are created under neutron irradiation and accumulated in the beryllium matrix, resulting in the formation of gas bubbles.

In this work, beryllium reflector fragments irradiated for 15 years in the research reactor BR2 (SCK-CEN, Mol, Belgium) at temperatures below 120 °C and containing about 2 atomic per cent helium was vacuum annealed at two temperatures and various annealing times. Gas-induced porosity developed after annealing was investigated using synchrotron X-ray micro-tomography. This technology enables a non-destructive and quantitative analysis of the 3D morphology of the gas-induced porosity providing important insights into the kinetics of the gas bubble growth.

Using advanced post-processing of the micro-tomography data it has been possible to determine the volume fraction of gas bubbles and their size distribution, and reveal the formation of 3D bubble clusters. The importance of the data obtained for realistic modelling of the gas bubble growth during annealing is discussed.

INTRODUCTION

The forthcoming generation of fusion reactors will produce hydrogen isotopes, namely deuterium and tritium, as a fuel. Although deuterium is abundant in nature, the tritium isotope is beta-radioactive. It decays to ³He with a half-life time of 12.3 years and is typically obtained in neutron-induced nuclear reactions. Therefore, fusion reactors are being designed to achieve closed fuel cycles: at least one tritium nucleus should be generated per each tritium burnt in a fusion reaction. Accounting for unavoidable neutron losses and instant tritium decay, the tritium breeding ratio should be about 10-12% higher than unity. In the Helium Cooled Pebble Bed (HCPB) design concept of a fusion reactor, beryllium in form of pebble beds plays the role of a neutron multiplier to increase the tritium production per fusion neutron, thus closing the fuel cycle of the fusion reactor. Beryllium is known to be a very effective neutron multiplier, since, when hit by a high energy neutron, its nucleus often decays

with production of two neutrons (and two helium atoms). The excess neutrons can be used for tritium generation, thus closing the fuel cycle.

Both tritium and helium are produced in beryllium under neutron irradiation by transmutation. Being practically insoluble in the beryllium matrix, helium atoms precipitate into the bulk as well as onto grain boundaries and dislocations, resulting in helium bubble growth and substantial volume increase, i.e. swelling. Swelling depends both on the amount of helium accumulated in beryllium and on irradiation temperature. At temperatures below ~ 400 °C only very small (7-8 nm) faceted bubbles (if any) can be observed in a transmission electron microscope. At higher temperatures, the size of helium bubbles increases with the irradiation temperature, reaching, e.g., 140 nm at 695 °C [1]. Interconnected chains of bubbles are often observed at grain boundaries and sometimes within the grain body.

Beryllium irradiated at low temperatures exhibits low swelling, but it can swell more than 30% after post-irradiation annealing [2]. Moreover, the degree of swelling can be controlled by selecting annealing temperature and dwell time. Therefore, we used in this work annealing at two temperatures and various dwell times to study the kinetics of beryllium swelling.

Tritium accumulated in helium bubbles determines mainly the radioactive inventory of the spent pebble beds, bearing the risk of abrupt release under accidental conditions. On the other hand, helium bubbles abundantly formed along grain boundaries trigger intergranular brittle fracture, destroying the structural integrity of pebbles. As it was shown by gas thermal desorption experiments, the burst release of tritium and helium from the samples irradiated above 500 °C occurs simultaneously, which might be explained by the formation of pore channels connected with the sample surface [3], [4]. As a consequence, it is important to study the process of helium bubble formation and evolution of complicated pore networks to substantiate this hypothesis and to obtain important insights on the mechanisms of tritium release from beryllium.

Since X-ray tomography cannot distinguish between gas-filled bubbles and voids, we will not explicitly distinguish them in the following sections and call them just pores.

EXPERIMENTAL DETAILS

Samples

The samples used in this study were made of commercial beryllium grade S200E (Materion Brush Beryllium & Composites, USA) used for about 15 years as a neutron reflector in the material testing nuclear reactor BR2, SCK-CEN, Mol, Belgium. Outer parts of the beryllium reflector were exposed to the temperature of cooling water (~ 50 °C), while the temperature inside the reflector block could be somewhat higher (< 120 °C). This long-term irradiation resulted in a fission neutron fluence of 5.32×10^{22} n/cm² which corresponds to the generation of approximately 22500 appm He [2]. Tritium was also produced under neutron irradiation, however, due to a complex operation history it is difficult to calculate exactly its amount.

The S200E material, which utilizes attritioned powder (< 200 μ m), was consolidated by vacuum hot pressing (VHP). Typically, VHP is performed at temperatures in the range 1050-1150 °C and under a pressure of about 14 MPa during 36 hours. Like all other beryllium powder products, S200E contains coarsened BeO particles (0.1-0.5 μ m) heterogeneously

distributed along grain boundaries [5]. The oxide particles originate from the oxidation of raw powder [6]. The average grain size is about 10-13 μm . Unfortunately, this material was not available in the unirradiated state, therefore we used similar grade S200F as a reference.

For X-ray micro-tomography measurements, the irregularly shaped pieces with a size of about 0.5 mm were produced by crashing neutron reflector fragments. The samples were vacuum-annealed at 850 $^{\circ}\text{C}$ and 1000 $^{\circ}\text{C}$, respectively, for 0.5, 1, 5 and 10 hours.

X-ray measurements

The beam line ID19 [7] at the European Synchrotron (ESRF), Grenoble, France was used to acquire X-ray tomography data, which were subsequently processed to produce 3D images of the investigated samples.

Table 1: Summary of annealing and x-ray scanning conditions

Sample	Conditions	Voxel size, μm		
		1.4	0.28	0.175
p1	0.5h at 850 $^{\circ}\text{C}$	✓		
p2	1h at 850 $^{\circ}\text{C}$	✓	✓	✓
p3	5h at 850 $^{\circ}\text{C}$	✓	✓	✓
p4	10h at 850 $^{\circ}\text{C}$	✓		
p5	0.5h at 1000 $^{\circ}\text{C}$	✓		
p6	1h at 1000 $^{\circ}\text{C}$	✓		
p7	5h at 1000 $^{\circ}\text{C}$	✓	✓	
p8	10h at 1000 $^{\circ}\text{C}$	✓	✓	✓
p9	as irradiated	✓	✓	✓
p10	unirradiated	✓	✓	✓

Ten beryllium samples were scanned using the full-field parallel-beam in-line phase contrast imaging micro-tomography setup at the ESRF with variable sample-to-detector distances (15, 10 and 8 mm). The energy was set to 17.4 keV. The imaging detector used at the beam line was the chip of a CCD sensor based on the FReLoN design developed at the ESRF [8], with an array of 2048 \times 2048 pixels. The physical pixel size of the CCD is 14 μm . Different detector optics are available covering a range of effective pixel sizes from 0.18 to 30 μm . In our experiment the samples were imaged at effective pixel sizes of 1.4, \sim 0.3 and \sim 0.2 μm . The detector system consists of a thin single-crystal scintillator screen converting the X-ray intensity distribution to a visible-light image which is then magnified and projected onto the CCD via commercially-available microscope lenses. The sample stage is equipped with motors allowing horizontal translation of the sample in both dimensions, in addition to the tomographic rotation around the vertical axis.

For safety reasons, because of the radioactivity of the sample, each specimen was enclosed in a Plexiglas cylinder with double walls during measurements. To prevent unwanted motion of the samples during rotation we used a spring-loaded piston placed in the inner cylinder which pushed onto the sample. The glue used for this purpose in previous experiments [4] can penetrate the specimen through a pore network and should be avoided. Double confinement appears to be very useful, as after several consequent measurements the inner container broke under simultaneous action of irradiation and stress. Thus, only a subset of scheduled

measurements could be accomplished. Table 1 summarizes the successful measurements performed during the experiment.

Post processing and topological analyses

A substantial amount of data (~ 1 TByte) was collected during the experiments requiring advanced processing according to the following major steps: raw data assembling, pre-processing of raw data, volume decomposition, tomographic reconstruction, and post-processing [9]. The processed data are in the form of 2D gray scale images, which were subsequently segmented in binary (black and white, corresponding to solid and porous phases, respectively) 3D arrays using threshold values accurately chosen on the basis of the grey level frequency distribution.

Image filtering and segmentation

As the filters and different parameters used were the same for each sample, for sake of clarity we exemplify the image processing steps on the sample that was annealed for 10 hours at 1000°C .

The in-line phase contrast imaging setup enhances edges of pores. The data sets thus obtained are, in principle, amenable to processing by single-distance phase retrieval methods [10,11], but for the present study, they were simply reconstructed using a filtered back projection algorithm [12] with a ramp filter. Figure 1 shows that the interface between pore and solid phases in the image processed in this way is well defined.

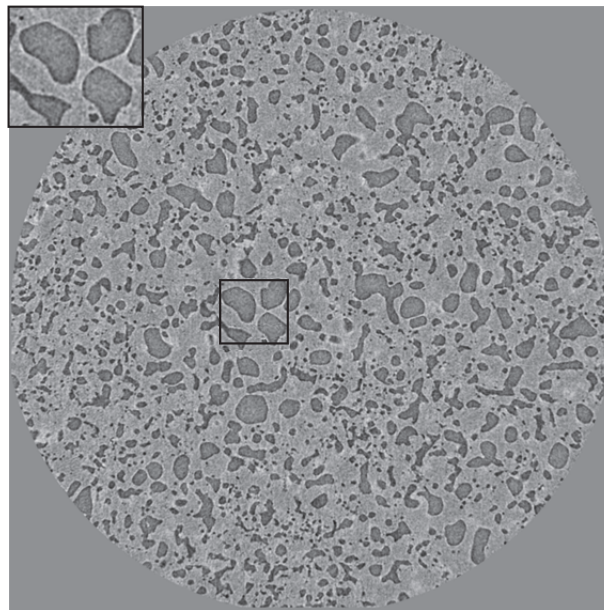


Figure 1: Example of an X-ray tomography slice in the central region of the sample. The inset on the top left corner is a magnification of the zone marked with the black frame.

The crucial step for the quantitative analysis of the images is the conversion of the grey scale 3D data array into solid and pore phases, i.e., the binarisation. Due to the significant contrast variation within the sample it was impossible to find a unique grey level threshold value to obtain a reliable separation between the phases (see Figure 2a and 2b). The binary image produced this way is rather noisy. Moreover, the inner volume of pores appears to be filled after binarisation with the solid phase (see insert in Figure 2a). Visual inspection of the raw images

shows that this is not the case (cf. insert in Figure 1), meaning that such artefacts should be corrected. The first step of the proposed approach is to apply a 3D median filter with a kernel of 3 voxel radius. The effect of this filter is shown in Figure 2d, and the resulting contrast histogram in Figure 2c. The image is blurred but the interface between the two materials is preserved, as the magnified region shows.

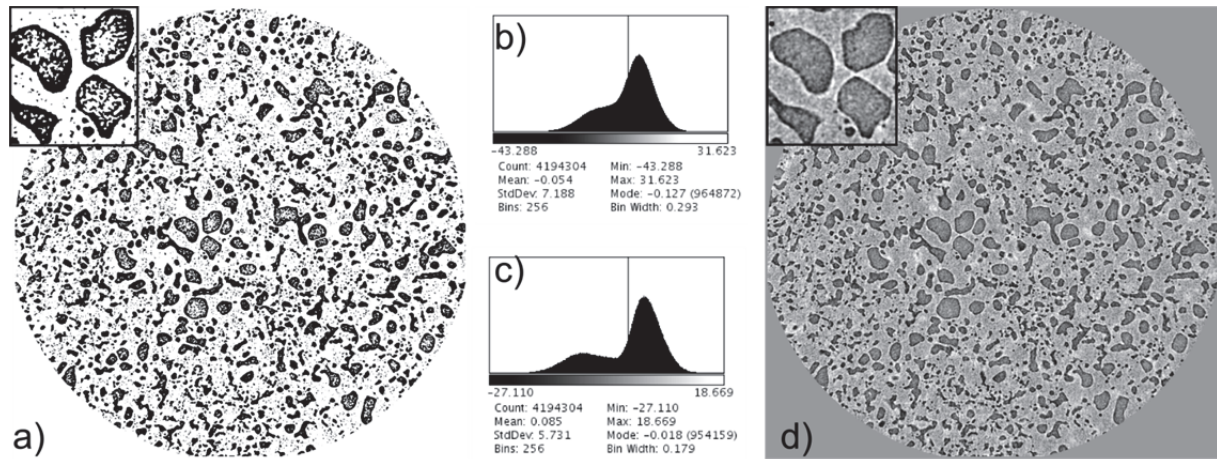


Figure 2: Coarse image segmentation a) using the threshold showed on the contrast histogram b). d) Outcome of the median filter application and c) related contrast histogram.

Owing to the application of the median filter, the two peaks are better separated in the histogram (see Figure 2c). The threshold is then easy to set by selecting the minimum between the two peaks. Unfortunately, some pores may still have “solid ghosts” (see Figure 3 and the magnified region).

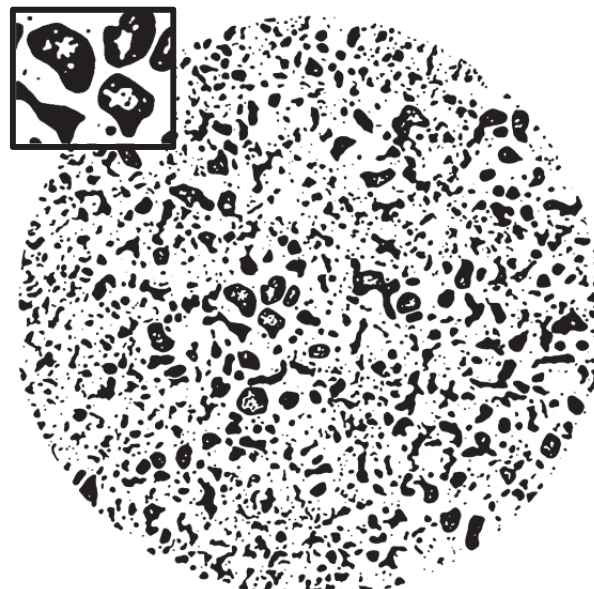


Figure 3: Same image as Fig.2 after application of the median filter and binarisation using the selected threshold. Artefacts within large pores may appear and should be removed.

The so-called “fill-hole” operator is used to remove these artefacts. It eliminates the solid voxels which are not connected with the big solid matrix and replaces them by the pore phase. In a refinement step, the remaining minor noisy structures are removed via a morphological opening operation with a spherical structuring element of 3 voxel radius. An example of the final images is shown in Figure 4: there are no more “solid” voxels trapped in the pore phase and the pore boundaries are preserved even after the application of the different filters described above (see figure 4b).

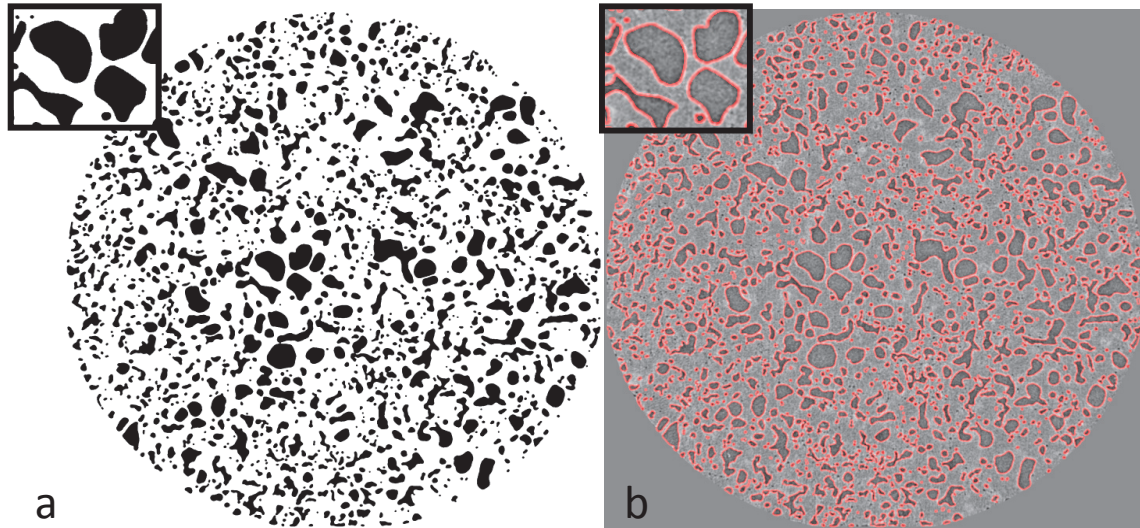


Figure 4: Results of the segmentation process: a) final binary image, b) the contours of the segmented structure were colored in red and superimposed on the original image.

The post-processing procedure and the set of parameters used were the same for all the samples. The error in determining the phase interfaces, if any, is thus human-independent.

Once the data arrays were separated in phases the quantitative analysis of each sample was made using the open source software iMorph [13,14]. The different algorithms applied are described in the next sections whilst the results are presented in the “Results and discussion” section.

Surface determination

To simplify the computations, a region of interest (ROI) was selected in each sample as the biggest parallelepiped inscribed in the sample volume.

The surface was evaluated using the gold standard “marching cube” algorithm [15], and the specific surface was then straightforwardly calculated. The 3D surface rendition of one sample is shown in Fig. 5.

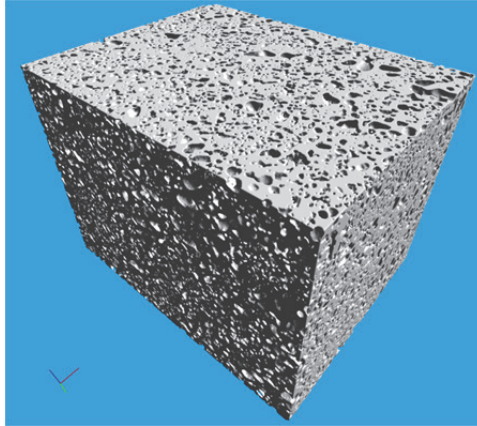


Figure 5: 3D surface rendering of the sample annealed for 10 hours at 1000°C. The region of interest displayed in the figure is a cube of 4.5mm width.

Porosity Analysis

The porosity analysis consists in subdividing the pores in the ROI into three distinct classes: closed porosity, open porosity, and percolation paths. The closed porosity class includes all pores that are completely embedded in the ROI. Conversely, the open porosity is comprised of pores which are connected with the outer surface of the ROI. Finally, the class of percolation clusters, which have been previously investigated for another beryllium batch in form of pebbles [16], includes only the pores linking two opposite faces of the ROI.

A connectivity analysis [17] was performed on the whole 3D matrix in order to discriminate these three porosity classes. Once the necessary labels are obtained, a simple numerical pass over the ROI faces allows identifying the porosity classes.

The 2D slice in Fig. 6 shows the results of the porosity analysis. In this image, a different color is used for each pore while the solid phase is tagged in white. The percolation cluster (salmon pink) amounts up to 90% of the total porosity.

Figure 6b is the 3D surface rendition of the pore phase using the same color palette.

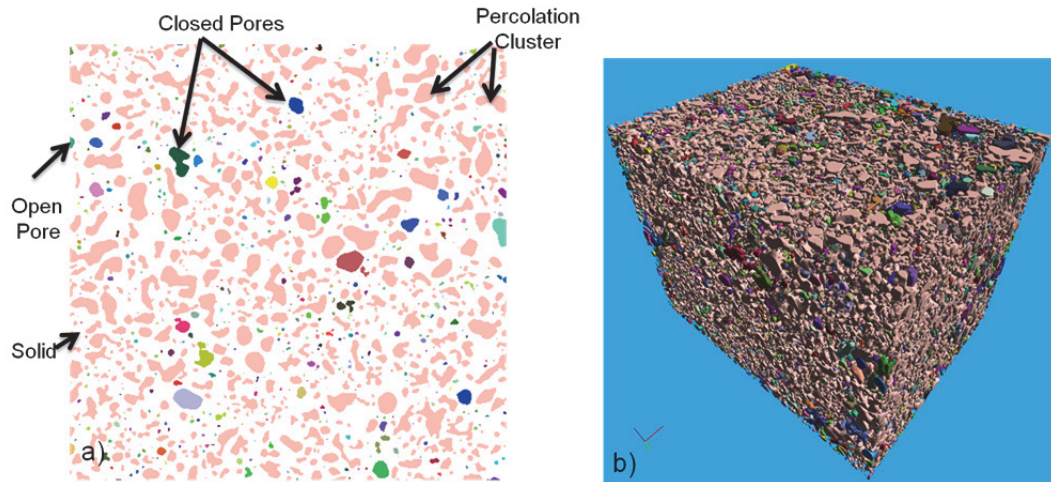


Figure 6: Porosity analysis on the example of the specimen p1 (0.5h@850°C): a) 2D slice where each color stands for a unique pore. In salmon pink: main percolation cluster; b) 3D rendition of the pore phase (same color palette as in a)).

Pore size estimation

As the vast majority of pore phase is made up of a unique large percolation pore, the pore diameter is estimated using the granulometry operator [18]. This operator mimics the mercury-based porosimetry. The standard algorithm consists in estimating the size of each pore by the morphological opening or closing of the pores' space. A morphological opening/closing operation by one structuring element size yields the estimation of the amount of structures of this size. By doing this operation with increasing sizes of structuring elements, one can obtain the pore size estimation for the whole material. In our case the sizes of the images (2048^3 voxels), even reduced to those of the ROI ($1400 \times 1400 \times 2048$ slices), do not allow using effectively this algorithm, as the calculation would take too long. Instead, we developed a time optimized algorithm (implemented in iMorph) which allows handling such volumes within a reasonable time (less than 2 hours). This algorithm uses the distance map to calculate a first approximation of the biggest included spheres and then fills the void spaces by smaller spheres.

The reader can find a detailed explanation of the algorithm in [22]. In short, the algorithm fills up the pores' space by spheres; by means of a first distance map calculation, the radius of the maximum sphere inscribed in each pore is trivially estimated. This operation is done deploying a data structure that ensures a correct estimation by first calculating the biggest and then the smallest sphere sizes. An example of the granulometry operator results is shown in Figure 7.

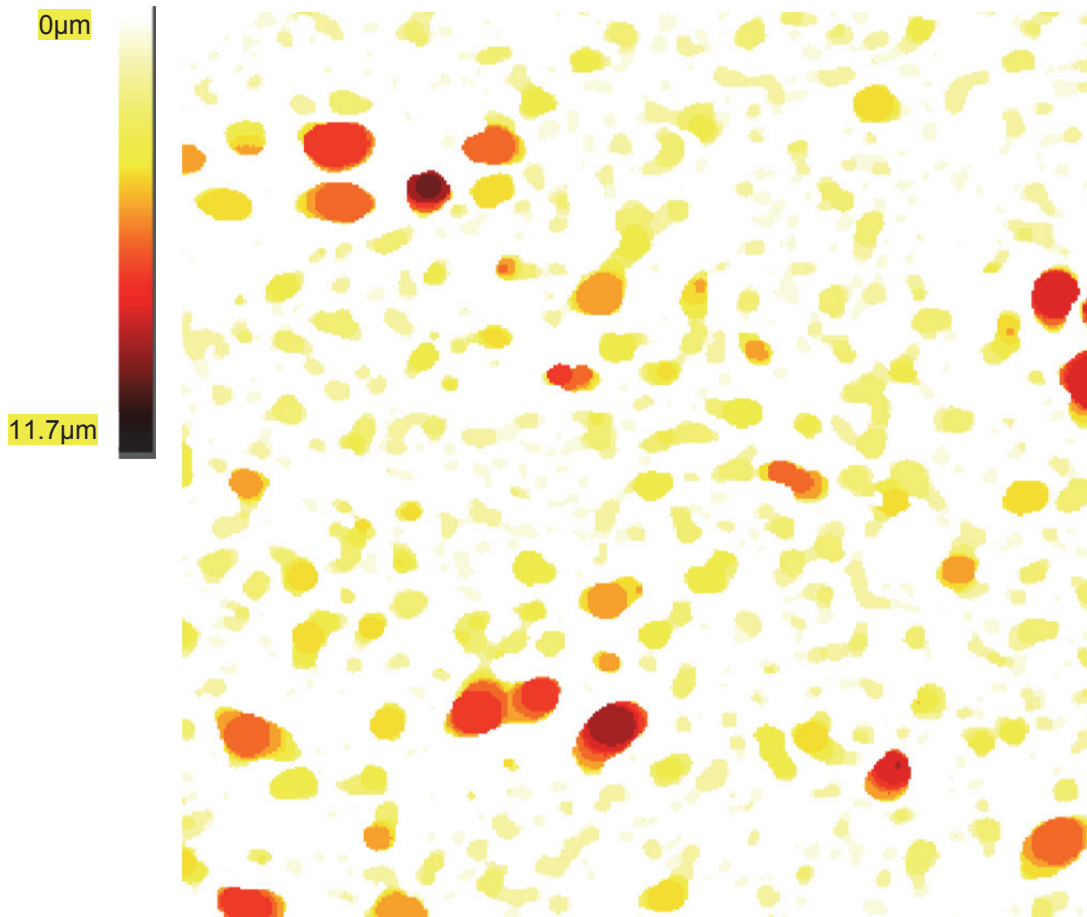


Figure 7: 2D map of the diameters as a result of the granulometry operator. Each color stands for a pore size.

Tortuosity

The tortuosity T was defined by Carman [23] as the squared ratio of the geodesic length L_{min} between two points, p_1 and p_2 , of the same phase and the Euclidean distance between them:

$$T(p_1, p_2) = \frac{L_{min}(p_1, p_2)^2}{\|p_1 - p_2\|}$$

The geodesic length is calculated as the length of the shortest path connecting two points of the same phase without leaving this phase, while the Euclidean distance is measured along a straight line connecting the points.

The geodesic length can be calculated using the fast marching method [19], whereas the propagation is possible only in the pore phase. Unfortunately, due to the enormous number of possibilities, it is impossible to perform this computation for each pair of points of the pore phase in the image. This is why we defined a plane-to-plane tortuosity. In this case the propagation starts from one face of the ROI and continues in the direction of the opposite face. As we impose a uniform speed modulus (=1), the arrival time of the front is equal to the geodesic length between the point of arrival and the closest geodesic point on the starting plane.

Figure 8 shows the map of geodesic lengths: each color stands for a range of lengths while the borders of the colored regions show the local shape of the propagation front.



Figure 8: Geodesic length map obtained with a second order fast marching method.

From this geodesic length map we extract the mean tortuosity and its standard deviation only on the opposite plane. The propagation calculation was done three times, one for each of the opposite face pairs of the ROI parallelepiped.

RESULTS AND DISCUSSION

Phenomenon of out-of-pile swelling

Change of sample dimensions under irradiation (swelling) is commonly observed in materials under irradiation in a rather narrow range of temperatures ($0.3-0.6 T_{\text{melt}}$, where T_{melt} is the melting temperature) which depends on the investigated material. Although swelling is usually associated with formation of voids (or often helium filled bubbles), the origin of the volume increase is due to the volume brought in by the interstitials captured on various point defect sinks (dislocations, irradiation loops and grain boundaries). Vacancies and interstitials produced by irradiation in equal amounts should recombine with each other, but in reality more vacancies are left in the matrix, while interstitials are more effectively captured at sinks than vacancies. The difference in interaction of point defects with sinks (called bias or preference) can have various origins: (i) preference in elastic interaction of interstitials with dislocations in comparison with vacancies; (ii) different clustering behavior of vacancies and interstitials in the core of atomic displacement cascades; (iii) 1D diffusion of interstitials versus 3D diffusion of vacancies, etc.. This slight unbalance between vacancies and interstitials capturing in sinks results in a net volume increase.

At a first glance, it is difficult to explain out-of-pile swelling of materials upon annealing. Interstitials generated during irradiation annihilate on sinks shortly after the end of irradiation and are no longer available during annealing. However, thermal vacancies generated at grain boundaries can provide the necessary driving force for swelling. Under neutron irradiation, helium atoms generated by nuclear transmutations preserve small helium-filled bubbles from dissolution, thus allowing them to reach the critical size after which they can grow by accumulation of vacancies.

DFT calculations [24] and resistivity recovery experiments [25] predict rather low vacancy formation energy (~ 0.8 eV) in beryllium. Therefore, substantial swelling observed during annealing in beryllium can be probably explained by emission of thermal vacancies and pre-existence of helium bubble nucleation centers in the form of helium-vacancy clusters due to high helium concentration produced during irradiation.

Porosity Analysis

Quantitative information about the pore phase upon annealing can be obtained by using the tomographic processing methods described in the previous sections.

Already after 1 hour of annealing at 850°C , volumetric swelling of beryllium is found to reach 15-20%, depending on the spatial resolution used. From the methodological point of view it is interesting to assess how the selected spatial resolution (voxel size) affects the quantitative results.

Generally, as the spatial resolution improves, the pores are better localized, so that the pores detected as overlapping at low resolution are not touching each other anymore at higher resolution. Hence, the volume of percolation pores (overlapped or connected) decreases, while the number of closed and open pores increases (see Figure 9).

The swelling values obtained for the two lower voxel sizes (0.28 and $0.175 \mu\text{m}$) are expected to be similar and reveal swelling rates close to the values measured by density or dimension

changes. As a consequence, the difference of about 2% (s. Figure 9) should be possibly attributed to the statistical scattering of the results for various samples.

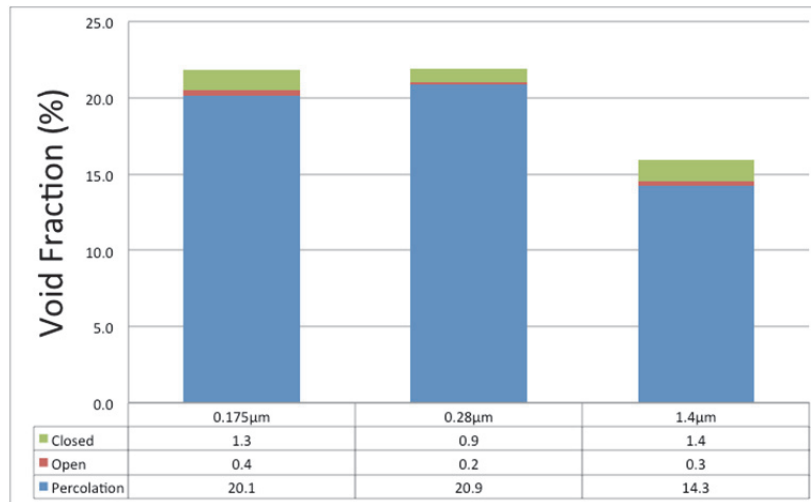


Figure 9: Effect of spatial resolution on the found swelling percentages (sample annealed for 1h at 850°C). Resolutions are expressed as the pixel size.

Figure 10 shows the effect of annealing time on the evolution of the porosity network. The as-irradiated sample shows a very low amount of closed porosity: this residual porosity can be attributed to the pores formed during material fabrication. Similar density of pores was also observed in the non-irradiated material. Even half an hour of annealing at 850°C is sufficient for percolation clusters to form, contributing by more than 90% to the total porosity (see Figure 6b).

The volume fraction of the percolation pores decreases as the annealing time increases, whereas the fraction of the closed pores grows. This behavior can be tentatively explained by the same argument as for measurements with varying spatial resolution. The pore size increases via annealing, thus large pores can be better estimated with the same resolution. As a consequence, the fraction of percolation porosity decreases, whereas that of closed and open porosity increases at the expense of percolation. The changes in the fractions of percolation and closed pores (~2-3%) are comparable with the anticipated scattering of the results between various samples.

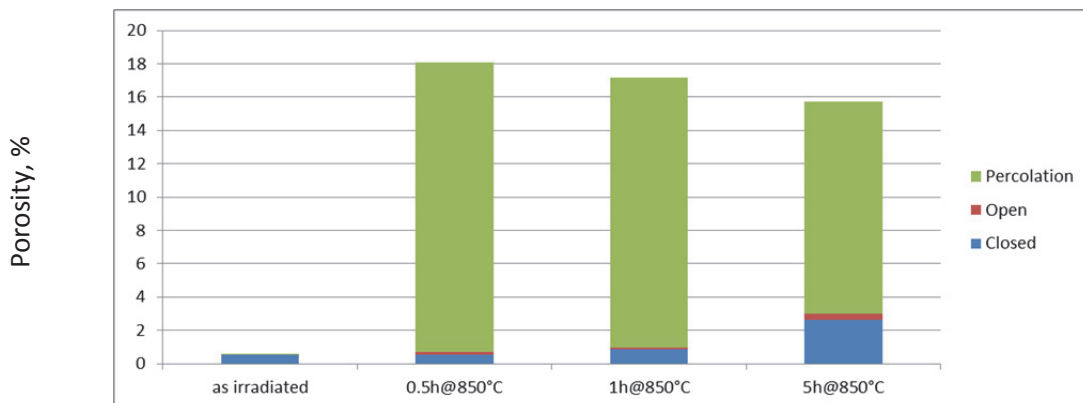


Figure 10: Effect of annealing time on porosity evolution at T=850°C.

Pore size estimation

Pore size distribution obtained by the granulometry operator described above is presented in Figure 11. As anticipated, the increase of annealing temperature results in a notable increase of the average pore radius.

The pore size distributions of the samples annealed at 850 °C and those annealed at 1000 °C are very different. Actually, there is barely any pore radius larger than 3 micron in the samples annealed at 850 °C, while this size represents the majority of pores in the samples annealed at 1000 °C. A small amount of measured pores have a radius of up to about 1.4 μm explaining the difference noticeable in Figure 9, comparing the different experimental resolutions.

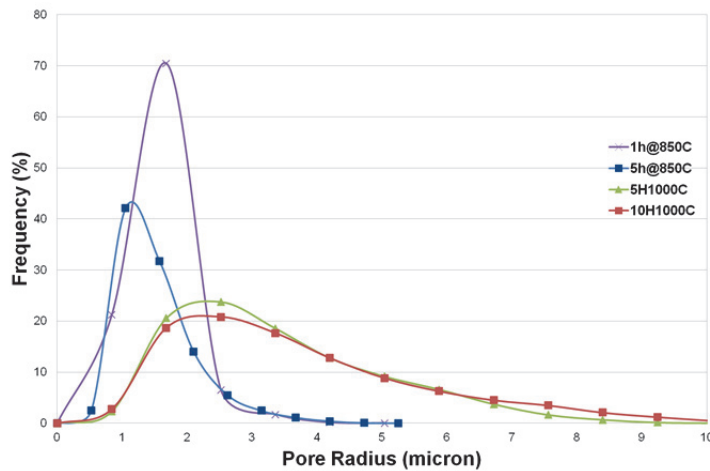


Figure 11 Effect of temperature and annealing time on the pore size distribution.

A similar size distribution obtained subdividing the pore population in pore classes shows that closed porosity is dominated rather by the presence of smaller pores, significantly more than in the case of pore cavities located along the percolated paths. However, large closed pores are also present.

Tortuosity

Table 2 reports the tortuosity values for the different samples.

Table 2 : ROI plane-to-plane tortuosity values for two directions

	Tortuosity (reconstruction plane)	Standard Deviation	Tortuosity (gravity direction)	Standard Deviation
1h@850C	1.51	0.11	1.61	0.1
5h@850C	1.24	0.05	1.33	0.03
5h@1000C	1.44	0.1	1.56	0.08
10h@1000C	1.49	0.1	1.59	0.07

A small anisotropy is observable between the reconstruction plane tortuosity and the tortuosity orthogonal to this plane. The difference is significant: about one standard deviation. No appreciable trend can be stated as a function of the temperature and/or the annealing time.

A more detailed analysis of the tortuosity, as in [26], may yield a better anisotropy quantification of the different samples. However, no preferential texture along rotation axis should be expected in the investigated samples. Therefore, any observed anisotropy should be ascribed to the geometry of the data acquisition method.

Visual inspection of obtained 3D images

X-ray tomography studies provide a unique opportunity to investigate the 3D morphology of the porosity of beryllium developing during neutron irradiation of this material. An example of a large pore found in an as-irradiated sample is shown in Figure 12. Only thorough visual inspection of the 3D object allowed concluding that this cluster is, in fact, a shell of pores around two grains. Bearing in mind that the raw material was fabricated by a powder metallurgy method, one can safely assume that the grains were initial powder particles which were occasionally not well sintered with the rest of the matrix.

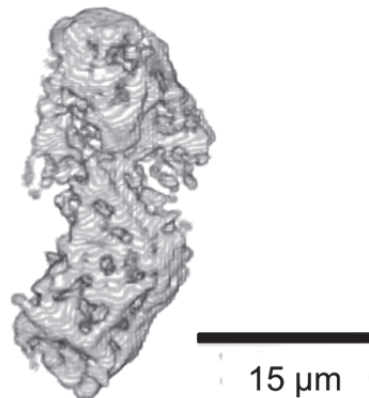


Figure 12: Example of the largest pore found in an as-irradiated sample. The pore phase is shown in grey.

We also inspected the porosity evolution in the samples after annealing. Inasmuch as percolation porosity constitutes more than 90% of the total porosity, it is very difficult to determine accurately the topology of the percolation network. It was often observed in our previous optical microscopy studies [27] that larger pores are formed at grain boundaries and triple grain junctions. Such pores frequently form chains along grain boundaries which can overlap and form a channel. An example of such channels is shown in Figure 13, which presents the cross section of a percolation cluster (13.73% of the ROI volume $0.26 \times 0.26 \times 0.21 \text{ mm}^3$) formed after 1 hour annealing at 850°C . The pore phase is shown in white. The pore-free areas are individual grains. The major part of pores is concentrated along the grain boundaries. Chains of pores are clearly visible at the lower left corner of the cross-section. We suppose that these chains of larger pores decorate grain boundary triple junctions. Formation of percolation channels is important for the release of tritium accumulated inside helium-filled bubbles. Once formed, they result in gas release burst. These channels are most likely to be formed by the coalescence of preferentially growing helium bubbles located at the grain boundaries or triple junctions.

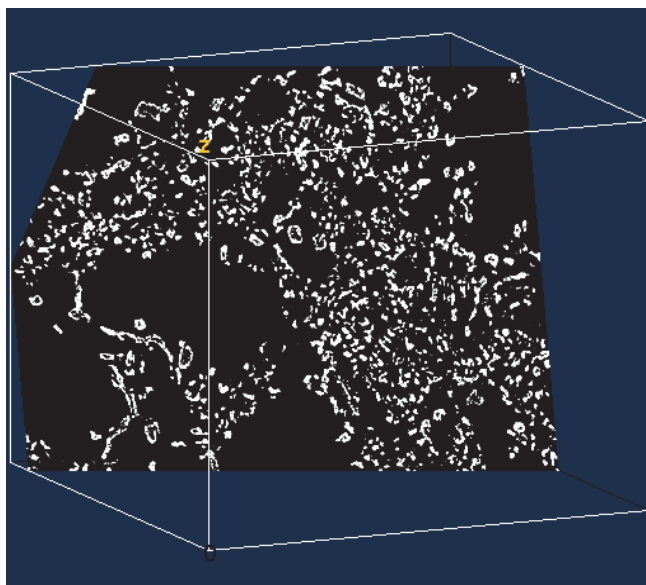


Figure 13: Channels of pores presumably along grain boundaries and grain boundary triple junctions in the sample annealed at 850°C for 1 hour.

CONCLUSION

Annealing of beryllium samples irradiated at low temperature provides an interesting method to mimic the effects of high temperature irradiation of beryllium and to study the kinetics of the related porosity build-up. However, shorter annealing times and/or lower temperatures need to be used to understand the initial stages of this process. Investigation of the effect of out-of-pile annealing on beryllium irradiated at low temperatures can be also of interest for nuclear applications such as conventional nuclear reactors and spallation sources where beryllium is used (or planned to be used) as a reflector and neutron multiplication material. In the case of accidental loss of coolant the temperature of a beryllium block can be increased above 600 °C where substantial swelling occurs. Therefore, our study provides results on the porosity evolution which could occur as a consequence of such an accident.

Beryllium produced by the VHP method always contains some amount of fabrication porosity. Without annealing, irradiated samples present low porosity, which is similar to that of unirradiated samples. Therefore, we conclude that both unirradiated samples and the samples before annealing contain mainly porosity related to the fabrication process. Although some big pores (presumably formed during material fabrication) are present, no percolation clusters were observed. Oxidation along grain boundaries can be guessed, which is in accordance with oxidation of the source powder. It is known that powder beryllium materials with a substantial amount of beryllium oxide are prone to form cracks along grain boundaries which, together with helium bubble channels, result in their severe embrittlement under neutron irradiation.

Porosity kinetics in an annealing process appears to be very fast. Even after a very short annealing time at very low temperatures, percolation clusters emerge and constitute the major part of the observed porosity. Careful visual inspection of big percolation clusters suggests that interconnected channels are readily formed along grain boundaries and especially along the edges where three or more grains come into mutual contact (triple junctions).

X-ray tomography provides a unique opportunity to quantitatively characterize porous materials. This technique and the advanced analysis methods presented in this work can be

used for many applications including, e.g., nanopore sieves and porous hydrogen storage materials. These methods can be used for the simulation of liquid and gas flow through porous media, which are important for the above mentioned applications.

ACKNOWLEDGMENTS

The authors would like to thank Patrick Colomp (ESRF Safety Group), Elodie Boller and Jean-Paul Valade (ESRF ID19 beamline) for their help in designing and manufacturing the sample containers. ESRF granted beamtime for this study via proposal no. MA-760. T. W. acknowledges support from the French research networks (RTRA) “Digiteo” (grant 2009-79D) and “Triangle de la Physique” (grant 2009-034T) and from the Agence Nationale de la Recherche (EQUIPEX project “NanoimagesX”, grant ANR-11-EQPX-0031).

REFERENCES

- [1] M. Klimenkov, V. Chakin, A. Moeslang, R. Rolli, *J NUCL MATER* 443 (2013) 409–416.
- [2] A. Leenaers, G. Verpoucke, A. Pellettieri, L. Sannen, S. van den Berghe, *J NUCL MATER* 372 (2008) 256–262.
- [3] E. Rabaglino, J. Baruchel, E. Boller, A. Elmoutaouakkil, C. Ferrero, C. Ronchi, T. Wiss, *NUCL INSTRUM METH B* 200 (2003) 352–357.
- [4] A. Möslang, R.A. Pieritz, E. Boller, C. Ferrero, *J NUCL MATER* 386–388 (2009) 1052–1055.
- [5] H. Suhonen, F. Xu, L. Helfen, C. Ferrero, P. Vladimirov, P. Cloetens, *Int J Mat Res* 103 (2012) 179–183.
- [6] S. P. Ablen, R. D. Field, M. Mataya, in: 2nd IEA International Workshop on Beryllium Technology for Fusion, Jackson Lake Lodge, Wyoming, USA, September 6-8, 1995.
- [7] T. Weitkamp, P. Tafforeau, E. Boller, P. Cloetens, J.-P. Valade, P. Bernard, F. Peyrin, W. Ludwig, L. Helfen, J. Baruchel, *AIP Conf. Proc.* 1221 (2010) 33–38.
- [8] J.-C. Labiche, O. Mathon, S. Pascarelli, M.A. Newton, G.G. Ferre, C. Curfs, G. Vaughan, A. Homs, D.F. Carreiras, *Rev. Sci. Instrum.* 78 (2007) 91301.
- [9] R. Pieritz, J. Spino, P. Vladimirov, C. Ferrero, *Int J Mat Res* 103 (2012) 250–257.
- [10] D. Paganin, S.C. Mayo, T.E. Gureyev, P.R. Miller, S.W. Wilkins, *J Microsc* 206 (2002) 33–40.
- [11] T. Weitkamp, D. Haas, D. Wegrzynek, A. Rack, *J Synchrotron Rad* 18 (2011) 617–629.
- [12] A. Mirone, E. Gouillart, E. Brun, P. Tafforeau, and J. Kieffer, *NUCLEAR INSTRUMENTS & METHODS IN PHYSICS RESEARCH SECTION B*, Volume: 324, Pages: 41-48 (2014)
- [13] E. Brun, iMorph: IDDN FR 0001.270002.000.S.P.2009.000.21000, CNRS, 2009.
- [14] E. Brun, J. Vicente, F. Topin, R. Occelli, *Cellular Metals for Structural and Functional Applications* (2008).
- [15] W.E. Lorensen, H.E. Cline, in: M.C. Stone (Ed.), the 14th annual conference, pp. 163–169.
- [16] J. Ohser, C. Ferrero, O. Wirjadi, A. Kuznetsova, J. Düll, A. Rack, *Int J Mat Res* 103 (2012) 184.
- [17] T.H. Cormen, C.E. Leiserson, R.L. Rivest, *Introduction to algorithms*, MIT press, 1990.
- [18] P. Soille, *Morphological image analysis: Principles and applications*, 2nd ed., Springer, Berlin, New York, 2003.

- [19] J.A. Sethian, Proceedings of the National Academy of Sciences 93 (1996) 1591–1595.
- [20] E.W. Dijkstra, Numer. Math. 1 (1959) 269–271.
- [21] S. Beucher, Image and Vision Computing 25 (2007) 405–415.
- [22] E. Brun, M. Camille, De l'imagerie 3D des structures à l'étude des mécanismes de transport en milieux cellulaires, 2009.
- [23] P.C. Carman, Transactions - Institution of Chemical Engineers 15 (1937) 150–166.
- [24] M.G. Ganchenkova, P.V. Vladimirov, V.A. Borodin, Vacancies, interstitials and gas atoms in beryllium, J Nucl Mater 386-388 (2009) 79-81.
- [25] J. C. Nicoud, J. Delaplace, J. Hillairet, D. Schumacher, Etude des défauts créés dans beryllium par irradiation a basse temperature, J Nucl Mater 27 (1968) 147-165.
- [26] E. Brun, J. Vicente, F. Topin, R. Occelli, Proc. CMDS11 (2008) 121-127-121-127.
- [27] V. Chakin, R. Rolli, A. Moeslang, P. Kurinskiy, P. Vladimirov, C. Ferrero, R. Pieritz, W. van Renterghem, Phys Scr T145 (2011) 14012.

Development of thermo-mechanical computational model for circular beryllium reflector

Sergey V. Evropin, Georgy M. Kalinin, Yuriy I. Trifonov
(JSC "NIKIET" Moscow)

Leonid S. Gitarsky, Ilya A. Gvozdikov, Victor S. Sizenev
(JSC "KOMPOZIT" Moscow region)

ABSTRACT

Utilization of beryllium as a reflector for different purpose nuclear power installations allows to reduce an amount of fuel in a reactor core and thus to decrease essentially its dimensions. This may have a decisive significance especially in the case of the mass-size limitations. From the viewpoint of the serviceability, such designs can be considered as an entire circular beryllium reflector subjected to combined thermal and mechanical loadings as well as neutron irradiation.

The computational model developed in frames of this work describes a stress-strain state (SSS) arising under influence of permanent mechanical and thermal fields at an initial steady-state stage of the beryllium reflector design operation (without taking into account irradiation effects). The model can be employed for all main texture types of beryllium half finished products produced by industrial enterprises: isotropy structure (powder HIP-technology), texture of extruded Be (extrusion of HP or powder billet) and texture of forged Be (forging of HP or powder billet) as well as Be made by HP. Used while developing the model were physical and mechanical properties of the Be reactor-grade half finished products.

The work contains examples of SSS computation and functional dependencies of its variation for the different types of Be material being utilized for the circular reflector design at different combinations of temperature gradients and mechanical loadings.

INTRODUCTION

Today beryllium is widely used with high efficiency as a material of a reflector for various types of nuclear reactors especially in the case of mass-size limitations. Depending on a purpose, working conditions and a design of the reflector its operating parameters can alter in a wide range of temperatures and fast neutron fluxes attaining the values higher than 400°C and 10^{21} n/cm² correspondingly.

At mass-size restrictions imposed upon a nuclear reactor the reflector of such an installation represents as a rule a compact circular design exposed to thermal and mechanical loadings as well as neutron irradiation. While estimating its serviceability during a whole period of operation from a viewpoint of a design integrity it is obvious that the first two factors determine workability at an initial period and together with irradiation – during the whole period of operation.

The present paper is dedicated to the development of a computational model describing a stress-strain state (SSS) of a beryllium circular reflector subjected to thermal and mechanical loadings conformably to the main types of beryllium half finished products being manufactured at present by up-to-date industrial enterprises. Thus this model is intended to estimate serviceability at the beginning of beryllium reflector operation as a part of nuclear

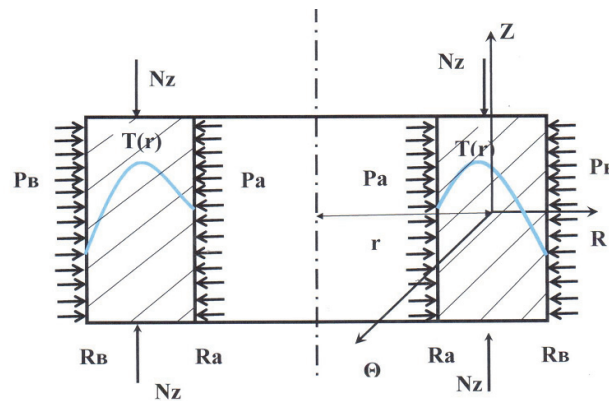
reactor. To comprehend the main types of beryllium half finished products the model has been extended to transversal-isotropic medium which involves all principal texture types for beryllium products:

- extruded beryllium (axial texture [1010]; for instance TVR grade);
- isotropy beryllium (for instance TIP grade);
- beryllium after uniaxial forging (axial texture [0002]; for instance TShPR grade).

To realize calculations with the help of the model developed the experimental results on temperature expansion factors (TEF) and mechanical properties for the corresponding beryllium grades at various temperatures in the range 20 – 650°C have been used.

1. DESCRIPTION OF COMPUTATIONAL MODEL

Computational model of the beryllium reflector represents an entire circular design (figure 1) being under an impact of an axially-symmetric temperature field $T(r)$, external (P_b) and internal (P_a) radial stresses (pressure) as well as an axial mechanical loading (N_z) at a butt-end of the reflector.



- N_z - axial loading at a butt-end of the thick-walled shell;
 P_b and P_a – pressure at outer and inner cylindrical surfaces;
 $T(r)$ – axi-symmetric temperature function ;
 R, θ, Z – designation of the axes (cylindrical coordinates);

Figure 1. Computational design of the circular beryllium reflector

The development of the model was directed at an extension of “classical” models describing the SSS of isotropic, thermally and mechanically loaded, thick-walled shells to anisotropic ones as applied to the main texture types of beryllium semi-products namely extruded rods (TVR grade) and forged discs (TShPR grade) as a materials for beryllium reflector fabrication. Besides, the experimentally measured temperature dependencies of the TEF for TVR and TShPR grades have been utilized for computation with this model.

From the mathematical viewpoint it means a substitution of TEF tensor components for the isotropic material (figure 2b) in the equations of Hook’s Law with that for anisotropic ones (figure 2a – TVR grade and figure 2c – TShPR grade). In an addition it was taken into account that all tensor components represented temperature dependent functions [$\alpha_{ij} = \alpha_{ij}(t)$]. Conventional signs in the figure 2 are the following: α - TEF for isotropic structure; $\alpha_{a/c}$ and

α_a – accordingly radial and axial TEF for TVR grade; α_a and α_c - accordingly radial and axial TEF for TShPR grade.

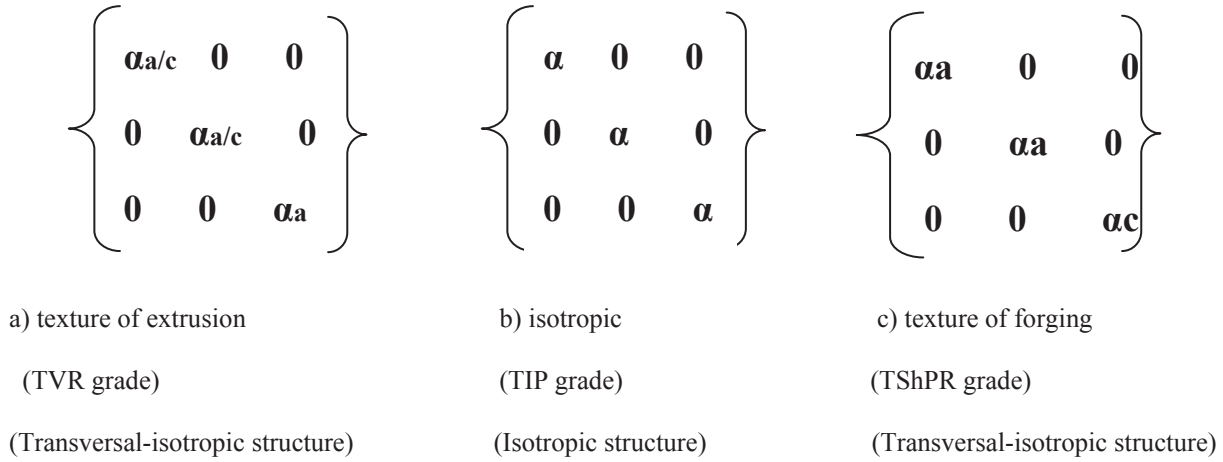


Figure 2. The view of the tensors of temperature expansion factor for main types of beryllium semi-products

2. SOLUTION OF THERMAL-ELASTIC PROBLEM FOR THE THICK-WALLED CYLINDRICAL SHELL WITH TRANSVERSAL-ISOTROPIC STRUCTURE

As a whole, while solving the thermal-elastic task for the thick-walled cylindrical shell with transversal-isotropic structure the sequence of mathematical operations corresponding to that for the “classical” elastic problem [1, 2, 3] has been applied (are not set forth in frames of present paper). As a result the set of mathematical equations has been deduced intended for calculation of principal stresses (σ_{rr} ; $\sigma_{\theta\theta}$; σ_{zz}) through the volume of the shell in cylindrical coordinates:

$$\sigma_{rr} = \frac{E \times \mu}{(1+\mu)(1-\mu)} \left[2\alpha_{rr} + \alpha_{zz} + \frac{(1-2\mu)}{\mu} \alpha_{rr} \right] \frac{1}{r^2} \left[\frac{r^2 - R_a^2}{R_b^2 - R_a^2} \times \int_{R_a}^{R_b} rT(r)dr - \int_{R_a}^r rT(r)dr \right] + \frac{P_a R_a^2 - P_b R_b^2}{(R_b^2 - R_a^2)} - \frac{(P_a - P_b) R_a^2 R_b^2}{(R_b^2 - R_a^2)} \frac{1}{r^2},$$

$$\sigma_{\theta\theta} = \frac{E \times \mu}{(1+\mu)(1-\mu)} \left[2\alpha_{rr} + \alpha_{zz} + \frac{(1-2\mu)}{\mu} \alpha_{rr} \right] \frac{1}{r^2} \left[\frac{r^2 + R_a^2}{R_b^2 - R_a^2} \int_{R_a}^{R_b} rT(r)dr + \int_{R_a}^r rT(r)dr \right] - T(r)r^2 + \frac{P_a R_a^2 - P_b R_b^2}{(R_b^2 - R_a^2)} + \frac{(P_a - P_b) R_a^2 R_b^2}{(R_b^2 - R_a^2)} \frac{1}{r^2},$$

$$\sigma_{zz} = \frac{E}{(1+\mu)(1-\mu)} \left[\alpha_{zz} + \mu \alpha_{rr} \right] \frac{1}{r^2} \left[\frac{2r^2}{R_b^2 - R_a^2} \int_{R_a}^{R_b} rT(r)dr - T(r)r^2 \right] + \frac{N_z}{\pi(R_b^2 - R_a^2)}.$$

where: E – modulus of elasticity for Be; μ - Poisson’s ratio for Be; R_a , R_b and r – internal, external and variable radii correspondingly; P_a , P_b – internal and external pressures correspondingly; N_z – axial loading; α_{rr} – radial components of TEF tensor ($\alpha_{rr} = \alpha_{a/c}$ and $\alpha_{rr} = \alpha_a$ for TVR and TShPR grades correspondingly); α_{zz} – axial component of TEF tensor ($\alpha_{zz} = \alpha_a$ and $\alpha_{zz} = \alpha_c$ for TVR and TShPR grades correspondingly).

3. ANALYSIS OF A STRESS-STRAIN STATE FOR THE CIRCULAR BERYLLIUM REFLECTOR

The beryllium reflector being located opposite to the reactor core is significantly affected by operating parameters of the core that results in:

- arising of temperature gradients in the material of a reflector due to heat transfer from a core and heat generation because of interaction between substance and neutron and γ -radiation as well as possible nuclear reactions inherent in the beryllium under irradiation [4];
- arising of mechanical loadings due to possible contact interaction with a core casing and fasteners of reflector as a part of nuclear installation.

Given below is an analysis of the individual parameters influence on SSS of beryllium reflector. An example of computation has been performed for the circular shell with the following parameters:

- 1) Geometrical
 - Ra – internal radius – 200 mm;
 - Rb – external radius - 400 mm;
 - L – height of cylinder - 1000 mm.
- 2) Temperature:
 - Ta – 600°C;
 - Temperature dependence – linear and parabolic;
 - Temperature gradient - 10 degrees.

3.1 Influence of temperature field

a) Linear temperature function

Internal stresses distribution arising in thick-walled cylindrical shells made of TVR and TShPR beryllium grades at axial-symmetric linear (for cylindrical coordinates) temperature field ($T_a=600^\circ\text{C}$) is shown in figures 3 and 4 correspondingly. With linear temperature function increasing from center to periphery of cylindrical shell (figure 3), the inner regions of shell are subjected to all-round tension at significantly lower level of radial stresses (σ_{rr}) compared to axial (σ_{zz}) and circumferential ($\sigma_{\theta\theta}$) ones while outer regions are compressed in axial and circumferential directions at low level of radial tensile stresses. Eliminating radial stresses from consideration because of their low magnitude the maximal absolute values of axial and circumferential stresses are observed at outer and inner surfaces of a shell and in terms of one degree temperature gradient they amount $\approx 3,0$ MPa/degree and $2,4$ MPa/degree for $\sigma_{\theta\theta}$ and σ_{zz} accordingly in the case of TShPR grade. For TVR grade $\sigma_{\theta\theta}$ and σ_{zz} are similar on magnitude but in a reverse ratio.

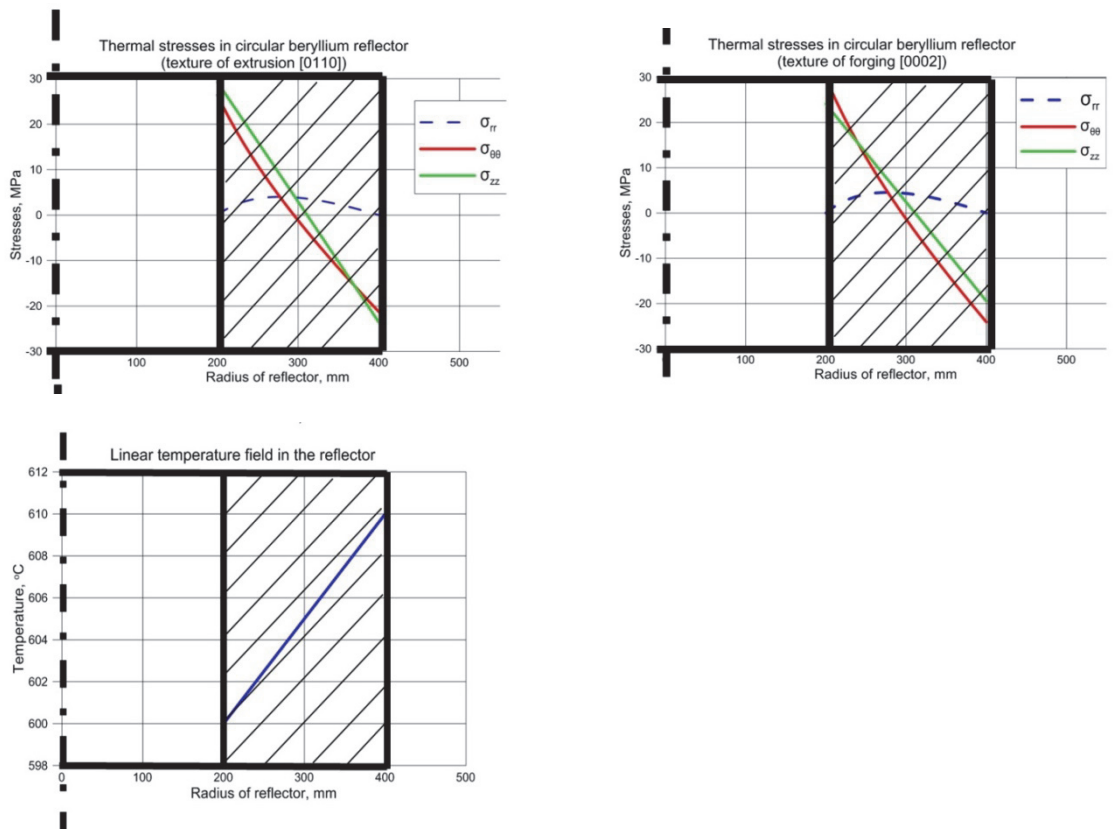


Figure 3. The stress distribution in the circular beryllium reflector with linearly growing temperature field

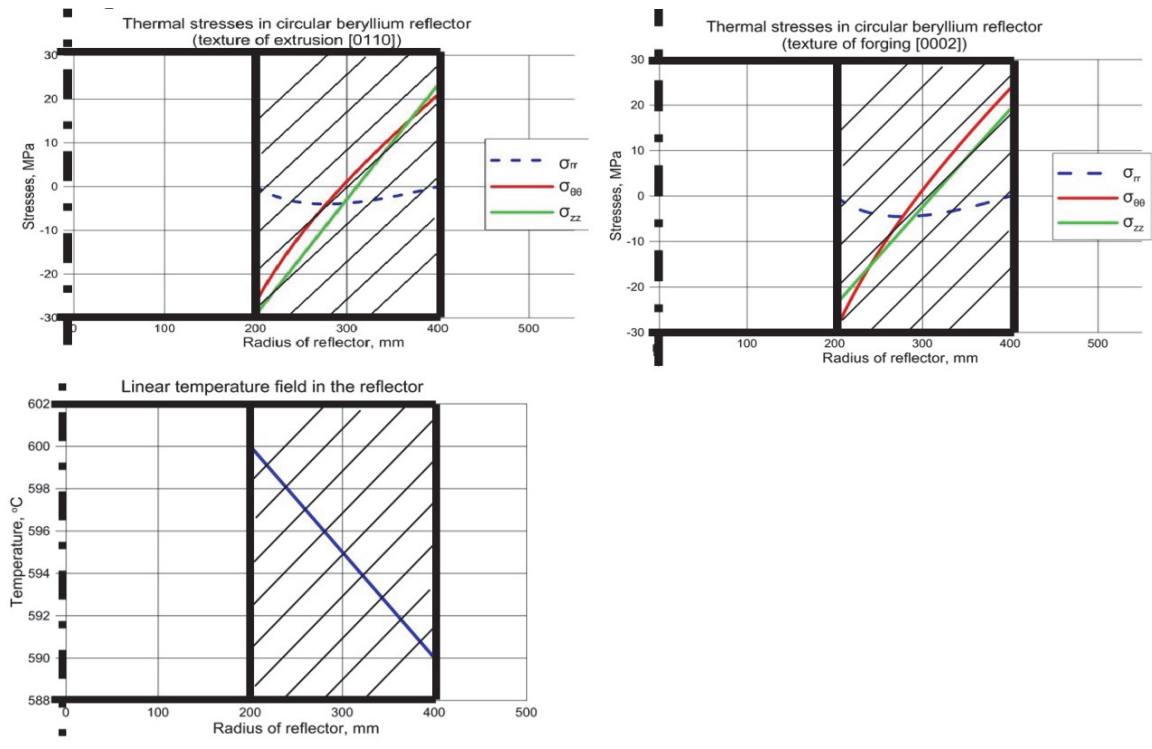


Figure 4. The stress distribution in the circular beryllium reflector with linearly falling temperature field

At decreasing temperature field from center to periphery of shell (figure 4) the situation is inverse in terms of ratio and sign of stresses.

b) Parabolic temperature function

Internal stress distributions [$\sigma_{rr}(r)$, $\sigma_{\theta\theta}(r)$ and $\sigma_{zz}(r)$] in the case of parabolic temperature function when the central area of reflector is at higher temperature (“hot heart”) are shown in figure 5 ($T_a=600^\circ\text{C}$). As is the case with linear temperature, σ_{rr} is nearly an order lower on absolute value than $\sigma_{\theta\theta}$ and σ_{zz} which reach top values directly at inner and outer surfaces of the shell: $\sigma_{\theta\theta} \approx 3,2 \text{ MPa/degree}$, $\sigma_{zz} \approx 3,5 \text{ MPa/degree}$ for TVR grade and $\sigma_{\theta\theta} \approx 3,6 \text{ MPa/degree}$, $\sigma_{zz} \approx 2,9 \text{ MPa/degree}$ for TShPR grade. Thus the ratio between $\sigma_{\theta\theta}$ and σ_{zz} changes inversely at transition from texture of extrusion (axial of texture – [1010]) to texture of forging (axial texture – [0002]).

As far as structural strength is concerned, the case of parabolic temperature field with “hot heart” reviewed above is the least favorable, due to occurrence of the maximum tensile stress on the external and internal cylindrical surfaces of the reflector.

The results of computational analysis with the model developed are given in Table 1 for the cases with tensile stresses at outer and inner cylindrical surfaces both for linear and parabolic temperature distributions.

3.2 Influence of mechanical loadings

«Classical» task describing thick-walled cylindrical shell subjected to an internal P_a and external P_b pressure is discussed in many books on «theory of elasticity and strength of materials». To treat it as a separate task with regard to beryllium circular reflector does not make sense, since the solution of this problem in terms of stresses does not depend on the elastic properties of the material and is universal for all metals in the field of elastic deformations, and his being a trivial task.

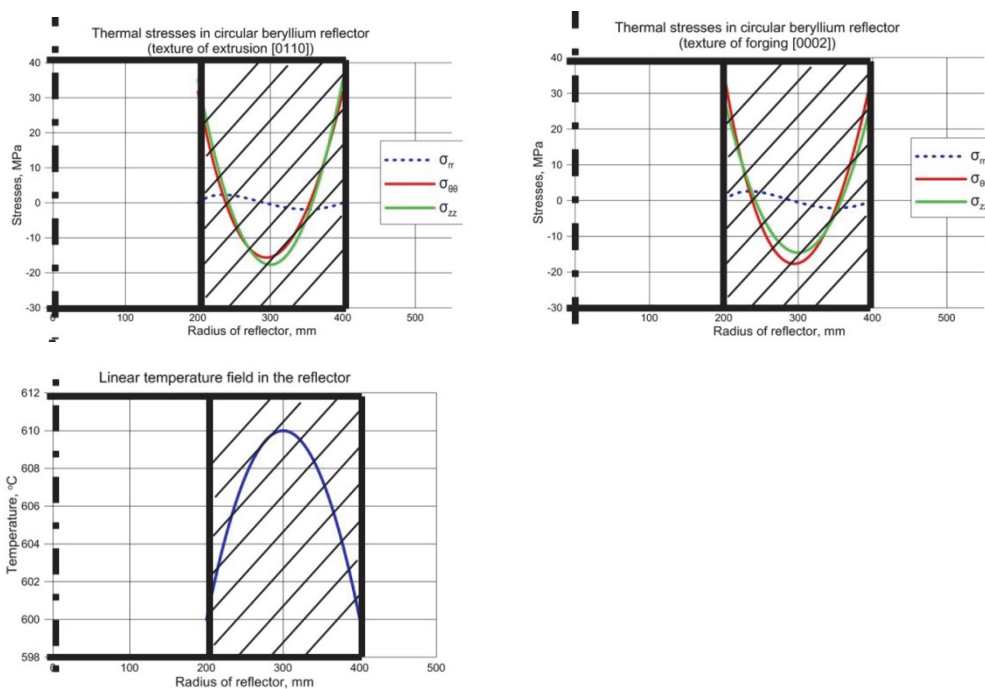


Figure 5. The stress distribution in the circular beryllium reflector with parabolic temperature field (“hot heart”)

The model includes the solution of such tasks under combined action of thermal and mechanical loads. Review of a decision of this task in relation to the ring бериллиевому reflector in the combined effect of temperature fields and mechanical loading may be interesting from the point of view to find the possibility for reducing the level of tensile thermal stresses on the surface of the reflector. So, for example, for the most adverse case of parabolic temperature function with “hot heart”, one can find the value of external radial pressure (P_b) and axial compressive loading ($-N_z$), which will reduce hazardous tensile stresses on its outer and inner surfaces (Fig. 6 and 7). Figure 6 shows diagrams of thermal stresses for accepted geometry of the reflector at the following parameters: parabolic axisymmetric temperature field (“hot heart”); the temperature on the inner surface - 600°C; the temperature gradient is 10 degrees and imposed external radial pressure - 10 MPa. As a result the circumferential tensile stresses at the external and internal surfaces are being reduced to less than 15 MPa from more than 30 MPa, corresponding to the influence of only temperature field (upper graph in figure 5). Axial compressive load applied to the front surface of the reflector of an order 1000 ton (approximately 26,5 MPa pressure), also practically compensates the action of tensile stress σ_{zz} (figure 7).

Table 1. Tensile temperature stresses at the lateral surfaces of the circular beryllium reflector made of beryllium with texture of extrusion (TVR grade) and texture of forging (TShPR grade)

T°C	Maximal circumferential tensile stresses per 1 degree temperature gradient at outer cylindrical surface $\sigma_{\theta\theta}$ (MPa/degree)				Maximal axial tensile stresses per 1 degree temperature gradient at outer cylindrical surface σ_{zz} (MPa/degree)			
	Linear (t°C) function		Parabolic (t°C) function		Linear (t°C) function		Parabolic (t°C) function	
	TVR grade	TShPR grade	TVR grade	TShPR grade	TVR grade	TShPR grade	TVR grade	TShPR grade
200	1,8	2,0	2,1	2,4	2,0	1,5	2,4	1,8
300	2,0	2,2	2,4	2,7	2,2	1,8	2,7	2,1
400	2,2	2,5	2,6	3,0	2,5	2,0	2,9	2,4
500	2,4	2,7	2,9	3,3	2,7	2,2	3,2	2,6
600	2,6	3,0	3,2	3,6	2,9	2,4	3,5	2,9
650	2,7	3,1	3,3	3,7	3,0	2,5	3,6	3,0

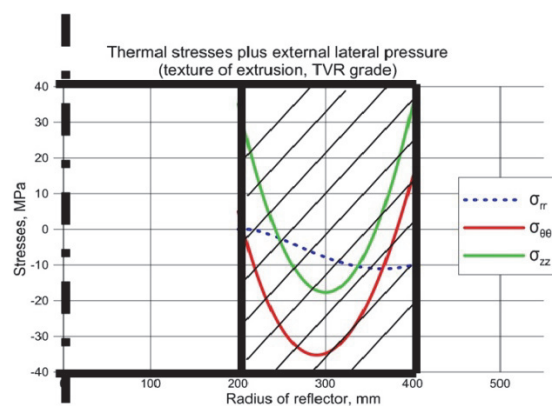


Figure 6. Stress distributions in the circular beryllium reflector at joint effect of parabolic temperature field and external radial load P_b

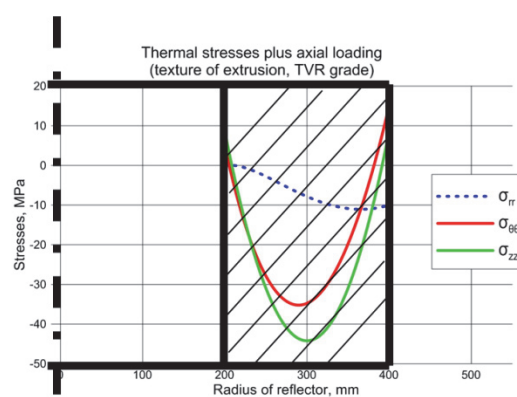


Figure 7. Stress distributions in the circular beryllium reflector at joint effect of parabolic temperature field and external axial load N_z

Developed in frames of present activity is thermo-mechanical model which is intended to calculate SSS for circular beryllium reflector at simultaneous effect of thermal and mechanical loads which arise as a rule in the circular reflector of nuclear power installation at mass-size limitations.

Utilizing the results of SSS computation with the help of this model one can perform strength estimation provided that the mechanical properties of material at operating temperatures are known. Thus the results of strength estimations for TVR grade beryllium in the operating temperature range 200÷650°C are given in Table 2. The table contains the values of maximum permissible temperature gradients exceeding of which leads to surface cracks formation.

If the reflector is additionally affected by external mechanical loadings then the results of computation can alter in one or the other side depending upon the direction and sign of forces. Once again it is necessary to underline that the relevant model permits to obtain strength estimations without taking into account an effect of neutron radiation. As a result of irradiation structural damage of Be crystal lattice, swelling and He accumulation takes place, thus leading to degradation of physics and mechanical properties [3,4]. Such changes will influence significantly upon the results of strength estimations.

Table 2. The results of strength estimation for circular beryllium reflector made of TVR grade subjected to only temperature loadings.

T (°C)	Estimation on circumferential stresses			Estimation on axial stresses		
	$\sigma_{\theta\theta}$ /degree (MPa/degree)	σ_B MPa	ΔT (°C) (Maximum permissible)	σ_{zz} /град (MPa/degree)	σ_B MPa	ΔT (°C) (Maximum permissible)
200	2,2	390	177	2,4	520	216
300	2,4	385	160	2,7	460	170
400	2,6	360	138	2,9	380	131
500	2,9	320	110	3,2	310	96
600	3,2	240	75	3,5	235	67
650	3,3	155	47	3,6	160	44

Outcomes:

1. Developed in frames of an elastic approach is the model permitting to compute SSS through the volume of the circular beryllium reflector subjected to temperature gradients and mechanical loadings. The model is applicable to the materials with transversal-isotropy structure thus covering all main types of beryllium half-finished products produced by modern industrial enterprises.

2. With the help of the model the analysis of operating conditions influence upon the view of SSS and value of stress tensor components has been performed for the circular reflector made of TVR and TShPR beryllium grades. Used while performing computation were the experimental data on thermal expansion coefficients and mechanical properties of the grades mentioned.

3. As an example, the strength estimations for TVR grade beryllium have been carried out which have determined the peak values of permissible temperature gradients at axial-symmetric parabolic temperature field of circular reflector.

REFERENCES

1. N.I. Bezukhov «Fundamentals of the theory of elasticity, plasticity and creep», «Higher school», 1968.
2. I.A. Birger, R.R. Mavlutov «Strength of materials», «Science», 1986.
3. S.G. Lechnickiy «Theory of elasticity for anisotropic materials», «Higher school», 1968.
4. G.A. Serniaev «Irradiation damage of Beryllium», 2001.

Development of Beryllium Pebbles with Fine Grain Structure for Fusion Application

I.B. Kupriyanov^a, G.N. Nikolaev^a, S.K. Zavjalov^a, L.A. Kurbatova^a, N.E. Zabirowa^a,
M. Zmitko^b

^a *A.A. Bochvar High Technology Research Institute of Inorganic Materials, Moscow, Russia*
^b *Fusion for Energy (F4E), Barcelona, Spain*

ABSTRACT

This paper presents some results of development and characterization of beryllium pebbles with average pebble size of 1.2 – 1.3 mm and different average grain sizes (~ 13-14 μm , ~50-51 μm and 615 μm) produced by powder metallurgy. Microstructure and chemical composition, as well as packing density and pebble size distributions for the pebbles produced are presented.

1. INTRODUCTION

Beryllium is the primary candidate material for use as the neutron multiplier in the helium cooled pebble-bed (HCPB) breeder blanket for use in a future fusion power reactor. Under neutron irradiation, helium and tritium are produced in beryllium. The key issues in neutron irradiation of beryllium are helium-induced swelling and tritium retention and release. Due to safety requirements, the in-pile tritium release should be sufficiently high to avoid risk to personal in the case of a serious accident in the fusion power plant leading to the abrupt release of all accumulated tritium.

In the present HCPB breeder blanket design, beryllium is used in the form of pebbles with diameter of ~1 mm, having inherently large grains in the 200-1000 μm range because of the fabrication by “Rotation Electrode Method” or “Fluoride Reduction Process” [1-5]. However, it is expected that in beryllium with fine grain structure (i.e., average grain size of a few micrometers), helium and tritium release can be significantly increased [6-7]. In order to produce pebbles with fine grain structure, R&D were performed at the Bochvar Institute. Three experimental batches of Be pebbles with an average pebble size of 1.2 – 1.3 mm and different average grain sizes (~ 13-14 μm , ~50-55 μm and 615 μm) has been fabricated by powder metallurgy method and then characterized.

This paper presents the results of development of a fabrication method to produce beryllium pebbles with fine grain structure and characterization of three batches of beryllium pebbles fabricated with average pebble size of 1.2 – 1.3 mm and different average grain sizes (~ 13-14 μm , ~50-51 μm and 615 μm).

2. FABRICATION OF BERYLLIUM PEBBLES BY POWDER METALLURGY

The technology for powder metallurgy fabrication of Be pebbles was developed for the production of the experimental batches of pebbles. The process consists of the following key steps:

1. Fabrication of Be billet with the required grain size and chemical composition;
2. Billet fragmentation (to ~ 10 mm pieces) by hydraulic press;
3. Further fragmentation in jaw crusher;
4. Intermediate screen sizing (+ 1.0 – 1.6 mm);
5. Balling in ball milling;
6. Cleaning in water/Etching in HNO₃/Cleaning in water/Drying;
7. Final screen sizing (+ 0.8 – 1.25mm).

Manufacturing of Be pebbles is described in detail in Ref. [8].

The average grain size and chemical composition of Be pebbles mostly depend on average grain size and chemical composition of initial Be billets (Step 1), and shape and pebbles size distribution depend on milling parameters and screen sizing (Steps 2-7).

The following initial materials were used for the fabrication of three types of beryllium pebbles:

1. For the Be pebbles with average grain size <30 μm (Type 1) the vacuum hot pressed (VHP) Be billet with average grain size of <30 μm was used;
2. For the Be pebbles with average grain size of 30-60 μm (Type 2) the hot isostatic pressed (HIP) Be billet was used with an average grain size of 50-60 μm, which was produced from ball-shaped powder;
3. For the fabrication of Be pebbles with average grain size >100 μm (Type 3) the Be ingot with an average grain size of >100 μm was used.

Three experimental batches of beryllium pebbles (~0.9 kg total amount) with average pebble size of 1.2 – 1.3 mm and three average grain sizes were fabricated by this technology.

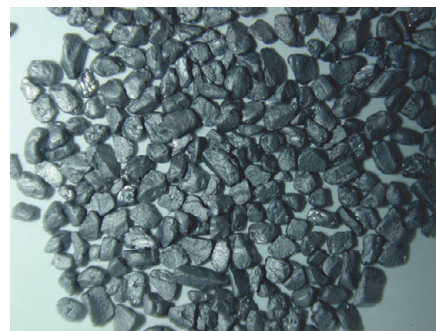


Fig. 1. Photo of beryllium pebbles

3. CHARACTERIZATION OF BERYLLIUM PEBBLES

3.1. Shape and size of pebbles

Photos of beryllium pebbles from the experimental batch are presented in Fig. 1. The pebbles could be characterized as the irregular shaped with round corners. To determine the pebbles dimensions, 100 pebbles were taken from the top and the bottom parts of a container with pebbles. Two dimensions were measured for each pebble: the biggest (L_1) and the smallest (L_2) which is perpendicular to the biggest one. With these measurements the average size $L_{ave} = L_1 + L_2 / 2$ and the aspect ratio L_1 / L_2 were calculated for every pebble. The measurements were carried out using a BMI-1 optical instrumental microscope at 20-x magnification. The results of calculations are summarized in Table 1. The average pebble size calculated on the basis of these measurements is 1.27-1.29 mm. The pebble size distribution is presented in Fig. 2.

Attention is drawn to the fact that more than 30 % of pebbles have larger average size than it expected from the size of the sieves used (0.8 – 1.25 mm). The probable reason for this is that ~33 % of pebbles have the aspect ratio $L_1 / L_2 > 1.5$ and the pebbles, having average size > 1.25 mm but the L_2 dimension less than 1.25 mm, can pass through the sieve with cell size of 1.25 mm.

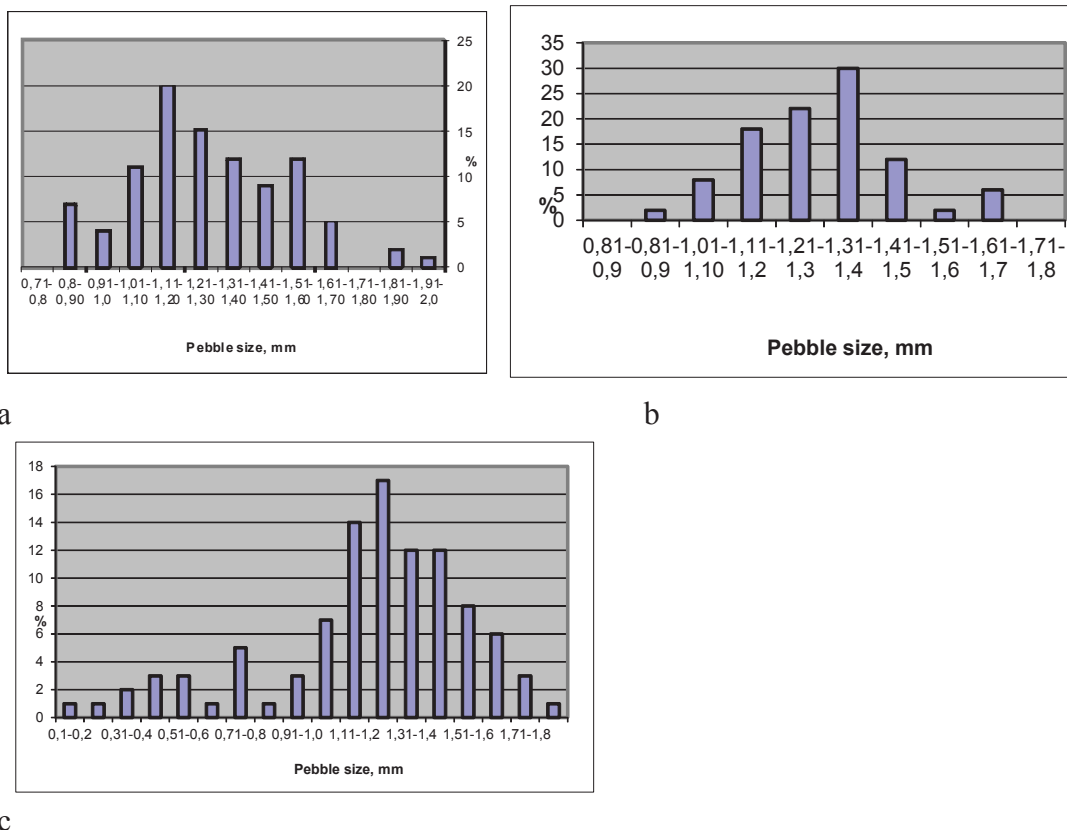


Fig. 2. Pebble size distribution, where
a - Type 1 (13-14 μm), a.p.s ~1.27 mm
b - Type 2 (50-51 μm), a.p.s ~1.29 mm
c - Type 3 (614-615 μm), a.p.s ~1.21 mm

Table 1 Shape and size of beryllium pebbles

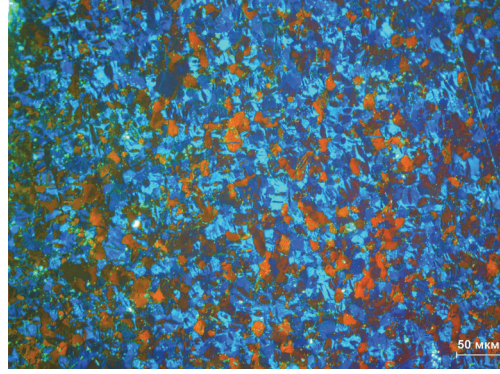
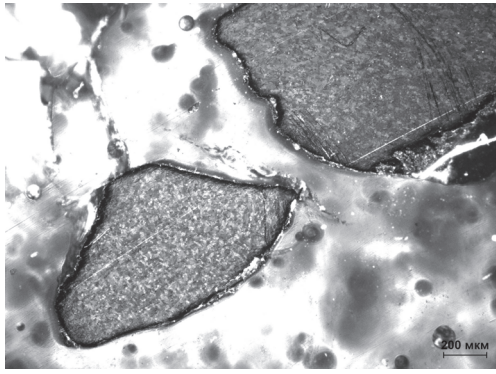
Type of pebbles	Average pebble size $\Sigma (L_{ave})$, mm	Max dimension $(L_{ave})_{max}$, mm	Min dimension $(L_{ave})_{min}$, mm	Fraction with aspect ratio $L_1/L_2 \leq 1.5$ %	Fraction with aspect ratio $L_1/L_2 > 1.5$ %
Type 1 ($<30 \mu\text{m}$)	1.27	1.98	0.83	67	33
Type 2 (30-60 μm)	1.29	1.65	0.94	78	22
Type 3 ($>100 \mu\text{m}$)	1.21	1.82	0.18	66	34

3.2. Chemical composition

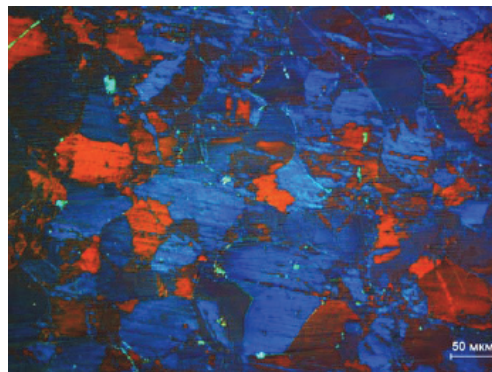
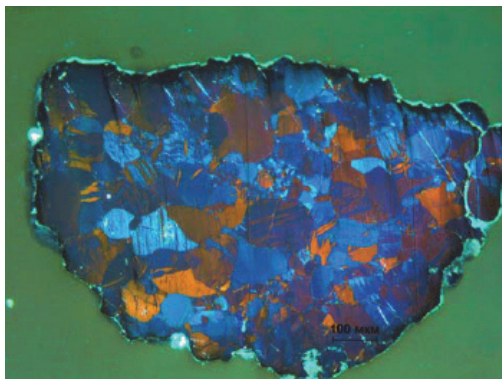
Chemical composition of three types of the pebbles is presented in Table 2. The main purpose of this development stage was to define a fabrication method for beryllium pebbles with fine grain structure, so we did not prescribe the narrow limits on chemical composition of initial materials.

3.3. Microstructure

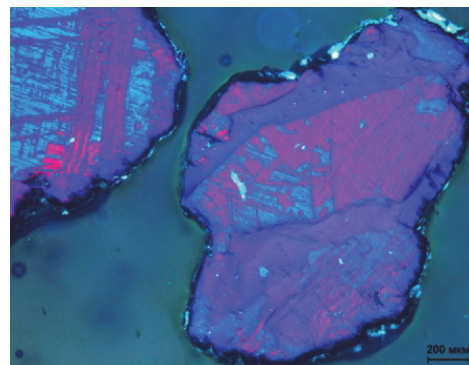
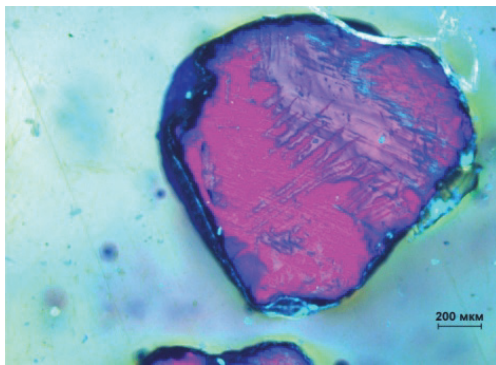
Typical microstructure of three types of beryllium pebbles is shown in Fig. 3. Average grain sizes are of 13 – 14 μm , 50-51 μm and 614-615 μm for pebbles of Type 1, Type 2 and Type 3, correspondingly (Table 3). The surface of the pebbles is characterized by a noticeable microtoughness that is a result of the intensive deformation processes occurring in a near-surface layer of the pebbles during their fabrication (Fig. 4).



a



b



c

Fig. 3. Microstructure of beryllium pebbles (metallography, polarized light), where a - Type 1 (13-14 μm), b - Type 2 (50-51 μm), c - Type 3 (614-615 μm)

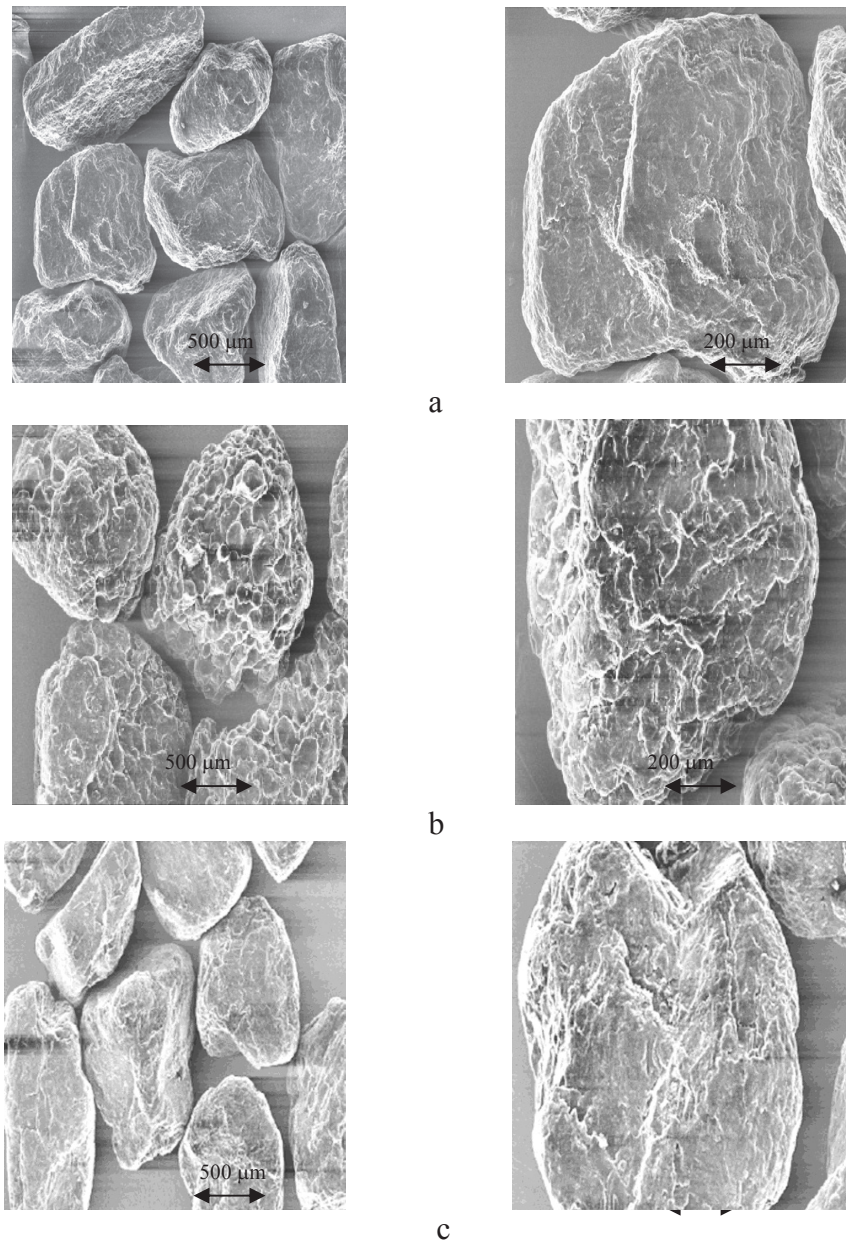


Fig. 4. Surface morphology of the pebbles (SEM), where a - Type 1 (13-14 μm), b - Type 2 (50-51 μm), c - Type 3 (614-615 μm)

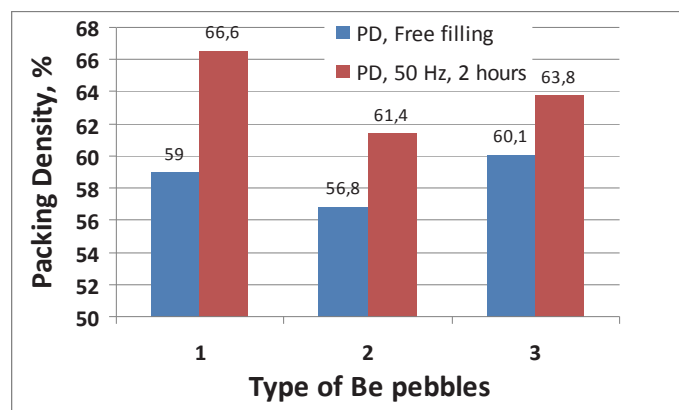


Fig. 5. Packing density (PD) of beryllium pebbles before and after vibration (50 Hz, 2 hours)

Table 2
Chemical composition of beryllium pebbles

Element	wt %		
	Type 1 (13-14 μm)	Type 2 (50-51 μm)	Type 3 (614-615 μm)
Be	base	base	base
Fe	0.07	0.025	0.15
Al	0.011	0.0051	0.014
Si	0.019	0.013	0.013
O ₂	1.17	0.28	0.39
C	0.075	0.076	0.064
Mn	0.0023	0.0023	0.0069
Mg	0.0016	0.0023	0.0012
Ni	0.0051	<0.001	0.016
Cr	0.025	0.011	0.052
Ti	0.0086	0.001	0.02
Ca	0.0047	0.0035	0.0037
Mo	0.0013	0.011	0.003
Zn	0.0014	0.0013	0.0008
U	0.0005	0.00001	0.0002
Ag	<0.0001	<0.0001	<0.0001
Co	<0.0005	<0.0005	<0.0005

Table 3
Grain size in different Types of beryllium pebbles

Type of pebbles	Average grain size, μm	Max grain size, μm	Min grain size, μm
Type 1 (<30 μm)	13-14	30	5
Type 2 (30-60 μm)	50-51	64.7	34.6
Type 3 (>100 μm)	614-615	1163.5	216.7

3.4. Packing density

Packing density of beryllium pebbles was defined at RT on 200 cm³ of pebbles, using a measuring cell with 70 mm in diameter and 200 mm in the height (no vibrations were applied). The packing density was 1.09 and 1.05 g/cm³ (Fig. 5) or ~59 and 56.8% of theoretical density of beryllium for pebbles of Type 1 and Type 2, correspondingly. After vibration (50 Hz, 2 hours) the packing density for Type 1 pebbles increased by ~12.6 % up to ~66.6 % of theoretical density of beryllium and for Type 2 pebbles it increased by ~8.1 % up to ~61.4 % of theoretical density of beryllium. The differences in packing density could be associated with different pebbles size distribution (Fig. 2) and surface roughness (Fig. 4) in three types of pebbles.

SUMMARY

The technology of fabrication of beryllium pebbles with fine grain structure by powder metallurgy has been developed and successfully implemented. Three experimental batches of Be pebbles with average pebble size of 1.2 – 1.3 mm and different average grain sizes (~13-14 μm, ~50-51 μm and 614-615 μm) have been fabricated and characterized. The technology seems is scalable for further industrial production of beryllium pebbles.

Microstructure examination shows that surface of the pebbles is characterized by a noticeable micro-toughness that is a result of the intensive deformation processes occurring in a near-surface layer of the pebbles during their fabrication.

Packing density at free filling was ~59, 56.8 and 60.1% of theoretical density of beryllium, correspondingly. After vibration (50 Hz, 2 hours) packing density of pebbles increased up to

~66.6 %, ~61.4 and 63.8 % of theoretical density of beryllium for Type 1 and Type 2 correspondingly.

ACKNOWLEDGEMENTS

This work was funded by European Fusion for Energy (Contract EFDA 05/994).

REFERENCES

- [1] T. Iwadachi, N. Sakamoto, K. Nishida, H. Kawamura, Production of various sizes and some properties of beryllium pebbles by the rotating electrode method, Proc. Third IEA Int. Workshop on Beryllium Technology for Fusion, Oct. 22-24, 1997, Mito, Japan, JAERI-Conf 98-001, p. 33-38.
- [2] M. Dalle-Donne, D.L. Baldwin, D.S. Gelles, L.R. Greenwood et al., Behavior of beryllium pebbles under irradiation, Proc. Third IEA Int. Workshop on Beryllium Technology for Fusion, Oct. 22-24, 1997, Mito, Japan, JAERI-Conf 98-001, p. 296-306.
- [3] M. Dalle-Donne, A. Goraieb, G. Piazza, G. Sordon, Measurement of thermal conductivity and heat transfer coefficient of a binary bed of beryllium pebbles, Proc. Third IEA Int. Workshop on Beryllium Technology for Fusion, Oct. 22-24, 1997, Mito, Japan, JAERI-Conf 98-001, p. 17-24.
- [4] T. Iwadachi, D. Schmidt, H. Kawamura, The distribution of impurities in beryllium pebbles produced by rotating electrode method, Proc. Of the 4th IEA Int. Workshop on Beryllium Technology for Fusion, Sept. 15-17, 1999, Karlsruhe, Germany, FZKA 6462, p. 15-24, 2000.
- [5] E. Ishitsuka, H. Kawamura, T. Terai and S. Tanaka, Effect of Oxide Layer on Tritium Release from Beryllium Pebbles, Proc. of 18th SOFT, Fusion Technology, vol. 2, 1994, p. 1345-1348.
- [6] E. Rabaglino, Helium and tritium in neutron irradiated beryllium, FZKA Report No.6939, 2006.
- [7] D. Baldwin, M. Billon, Diffusion/Desorption of tritium from irradiated beryllium, J. Nucl. Mater. 212-215 (1994) 948-953.
- [8] I. Kupriyanov et al. Production and investigation of beryllium pebbles with fine grain structure for the HCPB breeder blanket, Fusion Engineering and Design 87 (2012) 1338-1341.

Fabrication Considerations for Large Beryllium Structures

M. A. Gallilee^(a), G. Simmons^(b)

(a) CERN, CH-1211 Geneva 23, Switzerland

(b) 44036 S Grimmer Blvd, Fremont, CA 94538-6346, USA

ABSTRACT

Beryllium has been used for a number of years as the material of choice for the central beam vacuum chambers of the CERN LHC experiments. In the past, beryllium has been fabricated into vacuum chambers using various methods. Variations on the brazing process have been used; however this process required the use of fluxes and also materials which reduced the transparency of beryllium to the beam collision products. A more recent method, which was developed in conjunction with CERN and Materion Electrofusion, is electron beam (EB) welding of the vacuum chambers. This fabrication method allows that only beryllium is seen by any collision products of the beam-beam interactions of the LHC. Welding is therefore the preferred fabrication method.

A number of challenges were initially encountered during the development process of these welded chambers: insufficient weld equipment process control, material porosity, and fabrication of seamless tubes. Recently more challenges have arisen with thicker walled vacuum chambers, and leak paths opening during post fabrication heat treatment. These recent challenges have presented potential obstacles to the construction of new vacuum chambers for the LHC experiments. This paper will present these challenges and how they were overcome during the chamber fabrication process.

1. INTRODUCTION

During the period 2007/2008, the final integration phase was carried out for the beam vacuum chambers in the four large LHC experiments [1]. The design of these chambers dates back to the period 1994-2003 [2]. For the central interaction regions of the experiments, it is necessary to have a material that is as transparent as possible to the interaction products. One measure of the overall effectiveness of a material is given by the product of the radiation length (X_0) and Young's Modulus (E) to the power 1/3 [3]. Beryllium is a material that can be leak-tight whilst maintaining the strict ultra-high vacuum (UHV) requirements of the LHC of $< 10^{-10}$ mbar [5], at the same time having an extremely high Young's Modulus and radiation length.

For the first set of chambers installed in the LHC experiments, issues such as welding process control, bulk material porosity and fabrication of seamless tubing were solved to enable production of the chambers. Given the shutdown of the LHC between 2013 and 2014, the LHC experiments of ATLAS, CMS and LHCb have taken advantage of this time in order to change their central beryllium chambers [4]. During the manufacture of these new chambers, unexpected production challenges have arisen, such as welding of material greater than 1.0 mm in thickness, and leak-paths occurring in the bulk material after a post fabrication heating cycle.

2. WELDING PROCESS CONTROL

The chambers are composed of beryllium central sections and aluminium or stainless steel end flanges. During fabrication of the first set of chambers installed in the LHC experiments, several challenges were encountered during welding beryllium to beryllium and beryllium to aluminium. Relatively small variations in the electron beam caused significant variations in the quality of the welds. These small variations were determined to be caused by the weld equipment's inability to adequately control key parameters. After completion of the first set of chambers, the EB welding equipment was upgraded in order to significantly improve the ability to control all key welding process parameters. This equipment upgrade has proven to be very effective at minimizing variations during EB welding of subsequent chambers.



Figure 1: Hamilton Standard EB Welder.

3. MATERIAL POROSITY

Figure 2 shows the location of a small leak of the order 3×10^{-8} mbarl/s, found with a helium leak detector. On closer inspection with an electron microscope (Figure 3), a small surface defect was evident in the location of the leak. Further analysis revealed a high density inclusion, likely to be refractory material. This may have been where the leak was propagating. For this particular leak, the exact path was never found and the hypothesis for this was that the leak path was cut out during analysis. Tracing leak paths is notoriously difficult, especially leaks of this order of magnitude.

The risk has been reduced by analysing the material by x-ray in both the raw form, and for the rough machined product. It is important that the resolution of the x-ray is higher than the intended wall thickness of the final component. Any material found with an inclusion in the volume of material that would remain in the finished material is rejected. The current resolution for inclusions is 0.5 mm.



Figure 2: Small leak in machined material

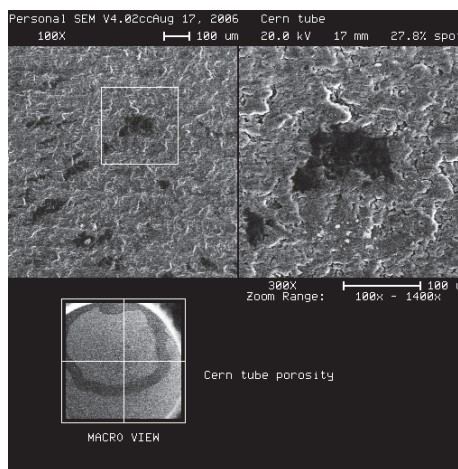


Figure 3: Electron microscopy of leaking area

4. SEAMLESS TUBE FABRICATION

After qualification of the bulk material, thin walled tubes are machined. To obtain the optimal performance of the LHC experiments, these thin walled tubes can have a wall thickness down to 0.8 mm over a length of up to 7.1 m. The particular beryllium grade used for these chambers is Materion grade S200F, which is manufactured by Vacuum Hot Pressing. Due to the manufacturing method, it is inevitable that very small pores will be present in the material. The key is having a thick enough wall so that a leak path cannot be established, but thin enough to allow the LHC experiments to exploit the mechanical properties of beryllium.

Figure 4 shows thin walled tubes of 1 m length that were machined from bulk S200F beryllium material. The tubes were manufactured with extreme precision using methods of gun drilling and turning. The tubes are so precise that tolerance stack-up, including straightness and circularity, can be less than 0.1 mm over the entire length. Leak-checks are carried out on the machined tube before welding into the assembly to ensure minimal risk.



Figure 4: Thin walled beryllium tubes machined from bulk material

5. THICK WALLED WELDING

During production of the latest LHC experimental chambers, it was found for EB welding that thicker beryllium walls were more susceptible to welding issues than thinner ones. Above 1 mm in thickness, the weld joint showed signs of spatter, possible cracking and lower yield strength when compared with thinner welds. As no welding standards exist for beryllium, the aluminium standard BS EN ISO 13919-2:2001 was used as a baseline. It was necessary to make concessions in certain cases of thick walled chamber welds, assessing whether they were “fit for purpose” rather than whether they adhered to the chosen standard. Figure 5 shows a thick walled beryllium chamber for LHCb during the assembly process.



Figure 5: LHCb beryllium chamber assembly

6. LEAK PATHS AFTER FABRICATION

At the start of the manufacture of the most recent beryllium chambers, it was found that, leak paths could open in the tube material during a bake cycle of the finished chamber. The bake cycle is up to 230 Celsius and used to ensure that the chamber can meet the necessary UHV requirements of the LHC. For this type of leak path, a step in the manufacturing sequence was introduced whereby the individually machined tubes were baked to 230 C and then checked for leaks before welding into the assembly. This reduced the risk that a leak would open later during the bakeout cycling of the assembly.

Other leak paths, such as the one shown in Figure 6, are more obvious. This is a crack that has been created as part of the weld, likely due to stresses created in the heat affected zone during shrinkage. For such leak paths, the only remedy was to cut and re-weld.



Figure 6: Crack adjacent to weld after assembly

7. CONCLUSIONS

In conclusion, beryllium is an excellent material for the central vacuum chambers of the LHC experiments. Some processing issues have been encountered during the production of the first and second generation vacuum chambers. It is now known how to deal with many of these issues. Still, it remains challenging to produce a beryllium vacuum chamber and at the same time meet the stringent requirements from the LHC beam vacuum.

REFERENCES

- [1] R.Veness *et al.*, Installation and Commissioning of Vacuum Systems for the LHC Particle Detectors, PAC09.
- [2] R.Veness *et al.*, Specification of New Vacuum Chambers for the LHC Experimental Interactions, PAC11.
- [3] R.Veness *et al.*, Design of beampipes for LHC experiments, Vacuum volume 64, issues 3-4, 2002 pp467-473.
- [4] M.Gallilee *et al.*, LHC Detector Vacuum System Consolidation for Long Shutdown 1 (LS1) in 2013-2014, PAC12.
- [5] LHC Design Report, Vol 1, Chapter 12 (vacuum), pp339, 2004.

Ab-initio study of hydrogen on beryllium surfaces

D.V. Bachurin, P.V. Vladimirov

*Institute for Applied Materials - Applied Materials Physics,
Karlsruhe Institute of Technology, 76344 Eggenstein-Leopoldshafen, Germany*

ABSTRACT

Static *ab-initio* calculations were performed for five various close-packed beryllium surfaces: basal, prismatic (type I and II), pyramidal (type I and II). The basal plane was found to be the most energetically favourable, while the energies of the prismatic and pyramidal planes were slightly higher. Up to five outermost atomic layers were involved in surface relaxation. The presence of the hydrogen atoms on the beryllium surface led to a noticeable reduction of the surface energy and to a significant interplanar relaxation in contrast with pure beryllium.

KEYWORDS

Beryllium; Hydrogen; Surface energy; *Ab-initio* calculations

1. INTRODUCTION

Presently beryllium and its alloys are considered as a material for fusion reactor blanket and plasma facing first wall. The interaction of hydrogen and its isotopes with beryllium surfaces leads to a significant change of the surface properties of the material. Knowing of the surface properties of the material is important for understanding adsorption, oxidation, corrosion and other surface phenomena. However, the *ab-initio* studies are limited mainly by consideration of basal plane only [1–4, 6], while structure and energy as well as the absorption of hydrogen atoms on the other surfaces of hexagonal close-packed (hcp) beryllium are purely covered in the literature [7–10]. The main goal of the present paper is to study the energy of five different beryllium surfaces and the effect of hydrogen on the surface energies.

2. CALCULATION DETAILS

Static *ab-initio* calculations were performed using simulation package VASP [11]. The standard pseudopotentials for beryllium and hydrogen were taken from VASP library. The projector augmented wave potential (PAW) was used to describe the interactions between ions and electrons. The generalized gradient approximation (GGA) of Perdew and Wang [12] was employed to determine the exchange-correlation energy.

Five various close-packed beryllium surfaces were investigated: basal, prismatic (type I and II), pyramidal (type I and II) (see Fig. 1). Since (0110) and (0111)-surfaces can be terminated in two possible ways, we have considered only the most stable "short" termination. The free surfaces were separated by a 17–23 Å thick vacuum region, which is, according to our tests, sufficient to avoid interaction between the two free surfaces due to periodic boundary conditions. The volume and the shape of the simulation cell were rigidly fixed during relaxation. No restrictions on the relaxation of atoms were imposed. The following optimized lattice constants $a = 2.265$ Å and $c = 3.562$ Å were used. A Fermi broadening of 0.2 eV and

the cut-off energy of 450 eV were chosen. The atomic structures were visualized with the program Jmol [13].

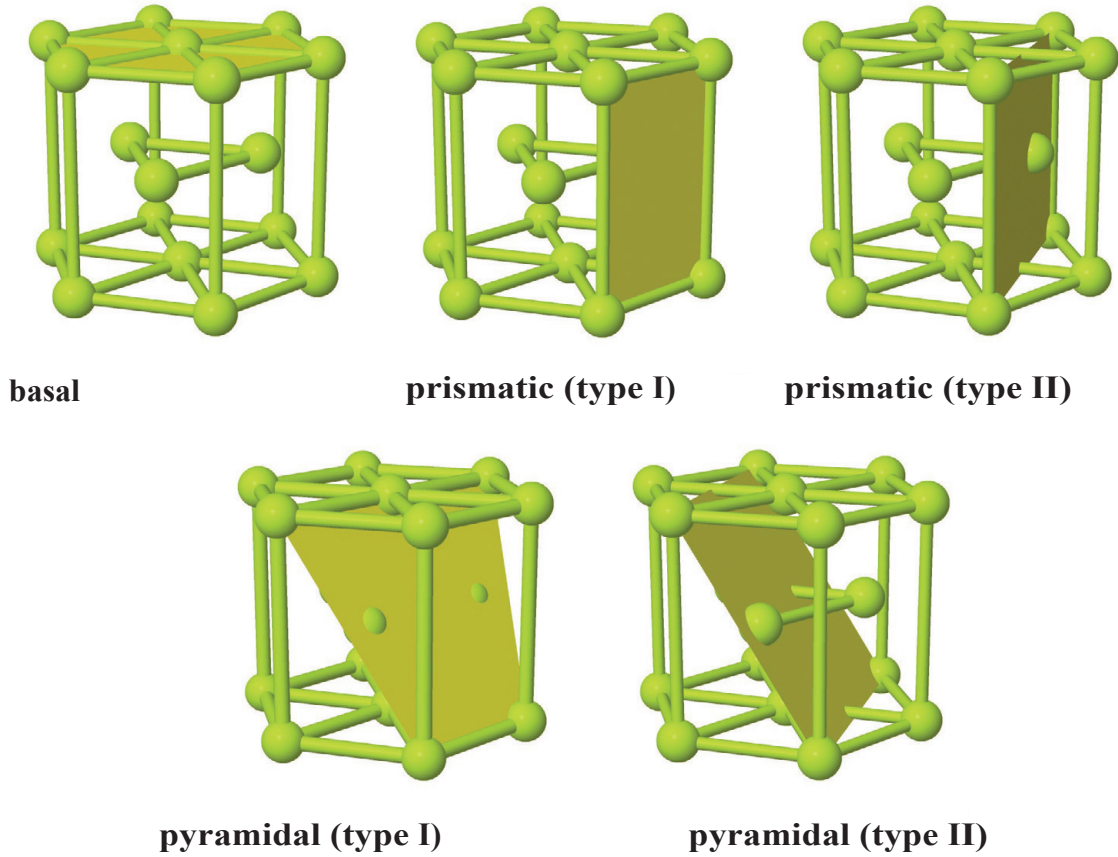


Figure 1 The main hcp crystallographic planes shown in unit cell: basal, prismatic (type I and II), pyramidal (type I and II).

The area of the free surfaces was chosen large enough to avoid the interaction of the hydrogen atom with its own images due to periodic boundary conditions. Certainly, it imposes restrictions on the possible thickness of the simulated sample, since we had to keep the number of atoms low to get reasonable calculation times. In order to check the convergence of the results with the size of supercell, different sizes of hcp crystal block were used (72–128 atoms). For convenience, a hydrogen atom was placed sequentially on the both free surfaces in all non-equivalent sites within the structural unit of the surface. The surface energy per unit area E_S of this system was calculated as follows:

$$E_S = \frac{1}{2S} (E_{total}^{Be+H} - -2E^H), \quad (1)$$

where E_{total}^{Be+H} is the total energy of the beryllium system containing two hydrogen atoms; E_{total}^{Be} is the total energy of the pure beryllium systems; $2E^H = -6.7179$ eV is the doubled energy of the hydrogen atom; S is the surface area. The surface energy of the system containing n adsorbed hydrogen atoms was determined using formula (1) with the only one difference, that the energy of n hydrogen atoms was subtracted, i.e. nE^H .

The basal and prismatic (type I and II) planes contain two non-equivalent positions for hydrogen, which we designate as 'a' and 'b', while pyramidal (type I and II) planes contain four non-equivalent positions (a, b, c and d). The initial position of hydrogen atom was in the plane formed by three (or four) neighbouring beryllium atoms.

3. SIMULATION RESULTS

3.1. Beryllium surface energies

The calculations shows that the basal plane is the most energetically favourable (see Table 1). The energy of prismatic (type I) and pyramidal (type I) planes are almost equal and found to be the second energetically favourable planes in beryllium. Prismatic (type II) and pyramidal (type II) are the planes with the highest surface energy. Comparison shows that our results are in a reasonable agreement with the previous *ab-initio* calculations [2, 4, 5, 15].

Table 1. Summary of the simulation details and the surface energies of pure hcp beryllium. N is the number of atoms in the simulation cell

Name	Plane	N	k -points	E_s (J/m ²)
Basal	0001	120	13 x 16 x 7	1.71
prismatic (type I)	0 $\bar{1}$ 10	120	14 x 7 x 12	1.80
prismatic (type II)	$\bar{2}$ 110	108	8 x 9 x 10	2.02
prismatic (type I)	01 $\bar{1}$ 1	120	7 x 14 x 10	1.83
prismatic (type II)	01 $\bar{1}$ 2	96	8 x 11 x 15	2.40

3.2 Interplanar relaxation in pure beryllium

Relaxation of the surface layers was found to be very significant in beryllium. Results are presented in Fig. 2 for all above-mentioned five beryllium surfaces. In the case of basal plane the interlayer spacing gradually decrease when approaching the center of the sample from 2.83% at the top and 0.02% at the sixth layer as demonstrated in Fig. 2a. It is noteworthy, that much more significant relaxation with alternating displacements is observed for prismatic (type I) and pyramidal (type I) planes. The top outermost layers exhibit maximal displacement which exceeds 20% of bulk value as displayed in Figs. 2b and 2d. Very considerable relaxation of only the two top layers was found for prismatic (type II) and pyramidal (type II) surfaces in beryllium. The displacements of the other inner layers do not exceed 3% with respect to ideal hcp lattice (see Figs. 2c and 2e). Thus, up to five outermost atomic layers in all five investigated beryllium surfaces are involved in surface relaxation.

We also considered the influence of the sample's thickness on the relaxation of atomic layers for all five beryllium surfaces. The calculations revealed that the increase of the number of layers does not have a strong impact on the magnitude of relaxation of outermost layers, however it does have noticeable effect on relaxation of inner layers as, for instance, in the case of prismatic (type I) and pyramidal (type I) planes (see Figs. 2b and 2d).

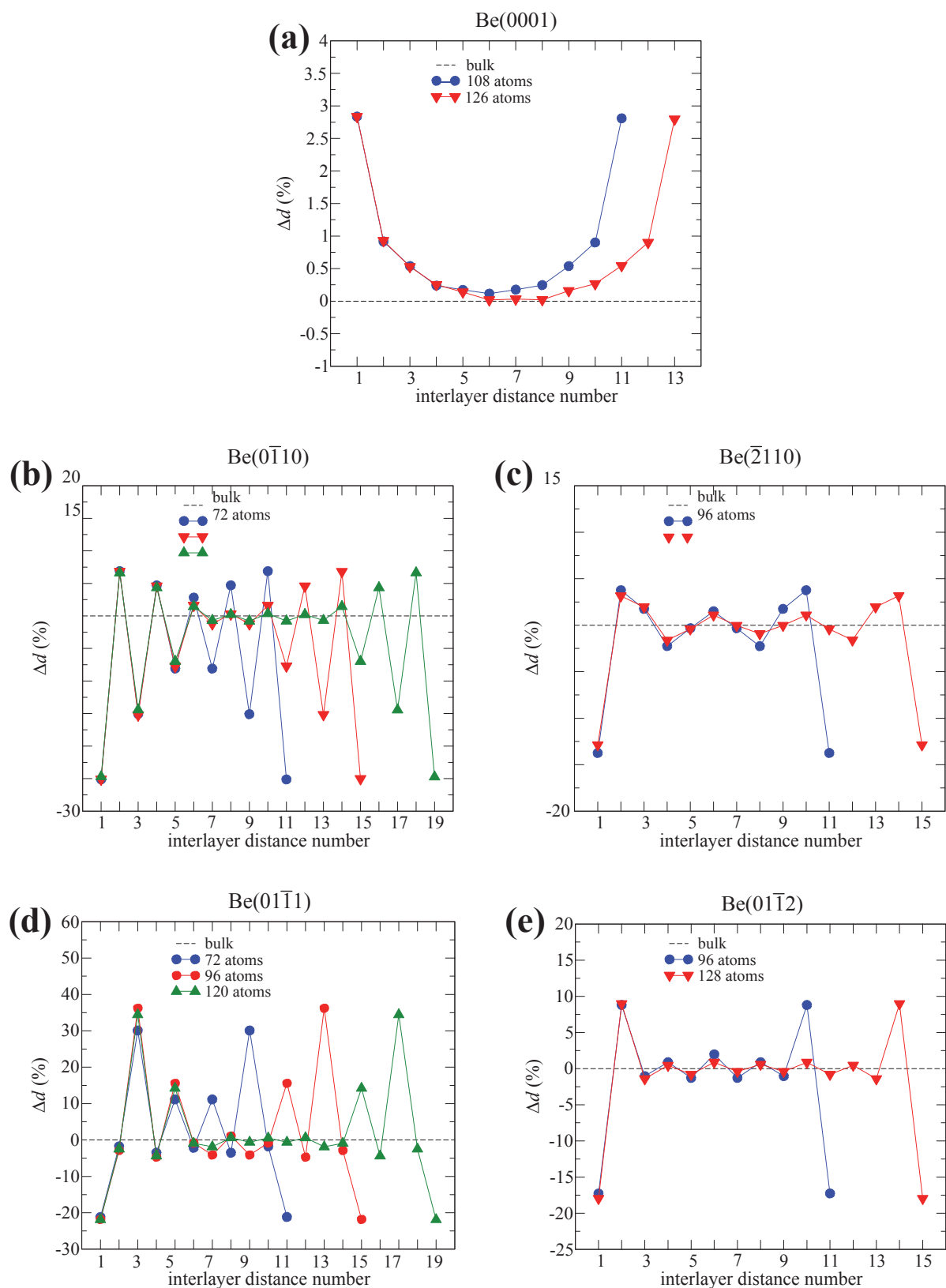


Figure 2. Relaxation of surface layers for various surfaces of pure beryllium. The value $\Delta d_{ij} = (d_{ij} - d)/d$ between the surface layers i and j (in % as compared with the interlayer spacing in the bulk). Lines interpolating the data points are guides to the eye.

3.3. Single hydrogen atom on beryllium surface

Basal. It is well-known that the hcp and fcc non-equivalent hollow sites (designated as 'a' and 'b' in Fig. 3a, respectively) on basal plane are two minimum energy locations for the hydrogen atom. In both cases the hydrogen reduces the surface energy up to 1.60 and 1.62 J/m² for hcp and fcc sites, respectively (see Fig. 4). The length of the beryllium-hydrogen bond was found to be 1.56 Å for both cases.

Prismatic (type I). Calculations show that the hydrogen atom moves from the initial position 'a' surrounded by the three beryllium atoms and settle on the bond between the two beryllium atoms as demonstrated in Fig. 3b. The length of the H-Be bond is 1.5 Å. The position 'b' is stable with the two bonds of 1.59 Å and one of 1.49 Å. Fig. 4 shows that the displacement of the hydrogen atom leads to a more pronounced surface energy reduction than in the case of the stable site 'b'.

Prismatic (type II). Similar to the prismatic (type I) plane the hydrogen atom is unstable in the initial position 'a' and has the minimum energy position on the bond between the two beryllium atoms (see Fig. 3c). The position 'b' is stable. The lengths of the two bonds are 1.48 Å, in the position 'a' and 1.68 Å, and 1.69 Å in the position 'b'. It is interesting to note that the 'b' is the only one site, where the presence of the hydrogen atom results in an increase of the surface energy as compared with the pure beryllium surface as illustrated in Fig. 4.

Pyramidal (type I). Relaxation of the four different structures revealed that there are only two stable sites for the hydrogen atom. Positions 'a' and 'b' are stable, while the two other positions 'c' and 'd' are not. During relaxation the hydrogen atom moves from the sites 'c' and 'd' into the site 'a' in the neighbouring structural unit as shown in Fig. 3d. The lengths of the bonds are 1.53 Å, 1.54 Å and 1.60 Å in the position 'a' and 1.49 Å, 1.62 Å and 1.62 Å in the position 'b'. The site 'a' is energetically more favourable than 'b' (see Fig. 4) and in both cases the presence of hydrogen decreases the surface energy.

Pyramidal (type II). The hydrogen atom moves from the initial position 'a' into the bond between the two beryllium atoms as shown in Fig. 3e. Position 'b' is stable. Similar to the previous case the sites 'c' and 'd' are unstable. Minimization of the energy results in a displacement of the hydrogen atom from the sites 'c' and 'd' into the site 'a' in the neighbouring structural unit. The lengths of the bonds are 1.47 Å, and 1.48 Å in the position 'a' and 1.45 Å, 1.61 Å and 1.62 Å in the position 'b'. The disposition of the hydrogen in the site 'a' leads to a more noticeable surface energy reduction unlike in the site 'b' as seen in Fig. 4.

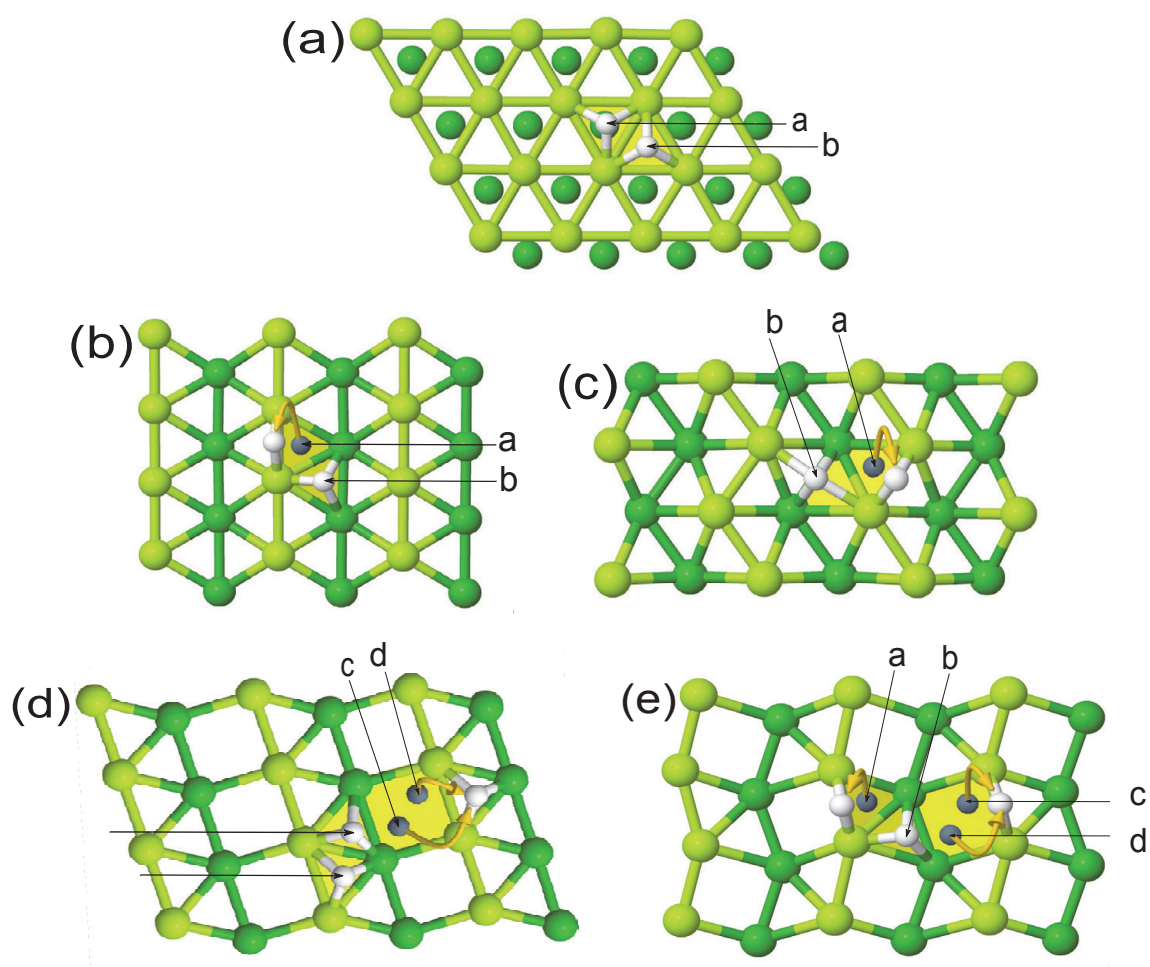


Figure 3. Minimum energy configurations of single hydrogen atom on beryllium surfaces: (a) basal; (b) prismatic (type I); (c) prismatic (type II); (d) pyramidal (type I); (e) pyramidal (type II). The top outermost layer (green) and the layer beneath it (dark green) are shown. The symbols a, b, c and d indicate the non-equivalent positions of the hydrogen atom on the corresponding surfaces. The orange arrows show the displacement of hydrogen from its initial position after relaxation. The structural unit of every surface is highlighted in yellow.

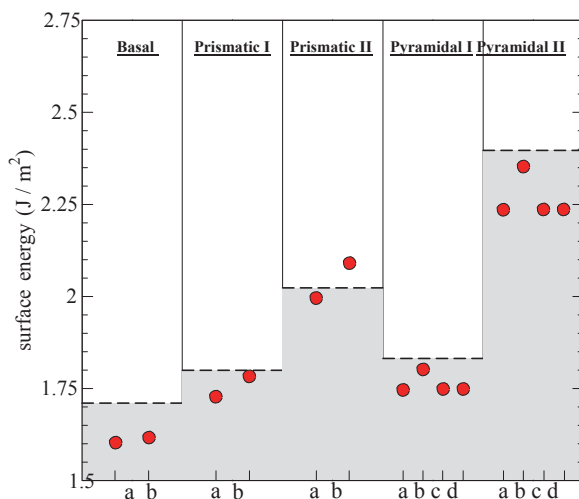


Figure 4. Influence of hydrogen on beryllium surface energy. The symbols a, b, c and d on the abscissa axis designate the non-equivalent positions on the corresponding surfaces. Horizontal dashed lines indicate the surface energies in pure beryllium.

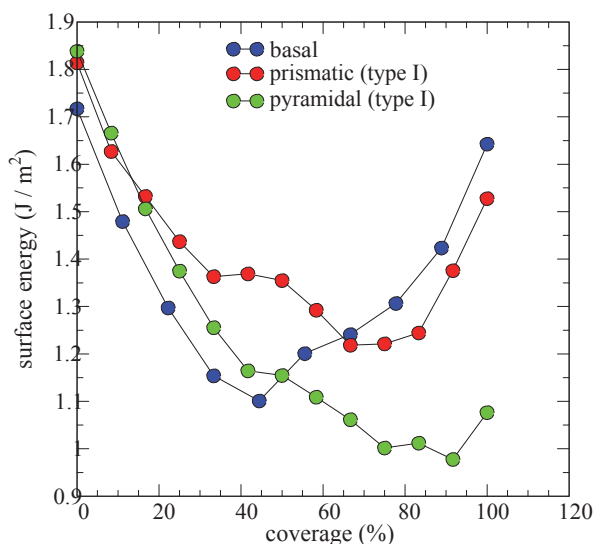


Figure 5. Surface energy of various beryllium planes as a function of the surface coverage. Lines interpolating the data points are guides to the eye.

3.4. Hydrogenation of the beryllium surfaces

The dependence of the surface energy on hydrogen coverage was calculated for three the most energetically favourable planes in pure beryllium: basal, prismatic (type I) and pyramidal (type I). For convenience, the separate samples with smaller free surface area and the larger size along the direction perpendicular to it were taken. We have introduced also here a somewhat different definition of the coverage. Namely, it was defined as a ratio of the total amount of the hydrogen atoms to the number of beryllium surface atoms. Thus, in all cases the maximum surface coverage was 100%, which corresponded to nine hydrogen atoms on basal plane and twelve atoms on prismatic (type I) and pyramidal (type I) planes. Note, that the hydrogen atoms were initially disposed at the minimum energy sites (see Figs. 3a,b and d). The further coverage of the surfaces was carried out gradually and not according to the principle of minimum energy.

The results the hydrogenation of the beryllium surfaces are presented in Fig. 5. As seen, the surface energy first reduces, reaches a minimum and thereafter increases while the coverage proceeds. Thus, up to a certain point, which is different for different beryllium planes, the further hydrogenation of the free surfaces is not energetically favourable anymore. It is interesting to note that when the coverage exceeds 50%, the pyramidal (type I) plane becomes the most favourable one as displayed in Fig. 5, while basal plane, on the contrary, energetically unfavourable. It should be mentioned, that for all three considered planes the energy of hydrogenated surfaces is always smaller than the energy of the corresponding pure surface. Analysis of the relaxed structures showed that at high coverages the adsorption sites are bridge locations for basal plane with the length of the H-Be bond of approximately 1.47 Å. The bridge-type sites 'a' and the new bridge-type positions on the second surface layer are adsorption sites for (0110) plane. In the case of (0111) surface the adsorption sites are positions 'a' and the new bridge-type sites between the first and the second surface layers.

3.5. Interplanar relaxation of the hydrogenated beryllium surfaces

It should be noted, that we have considered the second outermost layer also as a surface layer for prismatic (type I and II) and pyramidal (type I and II) planes, since the hydrogen atoms form the bonds with the atoms located in the second layer.

Comparison of the interplanar relaxation of 100% hydrogenated beryllium surfaces with the corresponding pure ones is demonstrated in Fig. 6. As seen, the presence of the hydrogen on the basal plane results in a noticeable increase of the interlayer distances. It is interesting to note that only the surface atomic layer exhibits significant expansion, while the interplanar spacings for all other planes are close to the ideal hcp lattice value. The influence of the hydrogen on the surface relaxation is even more spectacular in the case of prismatic (type I) and pyramidal (type I) planes. The hydrogenation of these surfaces leads to change of the sign of the interlayer displacement. Namely, the compression of the interplanar spacings is replaced by the tension of these layers and vice versa as clearly shown in Fig. 6b and 6c.

4. DISCUSSION AND CONCLUSIONS

The top layers of the surface shows the largest relaxation in percent of interlayer spacing, which is also typical for other materials with hcp crystal lattice [14]. Our results concerning to basal and prismatic (type I) planes are in a reasonable agreement with the previous works [2, 3, 6–10], while the results for prismatic (type II) and pyramidal (type I and II) beryllium surfaces are new.

Analysis of the electron density distributions for every considered surface confirms the tendency of hydrogen atom to move from the sites with low and settle on the sites with high electron density. Here we omit these figures for brevity.

A number of earlier studies [15, 16] have argued that in the case of basal plane the bridge position is the stable adsorption site for monolayer coverage of hydrogen. Later Stumpf and Feibelman [17] figured out that at lower coverages the hcp site was found to be favourable. These are in a good agreement with our outcomes. However, our results are in contradiction with the recent study [18], where it is maintained that the minimum energy position of the single hydrogen atom is almost in the original surface plane at equal distance from three surface beryllium atoms.

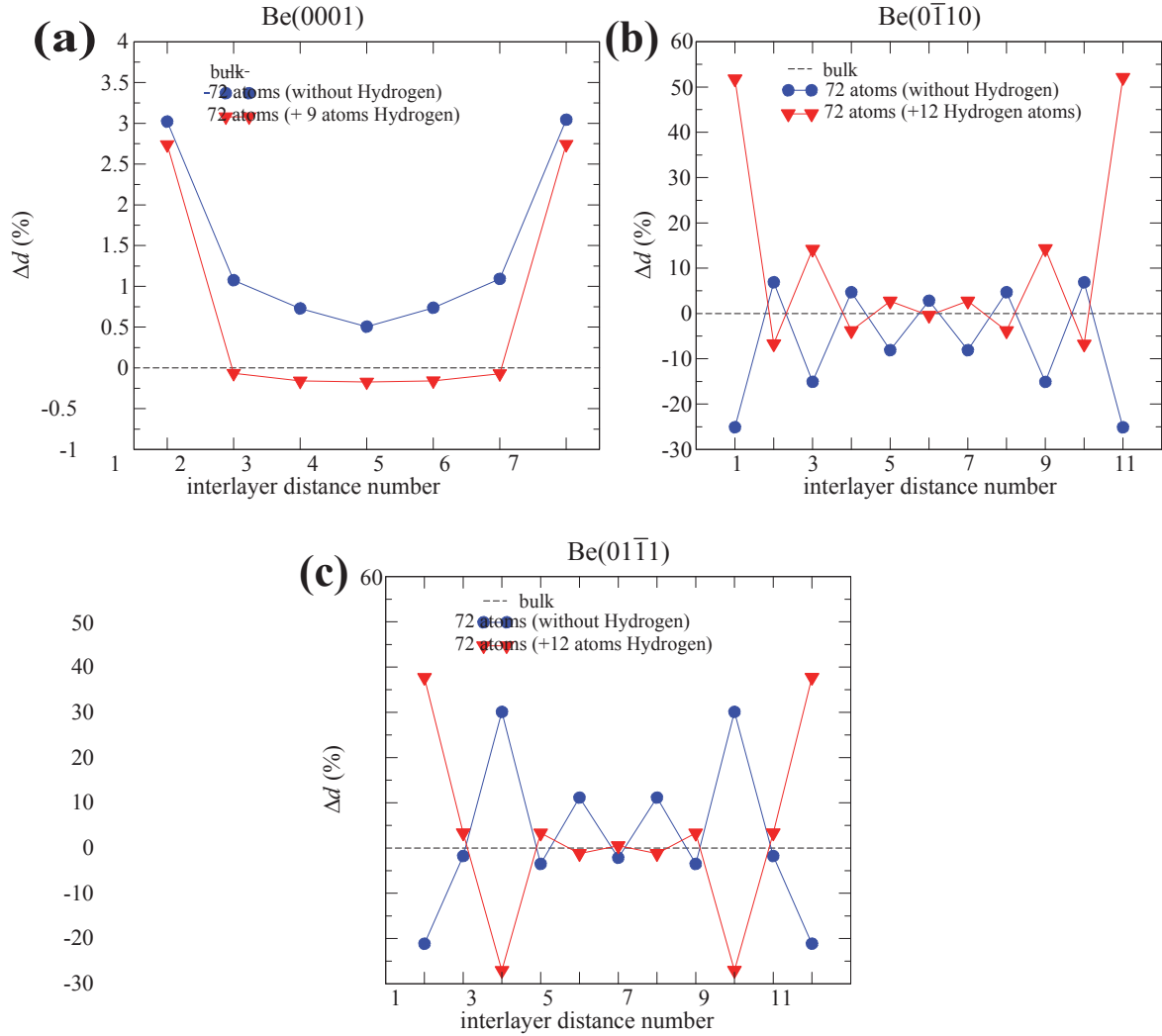


Figure 6. Comparison of relaxation of surface layers in pure beryllium and in beryllium with 100% hydrogen coverage for various surfaces. The value $\Delta d_{ij} = (d_{ij} - d)/d$ between the surface layers i and j (in % as compared with the interlayer spacing in the bulk). Lines interpolating the data points are guides to the eye.

Our calculations show that the bridge position of the single hydrogen atom is energetically favourable on the prismatic (type I and II) and pyramidal (type I) planes (see Figs. 3b, 3c and 3e).

Recent study of hydrogenation of (0001) beryllium surface [18] demonstrated that the adsorption energy has a minimum at the coverage of approximately 20%, which is in a contradiction with our simulations (see Fig. 5). Moreover, the method of calculation of the surface coverage in [18] is doubtful.

In this work surface energies of the main closed packed beryllium surfaces were calculated. The relaxation patterns previously found for basal and prismatic (type I) surfaces were confirmed and similar behaviour was found for prismatic (type II) and pyramidal (type I and II) surfaces not considered previously. It was shown that presence of hydrogen atom on any of the five studied beryllium surfaces (excepting the site 'b' on the prismatic (type II) plane) leads to a noticeable reduction of the surface energy. This finding is important for fusion devices where hydrogen interaction with beryllium surfaces is unavoidable.

ACKNOWLEDGMENTS

This work, supported by the European Communities under the contract of Association between EURATOM and Karlsruhe Institute of Technology, was carried out within the framework of the European Fusion Development Agreement. The views and opinions expressed herein do not necessarily reflect those of the European Commission.

REFERENCES

- [1] Antonelli A, Khanna S N and Jena P 1993 *Surf. Sci. Lett.* **289** L616
- [2] Wachowicz E and Kiejna A 2001 *J. Phys.: Condens. Matter* **13** 10767
- [3] Lazzeri M and de Gironcoli S 1998 *Surf. Sci.* **402–404** 715
- [4] Wu X, Wang R and Wang S 2010 *Appl. Surf. Sci.* **256** 3409
- [5] Vitos L, Ruban A V, Skriver HL and Kollár J. 1998 *Surface Sci* **411** 186
- [6] Li Y, Yang Y, Sun B, Wei Y and Zhang P 2011 *Physics Letters A* **375** 2430
- [7] Hofmann Ph, Pohl K, Stumpf R and Plummer E W 1996 *Phys. Rev. B* **53** 13715
- [8] Lazzeri M and de Gironcoli S 2002 *Phys. Rev. B* **65** 245402
- [9] Ismail, Hoffmann Ph, Baddorf A P and Plummer E W 2002 *Phys. Rev. B* **66** 245414
- [10] Tang S J, Jeng H T, Hsue C S, Ismail, Sprunger P T and Plummer E W 2008 *Phys. Rev. B* **77** 045405
- [11] Kresse G and Hafner J 1993 *Phys. Rev. B* **47** 558
- [12] Perdew JP and Wang Y 1992 *Phys. Rev. B* **45** 13244
- [13] Jmol: an open-source Java viewer for chemical structures in 3D. <http://www.jmol.org/>
- [14] Zolyomi V, Kollár J and Vitos L 2008 *Phys. Rev. B* **78** 195414
- [15] Yu R and Lam P K 1989 *Phys. Rev. B* **39** 5035
- [16] Feibelman P J 1993 *Phys. Rev. B* **48** 11270
- [17] Stumpf R and Feibelman P J 1995 *Phys. Rev. B* **51** 13748
- [18] Allouche A 2008 *Phys. Rev. B* **78** 085429

Hydrogen Interaction on Beryllium (0001) Surface

C. Stihl¹ and P. Vladimirov¹

¹*Karlsruhe Institute of Technology (KIT), Institute for Applied Materials - Applied Materials Physics (IAM-AWP), Hermann-von-Helmholtz-Platz 1, 76344 Eggenstein-Leopoldshafen, Germany*

ABSTRACT

The interaction of hydrogen atoms adsorbed on the basal beryllium surface is examined as a part of a multiscale modelling approach to hydrogen desorption using static ab initio calculations. In order to be able to predict energies of arbitrary adsorption structures, a truncated cluster expansion is obtained from a fitting procedure to total energies of chosen structures calculated by ab initio computations. It is found that truncation of the cluster expansion at pairwise interaction energies seems to be sufficient to estimate the energies of the chosen structures with acceptable accuracy. Metropolis Monte Carlo Simulations based on this set of interaction energies give no reason to predict significant associative desorption of hydrogen at coverages below 0.5 monolayer.

1. INTRODUCTION

Beryllium is considered as a candidate material for the first wall cladding [RFB⁺97] and as a neutron multiplier [EIB⁺99, HDF⁺03] in the tritium breeding blankets of the next generation fusion reactors ITER and DEMO. Both applications expose beryllium to significant fluxes of fast neutrons and hydrogen isotopes from the fusion plasma. Thus, accumulation of directly implanted hydrogen isotopes as well as helium and tritium from the reactions ${}^9\text{Be}(n, \alpha){}^6\text{He}$, $e(\beta^-){}^6\text{Li}(n, \alpha){}^3\text{H}$ and ${}^9\text{Be}(n, 2n)2{}^4\text{He}$ takes place in the beryllium. As a consequence, i.a. temperature and radiation flux dependent dynamics lead to the formation of structures such as voids and bubbles filled with a gas of hydrogen isotopes and/or helium. Therefore, there is a plethora of experimental work examining all kinds of interactions between beryllium, hydrogen isotopes and helium which influence these dynamics, see e.g. [LK92, VCU⁺98, CO02, RLd08]. Naturally, the governing adsorption and desorption mechanisms at the surface are of great importance for hydrogen isotope retention and release as the surface is the boundary region that needs to be overcome in both, experiments including degassing of beryllium like thermal programmed desorption (TPD) as well as the evolution of gas filled bubbles within the bulk material. Thus, obtaining reliable models of tritium retention and release from beryllium also requires an accurate description of hydrogenated beryllium surfaces which needs to include the interaction of adsorbed hydrogen as well.

This work therefore consists of a first attempt to access the hydrogen interaction on the surface in two steps. First, the interaction is accessed directly by ab initio calculations on atomic scales. Subsequently, those findings are parameterized by the determination of a set of effective interaction energies constituting a truncated cluster expansion in a first attempt to give a prediction of the interaction between the hydrogen atoms in larger scale systems.

2. AB INITIO CALCULATIONS

This section gives a summary of the calculations conducted using the Vienna Ab Initio Simulation Package (VASP) [KF96b, KF96a], as well as their setup including the most important algorithmic parameters chosen.

2.1 Calculation Details and the Simulation Cell

All calculations were conducted using the projector augmented wave (PAW) pseudo potentials [Blö94, KJ99] referencing all-electron calculations using the generalized gradient approximation (GGA) as proposed by Perdew and Wang [PW92] provided with VASP. Extensive testing led to a cut-off energy for the plane wave basis set of 450 eV, γ centered k-point grids corresponding to a grid at least as dense as $13 \times 13 \times 13$ for a $1 \times 1 \times 1$ simulation cell and a first order smearing method of Methfessel and Paxton [MP89] with a width of 0.58 eV. These settings yield lattice parameters for a perfect beryllium crystal of $a = 2.273 \text{ \AA}$ and $c = 3.545 \text{ \AA}$.

The beryllium surface is modeled as a beryllium slab consisting of six beryllium layers separated by a gap equivalent to $3.5c$. Every beryllium layer is initialized on positions as they were obtained from a relaxation of a symmetric beryllium slab consisting of 12 layers, hydrogenated by a 0.5 monolayer of adsorbed hydrogen on HCP adsorption sites. Numbering the layers beginning with the top one, the atoms of the first three layers of beryllium are allowed to move freely, the next three layers are kept fixed to their relaxed positions and the rest of the original 12 layer slab was removed, see figures 1a and 1b for the resulting simulation cell setup. This choice is the result of subsequently removing the lowest beryllium layer while keeping the now lowest three layers of beryllium fixed, monitoring the resulting deviation of the adsorption energy calculated by (2) in comparison to the system consisting of all 12 layers of beryllium. This cell minimizes the computational effort by removing as many beryllium layers as possible while introducing an error of $\lesssim 0.003 \text{ eV}$, which is significantly smaller than the expected accuracy of approximately 0.01 eV, in the calculated adsorption energy and preserving the expected monotonically nonincreasing saturation of the interaction of adsorbed hydrogen with increasing distances as tested by calculations with simulation cells of different lateral dimensions.

2.2 Hydrogen Adsorption and Interaction

We found two stable, energetically nonequivalent adsorption sites named HCP and FCC whose names are chosen according to the hypothetical positions of additional substrate atoms stacked in the AB- and ABC-pattern of HCP and FCC structures, respectively. This was achieved by sampling the potential energy surface (PES) an isolated hydrogen atom is subject to on the beryllium surface. For that purpose, a dragging technique was deployed in which the lateral coordinates of the hydrogen atom were fixed while the distance to the surface was adjusted by the relaxation. Fitting the inherently lattice periodical function

$$E(\vec{r}) = E(x, y) = \sum_{m,n=-2}^2 a_{m,n} \cos(\vec{k}_{m,n} \cdot \vec{r}) + a_{m,n} \sin(\vec{k}_{m,n} \cdot \vec{r}) \quad (1)$$

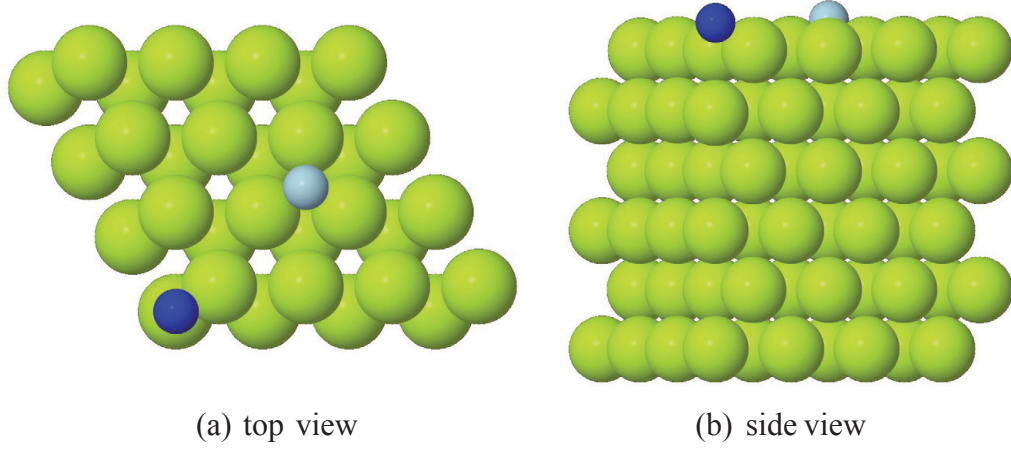


Figure 1: Pictures of the simulation cell. The green balls depict beryllium ions, the blue ones hydrogen ions. A darker and lighter blue ball indicates hydrogen adsorbed on the HCP and FCC adsorption site, respectively. The two nonequivalent adsorption sites are explained in subsection 3.2.

with $\vec{k}_{m,n} = m \cdot \vec{k}_1 + n \cdot \vec{k}_2$ ($\vec{k}_i = \frac{2\pi}{\vec{a}_i(\vec{a}_j \times \vec{a}_k)} \vec{a}_j \times \vec{a}_k$ and cyclical) for lattice vectors $\vec{a}_{i,j,k}$ via the coefficients $a_{m,n}$ and $b_{m,n}$ to energies obtained by such calculations then yields the PES shown in figure 2.

The PES clearly indicates the existence of the two stable HCP and FCC adsorption sites as minima. It also reveals clear maxima at the ontop positions of hydrogen, as well as a saddle point at the bridge position right between the HCP and FCC minima. We therefore consider only two possible adsorption sites in what follows. The adsorption energies given by the differences

$$E_{\{\text{FCC,HCP}\}} = E_{\text{sys}} - E_{\text{slab}} - \frac{1}{2} E_{\text{molecule}} \quad (2)$$

of the configuration energy of the complete system comprising beryllium and hydrogen E_{sys} , the energy of the clean slab E_{slab} only, and the total energy of a hydrogen molecule $E_{\text{molecule}} \approx -6.718$ eV as found by a corresponding ab initio calculation amount to

$$\begin{aligned} E_{\text{FCC}} &= -0.54 \text{ eV} \\ E_{\text{HCP}} &= -0.60 \text{ eV}. \end{aligned} \quad (3)$$

We thus define the coverage $\theta = 1.0$ (1.0 monolayer) as the coverage in which every such adsorption site is occupied by a hydrogen atom, resulting in a ratio of at most two hydrogen atoms per beryllium atom in the first substrate layer.

To examine the interaction between hydrogen atoms on the surface, systems containing two hydrogen atoms adsorbed at various distances were relaxed, see figures 3 for a representative selection of such systems. The energy contributions arising due to the interaction of the adsorbed hydrogen atoms $E_{\text{interaction}}$ are given by

$$E_{\text{interaction}} = E_{\text{system}} - m \cdot E_{\text{FCC}} - n \cdot E_{\text{HCP}} - E_{\text{slab}}$$

for a system containing m and n hydrogen atoms occupying FCC and HCP sites, respectively. Energies obtained from this expression are plotted in Fig. 4. Due to the finite

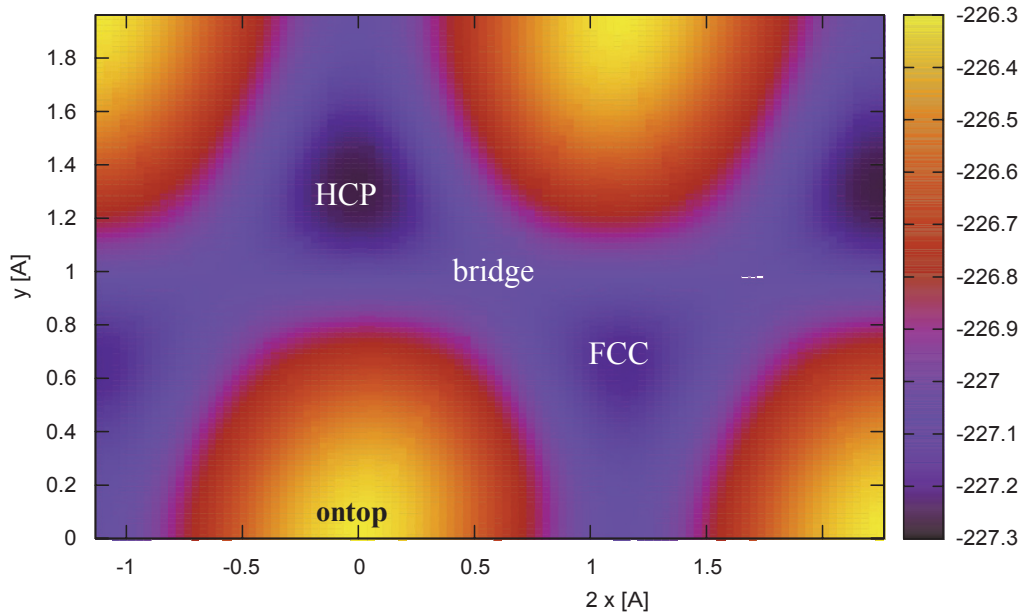


Figure 2: PES of a single hydrogen adsorbed on the beryllium surface given in total energies. The energetically nonequivalent FCC and HCP adsorption sites clearly show as minima of different depths in the bottom right and top left area of the image. The PES clearly encounters maxima at the ontop positions and a saddle point at the bridge positions right between the HCP and FCC positions.

accuracy of the underlying ab initio calculations, which is conservatively estimated to be approximately 0.01 eV, interaction energies between hydrogen atoms adsorbed at distances larger than 3 Å are neglected and the resulting set of considered interaction energies are summarized in Table 1.

Table 1: Energy contributions arising from hydrogen interaction up to third next neighbors (3nn).

interaction	distance	energy
1nn, fcc-hcp	1.82 Å	0.55 eV
2nn, hcp-hcp	2.34 Å	0.09 eV
2nn, fcc-fcc	2.37 Å	0.09 eV
3nn, fcc-hcp	2.62 Å	0.04 eV

3. METROPOLIS MONTE CARLO SIMULATIONS

This section gives a summary of the conducted Metropolis Monte Carlo Simulations as well as the process that led to a first parameterization necessary to connect these simulations to the findings obtained by ab initio calculations as described in the previous section.

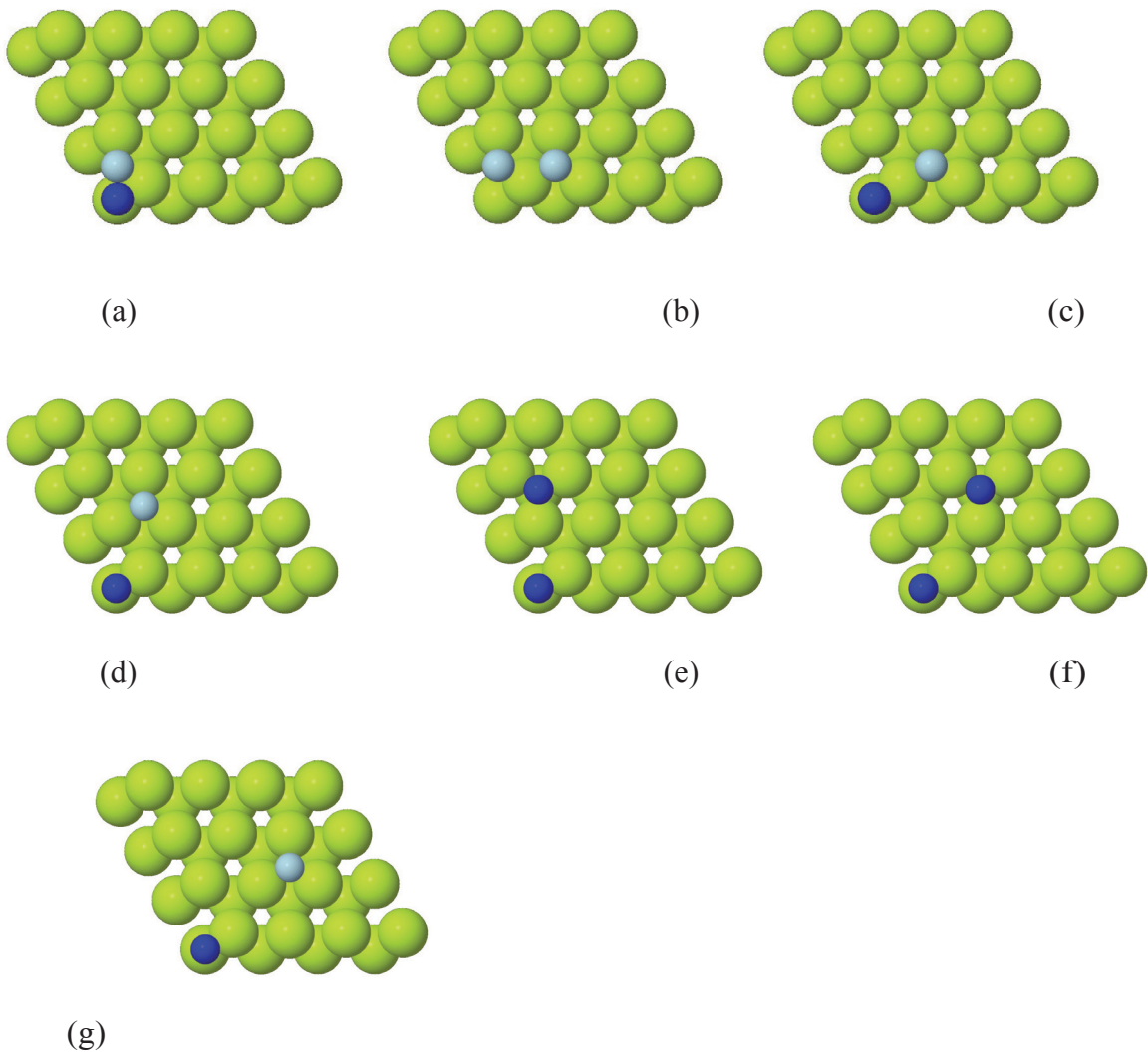


Figure 3: Representative selection of initial configurations relaxed to examine the interaction of hydrogen adsorbed to the beryllium surface.

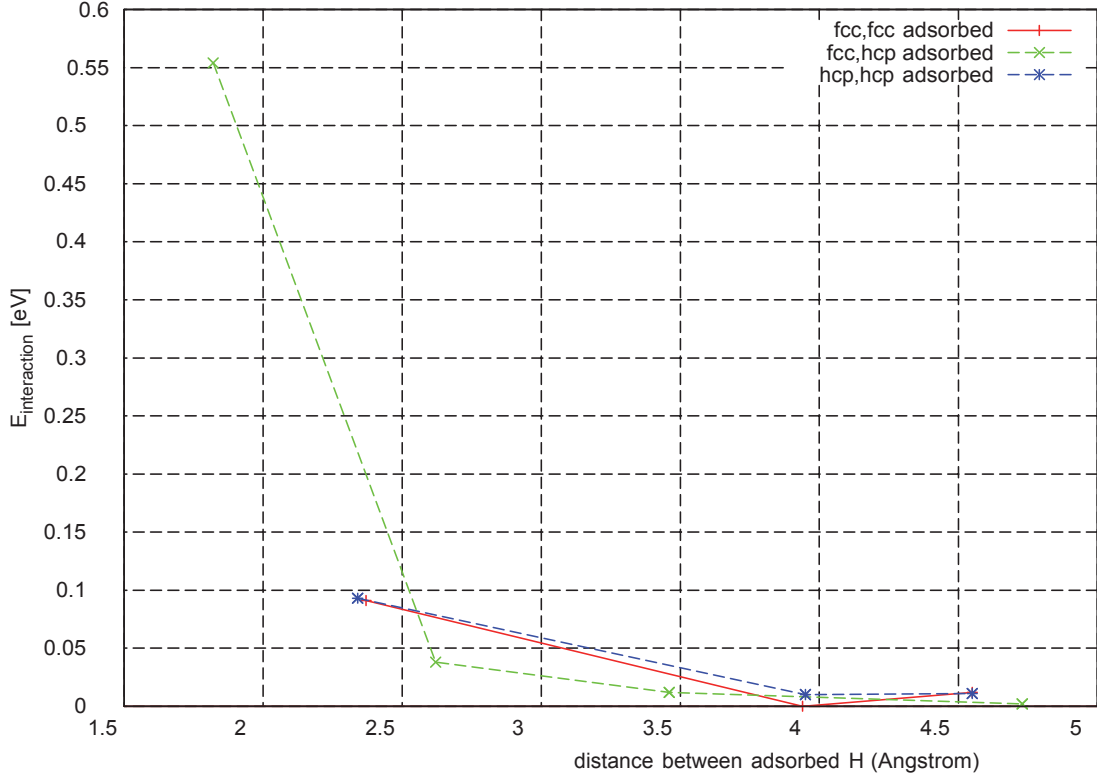


Figure 4: Interaction energy of hydrogen atoms versus the distance between them.

3.1 Parameterizing Ab Initio Energies

While ab initio calculations reliably yield the total groundstate energy, they are rather computationally expensive. Thus, ab initio calculations are limited to very small simulation cells. Our approach therefore is to apply the cluster expansion method [SDG84, Jan12a] for the parameterization of total energies of small systems in a way that allows to predict the energy of larger systems.

We attempt to map this system onto a rigid lattice gas model. [Jan12b] In this model hydrogen atoms are allowed to occupy only two different adsorption sites and their interactions amongst each other as well as with the beryllium atoms are described by a model hamiltonian including single particle, pairwise and if necessary higher order contributions. [SDG84, Jan12a]

In this model every possible configuration $\vec{\sigma}$ is described by site occupancies σ_i on the given lattice of adsorption sites. The energy of the system E_{sys} can be approximated using the cluster expansion as

$$E_{sys}(\vec{\sigma}) - E_{slab} = \sum_i E_i \sigma_i + \sum_{i,j} E_{(i,j)} \sigma_i \sigma_j + \sum_{i,j,k} E_{(i,j,k)} \sigma_i \sigma_j \sigma_k + \dots \quad (4)$$

The cluster expansion thus links the total system energy systematically to sums of “cluster” contributions associated with single particle energies E_i , pairwise interaction energies $E_{i,j}$, and so on. This representation is exact if all terms of all sums are taken into account, thus yielding an infinite expression which leads to the necessity to truncate the expansion. We chose to truncate (4) after the second and/or after the third order considering either pairwise interactions only, or adding interactions between three hydrogen atoms, if necessary.

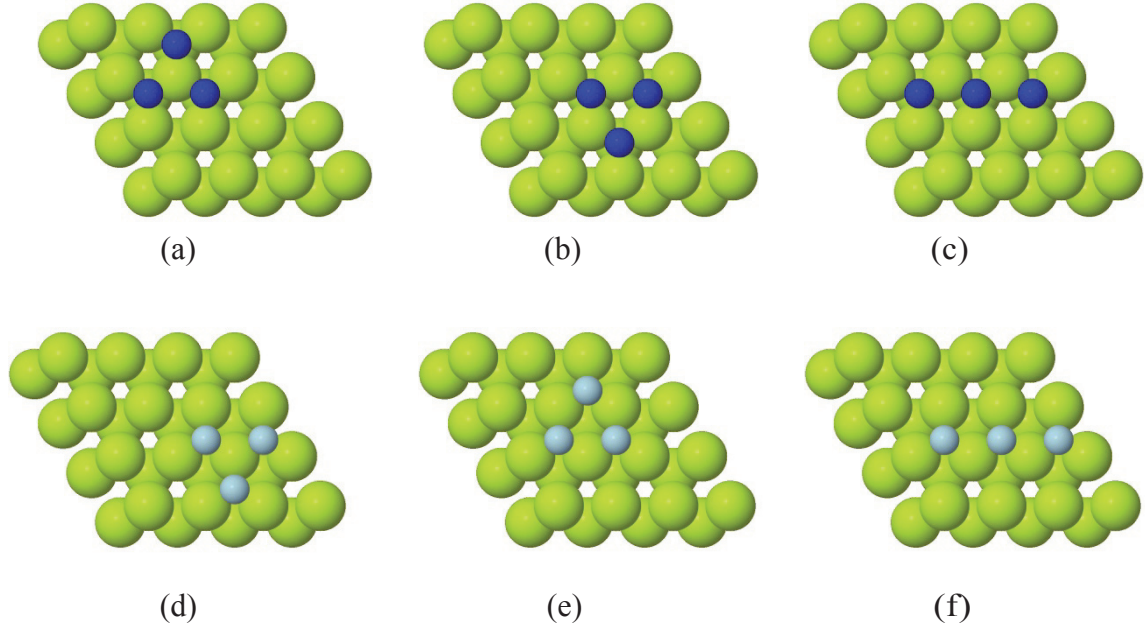


Figure 5: Additional clusters necessary to include contributions due to three particle interactions.

In both cases, every sum in (4) was truncated as suggested by the hydrogen interaction range found in the previous section and summarized in Table 1. This leads to the consideration of cluster interactions corresponding to those shown in Figures 3a, 3b plus its HCP counterpart, and 3c for the truncation at pairwise interactions and, addition ally, cluster interactions corresponding to clusters shown in Figure 5 for the truncation including contributions due to triple hydrogen interactions. This approach leads to systems of linear equations of the form of (4) which can be solved approximately by choosing optimal sets of effective interaction energies.

The interaction energies associated with the considered clusters are optimized to minimize the overall error

$$\Delta E = \sum_{systems} (E_{sys} - E_{ce})^2, \quad (5)$$

where E_{sys} is the ab initio result and E_{ce} is the estimation based on the truncated cluster expansion of a given system using the least squares (“lstsq”) algorithm provided by the “scipy” library [JOP+]. The sum in this expression extends over the systems containing only the clusters themselves and additionally those shown in Figures 6 plus their hcp-fcc-interchanged counterparts. The results of these optimizations are summarized in Table 2.

As this work is done as a part of a multiscale modeling approach to desorption, the aim of our simulation is to find an upper bound for a critical hydrogen coverage that forces the adsorbed hydrogen to occupy first neighbor sites as shown in Figure 3a. These type of patterns are known to be necessary precursors for the associative desorption process as suggested by our ab initio molecular dynamics simulations. From this perspective the relatively large errors seem to be acceptable, especially considering the overestimation of the repulsive interaction depicted in Figure 3a will tend to give rise to a higher upper bound. As the additional three particle interactions do not lead to a significant reduction of the overall estimation error (cf. total errors given in tab. 2), the purely pairwise truncation is deployed in the following Metropolis Monte Carlo Simulations.

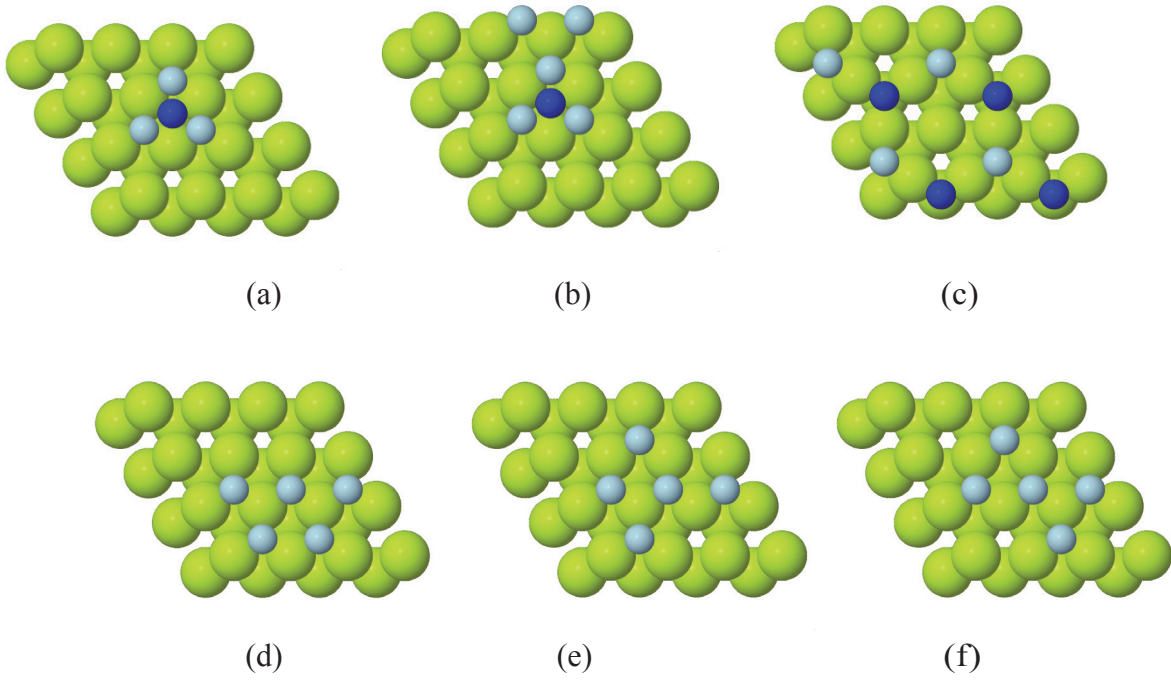


Figure 6: Representative selection of estimated structures using the truncated cluster expansions. Additionally to the selection shown here, their hcp-fcc-interchanged counter-parts were also estimated.

3.2 Metropolis Monte Carlo Simulations

We implemented a Metropolis Monte Carlo code that samples for minimal energy configurations using the truncated cluster expansion found as described in the previous subsection. The algorithm consists of the following procedure:

1. Generate a random occupation of a given coverage θ .
2. For every adsorbed hydrogen atom and until a given threshold value $m(\theta)$ is reached:
 - Check for possible diffusion hops to directly adjacent (1NN), empty sites.
 - Randomly choose one of those diffusion hops.
 - If the system energy would decrease, always execute the hop.
 - Otherwise, do the hop with a probability $p_T(\Delta E) = \exp\left(-\frac{\Delta E}{k_B T}\right)$.
 - Save system configuration if the energy is the lowest energy found so far.
3. Write minimal energy system configuration.

In the conducted overall 75 runs per coverage, the following measures were taken to avoid trapping in local energy minima. The initial random occupations consisted of those with equally occupied HCP and FCC sites, as well as those made purely out of FCC or HCP sites. The minimum number of possible moves per hydrogen atom was chosen to be $m(\theta) = \theta \cdot \text{sites} \cdot (1 - \theta) \cdot \text{sites}$, which implements the simple rule of giving every adsorbed hydrogen as many chances to do a diffusion hop as there are free adsorption sites in the system. For the chosen system size of 20000 sites this corresponds to thresholds of up to 100 million moves per run. Furthermore, runs were performed at three different “temperatures” T , making energetically unfavorable hops an impossible, a rare or a frequent event. Choosing those runs

that led to the smallest configuration energies then yields the outcomes shown in figures 7, 8a and 8b. Figure 7 shows the estimated adsorption energy per hydrogen atom referenced to the hydrogen molecule as given by

$$E_{ads} = \frac{E_{ads} - E_{slab} - \frac{n}{2} \cdot E_{molecule}}{n}$$

for n adsorbed hydrogen atoms with the total energy of the hydrogen molecule $E_{molecule}$. Figures 8a and 8b show the occupation of HCP and FCC adsorption sites in the random, initial configuration and in the configuration with lowest energy found, respectively.

Table 2: Optimization results for the pairwise and triplewise cluster expansion truncations. The estimation errors ΔE_{pair} and ΔE_{triple} are normalized to the number of adsorbed hydrogen atoms, ΔE is calculated as given by (5).

structure #	ΔE_{pair} eV	ΔE_{triple} eV	figure/description
1	0.0	-0.01	fig. 3b/FCC-FCC-2NN
2	-0.01	0.0	interchanged fig. 3b/HCP-HCP-2NN
3	0.06	0.06	fig. 3a/FCC-HCP-1NN
4	0.03	0.02	fig. 3c/FCC-HCP-3NN
5	-0.02	-0.03	single H, on FCC site
6	-0.03	-0.04	single H, on HCP site
7	0.01	0.0	fig. 5a
8	0.02	0.01	fig. 5b
9	-0.02	0.01	fig. 5c
10	0.01	0.0	fig. 5d
11	0.02	-0.01	fig. 5e
12	-0.02	0.01	fig. 5f
13	-0.02	-0.02	fig. 6a
14	0.02	0.01	interchanged fig. 6a
15	-0.04	-0.03	fig. 6b
16	-0.03	-0.01	interchanged fig. 6b
17	-0.01	-0.01	fig. 6c
18	0.0	0.0	fig. 6d
19	0.0	0.01	interchanged fig. 6d
20	0.01	0.0	fig. 6e
21	0.02	0.01	interchanged fig. 6e
22	0.0	0.0	fig. 6f
$\sqrt{\Delta E}$	≈ 0.107	≈ 0.092	

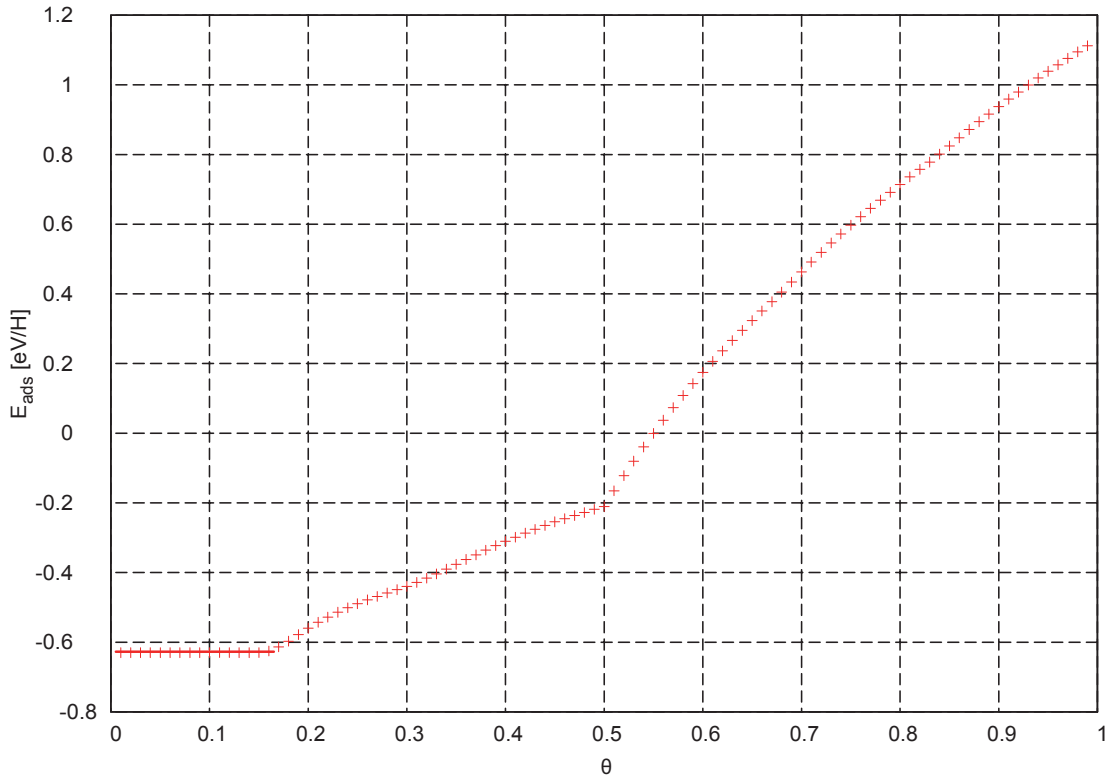
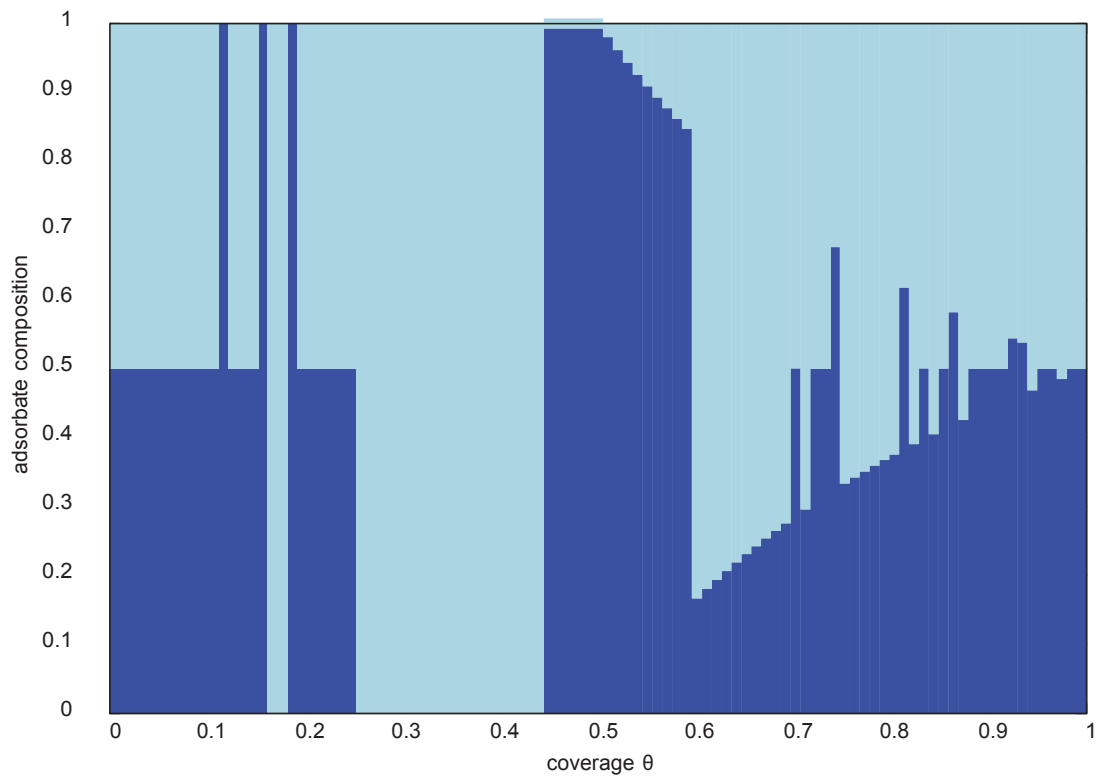


Figure 7: Plot of the adsorption energy per hydrogen referenced relative to the hydrogen molecule versus coverage θ .

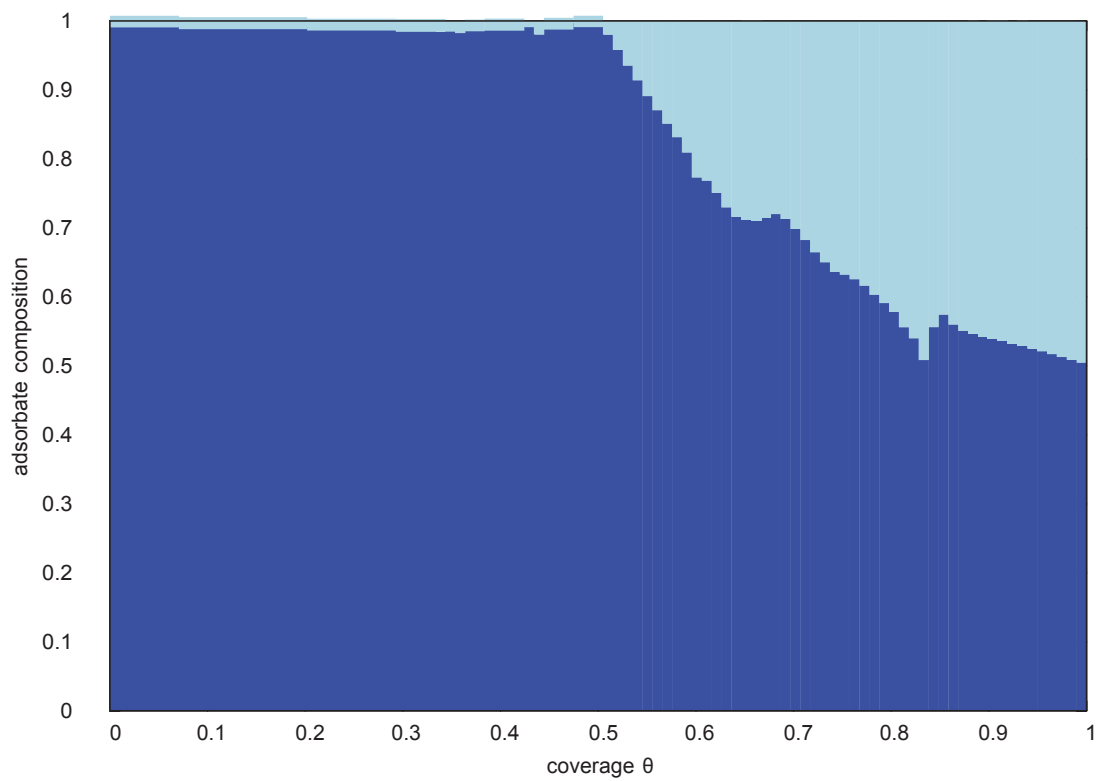
4. DISCUSSION AND CONCLUSIONS

We find the HCP and FCC adsorption sites to be stable at low coverages with the HCP site being the energetically favorable adsorption site which is in agreement with the findings of Stumpf and Feibelman [SF95]. However, our findings thereby disagree with a more recent study [All08], which finds the adsorption sites to be right within the first beryllium layer instead of slightly elevated above it and also finds additional stable sites up to $\frac{12}{9}$ adsorbed hydrogen atoms per beryllium atom in the first layer of the slab. A common finding of previous ab initio examinations of hydrogen adsorbed on the basal beryllium surface is a stable bridge adsorption site, see e.g. [SF95, All08, Fei93]. We think this might be an artifact introduced by the small 1×1 simulation cells deployed in these calculations, as those naturally lead to high coverages and the enforcement of a symmetry that rules out superstructures in the adsorbed hydrogen layer by periodic boundary conditions.

The truncation of the cluster expansion at pairwise interactions is a preliminary choice to find a trade-off between accuracy and calculation speed. The accepted errors seem to be too large to consider the current cluster expansion an accurate representation of the actual energetics and certainly needs further refinements. Ideally, the estimation error should not substantially exceed the accuracy of the ab initio calculations estimated to be of about 0.01 eV per atom for any structure. Also, the current selection of the structures whose energies were calculated using VASP might not be completely representative, particularly because it currently lacks structures of high coverages.



(a) initial composition



(b) final composition

Figure 8: Plots of occupied adsorption site compositions versus coverage θ , darker color indicates HCP portion, lighter FCC portion.

The dependence of the adsorption energy per hydrogen atom on the coverage depicted in Figure 7 shows a nearly constant adsorption energy corresponding to the adsorption of hydrogen at HCP sites up to a coverage $\theta \approx 0.15$. This feature can readily be explained by the observation that the hydrogen-hydrogen interactions extend to third nearest neighbors (12 neighbors), thus, at coverages below $\frac{2}{13} \approx 0.154$, hydrogen can be distributed on the surface evenly at HCP sites with distances greater than the interaction range effectively eliminating any interactions among the hydrogen altogether. With the considered hydrogen interactions coming into play for $\theta \gtrsim 0.15$, the adsorption energy per hydrogen atom starts to decrease and evolves into a cusp at $\theta = 0.5$. The occupied adsorption site compositions given in Figures 8a and 8b show that until a coverage of 0.5, every available HCP adsorption site is occupied independently of the initial composition of the occupied sites, thus avoiding first neighbor interactions completely. The steep slope setting in at $\theta > 0.5$ marks the onset of the occupation of FCC sites with unavoidable first neighbor interactions. As mentioned above, first neighbor fcc-hcp pairs are necessary for associative desorption. The present simulations imply an upper bound for the critical coverage given by the chosen truncated cluster expansion of $\theta = 0.5$.

As already noted, the chosen cluster expansion definitely needs further refinement. Considering the largest possible critical coverage of 0.5 monolayer was reproduced, a natural starting point seems to be the cross validation of the truncated expansion using several structures of high coverages up to $\theta = 0.5$. If the predicted energies for these configurations differ significantly from those energies obtained by ab initio calculations, a refinement of the truncation is certainly necessary. Moreover, considering there are no degrees of freedom which may explicitly address the relaxation of beryllium atoms in response to the presence of hydrogen within our rigid lattice type of approach suggests additional degrees of freedom might be useful to effectively account for those beryllium relaxations.

5. ACKNOWLEDGMENTS

This work, supported by the European Communities under the contract of association between EURATOM and Karlsruhe Institute of Technology, was carried out within the framework of the European Fusion Development Agreement. The views and opinions expressed herein do not necessarily reflect those of the European Commission.

REFERENCES

- [All08] A. Allouche. Density functional study of hydrogen adsorption on beryllium (0001). *Phys. Rev. B*, 78:085429, Aug 2008.
- [Blö94] P. E. Blöchl. Projector augmented-wave method. *Phys. Rev. B*, 50:17953–17979, Dec 1994.
- [CO02] V.P. Chakin and Z. Ye Ostrovsky. Evolution of beryllium microstructure under high-dose neutron irradiation. *Journal of Nuclear Materials*, 307–311, Part 1(0):657 – 663, 2002.
- [EIB+99] F Elio, K Ioki, P Barabaschi, L Bruno, A Cardella, M Hechler, T Kodama, A Lodato, D Loesser, D Lousteau, N Miki, K Mohri, R Parker, R Raffray, D Williamson, M Yamada, W Daenner, R Mattas, Y Strebkov, and H Takatsu. Engineering design of the ITER blanket and relevant research and development results. *Fusion Engineering and Design*, 46(2–4):159 – 175, 1999.

- [Fei93] Peter J. Feibelman. Structure of h-covered be(0001). *Phys. Rev. B*, 48:11270–11276, Oct 1993.
- [HDF+03] S. Hermsmeyer, B. Dolensky, J. Fiek, U. Fischer, C. Kohly, S. Malang, P. PeresIavtsev, J. Rey, and Z. Xu. Revision of the EU helium cooled pebble bed blanket for demo. In *Fusion Engineering*, 2003. 20th IEEE/NPSS Symposium on, pages 440–445, 2003.
- [Jan12a] A.P.J. Jansen. How to get kinetic parameters. In *An Introduction to Kinetic Monte Carlo Simulations of Surface Reactions*, volume 856 of *Lecture Notes in Physics*, pages 73–119. Springer Berlin Heidelberg, 2012.
- [Jan12b] A.P.J. Jansen. A stochastic model for the description of surface reaction systems. In *An Introduction to Kinetic Monte Carlo Simulations of Surface Reactions*, volume 856 of *Lecture Notes in Physics*, pages 13–36. Springer Berlin Heidelberg, 2012.
- [JOP+] Eric Jones, Travis Oliphant, Pearu Peterson, et al. *SciPy: Open source scientific tools for Python*, 2001.
- [KF96a] G. Kresse and J. Furthmüller. Efficiency of ab-initio total energy calculations for metals and semiconductors using a plane-wave basis set. *Computational Materials Science*, 6(1):15 – 50, 1996.
- [KF96b] G. Kresse and J. Furthmüller. Efficient iterative schemes for ab initio total-energy calculations using a plane-wave basis set. *Phys. Rev. B*, 54:11169–11186, Oct 1996.
- [KJ99] G. Kresse and D. Joubert. From ultrasoft pseudopotentials to the projector augmented-wave method. *Phys. Rev. B*, 59:1758–1775, Jan 1999.
- [LK92] V. Lossev and J. Küppers. Interaction of hydrogen atoms with beryllium (0001) surfaces. *Journal of Nuclear Materials*, 196–198(0):953 – 957, 1992. *Plasma-Surface Interactions in Controlled Fusion Devices, Proceedings of the Tenth International Conference on Plasma-Surface Interactions in Controlled Fusion Devices*.
- [MP89] M. Methfessel and A. T. Paxton. High-precision sampling for brillouin-zone integration in metals. *Phys. Rev. B*, 40:3616–3621, Aug 1989.
- [PW92] John P. Perdew and Yue Wang. Accurate and simple analytic representation of the electron-gas correlation energy. *Phys. Rev. B*, 45:13244–13249, Jun 1992.
- [RFB+97] A.R Raffray, G Federici, V Barabash, H.D Pacher, H.W Bartels, A Cardella, R Jakeman, K Ioki, G Janeschitz, R Parker, R Tivey, and C.H Wu. Beryllium application in iter plasma facing components. *Fusion Engineering and Design*, 37(2):261 – 286, 1997.
- [RLd08] W. Van Renterghem, A. Leenaers, and S. Van den Berghe. Tem investigation of long-term annealed highly irradiated beryllium. *Journal of Nuclear Materials*, 374(1–2):54 – 60, 2008.
- [SDG84] J.M. Sanchez, F. Ducastelle, and D. Gratias. Generalized cluster description of multicomponent systems. *Physica A: Statistical Mechanics and its Applications*, 128(1–2):334 – 350, 1984.
- [SF95] Roland Stumpf and Peter J. Feibelman. Interaction of hydrogen with the be(0001) surface. *Phys. Rev. B*, 51:13748–13759, May 1995.
- [VCU+98] S.P. Vagin, P.V. Chakrov, B.D. Utkelbayev, L.A. Jacobson, R.D. Field, and H. Kung. Microstructural study of hydrogen-implanted beryllium. *Journal of Nuclear Materials*, 258–263, Part 1(0):719 – 723, 1998.

Numerical research of the beryllia ceramics formation process

U. K. Zhapbasbayev¹, G. I. Ramazanova¹, Z. K. Sattinova²

¹*Kazakh-British Technical University, Almaty, Kazakhstan*

²*L.N. Gumilyev Eurasian National University, Astana, Kazakhstan*

e-mail: gaukhar.ri@gmail.com

ABSTRACT

Simulation results of the formation process of the ceramic fabrications by a hot molding method are presented. Mathematical model describes motion and heat exchange of the liquid thermoplastic slurry of beryllia including the aggregate state change. Velocity and temperature fields during the formation process in the bushings with flat cavity are obtained. Heat flow distribution at the wall of the form-building cavity is demonstrated. The increase of the slurry density during the transition from the liquid state into the viscous–plastic and solid–plastic states is defined.

KEYWORDS

Thermoplastic slurry; Formation process; Solidification; Viscous–plastic state; Solid–plastic state

1. INTRODUCTION

The method of hot molding includes motion and heat exchange of the slurry in the liquid state, as a solid–liquid mixture and as a solid–plastic mixture [1,2]. At stages of filling the form-building cavity and holding under pressure, it is very important to ensure a most structure destruction for obtaining the homogeneous slurry [2]. It is achieved by ultrasonic (US) exposure [2,3]. Minimal friction upon walls of the form-building cavity and maximal plasticity must be reached during the solidification process, to avoid the destruction of the newly formed structure of the molding.

Hydrodynamics of thermoplastic slurry during molding relates to the class of the physical processes of flow and deformation. Slurry flow maintains its configuration after leaving the feeder. It was found during experiments, that for considered molding velocities, the flow of the thermoplastic slurry in the casting mould is laminar [2]. The slurry arrives in the mold at the temperature of 75°C and cools down up to 45°C, at which the molding can be extracted from the mold without buckling [2].

Development and realization of the hot molding method mainly have an empirical nature [5,6], and carrying out of the detailed analysis of the motion and heat exchange will allow to more soundly study the ceramics formation process. Below, the modeling of the ceramics formation process of beryllia by hot molding method is presented.

2. RHEOLOGICAL MODEL OF THE THERMOPLASTIC SLURRY

Thermoplastic slurry (high-viscous suspension) is a two phase dispersed system, where solid mineral phase is beryllia powder, and liquid phase is an organic binder. Organic binder consists of 3 components: paraffin, beeswax and oleic acid in the ratio of 0.82: 0.15: 0.03. Thermoplastic slurry with thixotropic nature of flow can be related to viscous–plastic fluids of Shvedov–Bingham within the range of shear rate of $0.005 - 1200s^{-1}$ [2,4]:

$$\tau = \tau_0 + \mu \frac{\partial u}{\partial y} \quad (1)$$

where τ is the shear stress; τ_0 is yield point; μ is plastic viscosity coefficient, $\partial u/\partial y$ is the change of the longitudinal velocity along y coordinate.

Ultrasonic exposure influences on the rheological properties of the slurry. Plastic viscosity coefficient, μ , and yield point, τ_0 , of the slurry depend on temperature, T , and mass fraction of the binder, ω . The experimental data of μ and τ_0 before ultrasonic exposure for the binder mass fraction $\omega = 0.117$ are described by empirical dependences according to the experimental data of [2,5,6]:

$$\mu(T) = 293.6259 \cdot \exp(-0.05816 \cdot T) \quad (2)$$

$$\tau_0(T) = 11.4 + 11.41 \cdot \exp\left(-\frac{T-70.05}{5.47}\right) \quad (3)$$

and after ultrasonic exposure:

$$\mu(T) = 629.544 \cdot \exp(-0.0709 \cdot T) \quad (4)$$

$$\tau_0(T) = 18.1 + 8.3 \cdot \exp\left(-\frac{T-69}{4.8}\right) \quad (5)$$

The temperature is defined in Celsius's $^{\circ}C$ in empirical dependences (Eqs. (2)–(5)).

Density of the thermoplastic slurry is defined by the concentration of the binder and densities of the beryllia powder and the binder:

$$\rho = \frac{\rho_{ber} \cdot \rho_{bin}}{(1-\omega)\rho_{bin} + \omega\rho_{ber}} \quad (6)$$

where ρ_{ber} is the density of the beryllia, ρ_{bin} is the density of the binder, ω is relative mass content of the binder normalized to unity.

Density of the binder depends on the temperature and is determined from empirical equation according the experimental data [6]:

$$\rho_{bin}(T) = 0.852 + 0.0725 \cdot \cos[\pi(0.01786 \cdot T - 5.3274)] \quad (7)$$

The density of the beryllia is $\rho_{ber} = 3.02 \text{ g/cm}^3$. The density of the binder ρ_{bin} in the range of temperature between $75^{\circ}C$ and $45^{\circ}C$ is changed within 0.7840 g/cm^3 and 0.8845 g/cm^3 and the density of the thermoplastic slurry during solidification increases from 2.2643 g/cm^3 to 2.3548 g/cm^3 .

As it was determined experimentally in [1,4,5], ultrasonic exposure has almost no influence on either thermal conductivity or thermal capacity. Both the thermal conductivity, λ , and thermal capacity, c_p , depend on the temperature in accordance with (8) and (9):

$$\lambda(T) = 1.6 + 4.8 \cdot \exp(-0.017 \cdot T) \quad (8)$$

$$c_p(T) = 70 + 1070 \cdot \exp(0.0027 \cdot T) \quad (9)$$

Thus, rheological properties of the beryllia thermoplastic slurry are functions of temperature, and an aggregate transformation of liquid suspension into solid–plastic state during the forming process is occurred.

3. MATHEMATICAL MODEL

A flow and a heat exchange of thermoplastic slurry in a bushing are considered. The bushing has a form-building flat cavity (Fig.1). Heat exchange with the coolant occurs on the outer surface of the bushing.

The flat cavity has a thickness of $2y_1 = 0.0015\text{ m}$, a width of $B = 0.03\text{ m}$ and a length of $L = 0.071\text{ m}$. The cooling contour of the bushing is divided into 3 parts. Temperature of the cooling water in the first part is $\theta_1 = 73^\circ\text{C}$, in the second part is $\theta_2 = 59^\circ\text{C}$, in the third part is $\theta_3 = 45^\circ\text{C}$.

The liquid slurry flows in the cavity with the initial temperature of $\theta_0 = 75^\circ\text{C}$. The mass of slurry is cooled and solidified during the movement. At the exit of the cavity, it becomes a structural form. Motion of the thermoplastic slurry is a laminar flow. The feature of the beryllia slurry is its high thermal conductivity: however Prandtl number $Pr = \mu c_p / \lambda$ is much higher than unity due to high viscosity of the thermoplastic slurry. Density of the slurry is variable and increases with solidification.

The problem is studied in Cartesian axes of z and y . OZ axis coincides with the cavity axis direction, and OY axis is radially directed to the cavity axis. Molding velocity is directed vertically downward along the axis OZ . Radial component of the velocity along the axis OY originates from the cooling of the liquid slurry on the side of the wall. An intensive circulation of water occurs in the cooling contours. Therefore wall temperature of each part of the cavity is believed to be equal to the temperature of the cooling fluid.

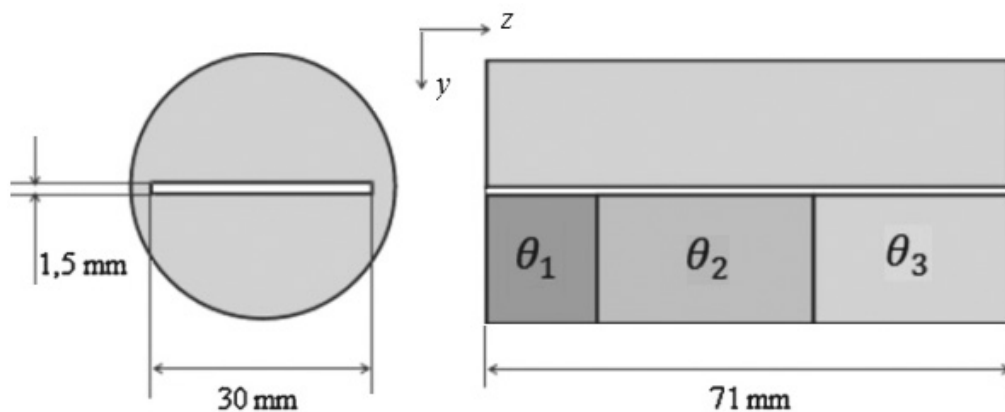


Fig. 1. Bushing diagram of a flat cavity

Rheological properties of the liquid slurry are changed as a result of solidification, and the heat of phase transition is released on the surface of the aggregate transition. Cooling of the slurry may lead to the irregularity of the temperature profile and rheological properties of the pressed out slurry. Solidification begins on the side of the wall, while the slurry may be in liquid state in the center of the cavity. As a result, replenishment by the liquid slurry for the compensation of internal volume shrinkage in the cooling zone of the cavity may occur.

The motion of the slurry is considered to be steady-state along the direction of the molding velocity and for its investigation a set of motion equations of non-Newtonian fluids involving the Shvedov-Bingham model for expression of τ according to Eq. (1) is used [9,10]:

$$\rho u \frac{\partial u}{\partial z} + \rho v \frac{\partial u}{\partial y} = -\frac{dp}{dz} + \frac{\partial}{\partial y} \left(\mu \frac{\partial u}{\partial y} \right) + \frac{\partial \tau_0}{\partial y} + \rho g \quad (10)$$

$$\frac{\partial \rho u}{\partial z} + \frac{\partial \rho v}{\partial y} = 0 \quad (11)$$

$$\rho u c_p \frac{\partial T}{\partial z} + \rho v c_p \frac{\partial T}{\partial y} = \frac{\partial}{\partial y} \left(\lambda \frac{\partial T}{\partial y} \right) + H_k \left(u \frac{\partial \rho}{\partial z} + v \frac{\partial \rho}{\partial y} \right) + \mu \left(\frac{\partial u}{\partial y} \right)^2 \quad (12)$$

The following notations are here used: z, y – axial and radial coordinates; u, v – components of the velocity vector; $p, \rho, T, \tau_0, c_p, \mu, \lambda$ – pressure, density, temperature, shear stress, coefficients of thermal capacity, viscosity and heat conductivity of the slurry, respectively.

The heat of aggregate transition of the beryllia slurry is found by experimental data and is equal to $H_k = 7800 \text{ J/kg}$ [4]. Rheological properties of the slurry are expressed according to the previously mentioned empiric equations (2) – (9).

Condition of conservation of the mass flow rate permits to define a pressure gradient for pressing out thermoplastic slurry from the molding mold [9]:

$$\int_S \rho u \, dS = \rho_0 u_0 S \quad (13)$$

where S is cross-section area of the cavity.

Both velocity and temperature distributions at the inlet are considered to be constant along the cross-section of the cavity and all the thermo-physical properties of the slurry are constant:

$$\text{if } z = 0: \quad u = u_0, \quad v = 0, \quad T = \theta_0 \quad (14)$$

Symmetry conditions are assumed at the cavity axis:

$$\text{if } z > 0, \quad y = 0: \quad \frac{\partial u}{\partial y} = \frac{\partial T}{\partial y} = v = 0 \quad (15)$$

For the longitudinal velocity, the conditions of sticking and sliding are set at the wall, depending on the aggregate state of the slurry. It is assumed that the temperature of the cavity wall at each zone is maintained to be constant and equal to the temperature of the cooling fluid. Marking the water temperature in the first, second and third contours as $\theta_1, \theta_2, \theta_3$, respectively, the boundary conditions for the temperature at the wall are achieved [12]:

$$T = \theta_1, \quad u = 0 \quad (16)$$

if $0 \leq z < l_1, \quad y = y_l$.

$$T = \theta_2, \quad -\frac{dp}{dz} = \frac{1}{y_1} \left[\tau_{0w} + \left(\mu \frac{\partial u}{\partial y} \right)_w \right] \quad (17)$$

if $l_1 \leq z < l_2, \quad y = y_l$.

$$T = \theta_3, \quad -\frac{dp}{dz} = \frac{1}{y_1} \left[\tau_{0w} + \left(\mu \frac{\partial u}{\partial y} \right)_w \right] \quad (18)$$

if $l_2 \leq z < l_3, \quad y = y_l$.

Eqs. (10)–(18) can be presented in the dimensionless form for the convenience. Coordinates z, y are divided by the half thickness y_1 , velocity components u and v – by v_0 , pressure – by the value of dynamic head $\rho_0 u_0^2$, temperature T – by θ_0 , density, yield point, coefficients of thermal capacity, viscosity, thermal conductivity – by their values at the temperature θ_0 . The equations in the dimensionless form include Reynolds number Re , Prandtl number Pr and Eckert number Ec .

The system of Eqs. (2) – (13) is solved numerically at boundary conditions of Eqs. (14)–(18) [7,9]. The considered zone is broken down into elementary cells with sides $\Delta z_i, \Delta y_j$. Difference analogues of the motion equation (10) and energy equation (12) were obtained by the Crank-Nicolson method of the second order precision, and difference analogue of Eq. (11) – by two-layer scheme of the second order precision. Pressure gradient is defined by the splitting method [7,8] from the condition of flow rate conservation (Eq.(13)).

4. DISCUSSION OF THE CALCULATED DATA

Calculations were carried out for the slurry with account of rheological properties before and after ultrasonic exposure. In Fig. 2. the distributions of the temperature and the longitudinal component of the velocity in three thermal contours of the flat bushing at the thickness of the cavity of $2y_1 = 0.0015 \text{ m}$ and molding velocity of $u_0 = 0.2 \text{ m/min}$ without and with ultrasonic exposure, are demonstrated. The longitudinal component of the velocity and the temperature of the slurry at the inlet, of the channel are constant along the cross-section, and are equal to $u = u_0, T = T_0$. The profile of the longitudinal component of the velocity attains the shape of shear flow of the fluid near the inlet section due to high viscosity of the thermoplastic slurry (Fig. 2).

Sliding velocity at the wall is almost zero. Wall temperature in the first cooling contour is $\theta_1 = 73^\circ\text{C}$ and the temperature field is changed from 75°C to 73°C in this zone. Temperature isolines (isotherms) show the zones of the constant temperature and internal structure of the slurry being in liquid state.

Wall temperature is $\theta_1 = 59^\circ\text{C}$ in the second cooling contour. Dynamic viscosity, $\mu(T)$, density, $\rho(T)$, and yield point, $\tau_0(T)$, increase with temperature decrease, and viscous-plastic property of the slurry begins to be evident. The slurry slides along the cavity wall, and sliding velocity increases along the length of the second contour during motion down. It resulted in that profile of the longitudinal component of the velocity down the flow will level with constant center in the near-axial zone (Fig. 2).

A growth of heat extraction of wall in the second cooling contour leads to a reduction of the temperature field (Fig.2). There is a transition zone in the beginning of the second contour, where the temperature field is variable and expresses the transition of the slurry from the liquid state into the viscous-plastic state. The temperature of the slurry is changed from 73°C to 59°C and defines upper boundary of the zone with constant temperature 59°C . The slurry is in viscous-plastic state near the wall due to the heat extraction, while the slurry in the central part of the cavity is in a liquid state. The presence of different structural states along the cross-section results in the change of the rheological and thermo-physical properties of the slurry.

The wall temperature in the third cooling contours is equal to $\theta_3 = 45^\circ\text{C}$, which leads to the further cooling of the slurry and reduces the temperature from 59°C to 45°C in the transition

zone. According to the experimental data, change in aggregate state takes place at the temperature of $\theta_f = 55^\circ\text{C}$. In Eq. (12) for energy, the heat release during the change of aggregate state occurs due to solidification of the viscous-plastic slurry. Solidification leads to a density change of the slurry.

There are density gradients $\frac{\partial \rho}{\partial z}, \frac{\partial \rho}{\partial y}$ in the transition zone, and the heat of change of the aggregate state influences on the distribution of the temperature field.

Further growth of sliding velocity is observed in the third contour. This results in leveling of the longitudinal component of the velocity u along the cross section of the cavity and there is almost piston-like distribution of u at the outlet of the bushing (Fig. 2). The transition from viscous-plastic state (green zone in Fig. 2) into solid-plastic state (blue zone in Fig. 2) takes place in this zone, where rheological and thermo-physical properties of the slurry are homogeneous.

Comparing the temperature field of the slurry in the cavity without ultrasonic (Fig. 2a) and with ultrasonic exposure (Fig. 2b) one may notice the difference in isotherm distributions. Structural change of the slurry occupies more area in the case of ultrasonic exposure (Fig. 2b), than without ultrasonic exposure. It is explained by the increase of the slurry fluidness during ultrasonic exposure due to the change of rheological properties.

Calculation data confirm the experimental fact that, ultrasonic exposure, raising the fluidness of the slurry, reduces the molding velocity during the formation process to get ceramic fabrications.

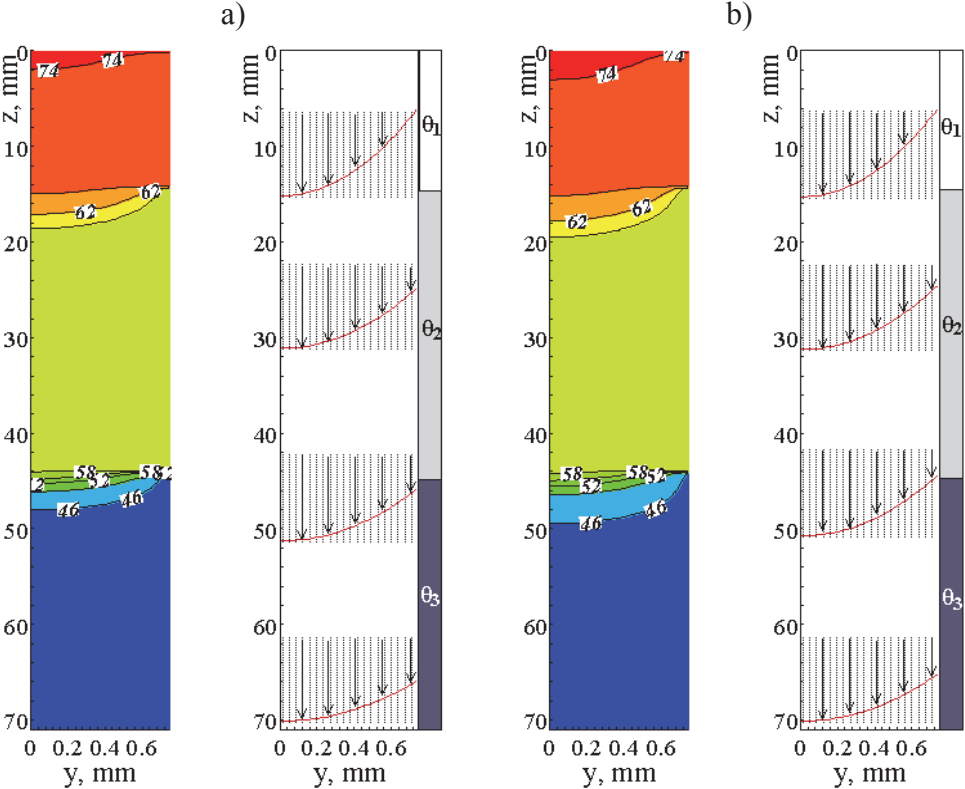


Fig. 2. Distribution of the temperature and longitudinal velocity in the cavity without (a) and with (b) ultrasonic exposure: $h = 0.00075 \text{ m}$, $u_0 = 0.2 \text{ m/min}$

Increase of molding velocity $u_0 = 0.4 \text{ m/min}$ by twice, while the other parameters stay the same, influences on the structural change of the slurry (Fig.3). Calculation data for without ultrasonic exposure (Fig.3.a) and with ultrasonic exposure (Fig.3.b) here are also shown. In contrast to the previous regime of formation, the increase of molding velocity leads to the extension of the transition zone of structural changes from one state into another. It is evident from the temperature distribution (Fig.3): the transition zone from liquid state (red) to viscous-plastic state (green) and the transition zone from viscous-plastic state (green) to solid-plastic state (blue).

Transition zones are expanded in the case with ultrasonic exposure and this is explained by a change in rheological properties of slurry and increase of slurry fluidity (Fig.3).

It can be seen from Figs.2 and 3 that transition zones have curvilinear convex surfaces with different areas. It can lead to uneven shrinkage of the slurry along the section of the form-building cavity.

The density of thermal flow at the wall describes a heat exchange between the slurry and the wall of cavity and can be expressed as:

$$q_w = -\lambda \left(\frac{\partial T}{\partial y} \right)_w$$

Variation of the density of thermal flow by the length of the cavity of flat bushing is shown in Fig.4. The wall temperature in the first cooling contour is $\theta_1 = 73^\circ\text{C}$, a small change of thermal flow density q_w at wall is observed and this is due to minor difference between the initial temperature of the hot slurry θ_0 and the wall temperature θ_1 . The reduction of wall temperature till $\theta_2 = 59^\circ\text{C}$ in the second cooling contour leads to a sharp increase of thermal flow density q_w in the narrow area of transition zone due to uneven reduction of the wall temperature from $\theta_1 = 73^\circ\text{C}$ to $\theta_2 = 59^\circ\text{C}$. Downwards by the direction of the motion, thermal flow density, q_w , steadily approaches zero due to leveling of the slurry temperature field.

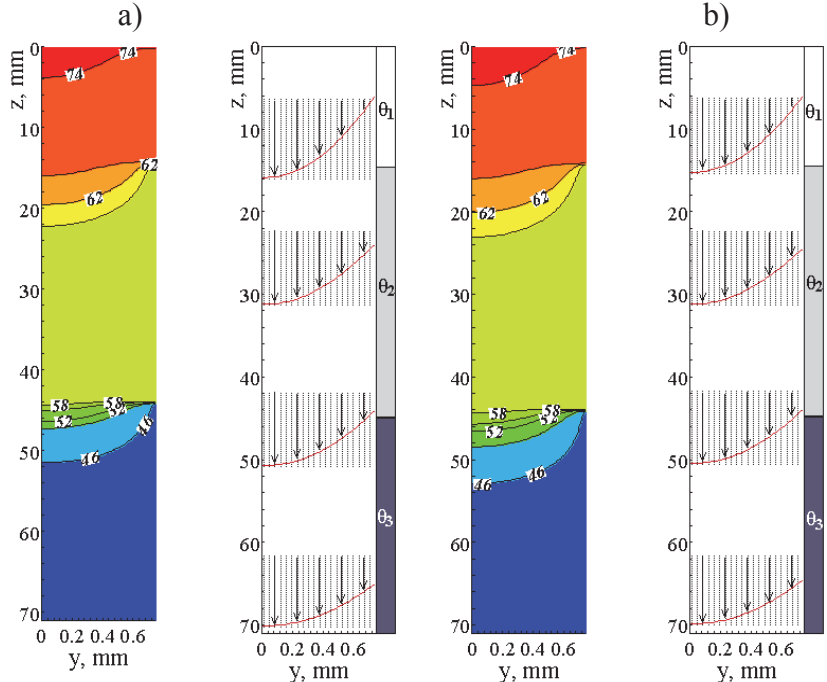


Fig. 3. Distribution of the temperature and longitudinal velocity in the cavity without (a) and with (b) ultrasonic exposure: $h = 0.00075 \text{ m}$, $u_0 = 0.4 \text{ m/min}$

Thermal flow density, q_w , in the third cooling contour changes similarly due to abrupt reduction of the wall temperature from $\theta_2 = 59\text{ }^\circ\text{C}$ to $\theta_3 = 45\text{ }^\circ\text{C}$ with a monotonic decrease by leveling of temperature field.

Process of transition of the slurry from one structural state into another in the cavity can be also analyzed through the change of the density. Change of the slurry density along the length of the axial plane of the cavity is demonstrated in the Fig.5.

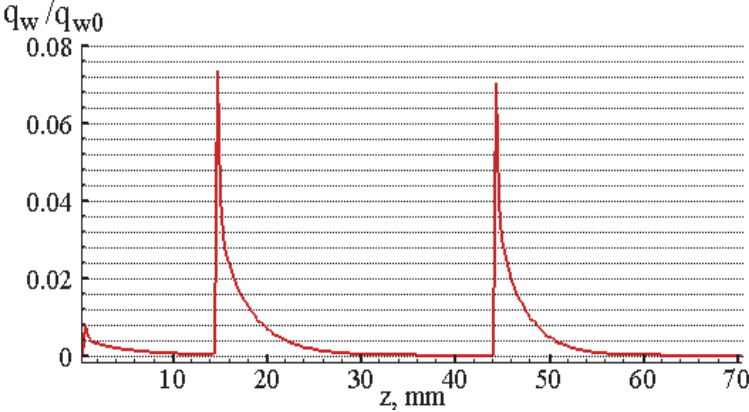


Fig. 4. Change of the thermal flow density at the wall along the length of the cavity:
 $h = 0.00075\text{ m}$, $u_0 = 0.2\text{ m/min}$

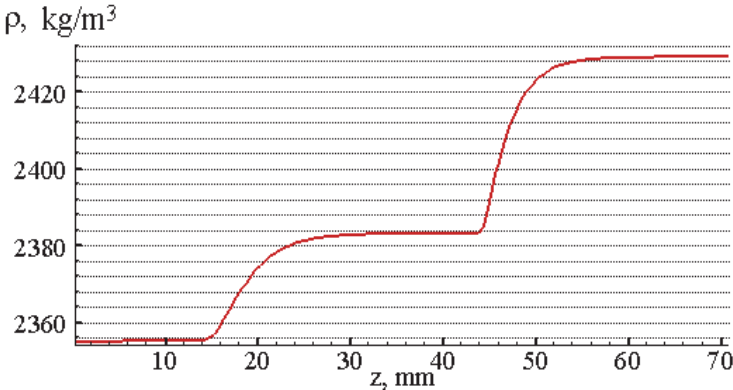


Fig. 5. Change of the density of the slurry along the length of the cavity: $h = 0.00075\text{ m}$, $u_0 = 0.2\text{ m/min}$

A change of density along the first cooling contour is small, i.e. the slurry maintains the initial liquid state. In the second contour, density of the slurry increases from 2355 to 2383 and is stable all the way of this part, i.e. a transition of the slurry from liquid state into viscous-plastic state is taken place. Density of the slurry increases from 2383 to 2429 in the third contour, the slurry is hardened and turns from viscous-plastic state into solid plastic state [5].

5. CONCLUSION

Investigation results show that the mathematical model describes all the stages of the ceramic molding including the changes of aggregate state. Ultrasonic exposure enhances the rheological properties and increases the fluidity of the thermoplastic slurry in the form-

building cavity. All the stages of the hot molding method of the thermoplastic slurry (liquid state, viscous-plastic state, solid-plastic state) can be presented by the changes of the longitudinal velocity and temperature along the length of the cavity. Density of heat flow at the wall of the form-building cavity is changed in accordance with the boundary conditions and expresses heat extraction at the wall. The slurry density increases during the transition from the liquid state into viscous plastic and solid-plastic states. Such a density distribution expresses balancing mechanism of volumetric changes of the slurry and is in a satisfactory compliance with the experiment [2,6].

Optimum conditions of the ceramic molding process by the hot molding method can be found with calculations, which will allow obtain the hardened fabrication with homogeneous structure of beryllia at the outlet.

REFERENCES

1. Akishin, G.P., Turnaev, S.K., Vaispapir, V.Ya., Gorbunova, M.A., Makurin, Yu. N., Kiiko, V.S., Ivanovskii, A.L. Thermal conductivity of beryllium oxide ceramic. *Refractories and Industrial Ceramics*, 2009; 50: 465-468.
2. Akishin, G. P., Turnaev, S. K., Vaispapir, V. Ya., Kiiko, V. S., Shein I. R., Pletneva E.D., Timofeeva M. N., Iva A. L. Composition of beryllium oxide ceramics. *Refractories and Industrial Ceramics*, 2011; 11: 377-381.
3. Dobrovolskii, A.G. Slurry Casting. Moscow: Metallurgiya, 1977. [in Russian]
4. Dvinskikh, Yu.V., Popil'skii, R.Ya., Kostin, L.I., Kulagin, V.V. Thermophysical properties of thermoplastic casting slips of some high-refractory oxides. *Ogneupory*, 1979; 12: 37–40. [in Russian]
5. Shakhov, S.A. Use of ultrasound in order to intensify molding of high-temperature thermocouple sheaths. *Refractories & Industrial Ceramics*, 2008; 49: 261-263.
6. Shakhov, S.A., Gagarin, A.E. Rheological characteristics of thermoplastic disperse systems treated with ultrasound. *Glass and Ceramics*; 2008; 65:122–124.
7. Anderson, J.D., Tannehill, J.C., and Pletcher, R.H. Computational Fluid Mechanics and Heat Transfer. Moscow: Mir, 1990. [Russian transl.]
8. Shakhov, S.A. Controlling the deformation behavior of thermoplastic slips with ultrasound. *Glass and Ceramics*, 2007; 64:354-356.
9. Zhapbasbayev, U.K., Ramazanova, G.I., Sattinova, Z.K. Mathematical model of hot-cast molding of ceramic. *Glass and Ceramics*, 2011, 68: 216-220.
10. Zhapbasbayev U.K., Kaltayev A., Bitsoyev G.D., Turnayev S.K. Hydrodynamics of moulding of ceramic articles from beryllium oxide with ultrasonic activation. *Proceedings ASME International Mechanical Engineering Congress and Exposition*, Orlando, Florida, 2005.

Molecular Dynamics Simulation of Atomic Displacement Cascades in Beryllium

V. A. Borodin^{1,2}, P. V. Vladimirov²

¹*NRC Kurchatov Institute, Kurchatov Square 1, 123182 Moscow, Russia*

²*Karlsruhe Institute of Technology, Karlsruhe, Germany*

ABSTRACT

We report a systematic molecular dynamics simulation of cascade damage production and annealing in beryllium. The studied energy range of self-ion primary recoils is 0.5-3 keV. The simulations show that point defects are produced in Be preferentially in well-separated subcascades generated by secondary and higher order recoils. A linear dependence of the point defect number on the primary recoil energy is obtained with the slope that corresponds to a formal atom displacement energy of ~ 21 eV. Most of the damage is created as single defects and the relatively high part of created point defects ($\sim 50\%$) survives the correlated recombination and becomes freely-migrating.

KEYWORDS

beryllium, cascade, simulation, molecular dynamics.

Beryllium is an important functional material for future fusion devices. The principal aim of using Be is the neutron multiplication, which means that Be parts (pebbles) in fusion reactor blanket are planned to work under intensive neutron irradiation. The fast neutrons will produce considerable amounts of both point defects and transmutation gases, which can have detrimental effect on the microstructure and macroscopic mechanical properties of Be parts. In order to predict the kinetics of microstructural development it is necessary, in particular, to know the rates of production of mobile self-defects (interstitials, vacancies and small clusters thereof) that contribute to the secondary radiation effects, such as the formation of large point defect clusters (dislocation loops, voids or gas bubbles) both inside the grain and on grain boundaries, the segregation of dopants at grain boundaries and interfaces, etc.

When fast neutrons penetrate a solid, they create considerable amounts of fast primary recoil atoms, which, in turn, create radiation damage. There exist empirical relations allowing to estimate the number N of atomic displacements for a primary recoil that has got an initial energy E , such as the Norgett-Robinson-Torrens (NRT) [Nor75] relation

$$N_{\text{NRT}} = 0.8 \frac{E}{2E_d}, \quad (1)$$

where E_d is the threshold energy for atom displacement. Unfortunately, equation (1) was derived assuming that the scattering of primary and higher order recoils can be treated in the framework of the binary collision approximation (BCA). Subsequent investigations have demonstrated that BCA is inapplicable to recoils with relatively low (keV to tens of keV) energies, which create damage in so-called collision cascades, where many atomic collisions occur in a strongly correlated mode. Correspondingly, equation (1) usually tends to distort (usually – overestimate) the number of defects produced by fast primary recoils.

Another reason for the overprediction of the defect production rate by eq. (1) is the neglect of the fact that after the cascade ballistic stage vacancy and interstitial defects are located in strongly localized regions. Before the defects leave the cascade area and diffuse into the surrounding volume, a certain part of them can be lost due to the correlated recombination.

The common technique for the estimation of damage production in collision cascades is molecular dynamics (MD). One can find in the literature detailed MD simulations of collision cascades in various materials (see e.g. [Nor98,Bac03]). However, to the best of our knowledge, no studies of cascade damage production are published for beryllium. Here we report some results of a MD investigation of point defect production and intra-cascade annealing in cascades caused in Be by fast self-ions.

The simulations were performed using the LAMMPS code [Pli95]. The interatomic forces are described with the atomic bond-order potential (ABOP) suggested in Ref. [Bjo09] modified so that at small interatomic distances (<0.8 Å) it would smoothly convert to the universal repulsive Ziegler-Biersack-Littmark potential [Zie85].

The simulation cell used in these calculations had orthorhombic shape with axis z oriented along the c -axis of hcp beryllium lattice, while x and y axes were along $\langle 1\bar{1}00 \rangle$ and $\langle 11\bar{2}0 \rangle$ directions, respectively. The simulation cell size was $184 \times 159.3 \times 180.8$ Å. The interatomic distance in the basal plane was 2.3 Å and c/a ratio – 1,572. The simulation cell contained 6.4×10^5 lattice sites. Periodic boundary conditions were applied along all three axes.

Initially several primary recoils with energies up to 10 keV were tested. These tests have demonstrated that starting from ~ 3 keV the primary ions propagated in the so-called subcascade regime, where the projectile trajectory remains straight for many interatomic distances until the projectile experiences a strong scattering on a target atom. Such knocked-on target atoms (secondary recoils) produce their own cascades ('subcascades') or, if fast enough, also propagate in the subcascade regime. Evidently, the ion propagation in such a mode can be successfully described in the BCA framework, so it makes little sense to accumulate detailed cascade statistics for primary recoil energies exceeding 3 keV. At the low-energy end, the lowest considered primary recoil energy was 0.5 keV because at lower energies the damage is created primarily in the form of individual Frenkel pairs and no cascades are produced.

Hence, the main calculations were performed for the recoil energies within the range of 0.5-3 keV (with the step of 0.5 keV) and at the temperature of 600 K. The relatively high temperature was selected in order to activate the diffusion of Be interstitials and to study the correlated recombination at post-ballistic stage. Before starting cascades, the lattice was pre-heated to 600K and equilibrated at this temperature. To launch a cascade, the momentum of one of the atoms was replaced with that corresponding to the desired primary recoil energy and oriented randomly in space. In this way, ten cascades at each energy were initiated. The time step for the MD simulation was 0.04-0.05 fs (depending on recoil energy) for the first 2 picoseconds and then switched to 1 fs. Electronic stopping was taken into account only at the stage of the primary recoil deceleration and switched off after 2 ps.

A two-stage temperature control scheme was applied during the intra-cascade defect annealing. At the first stage the simulation cell was kept at 600 K for 500-750 ps. Often this was sufficient in order to reach the state, when no interstitial-vacancy pair was separated by less than a certain cutoff ('maximum recombination distance'), selected here at the level of

15 Å). If this was not the case, the simulations were continued at elevated temperature (800 K) in order to accelerate the interstitial diffusion. The temperature during simulation was maintained using the Berendsen thermostat [Ber84].

In order to visualize point defects and their clusters, the raw MD data were post-processed using the extended Lindemann method [Bor12]. The method identifies vacant sites and displaced lattice atoms by surrounding all lattice sites with spheres of small radius (Lindemann spheres) and postulating that vacant are those sites that contain no atoms in their Lindemann spheres. Correspondingly, strongly displaced are those atoms that do not belong to any Lindemann sphere. Here the Lindemann sphere radius was taken equal to 0.7 Å.

The cascade dynamics in the current simulation can be separated into two stages. At the first (ballistic) stage the primary fast recoil generates dynamically multiple atomic displacements. The stage is very short, the peak damage is reached within 0.5-0.8 ps, while the ballistic movement of target atoms stops at 0.8-1.2 ps, depending on the primary recoil energy. Approximately 1 ps more is required for the equilibration of the remaining damage zones.

Typical samples of cascades at different primary recoil energies are shown in Fig. 1. One can easily notice that even at relatively low primary recoil energies the damage is produced predominantly by secondary and higher-order recoils. Only at the end of range the primary recoil contributes to the total damage through creation its own subcascade. Such mode of damage creation resulted in a specific spatial distribution of the damage after the end of ballistic stage: vacancies mostly decorated the cascade backbone, while interstitials were in small clouds at the ends of secondary and higher order trajectory branches.

Another characteristic feature of cascades in Be is the relatively large distance traveled by the primary recoils. In spite of quite large simulation cell dimensions, only recoils with the initial energy <2 keV remained completely within the simulation cell. At larger energies (sometimes also at 2keV, see Fig.1b) the primary recoil often crosses the cell boundary and continues in an image cell. This is not a big problem for simulation, however, because the parts of recoil trajectory in the main and in the image cells were usually well separated and the primary damage on these trajectory parts did not interact during subsequent annealing (which was always checked).

After the ballistic stage is over, the second stage of the intra-cascade annealing of closely separated vacancies and interstitials starts. To be specific, the onset of the second stage is selected here to be at 3ps.

Two typical examples of the correlated damage annealing are shown in Fig. 2. The major mode of damage annealing is the interstitial-vacancy recombination. It is due exclusively to interstitial-type defects that are mobile at 600 K, while vacancy jumps, though possible, are extremely rare at the simulation time scale. Remarkable is the relatively large recombination radius, which can reach 1 nm. After some time (~300 ps) the recombination nearly cancels out, because nearly all remaining interstitial defects shift sufficiently far from the recoil trajectory, where vacancies are concentrated.

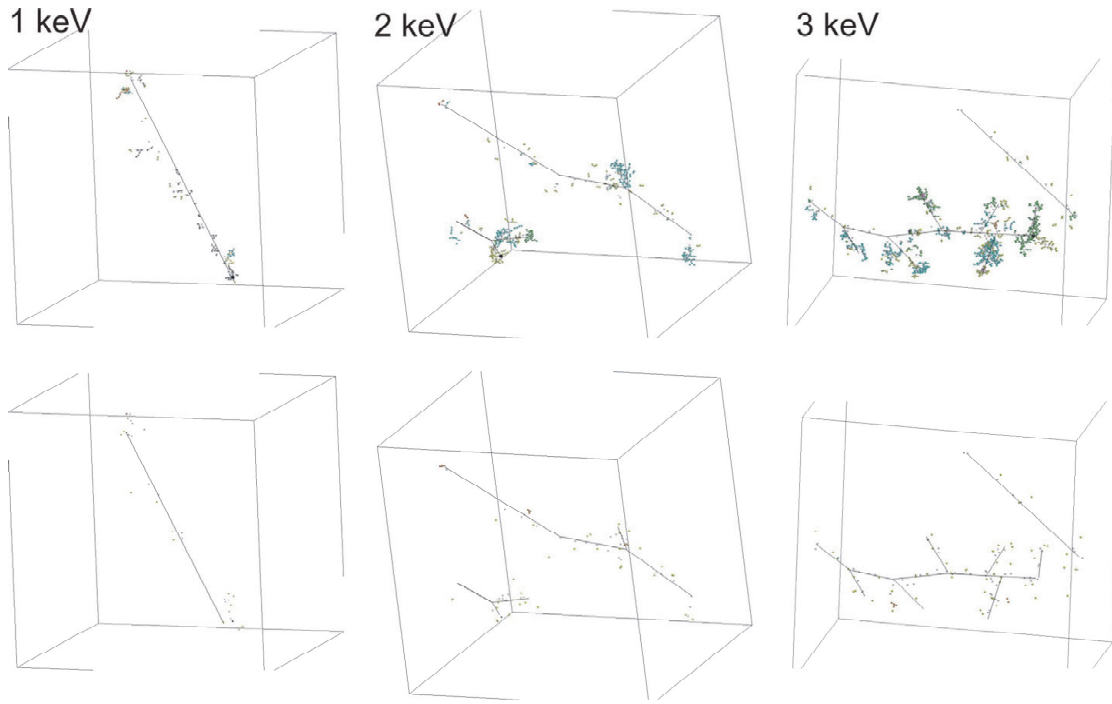


Fig. 1. Comparison of cascades at different recoil energies: close to the peak damage production (top row) and after the end of ballistic stage (bottom row). Lines mark the cascade backbones, that is the primary and secondary recoil trajectories (to guide the eye). The primary recoil trajectory start is marked by a red dot. Vacant lattice positions are shown with white spheres, while displaced atoms are coloured according to the defect size and type: light blue and blue for single interstitials and di-interstitials, yellow and orange for single vacancies and di-vacancies, respectively.

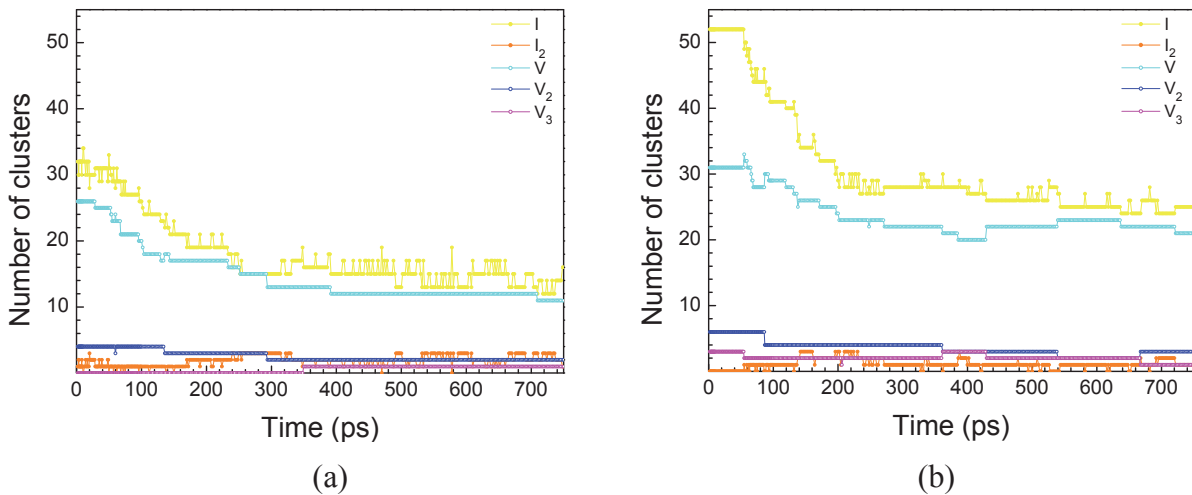


Fig. 2. The numbers of interstitials, vacancies and larger point defect clusters as a function of annealing time for cascades produced by a 2keV (a) and a 3keV (b) primary recoil. Colors correspond to defect sizes and types, as explained in the legend.

It can also be seen in Fig.2 that the major part of interstitials is in single defects. Interstitial-interstitial collisions are infrequent, though regular, but di-interstitials move even faster than single interstitials and have rather high probability to recombine with the vacancies dispersed along the primary recoil trajectory. The final average size distributions of interstitial defects after the end of correlated recombination are shown in Fig. 3. The figure confirms that the absolute majority of interstitial defects leaving the cascade region are mono-interstitials.

A relatively low share of di- and tri-interstitials (which are mobile in Be) can be also supplied as a part of freely-migrating defects.

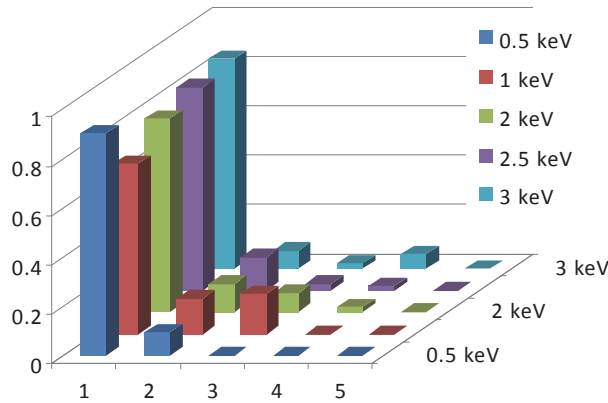


Fig. 3. The distribution of interstitial defects over sizes after long-term annealing for different recoil energies. Each bar gives the relative share of interstitials in clusters of particular size.

All vacancy clusters in the current simulations (i/e/ rare di- and tri-vacancies) were produced already at the ballistic stage. A part of them was removed during the intra-cascade annealing. However, vacancy clustering in the cascade zone after the end of the correlated recombination stage is too slow to be followed by MD.

Finally, Fig. 4 shows the variation of the total number of Frenkel pairs after the ballistic and annealing stages as a function of the primary recoil energy. As can be seen, the number of pairs generated at the ballistic stage is very similar to predictions of eq. (1) with the standard displacement energy for beryllium of $E_d = 25$ eV [Zie85]. In fact, the simulation results would be reproduced exactly using a slightly lower value of $E_d \approx 21$ eV. Interestingly, the similar dependence obtained using BCA Monte-Carlo code SRIM [Zie85] predicts less damage production than either the current simulations or NRT equation for the same displacement threshold of 25 eV.

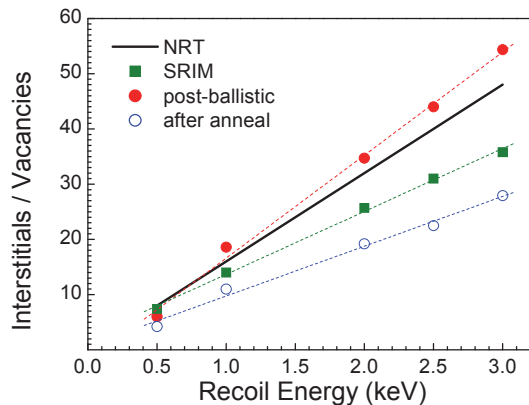


Fig. 4. The predicted numbers of Frenkel pairs after the ballistic and annealing stages vs. the primary recoil energy. For comparison, the predictions of eq. (1) and SRIM are shown. The curve marking is explained in the legend. All dot lines are to guide the eye.

After the end of the correlated recombination stage the linear dependence of the Frenkel pair number on the primary recoil energy persists, but the absolute value of the remaining defects is approximately half of that created at the ballistic stage.

CONCLUSIONS

Damage production by fast self-ions in beryllium is markedly different from that in more heavy metals. Even at relatively low primary recoil energies the displaced atoms are produced in the subcascade regime. As a result, the primary recoil trajectories are very long. The vacancies and interstitials decorate the cascade backbone, which is very different from the observations in heavier metals, where vacancies tend to form relatively compact core surrounded by a shell of interstitials. Due to the specific spatial arrangement of point defects, the correlated recombination within the cascades is relatively efficient, eliminating half of the primary damage. The interstitial defects that eventually escape from the cascade region into the bulk are nearly exclusively highly mobile mono-interstitials.

ACKNOWLEDGEMENT

The authors acknowledge the computer time grant provided by IFERC-CSC, Rokkasho, Japan in the frame of the Broader Approach in the Field of Fusion Energy Research as well as the financial support from the KIT Fusion Program.

REFERENCES

- [Nor75] M. J. Norgett, M. T. Robinson, and I. M. Torrens, Nucl. Eng. Des. 33 (1975) 50.
- [Nor98] K. Nordlund, M. Ghaly, R.S. Averback, M. Caturla, T. Diaz de la Rubia, J. Tarus, Phys. Rev. B 57 (1998) 7556.
- [Bac03] D.J. Bacon, Yu.N. Osetsky, R. Stoller, R.E. Voskoboinikov, J. Nucl.Mater. 323 (2003) 152.
- [Pli95] S. Plimpton, J.Comp. Phys., 117 (1995) 1; <http://lammps.sandia.gov>.
- [Bjo09] C. Björkas, N. Juslin, H. Timko, K. Vörtler, K. Nordlund, K. Henriksson, P. Erhart, J. Phys.: Cond. Matter 21 (2009) 445002.
- [Zie85] J.F. Ziegler, J.P. Biersack, U. Littmark, The Stopping and Range of Ions in Matter, Pergamon, New York, 1985; <http://www.srim.org>
- [Ber84] Berendsen HJC, Postma JPM., van Gunsteren WF, DiNola A, Haak JJR. Chem Phys 1984; 81:3684.
- [Bor12] Borodin VA. Nucl Instr Meth Phys Res B 2012; 282:33.

Appendix 1: Organisation



11th IEA International Workshop on Beryllium Technology (BeWS-11) 12-13 September 2013 Barcelona, Spain

For many years, the focus of the workshop has been on beryllium technology in fusion engineering development. Since 2005, the scope is expanded to include fission applications of beryllium as well.

The objective of this workshop is to disseminate results of research and technology development in areas relevant to beryllium utilization in nuclear power systems, both fission and fusion. Papers presenting original research in these topical areas are solicited for presentation and publication.

The BeYOND-V Workshop “Beryllium Opportunities for New Development” will be held in connection with the BeWS-10. BeYOND is working as a communication platform for researchers and industry with the aim to bring ITER to life and to prepare a “fast track” for DEMO.

INTERNATIONAL ORGANIZING COMMITTEE

<i>Anton Möslang (Chair)</i>	<i>Karlsruhe Institute of Technology, Germany</i>
<i>Christopher Dorn</i>	<i>Materion Brush Inc., Brush Beryllium & Composites, U.S.A.</i>
<i>Victor Pansyrny</i>	<i>A. A. Bochvar Institute, Russia</i>
<i>Masaru Nakamichi</i>	<i>Japan Atomic Energy Agency, Japan</i>
<i>Irina Tazhibayeva</i>	<i>Institute of Atomic Energy of National Nuclear Center, Kazakhstan</i>

PROGRAM AND LOCAL ORGANIZING COMMITTEE

<i>Angel Ibarra</i> <i>(Chair of local org. committee)</i>	<i>Ciemat, Spain</i>
<i>Pavel Vladimirov</i> <i>(Chair of progr. Committee)</i>	<i>Karlsruhe Institute of Technology, Germany</i>
<i>Aniceto Goraieb</i>	<i>Karlsruhe Beryllium Handling Facility GmbH</i>
<i>Vladimir Chakin</i>	<i>Karlsruhe Institute of Technology, Germany</i>

Appendix 2: Final Programme

BeWS-11 Final Program (12 – 13 September 2013)

Thursday, September 12

8:30 – 9:00 **Registration**

9:00 – 9:15 **Welcome**

Plenary Session

Chair: A. Möslang

M. Zmitko	F4E, EU	09:15	-	09:35	Development and Qualification of Beryllium Materials for the EU Test Blanket Module: Strategy and R&D Achievements
R. Giniyatulin	Efremov Institute, RF	09:35	-	09:55	Beryllium Materials for the ITER First Wall panels in Russian Federation
M. Nakamichi	JAEA, Japan	09:55	-	10:15	Recent Progress on R&D of Beryllides as Advanced Neutron Multiplier for DEMO Reactors in Japan
L. Ryczek, K. Smith	Materion, USA	10:15	-	10:35	Materion: Business Update and New Materials Capabilities

Break (25 min) 10:35 – 11:00

Technical Session 1: HIDOBE-01 PIE

Chair: M. Zmitko

A. Vītiņš	Institute of Chemical Physics, Latvia	11:00	-	11:20	Tritium Release from HIDOBE-01 (798 K) Beryllium Pebbles on Annealing with Simultaneous Electron Radiation and Magnetic Fields Review
M. Klimenkov	KIT, Germany	11:20	-	11:40	TEM Characterization of Beryllium Pebbles after Neutron Irradiation up to 3000 appm of Helium Production (HIDOBE-01)
E. Alves	IST, Portugal	11:40	-	12:00	Oxidation of Neutron Irradiated Be Pebbles
V. Chakin	KIT, Germany	12:00	-	12:20	Some Conclusions and Challenges from the HIDOBE-01 PIE Results

Lunch 12:20 – 14:00

Technical Session 2: Beryllides

Chair: M. Nakamichi

J.-H. Kim	JAEA, Japan	14:00	-	14:20	Preliminary Synthesis of Plasma-Sintered Binary Beryllides
P. Kurinskiy	KIT, Germany	14:20	-	14:40	Characterisation of Be-Ti rod fabricated by hot extrusion

V. Savchuk	Ulba Metallurgical Plant, Kazakhstan	14:40	–	15:00	Some Properties of the Tantalum Beryllides
K. Ochiai	JAEA, Japan	15:00	-	15:20	Nuclear Analysis of Beryllides as Advanced Neutron Multipliers for DEMO Blankets

Break (20 min) 15:20 – 15:40

Technical Session 2: Beryllides (cont'd) and Beryllium Safety

Chair: P. Kurinskiy

D. Wakai / M.Nakamichi	JAEA, Japan	15:40	–	16:00	Optimization of Beryllide Electrode Fabrication as Raw Material for Granulation by the Rotating Electrode Method
K. Yonehara / J.-H. Kim	JAEA, Japan	16:00	–	16:20	Prototypic Pebbles Fabrication of Titanium Beryllide with Different Chemical Composition
K. Munakata	Akita University, Japan	16:20	–	16:40	Oxidation Behavior of Be ₁₂ Ti Prepared by Plasma-sintering Method – Results of Step-wise Temperature Control Experiments
T. Shibayama / M.Nakamichi	Hokkaido University, Japan	16:40	-	17:00	Improvement of Irradiation Hardening Measurements for Be ₁₂ Ti by Nano-Indentation Method
K. Nojiri	NGK, Japan	17:00	-	17:20	Environmental Control of Beryllium in NGK

Workshop Banquet

21:00

Restaurant

Friday, September 13

Technical Session 3: Beryllium for Fusion

Chair: B.N. Kolbasov / R. Giniyatulin

Ch. Dorn	Materion, USA	9:00	–	9:20	Beryllium as a Fusion First Wall Material
M. Köppen	Forschungszentrum Jülich, Germany	9:20	-	9:40	Interaction of Energetic Ions with Beryllium and Be-containing Mixed Materials
R. Rolli	KIT, Germany	9:40	–	10:00	Tritium Release Properties of Beryllium Grades of Materion Corporation Production after Loading by Tritium/Hydrogen Gas Mixture
T. Weber	Forschungszentrum Jülich, Germany	10:00	–	10:20	High Heat Flux Testing of Beryllium Armoured Plasma Facing Components at Forschungszentrum Jülich
J. Reimann	KIT, Germany	10:20	–	10:40	Packing Experiments of Beryllium Pebble Beds for the Fusion Reactor HCPB Blanket

Break (20 min) 10:40 – 11:00

B.N. Kolbasov	Kurchatov Institute, RF	11:00	–	11:20	Some thoughts about beryllium resources, impurities in it and necessity of detritiation after irradiation
---------------	-------------------------	-------	---	-------	---

Technical Session 4: Beryllium for Fission

Chair: V. Chakin

S. H. Kang	KAERI, Korea	11:20	–	11:40	Radiation-induced Microstructure Evolution of Beryllium Reflector in Research Reactor Application
P. Vladimirov	KIT, Germany	11:40	-	12:00	X-ray Absorption Tomography of Neutron Irradiated Beryllium after Post Irradiation Annealing
Yu. I. Trifonov	NIKIET, RF	12:00	–	12:20	Development of Thermo-Mechanical Computational Model for Circular Beryllium Reflector

Lunch 12:20 – 14:00

Technical Session 5: Advanced Beryllium Production Technologies

Chair: Ch. Dorn

E. Vidal	Materion, USA	14:00	-	14:20	Materion's Technology Support to Fission and Fusion Programs
I.B.Kupriyanov	Bochvar Institute, RF	14:20	-	14:40	Development of beryllium pebbles with fine grain structure for Fusion Application

S. Mueller	Forschungszentrum Strangpressen, Germany	14:40	-	15:00	Extrusion of Beryllium Powder
M.A.Gallilee	CERN, Switzerland	15:00	-	15:20	Fabrication Considerations for Large Beryllium Structures
K. Smith	Materion, USA	15:20	-	15:40	Beryllium Health & Safety Update

Break (20 min) 15:40 - 16:00

Technical Session 6: Modeling of beryllium materials

Chair: P. Vladimirov

D. Bachurin	KIT, Germany	16:00	-	16:20	Ab-initio Study of Hydrogen on Beryllium Surfaces
Ch. Stihl	KIT, Germany	16:20	-	16:40	Hydrogen Interaction on Be (0001) Surface
Z.K. Sattinova L.N. Gumilyev	Eurasian National University, Kazakhstan	16:40	-	17:00	Numerical Research of the Beryllia Ceramics Formation Process
V. Borodin / P.Vladimirov	Kurchatov Institute, RF	17:00	-	17:20	Molecular Dynamics Simulation of Atomic Displacement Cascades in Beryllium

Final Conclusions 17:20 - 17:30
Adjourn 17:30

Appendix 3: Abstracts of presentations without submitted papers

Development and qualification of beryllium materials for the EU Test Blanket Module: Strategy and R&D achievements

M. Zmitko¹, Y. Poitevin¹, A. Moeslang², V. Chakin², P. Vladimirov², P. Kurinskiy²,
S. van Til³, L. Magielsen³, E. Alves⁴, G. Kizane⁵

¹*Fusion for Energy, Barcelona, Spain*

²*Institut fuer Materialforschung I, KIT, Karlsruhe, Germany*

³*NRG Petten, Petten, The Netherlands*

⁴*Instituto Tecnológico e Nuclear (ITN), Sacavém, Portugal*

⁵*Institute of Solid State Physics (ISSP), Riga, Latvia*

Europe has developed two reference breeder blankets concepts that will be tested in ITER under the form of Test Blanket Modules (TBMs) located in a common equatorial port of ITER: i) the Helium-Cooled Lithium-Lead (HCLL) concept which uses the eutectic Pb-15.7Li as both breeder and neutron multiplier, ii) the Helium-Cooled Pebble-Bed (HCPB) concept containing lithium ceramic pebbles as breeder and beryllium pebbles as neutron multiplier. Both concepts are using 9Cr-WVTa Reduced Activation Ferritic Martensitic (RAFM) steel as structural material, the EUROFER, and pressurized Helium technology for heat extraction.

The paper gives a brief general description of the European HCPB TBM design and the main design requirements including the requirements to beryllium multiplier material. The EU TBMs development and qualification plan with identification of the main milestones will be also presented.

The main part of the paper will be devoted to the presentation of beryllium materials development strategy, qualification plan and current status of research, development and characterization. The achieved results on fabrication technologies development, materials characterization and performance under TBM/DEMO relevant conditions, including the performance under neutron irradiation and thermo-mechanical performance will be overviewed.

Beryllium Materials for the ITER First Wall Panels in Russia Federation

R.Giniiatulin^{*1}, Igor Mazul¹, Alexander Gervash¹, Igor Kupriyanov², Victor Sizenev³,
Leonid Gitarsky³

¹*Efremov Institute, Saint-Petersburg, Russia*

²*Bochvar Institute, Moscow, Russia*

³*JSC "Kompozit", Korolev, Moscow Region, Russia*

The ITER first wall (FW) panels will be coated by the beryllium flat tiles. For the present time three beryllium grades (S-65, TGP-56FW and CN-G01) are accepted for the FW application. Basing on the present FW design about four tons of 8-mm thick tiles are required to cover Russian Federation (RF) responsibility in FW production (40% of the FW panels). The beryllium grades TGP-56FW and S-65 will be used for this purpose. The R&D works are performed in the frames of the preparation for serial tiles production.

The results of experimental machining of Be-tiles are presented. Electric discharge machining (EDM) was used to produce developed patches of the small Be-tiles from large cylindrical billet (D~520 mm, H~230 mm). Different cutting regimes were investigated where cutting ratio, thickness of the cutting material and EDM parameters were varied. Performed metallographic analysis showed that surface quality depends from cutting ratio. This helped to optimize cutting ratio to get acceptable surface quality. It was detected that different EDM cutting ratio gives different thickness of the damaged layer with it maximum thickness about 30 micrometers. This layer has cracks which are evidence of the stresses. The chemical milling was used to remove damaged layer.

The paper concludes that the industry in RF is ready to produce the tons of small-size beryllium tiles, but additional R&Ds for ITER-like plasma heat loads influence to the surface changes and components life-time are required.

Recent Progress on R&D of Beryllides as Advanced Neutron Multipliers for DEMO Reactors in Japan

M. Nakamichi, J-H. Kim

*Fusion Research and Development Directorate, Japan Atomic Energy Agency,
2-166, Omotedate, Obuchi, Rokkasho, Kamikita, Aomori, 039-3212, Japan*

DEMO reactors require advanced neutron multipliers that have higher stability at high temperature. Beryllium intermetallic compounds (beryllides) are the most promising advanced neutron multipliers. Development of the advanced neutron multipliers has been started between Japan and the EU in the DEMO R&D of the International Fusion Energy Research Centre (IFERC) project as a part of the Broader Approach activities. In Japan, beryllides fabrication R&D has been carried out in the DEMO R&D building at IFERC, Rokkasho. The Beryllium (Be) Handling Room has been installed in the DEMO R&D building. In this facility, synthesis, treatment, machining and characterizations of beryllides and its pebbles are being performed.

Because Beryllides are too brittle to allow production of the pebbles, establishing fabrication techniques for beryllides is a key issue for development of the advanced neutron multipliers. Conventional syntheses of the beryllides involve a powder metallurgy process involving a hot isostatic pressing method, a casting method, and an arc-melting method. However, beryllides synthesized conventionally are so brittle that it was not easy to fabricate the block or rod type by these methods.

On the other hand, a plasma sintering method has been proposed as a new technique for beryllides synthesis and joining because this method results in powder surface activation that enhances powder particle sinterability and reduces high temperature exposure. From the results of beryllide synthesis experiments, it was clarified that the not only disk type but rod type of beryllide has been successfully fabricated by the plasma sintering method.

To fabricate the prototypic beryllide pebbles using the plasma-sintered beryllide rod, the rotating electrode method (REM) was selected because the experience base for its use is broad for not only Be pebbles but also metallic pebbles in industry in general. The result of beryllide granulation revealed that the prototypic beryllide pebbles with 1 mm in average diameter were successfully fabricated.

In this study, the recent progress on R&D of beryllides as the advanced neutron multipliers in Japan will be presented.

Materion: Business Update and New Materials Capabilities

Lawrence Ryczek and Keith Smith

Materion Brush Beryllium & Composites

Materion is operating the most advanced Be facility in the world which includes the recently constructed Beryllium Primary Production Facility ("Pebble Plant"). A review of the current operational status is presented. The company has also made progress in the development and commercialization of advanced materials: metal matrix composites, aluminum-beryllium castings and amorphous alloys.

TEM characterization of beryllium pebbles after neutron irradiation up to 3000 appm of helium production (HIDOBE-01)

Michael Klimenkov^{1*}, Vladimir Chakin¹, Anton Möslang¹ and Rolf Rolli²

¹ Karlsruhe Institute of Technology, (IAM-AWP), Karlsruhe, Germany

² Karlsruhe Institute of Technology, (IAM-WBM), Karlsruhe, Germany

Beryllium in the form of pebbles is planned as neutron multiplier in the European Helium Cooled Pebble Bed (HCPB) concept of a DEMO breeding blanket. Beryllium pebbles with a diameter of 1 mm produced by the Rotating Electrode Method were subjected to transmission electron microscopy (TEM) studies after irradiation at the HFR, Petten, at temperatures of 686, 753, 861, and 968 K. The calculated helium production in the pebbles was in the range from 2090 to 3090 appm.

Microstructural investigations of irradiated beryllium using transmission electron microscopy (TEM) show the formation of gas bubbles or cavities as disks of hexagonal shape for all four irradiation temperatures. The disks were oriented in the (0001) basal plane with a height directed along the [0001] “c” axis. The average diameters of the bubbles increase from 7.5 nm in the specimen irradiated at 686K to 80 nm in the specimen irradiated at 968K. The bulk densities of bubbles accordingly decrease from $4.4 \cdot 10^{22}$ to $3.8 \cdot 10^{20} \text{ m}^{-3}$ with increasing irradiation temperature. The swelling of the pebbles measured based on TEM images increases from 0.6% at 686K up to 6.5% at 968 K.

Additionally, analytical investigations of precipitates in irradiated and unirradiated Be using Energy Dispersive X-ray analysis (EDX) for detection of elements with $Z > 6$ and Electron Energy Loss spectroscopy (EELS) were performed. The knowledge concerning influence of neutron irradiation on precipitates size and spatial distribution is important for the understanding of tritium release behavior, swelling and mechanical properties. The analytical investigations show that mainly Fe- or Si-rich precipitates are not homogeneously distributed in the pebble's material. They are located inside grains as well as on the grain boundaries. Two-dimensional elemental maps reveal the existence of areas with high concentration of precipitates as well as areas without any precipitates over the ranges of several micrometers. The precipitates tend to fill two dimensional intergrain surfaces. Such interfaces are visible in TEM as chains of precipitates in the unirradiated material or chains of bubbles in the irradiated material. The He bubbles ordered on the grain boundaries often show a size different from the bubbles located inside grains. The crystallographic orientation relationship of Be grains was also studied.

Oxidation of neutron irradiated Be pebbles

E. Alves¹, N. Catarino¹, L. C. Alves¹, S. van Til²

¹*IPFN, Instituto Superior Técnico Portugal*

²*NRG, Nuclear Research and consultancy Group, Netherlands*

In this study we present a detailed analysis of chemical composition and reactivity of Be pebbles exposed to neutron fluxes during the HIDOBE-01 campaign. The pebbles were irradiated up to 3000 appm He production. Irradiation defects can introduce changes on the mechanical and structural properties with impact on the chemical reactivity of the pebbles.

To get information on the influence of the irradiation the oxidation kinetics of Be pebbles follow a isothermal oxidation process at 700 °C under controlled atmosphere with a relative humidity of 55-60% H₂O. A different set was annealed in a mixture of 60%O₂+40%N₂ to assess the influence of the oxygen availability in the atmosphere. The oxide layer thickness was measured by ion beam analysis using the Rutherford backscattering technique (RBS) and the oxidation rate determined. The structural integrity of the pebbles was assessed by secondary electron microscopy (SEM). The results point to the formation of a stable BeO layer on the irradiated pebbles when annealed up to 700 °C in oxygen reach atmospheres. The oxidation rate is faster for the samples oxidized on H₂O atmosphere. Besides the atmosphere also the surface area plays a role on the oxidation rate. This result is valid at least during the first 18 h. Further studies are necessary to prove the long term stability of this layer.

Some Properties of the Tantalum Beryllides

S. Kozhakhmetov¹, B. Arinov², V. Savchuk², A. Vechkutov², B. Zorin²

¹ – *Institute of High Technology, Almaty, Kazakhstan*

² – *Ulba Metallurgical Plant, Ust-Kamenogorsk, Kazakhstan*

The paper presents the research results on synthesis of tantalum beryllides and study of some properties for obtained compounds. The work shows that Ta₂Be₁₇, TaBe₁₂ intermetallides can be obtained by powder metallurgy methods. The paper includes information on the synthesis modes for tantalum beryllides, the results of X-ray structure analysis, the microstructure research, data of density measurement, microhardness, electrical conductivity and other properties. The possible fields of application for these compounds are identified.

Key words: beryllium, tantalum, beryllide, synthesis, X-ray structural analysis, microstructure.

Nuclear Analysis of Beryllides as Advanced Neutron Multipliers for DEMO Blankets

K. Ochiai, J-H. Kim, M. Nakamichi

*Fusion Research and Development Directorate, Japan Atomic Energy Agency,
2-166, Omotedate, Obuchi, Rokkasho, Kamikita, Aomori, 039-3212, Japan*

Tritium needed as a fuel for fusion reactors is produced in the fusion blanket region by neutron capture reaction of lithium-6 (${}^6\text{Li}$). Neutron multiplier is required for adequate tritium breeding in the blanket of fusion reactors. Pure beryllium metal (Be) is one of the candidate materials for neutron multipliers in the fusion blanket. However, in fusion reactors including the demonstration fusion power (DEMO) reactors under high neutron flux and high temperature, some problems have been anticipated such as volumetric swelling and hydrogen generation reaction of Be. Accordingly, advanced neutron multipliers with lower swelling and higher stability at high temperature are desired in pebble-bed blankets where both neutron multipliers and tritium breeders are supposed to be loaded as type of pebble, which would greatly affect fusion reactor design, especially the blanket operating temperature.

Beryllium intermetallic compounds (beryllides) are the most promising advanced neutron multipliers. Development of advanced neutron multipliers has been started between Japan and the EU in the DEMO R&D of the International Fusion Energy Research Centre (IFERC) project as a part of the Broader Approach activities.

In Japan, synthesis and granulation of beryllide were successfully performed by a combination of the plasma sintering method and the rotating electrode method. As next step, we are starting to prepare a benchmark experiment using beryllide for fusion neutronics evaluation for DEMO blankets design.

In this study, the recent status of neutronics evaluation in the fusion blankets using Be including beryllide will be presented.

Oxidation Behavior of Be₁₂Ti Prepared by Plasma-sintering Method – Results of Step-wise Temperature Control Experiments

K. Munakata¹, K. Wada^{1*}, J.H Kim², M. Nakamichi²

¹*Faculty of engineering and resource science, Akita University,
1-1, TegataGakuen-machi, Akita, 010-8502, Japan*

²*Fusion Research and Development Directorate, Japan Atomic Energy Agency,
2-166, Omotedate, Obuchi, Rokkasho, Kamikita, Aomori, 039-3212, Japan*

Titanium beryllides such as Be₁₂Ti are alternatives to beryllium as the neutron multiplier of the fusion reactor blanket. Be₁₂Ti is known to have advantages over metallic beryllium in terms of high melting point, lower swelling, higher chemical stability and so forth. This time, the authors examined oxidation behavior of Be₁₂Ti sample fabricated by a plasma-sintering method. Oxidation behavior of Be₁₂Ti was experimentally studied under wet argon gas flow.

In the experiments, the plasma-sintered Be₁₂Ti samples were placed under a flow of an argon gas containing 10,000 ppm (1%) of water vapor. In our previous studies, the temperature of the samples had been raised from 313 K up to 1273 K with the ramp rate of 5 K/min, and then the reactor temperature had been held at 1273 K for more than 24 h. However, in this work, the reactor temperatures were differently controlled, in which the reactor temperatures were raised stepwise to 1273 K. At each temperature experimented, exposure of the plasma-sintered Be₁₂Ti sample to water vapor was continued until concentrations of hydrogen produced via oxidation of surface of the plasma-sintered Be₁₂Ti sample decreased to undetectable levels. Concentrations of hydrogen generated from the samples were measured with a gas chromatograph. After the experiments, the surface of the plasma-sintered Be₁₂Ti samples was characterized by SEM and XRD. The results of this new experimental approach are talked in the presentation.

Improvement of irradiation hardening measurements for Be₁₂Ti by nano-indentation method

Tamaki Shibayama¹, Jae-Hwan Kim², Masami Ando² and Masaru Nakamichi²

¹ *Center for Advanced Research of Energy and Materials
Faculty of Engineering, Hokkaido University,
Sapporo, Hokkaido 060-8628, Japan*

² *Fusion Research and Development Directorate, Japan Atomic Energy Agency,
Rokkasho-mura, Kamikita-gun, Aomori 039-3212, Japan*

Beryllium intermetallic compounds (beryllides) such as Be₁₂Ti are candidate materials for advanced neutron multipliers of fusion energy applications beyond DEMO. Recently, Japan Atomic Energy Agency (JAEA) has successfully developed the beryllides in large-scale production by the plasma sintering method. In the beginning of the development of new beryllides, the beryllides have small grains with several impurities and oxidized phases due to the sintering process after the mechanical alloying process. However, the plasma-sintered beryllides have relatively larger grains with less impurities and secondary phases such as Ti rich beryllide phase and unreacted raw materials compared to the former beryllides, it is quite difficult to evaluate irradiation hardening of the plasma-sintered beryllides by nano indentation method. Therefore we have to confirm the correlation between the hardness and the microstructure. We are making efforts to evaluate irradiation hardening of Be₁₂Ti when it updated. Our recent activities of irradiation hardening measurements effects on beryllides study will be presented.

The objective in this study is to improve irradiation hardening measurements by nano-indentation method, especially effects of inhomogeneous distributed microstructure on irradiation hardening in the beryllides.

In this study, we found the screening method to exclude the results obtained from the secondary phase comparing the elastic modulus or the stiffness by applied load vs. indenter displacement curve.

This paper has been prepared as an account of work assigned to the Japanese Implementing Agency under the Procurement Number IFERC T4PA03-JA within the "Broader Approach Agreement" between the Government of Japan and the European Atomic Energy Community.

Beryllium as a Fusion First Wall Material

C.K. Dorn¹⁾, E. E. Vidal¹⁾, and S. H. Goods²⁾

1) Materion Brush Inc., Brush Beryllium & Composites, 14710 West Portage River South Road, Elmore, Ohio 43416-9500 U.S.A.

2) SH Goods Consulting Services, 837 Leland Court, Livermore, California 94550-5832 U.S.A.

Tel: +1-510-415-9747, Fax: +1-419-862-4174, E-mail: chris.dorn@materion.com

Beryllium has been used as a plasma-facing material in fusion test reactors since the 1980s, and it has been designed into the ITER First Wall. There is a current effort in the U.S. to assemble a book on fusion wall materials, and there will be a chapter on beryllium, which will include:

- Introduction
- Candidate Materials for Fusion Wall Applications
 - How Beryllium is Made
 - Historical Use of Beryllium in JET
 - Current Use of Beryllium in JET
 - Specifications for Beryllium in ITER
- Basic Material Properties
 - Physical Properties
 - Mechanical Properties
 - General Considerations
 - Considerations Specific to Fusion Wall Applications
- Fabrication and Joining Technology
 - General Considerations
 - Considerations Specific to Beryllium
 - Considerations Specific to Fusion Wall Applications
 - Other ITER-Related Fabrication & Joining Results
- Irradiation Effects
 - Physical Properties
 - Micro- and Macrostructure
 - Thermal Properties
 - Mechanical Properties
- Tritium Retention and Erosion
- Summary and Conclusion

This presentation will highlight the information presented in this book chapter according to the above outline. The data presented will focus on the three ITER-approved beryllium grades: S-65 (U.S.A.), TGP-56FW (Russia), and CN-G01 (China).

Tritium release properties of beryllium grades of Materion Corporation production after loading by tritium/hydrogen gas mixture

R. Rolli¹, V. Chakin¹, A. Möslang¹, H.-C. Schneider¹, C. Dorn²

¹Institute for Applied Materials, Karlsruhe Institute of Technology, Hermann-von-Helmholtz-Platz 1, 76344 Eggenstein-Leopoldshafen, Germany

²Materion Corporation, 6070 Parkland Boulevard, Mayfield Heights, Ohio 44124-4191, U.S.A

In the European Helium-Cooled Pebble Bed (HCPB) blanket of a DEMO fusion power reactor, it is planned to use 1mm-diameter Be pebbles as the neutron multiplier. Tritium release and retention properties of Be are important safety issues for handling radioactive Be waste after end-of-life operation of the blanket. Be pebbles produced by the Rotating Electrode Process (REP) have a coarse grain size (several hundred microns). In principle, it is considered that hydrogen diffuses comparatively faster in metals which have small grain structure than in larger grain one. However for Be this statement is not so obvious, and therefore demands an experimental confirmation. Additionally, beryllium oxide (BeO) particles located in the grain boundaries seem to be effective traps for diffusing hydrogen. But this point also has to be experimentally confirmed in thermal desorption tests using Be grades with different BeO contents.

In this study, 4 mm-diameter, 2 mm-thick cylindrical specimens were made from five different Materion Brush Inc. beryllium grades. These are S-200F (11.2 μm average grain size, 1 wt.% BeO), S-65 (9.1 μm , 0.6 wt.%), S-65-H (9.7 μm , 0.5 wt.%), I-220-H (7.2 μm , 1.9 wt.%), and O-30-H (7.8 μm , 0.35 wt.%). These five Be grades were selected due to their significantly different average grain sizes and BeO contents.

The specimens were loaded by $^1\text{H}_2+0.05\% \text{ } ^3\text{H}_2$ gas mixture at a temperature of 773 K and a pressure of 400 kPa for 24 h. After that, they were tested by permanent heating mode with a rate of 0.117 K/s up to 1373 K and next duration at the maximum temperature for 10 h. During the heating, the specimens were purged by He+0.1 % $^1\text{H}_2$ gas mixture with 25 ml/min flow rate. The tritium release activity under the tests was measured by a proportional counter.

Subsequent examinations included optical and SEM investigations of the Be specimens both before and after thermal desorption tests. The analysis of the experimental results is used to rank the five Be grades according to their tritium release characteristics.

Presenting Author:

Rolf Rolli

Institute for Applied Materials, Karlsruhe Institute of Technology,
Hermann-von-Helmholtz-Platz 1, 76344 Eggenstein-Leopoldshafen, Germany
rolf.rolli@kit.edu

Phone: +49721 608 25883

Fax: +49721 608 25882

High heat flux testing of beryllium armoured plasma facing components at Forschungszentrum Jülich

T. Weber^{a,*}, J. Du^a, J. Linke^a, T. W. Loewenhoff^a, G. Pintsuk^a, M. O. Wirtz^a

^a*Forschungszentrum Jülich, Institute of Energy and Climate Research, Jülich, Germany*

The high temperature performance of materials is very important for many fields of research such as energy science, aerospace technology, accelerator, power plant technology and in particular in the field of plasma facing components for future fusion reactors. In these fields of research it is important to know how a material behaves under high steady state or transient heat fluxes resulting in high temperatures and strong temperature gradients, and how these environmental conditions affect the material properties and lifetime of a component.

With this respect, the electron beam facilities JUDITH 1 and JUDITH 2 [1] at Forschungszentrum Jülich GmbH are ideal test beds to investigate the high temperature performance of a wide range of materials. Cyclic quasi-stationary and transient heat loads can be simulated. Especially the location in a hot cell (JUDITH 1) and the qualification to handle beryllium (both machines) make these facilities an exceptional material testing setup.

The facilities mainly consist of a powerful electron gun (up to 200 kW), a vacuum chamber in which the samples are mounted, a number of diagnostic devices and a water cooling circuit. Thereby samples are scanned with a focussed electron beam with frequencies in the kHz range to achieve nearly homogeneous loading conditions. Due to a very flexible and individual programmable system for electron beam pattern generation, very homogeneous load distributions can be achieved during static load tests and highly realistic simulations of ITER relevant transient heat loads become possible. Furthermore, static and transient loads can be combined in one single experiment.

For both facilities the diagnostic devices comprise infrared pyrometers and infrared camera systems. Thermo couples can be installed at the sample and along the water circuit.

After the demonstration of the possibilities of the facilities, typical examples of electron beam loading experiments of plasma facing components using beryllium armour are presented.

- [1] P. Majerus, et al.; *The new electron beam test facility JUDITH II for high heat flux experiments on plasma facing components*; Fusion Engineering and Design 75 – 79 (365 – 369), 2005

*Corresponding author: tel.: +49 2461 61 5843, e-mail: tho.weber@fz-juelich.de (T. Weber)

Radiation-induced Microstructure Evolution of Beryllium Reflector in Research Reactor Application

Suk Hoon Kang*, Young-Bum Chun**, Yong Hwan Jeong, and Tae Kyu Kim

Korea Atomic Energy Research Institute, Daejeon, Korea

The lifetime of the beryllium reflector elements is usually determined by neutron radiation induced swelling, which results in a bending or cracking of the reflector parts. Therefore, investigation of radiation influence on dimensional stability of beryllium is very important. In this paper, the proton radiation damage of the beryllium grade manufactured by vacuum hot pressing (VHP) or hot extrusion (HE) was investigated to emulate the effect of neutron radiation. The beryllium samples were sliced into 1cm X 1cm square sheet. The surface of the sheet was electro-polished by 10% perchloric acid. The microstructure of beryllium was observed by electron backscattered diffraction (EBSD) and the grain size and preferred orientations were estimated. The electro-polished surface was irradiated by protons at room temperature; the acceleration voltage, and the proton amounts were 120 keV, and 2.0×10^{18} ions/cm², respectively. A TEM sample of proton irradiated beryllium sample was manufactured using focused ion beam (FIB), the sample was sliced into thin foil to be observed along the perpendicular direction of proton irradiation. The microstructure evolution during proton irradiation have been observed by bright field image and selective area diffraction pattern (SADP) of TEM. The beryllium target samples were radiated along two different directions; the first one was perpendicular and the other one was parallel to the extrusion direction. A strong fiber texture was developed in the beryllium manufactured by hot extrusion process; the basal plane in the majority of grains arranged along the extrusion direction. The radiation induced voids were observed to form preferentially on the basal plane. While the radiation direction was parallel with basal plane, the amounts of radiation damage seemed to be considerably reduced.

* *Corresponding Author*

Suk Hoon Kang

Email: shkang77@kaeri.re.kr

Tel : +82-42-868-8644, Fax : +82-42-868-8549

Materion's Technology Support to Fission and Fusion Programs

Edgar Vidal

Materion Brush Beryllium & Composites

Materion has made significant advances in research and development and sales and marketing of beryllium materials this past year. We will briefly review this year's activities that include: improvements in the development of a process to fabricate beryllium minispheres for fusion applications; S-65 beryllium has been produced for use in the ITER program; Materion has worked towards the production and characterization of our materials for use in high temperature gas-cooled power reactors (HTGR); and, a process to produce Flibe salts has been invented to support the Liquid Salt Reactor programs in the US and around the world.

Extrusion of Beryllium Powder

S. Mueller

*Forschungszentrum Strangpressen, TU Berlin, Sekr. TIB 4/1-2, Gustav-Meyer-Allee 25,
13355 Berlin; +49 30 314 72 732; soeren.mueller@tu-berlin.de*

A.Goraieb

*KBHF GmbH, KIT – Campus Nord, Gebäude 453, Hermann-von Helmholtz-Platz 1, 76344
Eggenstein-Leopoldshafen; +49 721 608 23 640*

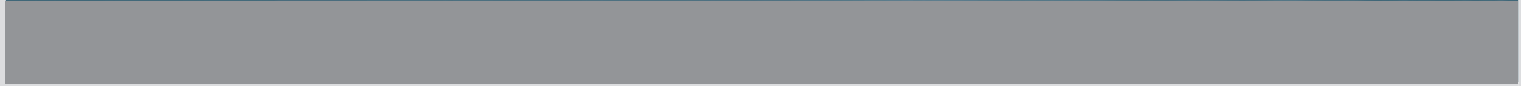
The extrusion of metal powders is used when the casting of the restiform semifinished products or of the billets for the extrusion is not possible. The metal powder has to be compressed before it can be extruded. This can either be done outside of the extrusion press or in the extrusion press. If the powders are precompressed outside of the extrusion press this is usually done by cold (CIP) or hot (HIP) isostatic pressing or sintering. If the extrusion press is vertically aligned loose powder can be filled in the container and then be compressed by the extrusion stem. Since most industrial extrusion presses have a horizontal construction layout the loose powder has to be canned in a metal case in order to make it possible to transport the powder into the press. After the filling the metal can is usually evacuated and sealed. During the extrusion itself the powder and the canning around the powder core will be extruded thus the surface of the extrudate will be the canning metal.

For the extrusion of Beryllium powder the extrusion in a metal canning has some positive side effects. The billet preparation for the extrusion can completely be done in a glove box. This means that the filling of the can, the evacuation and the sealing of the can by welding is all done in a glove box. Thus, if the billet is handled for the extrusion there is no exposition of the Beryllium to the environment. Since the canning material is also extruded together with the Beryllium also in the extruded form the Beryllium is contained inside of the can material. So again there is no exposition of the extruded Beryllium to the environment. Because of this the extrusion of Beryllium powder can be done outside of a glove box.

In order to test the described method for the extrusion a stainless steel cylinder was filled with Titanium powder as a substitute material and then heated up to 1000°C. The hot billet was then extruded to a solid rod. The steel can was designed that the cutting of the rod from the extrusion discard was only done in the steel. This concept was then transferred to the extrusion of Beryllium powder. The Beryllium powder was filled into a Titanium can which was evacuated and sealed by welding. The Titanium container was the placed into a thick-walled stainless steel canning which was also sealed by welding. Extrusion trials with these cans were then performed at different billet temperatures and different heating times.

Appendix 4: Participants

Name		Organization	Country
Eduardo	Alves	ITN/IST	Portugal
Dimitry	Bachurin	KIT	Germany
Vladimir	Borodin	NRC Kurchatov Institute	Russia
Vladimir	Chakin	KIT	Germany
Young-Bum	Chun	Korea Atomic Energy Institute	Korea
Christopher	Dorn	Materion Brush Inc.	U.S.A.
Mark	Gallile	CERN	Switzerland
Cedric	Garion	CERN	Switzerland
Radmir	Giniiatulin	Efremov Institute	Russia
Aniceto	Goraieb	KBHF Gmbh	Germany
Jutta	Howell	KIT	Germany
Suk Hoon	Kang	Korea Atomic Energy Institute	Korea
Jae-Hwan	Kim	Japan Atomic Energy Agency	Japan
Michael	Klimenkov	KIT	Germany
Michael	Koeppen	KIT	Germany
B.N.	Kolbasov	Kurchatov Institute	Russia
Igor	Kupriyanov	A.A. Bochvar Research Institute	Russia
Petr	Kurinskiy	KIT	Germany
Anton	Moeslang	KIT	Germany
Sören	Mueller	TU Berlin	Germany
Kenzo	Munakata	Akita University	Japan
Patricia	Murphy	Materion Brush Inc.	UK
Masaru	Nakamichi	Japan Atomic Energy Agency	Japan
Keigo	Nojiri	NGK Insulators	Japan
Kentaro	Ochiai	Japan Atomic Energy Agency	Japan
Joerg	Reimann	KIT	Germany
Rolf	Rolli	KIT	Germany
Lawrence	Ryczek	Materion Brush Inc.	USA
Victor	Savchuk	Ulba Metallurgical Plant	Kasakhstan
Z.K.	Sattinova	Eurasian National Univ. , Astana	Kasakhstan
Tamaki	Shibayama	Hokkaido University	Japan
Keith	Smith	Materion Brush Inc.	USA
Christopher	Stihl	KIT	Germany
Yurij	Trifonov	JSC „NIKIET“ Moscow	Russia
Edgar	Vidal	Materion	USA
Aigar	Vitins	University of Latvia	Latvia
Pavel	Vladimirov	KIT	Germany
Daisuke	Wakai	Japan Atomic Energy Agency	Japan
Thomas	Weber	Forschungszentrum Jülich	Germany
Kazuo	Yonehara	Japan Atomic Energy Agency	Japan
Milan	Zmitko	Fusion for Energy (F4E)	Spain



ISSN 1869-9669
ISBN 978-3-7315-0309-5

